

# **A high resolution Silicon Strip Telescope and its application at the DESY II Test Beam Facility.**

## **Dissertation**

zur Erlangung des Doktorgrades  
an der Fakultät für Mathematik, Informatik und  
Naturwissenschaften  
Fachbereich Physik  
der Universität Hamburg

vorgelegt von  
UWE KRÄMER  
aus Saarbrücken, Deutschland

Hamburg

2020

Gutachter/innen der Dissertation:	Prof. Dr. Erika Garutti Dr. Ties Behnke
Zusammensetzung der Prüfungskommission:	Prof. Dr. Erika Garutti Dr. Ties Behnke Prof. Dr. Robin Santra Prof. Dr. Ingrid-Maria Gregor Dr. Heinz Graafsma
Vorsitzende/r der Prüfungskommission:	Prof. Dr. Robin Santra
Datum der Disputation:	15.12.2020
Vorsitzender Fach-Promotionsausschusses PHYSIK:	Prof. Dr. Günther H. W. Sigl
Leiter des Fachbereichs PHYSIK:	Prof. Dr. Wolfgang Hansen
Dekan der Fakultät MIN:	Prof. Dr. Heinrich Graener



## Abstract

---

The next generation of experiments probe the region beyond the standard model of particle physics to a precision unreachable by current experiments. This necessitates the development of new detector systems, pushing current technologies to their limit in spatial, energy and time resolution. The development of such detectors requires facilities capable of testing detectors in a situation as close as possible to the final experiment, as well as external devices that allow an independent measurement beyond the limitations of the detector system. This is provided by test beam facilities that produce high energy particles for sensor testing and telescope systems providing high precision reference measurements.

The Lycoris telescope is a new detector designed for the DESY II Test Beam Facility. Project requirements such as the large active area, high precision and strong spatial constraints make commonly used strip and pixel sensors unusable as sensors for the Lycoris telescope. The telescope is therefore based on a hybrid silicon strip sensor developed for the ILC with a thickness of  $320\ \mu\text{m}$  with in metal signal routing allowing for a pitch of  $25\ \mu\text{m}$ . The system includes an integrated power-pulsed readout via the KPIX ASIC.

This thesis encompasses all steps towards the Lycoris telescope including: the design, the sensor assembly, the building and installation of the support structure, the tests of the sensors at the DESY II Test Beam Facility and performance studies of the Lycoris telescope using a dedicated strip track finding algorithm. The sensor is shown to achieve an average single plane efficiency of 96% with a single point resolution of  $7\ \mu\text{m}$ . The average noise level within the sensor is  $0.2\ \text{fC} = 1250\ \text{e}$  resulting in an average signal over noise ratio of 15. The telescope, using the dedicated strip track finding, is shown to reach similar efficiencies and is simulated to achieve a momentum resolution of about  $3.6 \times 10^{-6}\ \text{MeV}^{-1}$  within a 1 T magnetic field.

## Kurzfassung

---

Die nächste Generation von Experimenten erforscht die Region jenseits des Standardmodells der Teilchenphysik bis zu einer Präzision, die mit aktuellen Experimenten unerreichbar ist. Dies erfordert die Entwicklung neuer Detektorsysteme, die die derzeitigen Technologien in Bezug auf räumliche, energetische und zeitliche Auflösung an ihre Grenzen bringen. Die Entwicklung solcher Detektoren erfordert Einrichtungen, die in der Lage sind, die Detektoren in einer Situation zu testen, die dem endgültigen Experiment so nahe wie möglich kommt, sowie externe Geräte, die eine unabhängige Messung über die Grenzen des Detektorsystems hinaus ermöglichen. Dies wird durch Teststrahlanlagen, die hochenergetische Teilchen für Sensortests erzeugen, und durch Teleskopsysteme, die hochpräzise Referenzmessungen ermöglichen, gewährleistet.

Das Lycoris Teleskop ist ein neuer Detektor, der für die DESY II Test Beam Facility entwickelt wurde. Die große aktive Fläche, die hohe Präzision und die starken räumlichen Beschränkungen machen die üblicherweise verwendeten Streifen- und Pixelsensoren als Sensoren für das Lycoris Teleskop unbrauchbar. Das Teleskop basiert daher auf einem für den ILC entwickelten hybriden Silizium-Streifensensor mit einer Dicke von  $320\ \mu\text{m}$ , wobei eine neuartige Signalführung durch weitere Metall lagen im Silizium einen Streifenabstand von  $25\ \mu\text{m}$  zulassen. Das System verfügt über eine integrierte gepulste Auslese durch den KPiX ASIC.

Diese Arbeit umfasst alle Schritte auf dem Weg zum Lycoris Teleskop: die Konstruktion, die Sensormontage, den Bau und die Installation der Stützstruktur, die Tests der Sensoren an der DESY II Test Beam Facility und Leistungsstudien des Lycoris Teleskop unter Verwendung eines für das Teleskop entwickelten Streifenspursuchalgorithmus. Es wird gezeigt, dass der Sensor eine durchschnittliche Effizienz in einer einzelnen Ebene von 96% mit einer Einzelpunktauflösung von  $7\ \mu\text{m}$  erreicht. Der durchschnittliche Rauschpegel innerhalb des Sensors beträgt  $0.2\ \text{fC} = 1250\ \text{e}$ , was zu einem durchschnittlichen Signal-Rausch-Verhältnis von 15 führt. Es wird gezeigt, dass das Teleskop, unter Benutzung des entwickelten Streifenspursuchalgorithmus ähnliche Effizienzen erreicht und mittels Simulation wird gezeigt das eine Impulsauflösung von etwa  $3.6 \times 10^{-6}\ \text{MeV}^{-1}$  innerhalb eines 1 T Magnetfeldes erreicht wird.

# Table of Contents

<b>Abstract</b>	<b>iii</b>
<b>Table of Contents</b>	<b>v</b>
<b>Introduction</b>	<b>xi</b>
<b>I Theory</b>	<b>1</b>
<b>1 Theory of Particle Physics</b>	<b>3</b>
1.1 The Standard Model of Particle Physics . . . . .	3
1.2 Beyond the Standard Model . . . . .	5
<b>II Particle Detectors</b>	<b>9</b>
<b>2 Particle Interaction with Matter</b>	<b>11</b>
2.1 Energy Loss . . . . .	11
2.1.1 Ionization Losses of Heavy Particles . . . . .	12
2.1.2 Ionization Losses of Electrons and Positrons . . . . .	12
2.1.3 Single Interaction Losses . . . . .	14
2.1.4 Bremsstrahlung Losses . . . . .	15
2.2 Particle Deflection . . . . .	16
<b>3 Particle Detectors</b>	<b>19</b>
3.1 Physics of Semiconductors . . . . .	21
3.1.1 Doping . . . . .	22
3.1.2 pn-Junction . . . . .	22
3.1.3 Biasing a pn-Junction . . . . .	23
3.1.4 Charge Collection in a pn-Junction . . . . .	23

3.1.5	Segmented Collection Electrodes for Position Sensing . . . . .	25
3.2	Silicon Tracking Detectors . . . . .	28
3.2.1	Hybrid Sensors . . . . .	28
3.2.2	Monolithic Active Pixel Sensors . . . . .	30
<b>4</b>	<b>Particle Track Reconstruction</b>	<b>33</b>
4.1	Track Finding and Fitting . . . . .	33
4.2	Particle Reconstruction at Test Beams . . . . .	35
4.2.1	Global and Local Coordinate Systems . . . . .	35
4.2.2	Track Model . . . . .	37
4.2.3	Track Finding . . . . .	38
4.2.4	Track Fitting using GBL . . . . .	40
4.3	Alignment . . . . .	42
<b>III</b>	<b>DESY II and Lycoris</b>	<b>45</b>
<b>5</b>	<b>The DESY II Test Beam Facility</b>	<b>47</b>
5.1	The DESY II Synchrotron . . . . .	47
5.1.1	Test Beam Generation . . . . .	49
5.1.2	Beam characteristics . . . . .	51
5.2	The AIDA Trigger Logic Unit . . . . .	54
5.3	The EUDET Type Silicon Telescopes . . . . .	56
5.4	The PCMAG 1T Solenoid . . . . .	59
<b>6</b>	<b>The Lycoris Strip Telescope</b>	<b>61</b>
6.1	Project Requirements . . . . .	61
6.2	The SiD Sensor and Readout . . . . .	67
6.2.1	SiD Sensor . . . . .	68
6.2.2	KPiX ASIC . . . . .	73
6.3	The Sensor Configuration . . . . .	80
6.4	Mechanics . . . . .	85
6.4.1	Telescope Cassette . . . . .	86
6.4.2	Rail System . . . . .	88
6.5	The Data Acquisition System . . . . .	90
6.5.1	Hardware . . . . .	90
6.5.2	Firmware and Software . . . . .	95

---

<b>7</b>	<b>Module Assembly</b>	<b>99</b>
7.1	Assembly . . . . .	100
7.1.1	ASIC Assembly . . . . .	100
7.1.2	Kapton Flex Cable Gluing . . . . .	100
7.1.3	Wire-Bonding . . . . .	103
7.1.4	Frame Gluing . . . . .	104
7.2	IV/CV and Inter-strip using the Probe Station . . . . .	105
7.2.1	Probe Station Setup . . . . .	105
7.2.2	IV/CV Measurement Results . . . . .	108
7.2.3	Inter-strip measurement . . . . .	117
<b>IV</b>	<b>Data Analysis</b>	<b>121</b>
<b>8</b>	<b>Lycoris Telescope Setup at the DESY II Test Beam Facility</b>	<b>123</b>
8.1	Lycoris as a DUT . . . . .	123
8.2	Lycoris within the PCMAG to determine the resolution of the helix . . . . .	127
8.3	Data Taking . . . . .	130
8.3.1	Operation Modes . . . . .	130
8.3.2	Synchronization . . . . .	131
8.3.3	Available Data samples . . . . .	136
<b>9</b>	<b>Event Reconstruction</b>	<b>139</b>
9.1	Reconstruction overview . . . . .	139
9.2	Lycoris Data Analysis . . . . .	142
9.2.1	Charge Calibration . . . . .	143
9.2.2	External Trigger Data Analysis . . . . .	145
9.2.3	Internal Trigger Data Analysis . . . . .	156
9.3	Summary . . . . .	161
<b>10</b>	<b>Module Performance</b>	<b>163</b>
10.1	Operational Performance of the KPiX . . . . .	163
10.2	Calibration Performance . . . . .	166
10.2.1	Humidity Influence . . . . .	171
10.3	Internal Triggering Results at the Test Beam . . . . .	182
10.3.1	<i>Monster Event</i> Suppression . . . . .	184
10.3.2	Beam Test . . . . .	186

10.4 External Triggering Performance . . . . .	189
10.4.1 Noise Study . . . . .	190
10.5 Tracking results . . . . .	202
10.5.1 Charge of <i>Tagged Hits</i> . . . . .	202
10.5.2 Bias Voltage Impact on Lycoris Module Performance . . . . .	207
10.5.3 Single Point Resolution . . . . .	210
10.5.4 Single Plane Efficiency . . . . .	212
10.6 Summary . . . . .	213
<b>11 Lycoris Telescope Performance</b>	<b>217</b>
11.1 Lycoris Track Finding and Fitting . . . . .	217
11.1.1 Charge on Tagged Hits . . . . .	217
11.1.2 Hit Residuals . . . . .	218
11.2 Lycoris Telescope Tracking Efficiency . . . . .	219
11.3 Momentum Resolution of the Lycoris Telescope . . . . .	222
11.4 Summary . . . . .	224
<b>Conclusion and Outlook</b>	<b>225</b>
<b>Acknowledgments</b>	<b>229</b>
<b>Appendices</b>	<b>233</b>
A MIP stopping power . . . . .	235
B Silicon Properties . . . . .	236
C EUFAQ2 . . . . .	237
D Grey Code . . . . .	240
E Pin mapping . . . . .	241
F IV/CV switchbox . . . . .	242
G Custom cabling . . . . .	244
H The KPiX YAML file . . . . .	246
I <i>Kapton Flex Cable</i> gluing step by step . . . . .	250
J Lycoris track finding . . . . .	252
J.1 Strip road search . . . . .	252
J.2 Striplet finder . . . . .	253
K Alignment . . . . .	256
<b>List of Tables</b>	<b>261</b>

**List of Figures**

**263**

**Bibliography**

**277**





# Introduction

Particle physics investigates the fundamental forces and particles that make up the visible universe. The theory of particle physics has developed from the Rutherford model towards a more complex and complete theory. The Standard Model of Particle physics (SM) currently provides the best description of physics for the smallest constituents of the known universe.

While the SM has achieved great success in its descriptions and predictions, many aspects of particle physics are not explained by the SM such as, the necessary charge conjugation parity (CP) to describe the Matter-Antimatter asymmetry in the universe, the masses of neutrinos, the fundamental force of gravity which is not described within the SM, the hierarchy problem and the existence of dark matter and dark energy for which the SM does not provide valid candidates.

The search for Beyond Standard Model (BSM) theories that can explain these issues requires the development of new experiments such as the International Linear Collider (ILC), the Compact Linear Collider (CLIC) or the Circular Electron Positron Collider (CEPC) and Future Circular Collider (FCC). All of these experiments aim for higher sensitivities and require new detectors that push the boundaries of current detectors in resolution, radiation hardness and minimization of material budget to achieve the best possible measurement precision. Tests of these detectors need to be as close to their final environment as possible for validation.

The closest environment to particle physics experiment can be found at test beam facilities around the world such as the DESY II Test Beam Facility. Test beam facilities produce particles with energies a factor 1000 higher than radioactive sources in addition to supplying external devices such as silicon telescopes that provide precise knowledge to the particle location within the detector in order to probe into the sub structure of the detector far beyond its own capabilities.

In this thesis, a sensor designed for the Silicon Detector (SiD) [1], one of two planned detectors concepts for the ILC [2], was taken from the design stage to full functionality with

investigation into performance, assembly and handling. The motivation for this project is driven by the necessity of a new telescope that can work complementary to existing telescopes. The sensor used in this thesis itself provides an avenue to investigate future detector systems. The sensor is a hybrid strip sensor with pitch of  $25\ \mu\text{m}$  using a novel readout method that is achieved through metalization layer routing embedded into the sensor. The sensor provides a large active area coverage of  $92 \times 92\ \text{mm}^2$  with resolutions of about  $7\ \mu\text{m}$  and a small material budget for a hybrid sensor with  $320\ \mu\text{m}$  thickness as the entire readout and routing is integrated in a small area on the sensor eliminating the need for any support structure within the beam path. No detector of this type has ever been successfully assembled before and this thesis investigates both the assembly of the sensor and its performance. A new silicon telescope for the DESY II Test Beam Facility was designed, build and commissioned. The performance of this telescope and its dedicated strip track finding algorithm are investigated.

**Part I**

**Theory**



# Chapter 1

## Theory of Particle Physics

Physics is one of the fundamental fields of research, probing the basic laws of nature. Over time, physics branched into a large variety of research topics such as particle physics.

Particle physics focuses on understanding the smallest components of the universe, elementary particles that make up our universe and the fundamental forces through which they interact with one another. Particle physics as a field has made most of its strides in the 20<sup>th</sup> century during the development of the Standard Model of particle physics (SM). Different experiments have been carried out to hunt for predicted particles/phenomena and in doing so have probed the SM with high precision.

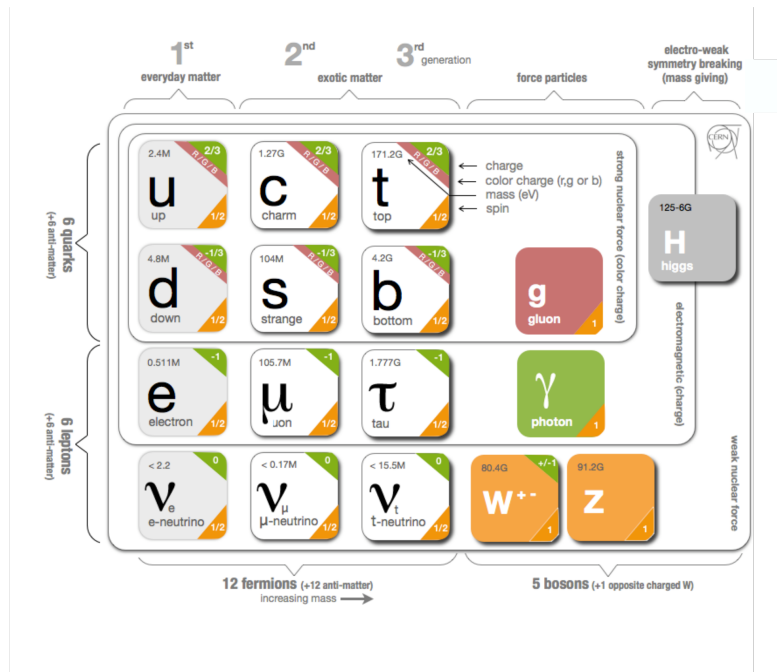
### 1.1 The Standard Model of Particle Physics

The Standard Model of particle physics (SM) [3] describes all known fundamental particles as well as the forces through which they interact. It was developed in the 1960s when the unification of the weak- and the electromagnetic interaction was predicted. Since then it accurately described experiments and survived the scrutiny of follow-up experiments, making accurate predictions to the existence of elementary particles <sup>1</sup>.

The different particles present within the SM are depicted in Figure 1.1. The particle content is split into multiple sub- and sub-sub-categories. The particles are split into two categories based on their spin. All particles with half integer spin are referred to as fermions and all particles with full integer spin are referred to as bosons. Each fermion has a corresponding anti-particle which has the exact same properties as the particle except that any charge the particle possesses has the opposite sign for the anti-particle.

---

<sup>1</sup>Elementary particles are all particles that are not composites of even smaller particles



**Figure 1.1** – The Standard Model of particle physics. Adapted from [4]

Fermions are further sub-categorized into leptons and quarks. Leptons are elementary particles that are split into two sub-categories. Charged leptons are particles that possess  $-1$  elementary (electric) charge<sup>2</sup> while neutral leptons, referred to as lepton neutrinos, possess no elementary charge and no mass.

Quarks are also split into two sub-categories based on their electric charge. Up-type quarks possess  $+2/3$  elementary charge while down-type quarks possess  $-1/3$  elementary charge. In addition to electric charge, quarks possess color charge. It has three different values which are referred to as red ( $r$ ), green ( $g$ ) and blue ( $b$ ). Similar to the electric charge they possess an opposite quantum number value referred to as anti-red ( $\bar{r}$ ), anti-green ( $\bar{g}$ ) and anti-blue ( $\bar{b}$ ) [5]. Neutrons and protons are made up of three quarks each and all composite particles consisting of three quarks are referred to as baryons. Composite particles consisting of two quarks are referred to as mesons. Baryons and Mesons are color neutral, either through a combination of all three colors, or through the combination of a color with its corresponding anti-color.

All fermions exist in what are referred to as particle generations. In each particle generation exists one type of each of the lepton and quark subcategories. The only difference between the generations is that with increasing generation number the mass of the par-

<sup>2</sup>Elementary charge is defined by the electric charge of the electron and is denoted as  $e$

ticles increases. Only the charged fermions with the lowest mass, the first generation of their corresponding sub-category, are stable and make up all forms of visible matter in the universe. Charged fermions of higher generations are unstable and decay into the first generation fermions with varying lifetimes depending on both the coupling of the particles to the interaction. Lepton neutrinos do not decay and are stable in the SM.

All interactions in the SM are mediated by bosons. The interactions describe the fundamental forces and are split into the strong, electromagnetic and weak interactions:

- The strong interaction is mediated by the massless, color charged gluons. The strong interaction is described by Quantum Chromo Dynamics (QCD) and the gluon couples only to particles possessing color charge.
- The electromagnetic interaction is mediated by the massless, neutral photon. The electromagnetic interaction is described by Quantum Electro Dynamics (QED) and the photon couples only to particles possessing electric charge.
- The weak interaction is mediated by the massive  $W$  and  $Z$  bosons. The  $W$  boson possesses an elementary electric charge of  $\pm 1$  whereas the  $Z$  boson is neutral.

The SM also provides a mechanism through which the masses of the elementary particles can be explained via coupling to a scalar potential that is referred to as the Higgs field. The Higgs field generates the masses of the  $W$  and  $Z$  bosons by a process that is referred to as spontaneous symmetry breaking which requires the existence of another massive boson, the Higgs boson[6]. The Higgs boson has been the last missing piece of the SM for a long time but was found in 2012 at the Large Hadron Collider (LHC) [7][8] and completes the Standard Model of particle physics.

## 1.2 Beyond the Standard Model

While the SM has provided accurate descriptions and predictions of both the interactions and existence of fundamental particles, many experiments have found results that are inconsistent with the SM. Many possible explanations exist, one of which is that SM is not complete and only valid at comparably low energies. Some of the unexplained aspects are:

- How does one include the fundamental force of gravity which is not included in the SM?

- Observations of the rotations of spiral galaxies have shown that their movement does not align to the prediction based on all visible matter within the galaxies. As such there must be a large amount of matter that does not interact electromagnetically which is referred to as Dark Matter (DM) [9] and for which the SM does not provide a good candidate.
- What type of energy is responsible for the accelerated expansion of the universe? Based on supernova measurements it is known that the expansion of the universe is accelerating implicating the existence of what is referred to as Dark Energy for which the SM does not provide a valid candidate [10].
- What is the reason for the existence of neutrino masses which were shown to exist in neutrino oscillation experiments[11]? In the SM all neutrinos are massless.
- Which process is responsible for the large discrepancy between matter and anti-matter in the observable universe? Processes exist in the SM which, via Charge Conjugation Parity (CP) violation in weak interactions, can produce more matter than anti-matter though the process in the SM cannot account for the size of the observed discrepancy [12].
- It is known that at some energy scale, latest at the Planck scale at around  $1 \times 10^{19}$  GeV new physics must exist. The Planck scale is the energy scale at which the force of gravity becomes of similar strength to the other interactions, therefore requiring a quantized formulation of gravity. New particles at such a scale would be of similar mass to the scale. The mass of the Higgs boson is affected by loop corrections to other fermions and bosons via renormalization. The Higgs coupling is proportional to the mass of the particle, meaning more massive particle would have larger contributions. It is therefore natural to expect that the mass of the Higgs is close to this scale of new physics. The experimental observation that it is not has no good explanation in the SM where the different couplings would have to cancel out one another down to the 17<sup>th</sup> digit which is considered an unnatural extreme fine tuning.

Theories that try to answer some of the open questions not answered by the SM are grouped into a category which is referred to as Beyond Standard Model (BSM) theories. The probing of both the SM and BSM theories can be split into direct and indirect measurements.

Direct measurements involve the search for new particles with masses higher than the particles in the SM. These measurements are typically done at high energy hadron colliders such as the LHC and its multi purpose detectors and current results indicate that any new particles would have masses in the multi-TeV range. To probe these regions there exist



proposals for even higher energy colliders such as the hadron collider variant of the Future Circular Collider (FCC-hh).

Indirect measurements on the other hand focus on finding deviations from SM predictions, be it in parameters of known particles such as the coupling of the Higgs boson or by searching for rare decays which are not allowed in the SM. Indirect searches are performed either at specialized experiments focusing on one aspect of the Standard Model allowing for extremely high mass sensitivity or at lepton colliders whose collision processes are well understood and as such allow for higher precision measurements of particles within their reach.

Future experiments looking to probe BSM theories indirectly are either currently in construction, like the Mu3e experiment searching for charged lepton flavour violation [13], or in a design phase such as future lepton colliders such as for example the International Linear Collider (ILC) [2]. Several more proposals for future experiments exist which are at varying states of development.

A common aspect of all of these experiments is the need for new high precision detectors beyond current capabilities.



## **Part II**

# **Particle Detectors**



# Chapter 2

## Particle Interaction with Matter

Precision measurements require a good understanding of the different interactions that particles can perform when interacting with matter in order to accurately evaluate the measurement results.

Interactions of particles with matter are typically separated into interactions of charged and interactions of neutral particles. For this thesis, only interactions performed by charged particles are of interest and described here. The interactions are based on either the electromagnetic or the strong interaction. Due to the short range of the strong interaction the electromagnetic interactions dominate all interactions and as a result, the focus in this chapter is put into understanding the electromagnetic interactions of particles with matter. These interactions can be split into two categories. The energy loss of the particle and the deflection of the particles trajectory. While both effects are unavoidable, the former is essential to detect the particles position while the latter hinders an accurate description of the particles trajectory and should be minimized where possible.

This chapter is based on the description provided by [3] which describes the interactions in more detail.

### 2.1 Energy Loss

The exact electromagnetic interaction of particles with matter depends on the type of particle and material as well as the momentum of the particle. For charged particles the processes are split into ionization, excitation, Bremsstrahlung, Cherenkov radiation and transition radiation. For photons they are split into the photoelectric effect, compton scattering and pair production.

For tracking detectors, only ionization, excitation and Bremsstrahlung are relevant and

are looked at in more detail. The exact loss of energy in an interaction cannot be predicted, as both the amount of interactions, as well as the energy loss per interaction are stochastic processes. The average energy loss on the other hand is very well understood though one has to discern between the energy loss of electrons/positrons and the energy loss of heavier particles.

### 2.1.1 Ionization Losses of Heavy Particles

The energy loss is given by the so called mass stopping power which is a density dependent average energy loss and described by the Bethe-Bloch formula which is given as [3]:

$$-\left\langle \frac{dE}{dx} \right\rangle = K z^2 \frac{Z}{A} \frac{1}{\beta^2} \left[ \frac{1}{2} \ln \frac{2m_e c^2 \beta^2 \gamma^2 T_{\max}}{I^2} - \beta^2 - \frac{\delta}{2} \right]. \quad (2.1)$$

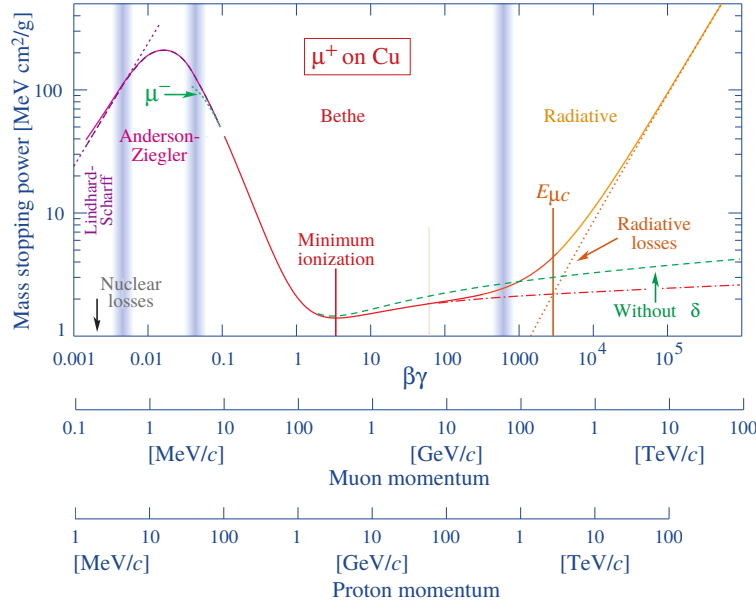
$\beta = \frac{v}{c}$  is the speed  $v$  expressed as fraction to the speed of light  $c$  and  $\gamma = \frac{E}{E_0}$  is the ratio between the particles total energy  $E$  and its rest energy  $E_0$ .  $K = 4\pi N_a r_e^2 m_e c^2$  is a constant depending on the classical electron radius  $r_e$ , the Avogadro number  $N_a$  and the electron mass  $m_e$ . The material thickness is given as  $x$  while  $I \approx 10 \text{ eV} \cdot Z$  is the average excitation potential. The correction factor  $\frac{\delta}{2}$  takes into account field extension limitations as a result of polarization of the traversing medium. The charge of the incident particles is given by  $z$ , while the target materials atomic number and the target materials atomic mass are given by  $Z$  and  $A$  respectively. The maximum kinetic energy that can be transferred to a free electron in a single collision  $T_{\max}$  is given by [3]:

$$T_{\max} = \frac{2m_e c^2 \beta^2 \gamma^2}{1 + 2\gamma \frac{m_e}{M} + \left(\frac{m_e}{M}\right)^2}, \quad (2.2)$$

where  $M$  is the mass of the particle. An example of the stopping power is given in Figure 2.1. The distribution has a minimum when  $\beta\gamma$  is close to three and particles in that range are referred to as Minimum Ionizing Particles (MIPs).

### 2.1.2 Ionization Losses of Electrons and Positrons

The mass stopping power for electrons differs, as the two particles are quantum-mechanically indistinguishable if the binding energy is ignored. Hence, transferring the full energy and no interaction both lead to the same result. For example, when all energy is transferred from the initial particle to the bound particle it is quantum-mechanically the exact same as if no interaction had taken place as in either case the final result is one electron at rest



**Figure 2.1** – Stopping power for a muons and protons in copper as a function of the momentum [3].

and the other electron with all available kinetic energy. As the stopping power is calculated based on the faster of the two electrons this has the result that the maximum energy that can be transferred to the bound electron is half the total kinetic energy as the two electrons are indistinguishable [3]:

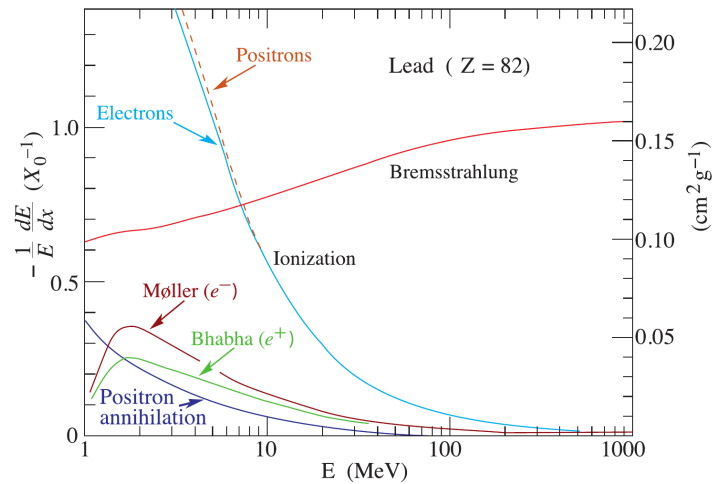
$$T_{\max} = \frac{1}{2} m_e c^2 (\gamma - 1). \quad (2.3)$$

The interaction is defined as Bhaba scattering for positrons and as Møller scattering for electrons in the case that the energy loss per collision is below 0.255 MeV [14]. The mass stopping power for electrons is calculated from the first moment of the Møller cross section under the assumption of a free atomic electron and is given by [3]

$$-\left\langle \frac{dE}{dx} \right\rangle = \frac{1}{2} K \frac{Z}{A} \frac{1}{\beta^2} \left[ \ln \frac{m_e c^2 \beta^2 \gamma^2 m_e c^2 (\gamma - 1)}{2I^2} + (1 - \beta^2) - \frac{2\gamma - 1}{\gamma^2} \ln 2 + \frac{1}{8} \left( \frac{\gamma - 1}{\gamma} \right)^2 - \delta \right]. \quad (2.4)$$

For positrons, the mass stopping power can be similarly calculated from the first moment of the Bhabha equation though they can both be expressed as an approximation from Berger and Seltzer as [15]:

$$-\frac{dE}{dx} = \rho \frac{0.153536}{\beta^2} \frac{Z}{A} \left[ B_0(T) - 2 \ln \left( \frac{I}{m c^2} \right) - \delta \right], \quad (2.5)$$



**Figure 2.2** – Mean energy loss of positrons and electrons in Lead [3].

where  $B_0(T)$  is referred to as the momentum dependent stopping power of the material which differs for electrons and positrons.

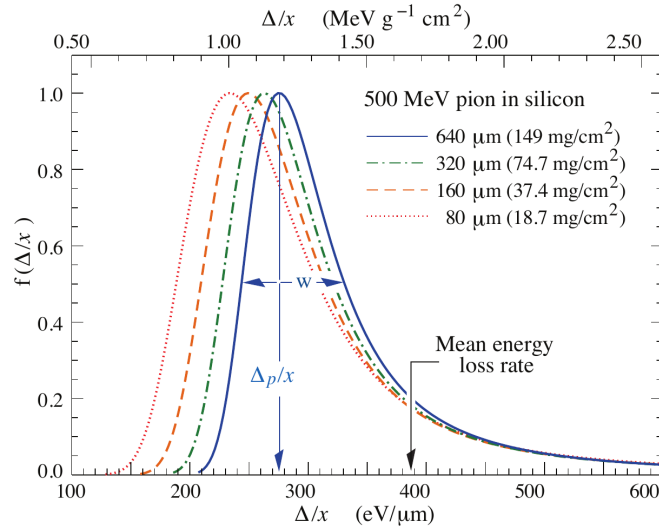
The full energy loss distribution for electrons and positrons is depicted in Figure 2.2. Even though the distributions for electrons/positrons and heavy particles are highly different, the minimum energy loss value differs only slightly between different particles as shown in Table 3 in the appendix.

### 2.1.3 Single Interaction Losses

While the average energy loss of particles in matter is well understood, the loss in a single interaction varies drastically. An example for the energy loss distribution in single interactions is given in Figure 2.3 for a 500 MeV pion traversing through silicon with different thickness. All distributions show an infinite tail to large values meaning a single interaction can result in a large transfer of energy to the material. Electrons produced in such interactions have a high amount of energy and can cause further ionization. They are referred to as  $\delta$ -electrons.

The distribution is described fairly well via a Landau distribution which is based on the Most Probable Value (MPV) and the width of the peak  $\sigma_L$  [16]. The MPV is significantly lower than the mean value that is described in the mean stopping power. The distribution also shows that while the tail is independent of the thickness, the MPV is affected strongly meaning that in thin silicon the variation of the energy loss is more pronounced.





**Figure 2.3** – Energy loss of 500 MeV pions in silicon of different thickness[3].

### 2.1.4 Bremsstrahlung Losses

For electrons and positrons a large fraction of their energy loss in interactions with material stems not only from ionization but from Bremsstrahlung. When electric charge is accelerated or decelerated photons are radiated. Radiation emitted due to deceleration as a result of deflection in the field of the nucleus is referred to as Bremsstrahlung. The energy loss for electrons and positrons with energies above 10 MeV are described as an exponential energy loss dependent on the initial energy:

$$-\frac{dE}{dx} = -\frac{E}{X_0}, \quad (2.6)$$

where  $X_0$  is the radiation length of the material that is defined as the average distance traveled for a high energy electron/positron until its energy is reduced by  $1/e$  of the initial energy. An approximation of the radiation length can be calculated to be [17]:

$$X_0 = \frac{716.4}{Z(Z+1) \ln\left(\frac{287}{\sqrt{Z}}\right) \rho}, \quad (2.7)$$

where  $\rho$  is the material density.

Bremsstrahlung photons can have energies high enough to perform pair production in which the photon is converted into an electron-positron pair through interaction with the nucleus if the energy of the photon is above  $2m_e$  or with an electron if the energy of the

photon is above  $4m_e$  in order to fulfill both energy and momentum conservation. The rest of the energy is then transferred as kinetic energy to the newly produced electron-positron pair. For extremely high energies this process can repeat with the newly produced pair, resulting in an evolving cascade of particles that is referred to as a particle shower. Showers can result in ambiguities in the track reconstruction but are crucial in the functionality of calorimeters in particle physics.

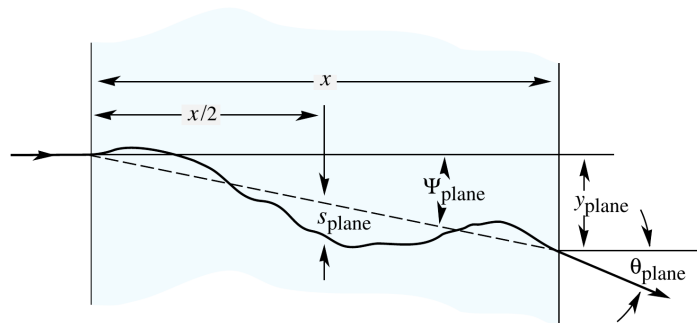
## 2.2 Particle Deflection

In addition to energy losses particles are also deflected via coulomb interactions with the nucleus. The interactions themselves typically follow the cross sections given by Rutherford though Hadrons can additionally be influenced by strong interactions. Multiple interactions can happen during the particles traversal through the material each of which influences the final deviation. This process is referred to as multiple coulomb scattering and is depicted in Figure 2.4.

The angular distributions of multiple scattering typically follow a Gaussian distribution with non Gaussian tails. The width of the inner 98 % quantile angular Gaussian distribution of the scattering distribution is given by the Highland-formula [18]:

$$\theta_{plane} = \frac{13.6 \text{ MeV}}{\beta c p} z \sqrt{\frac{x}{X_0}} \left[ 1 + 0.038 \ln \left( \frac{x z^2}{X_0 \beta^2} \right) \right], \quad (2.8)$$

where  $x/X_0$  is the thickness of the material in units of the radiation length. It is crucial to keep the material budget as low as possible for low momentum particles as the width of the angular deviations scales with  $1/p$ . The effect can be partially compensated by advanced



**Figure 2.4** – One dimensional sketch of multiple coulomb scattering of the particle in material [3].

---

reconstruction algorithms in which the particles deflection is taken into account during the reconstruction of the particle trajectory (see section [4.2.4](#)).



# Chapter 3

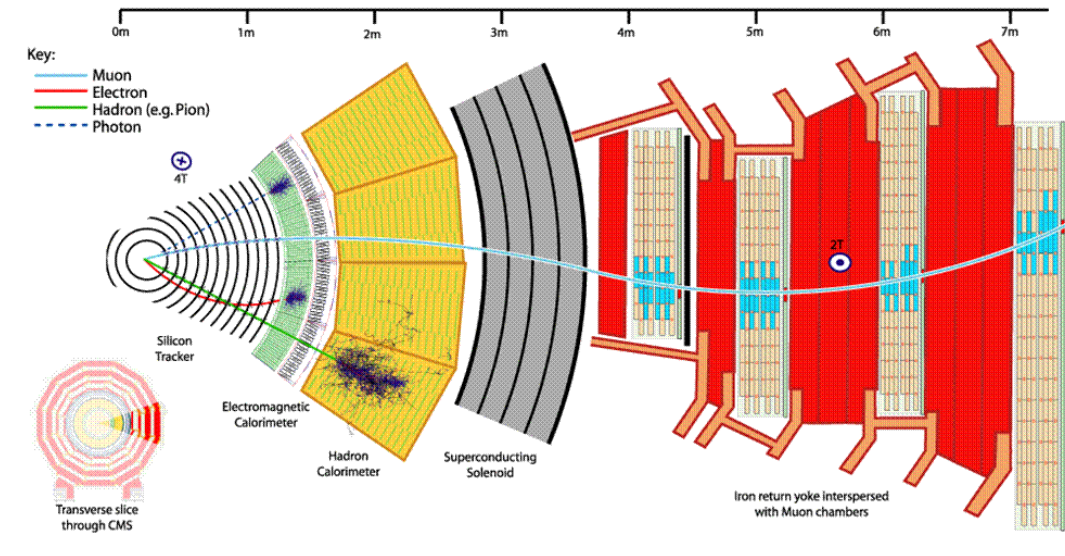
## Particle Detectors

Particle physics detectors are realized in multiple different concepts, ranging from bubble chambers [19] and calorimeters over Time Projection Chambers (TPC) [20] to semiconductor detectors [21]. Modern particle physics experiments utilize a combination of different detector types in order to perform a full reconstruction of the particle interactions, see Figure 3.1. Typical multi-purpose detectors such as the CMS detector consist of the following components:

- Tracking detectors are used to reconstruct the particles trajectory and point of origin with high precision. Within a magnetic field, an accurate reconstruction of the trajectory allows a precise determination of the momentum of charged particles via its curvature. For this purpose the tracking detector needs to have as little material budget as possible (see section 2.2).

The innermost tracking layer aims to reconstruct the interaction point as well as subsequent secondary decay vertices and is placed as close to the interaction point as possible. The outer layers instrument a significantly larger volume to more accurately determine the curvature in a magnetic field. The requirements of the tracking layers resolution increases with decreasing distance to the interaction point [3].

- Calorimeters are used to determine the particles energy by absorbing the particle. The calorimeters is both split in type and structure. The two types of calorimeters are, Electromagnetic CALorimeters (ECAL) used to measure the energy of photons, electrons and positrons and Hadronic CALorimeters (HCAL) used to determine the energy of hadrons. The main difference between the two components is their density and granularity. The two calorimeter structure are, a homogeneous calorimeter for which the entire volume is used to generate the interactions and be sensitive to

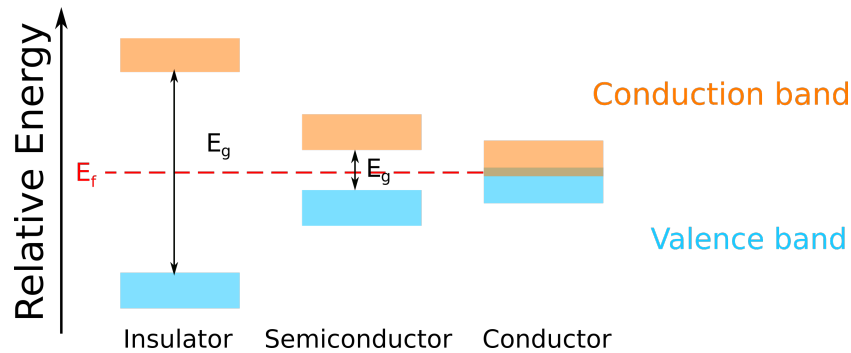


**Figure 3.1** – Slice of the different components of the CMS detector [22].

signal or a sampling calorimeter in which the sensitive detection material is interspersed with high density material to induce interactions. Material with large material budgets induce particle showers (see section 2.1.4). The showering splits the energy of a single high energy particle into multiple lower energy particles each of which is stopped and absorbed in the calorimeter [3].

- A magnet that is used to generate a strong magnetic field and an iron yoke used to ensure the magnetic field is homogeneous [3].
- Muon chambers which are lower granularity tracking detectors used to tag muons produced in the interaction. Particles other than muons typically are not able to reach the muon chambers as they will most often have been absorbed in the calorimeters. As the outermost detector layer muon chambers need to instrument a very large volume and are often optimized for cost [3].

The different components can be composed of different technologies all with distinct advantages and disadvantages. Tracking detectors for example can consist of, gaseous detectors such as a TPC, or semiconductor based technologies such as silicon [23]. As this thesis discusses a new silicon strip sensor, silicon tracking detectors and the basics of semiconductors are discussed in more detail below.



**Figure 3.2** – Band gaps for the different types of solids.  $E_f$  is the fermi energy and  $E_g$  is the band gap energy between the valence and conduction band.

### 3.1 Physics of Semiconductors

Semiconductors are materials whose conductivity lies between conductors and insulators. The difference in conductivity between the three groups is directly related to the band structure of the crystal and the resulting difference in the band gap  $E_g$ . The band structure describes the binding energy of electrons within a crystal based on a nearly free electron model. The band gap  $E_g$  is the energy difference between the valence band in which electrons are bound to atoms and the conduction band in which the electrons are in a quasi-free state.

In a system without any thermal excitation, as given at a temperature of 0K, no electrons are found within the conduction band for semiconductors and insulators. For conductors the valence- and conduction band possess at least partial overlap meaning there are always electrons within the conduction band capable of taking part in charge transport (see Figure 3.2) [21]. With increasing temperature thermal excitation of electrons within the valence band can, in the case of semiconductors, transfer enough energy to raise them from the valence band into the conduction band. This is not possible for insulators as their band gap is significantly larger than the typical energy that can be transferred through thermal excitation.

When an electron is lifted from the valence band to the conduction band it leaves behind an atom with a missing electron. Such empty spots are referred to as holes. The hole itself attracts electrons which can result in the situation in which an electron from an adjacent bond switches position into the hole and by that leaves a hole at its original position. This effectively results in the movement of positive charge through the valence band. The process in which an electron, which was excited into the conduction band becomes trapped

in a hole within the valence band is referred to as recombination [21].

### 3.1.1 Doping

The conductivity of semiconductors can be manipulated through implantation of impurities into the crystal structures. This process is referred to as doping of the semiconductor. This process creates energy levels between the valence and conduction band allowing for easier thermal excitation. Typically one differentiates between:

- Implanting an atom with more electrons than the crystal material (five for silicon doping) in which the implanted atom is referred to as a donor as it donates an electron to the conduction band.
- Implanting an atom with less electrons than the crystal material (three for silicon doping) in which the implanted atom is referred to as an acceptor as it provides one less electron resulting in an additional hole capable of accepting electrons in the valence band.

When a semiconductor is doped with donors the material is referred to as n-doped while semiconductors doped with acceptors are referred to as p-doped. Higher doping concentrations are referred to as  $n^+$  and  $p^+$  to differentiate between regions that only differ in their concentrations [21].

### 3.1.2 pn-Junction

When a p-doped and an n-doped semiconductor material are brought in contact, they create what is referred to as a pn-junction that functions as a diode. The different concentrations of electrons and holes at the pn-junction results in diffusion of electrons from the n-doped region to the p-doped region and diffusion of holes from the p-doped region to the n-doped region where they recombine and neutralize their charge contribution.

The donor and acceptor atoms, are embedded in the crystal lattice and are incapable of moving. This results in a positively charged region in the n-doped silicon and a negatively charged region in the p-doped silicon. This results in the creation of an electric field along the pn-junction with no free charge carriers, a depletion zone. The size of the depletion zone increases until the electric field strength is high enough to oppose the diffusion resulting in a state of equilibrium [21].



### 3.1.3 Biasing a pn-Junction

Applying a positive voltage level to the p-doped side and a negative level to the n-doped side of a pn-junction is a forward bias which reduces the size of the depletion zone. If the forward bias voltage is large enough it can result in a complete elimination of the potential barrier at which point the pn-junction becomes conductive.

Applying a negative voltage level to the p-doped side and a positive level to the n-doped side of a pn-junction is a reverse bias which increases the size of the depletion zone. In reverse bias, the thickness of the depletion zone  $w$  is given by the concentration of acceptors/donors ( $N_A/N_D$ ) in the doped silicon regions and the strength of the reverse bias voltage  $V_b$  [21]:

$$w = \sqrt{\frac{2\epsilon V_b}{e} \frac{N_A + N_D}{N_A N_D}} \stackrel{N_D \gg N_A}{\propto} \sqrt{\frac{V_b}{N_D}}. \quad (3.1)$$

The size of the depletion zone asymptotically reaches a maximum with increasing bias voltage. Voltage at which the size of the depletion zone no longer increases is referred to as the depletion voltage  $V_{\text{dep}}$ . When the bias voltage lies above the depletion voltage of the system, the operation is referred to as overdepletion in which the bias voltage applies an uniform electric field overlayed to the electric field present within the system due to the acceptor and donor. The pn-junction can be interpreted as a parallel plate capacitor the capacitance of which is proportional to:

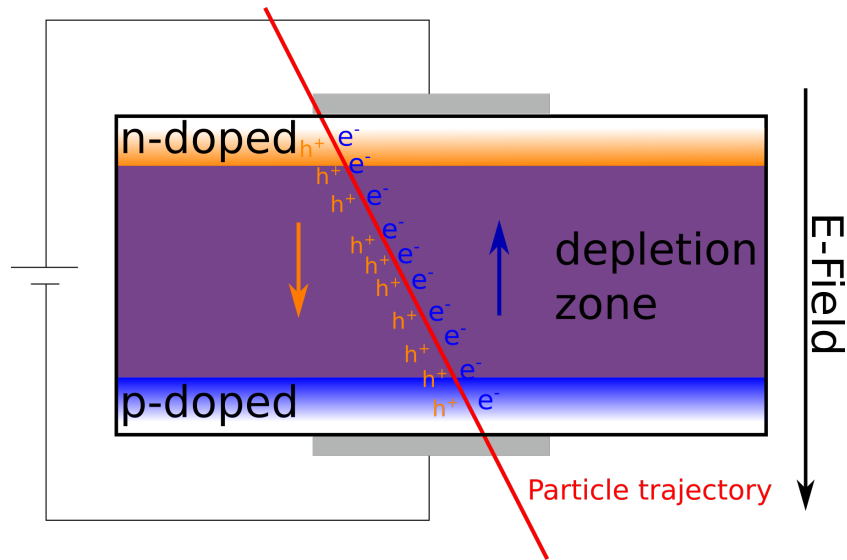
$$C_{pn} = \epsilon_0 \epsilon_r \frac{A}{w} \Rightarrow C_{pn} \propto \frac{1}{\sqrt{V_b}}, \quad (3.2)$$

which is used in measurements to determine the sensors depletion voltage level (see section 7.2).

### 3.1.4 Charge Collection in a pn-Junction

Charged particles traversing the material deposit energy through interaction with the material (see section 2.1) resulting in the creation of electron-hole pairs. Electron-hole pairs created within the depletion zone drift apart, towards the electrodes, as a result of the aforementioned electric field present within the depletion zone.

The drift of the charge results in an electric field change which induces charge on the collection electrodes which for a sensor are placed atop the doped silicon (see Figure 3.3). Electron-hole pairs created in non-depleted regions require diffusion to be collected which, unlike the drift, is a randomized motion. As a result, the charge collection via diffusion is



**Figure 3.3** – Charge drift in a reverse biased pn-junction generated by the energy loss of a traversing particle.

slower, making it more prone to charge loss due to recombination. Thicker depletion zones lead to more detectable deposited charge and are therefore beneficial for detection.

The drift velocity for a simple model based on a parallel plate capacitor is given by [21]:

$$v_d(x) = \mu_{e/h} \cdot E = \mu_{e/h} \cdot \frac{V_b}{w}, \quad (3.3)$$

where  $E$  is the electric field strength and  $V_b$  is the bias voltage.  $w$  is the thickness of the depletion zone and  $\mu_{e/h}$  is the electron/hole mobility within the material. The drift velocity increases with increasing field strength until at an electric field strength of about  $1 \times 10^5 \text{ V/cm}$  the drift velocity saturates at  $1 \times 10^7 \text{ cm/s}$ . A further increase in the electric field strength results in charge multiplication within the sensor as a result of collisions of drifting electrons with electrons in the depletion zone. Operation at very high electric field strengths can therefore result in an amplification of the signal but can also result in a breakdown of the diode which can damage it because of the significant currents involved. The bias voltage can be reduced below the breakdown voltage to stop the avalanche which is referred to as quenching.

The charge collection time depends on the reverse bias applied to the sensor. The collection time differs between sensors not fully depleted and sensors operated in overdepletion [21]. For an overdepleted sensor ( $V_{\text{dep}} > V_b$ ), the maximum time required for the system to collect all charge is calculated for electrons/holes that are required to travel the

full thickness  $w$  of the depletion zone [21]:

$$t_{ce/he} = \frac{d^2}{2\mu_e/hV_{\text{dep}}} \ln\left(\frac{V_b + V_{\text{dep}}}{V_b - V_{\text{dep}}}\right). \quad (3.4)$$

For a sensor with thickness  $w = 300 \mu\text{m}$  a depletion voltage of  $V_{\text{dep}} = 40\text{V}$  and a bias voltage of  $V_b = 65\text{V}$  this results in a charge collection time of 11 ns (31 ns) for electrons (holes). This presents the lower limit of the time resolution achievable by the technology. Improvements to the readout speed can be achieved by reducing the thickness of the sensor at the cost of charge collected and increased fluctuations as mentioned in section 2.1.3.

The actual movement of the electrons/holes within the system is a superposition of the drift induced by the electric field and the diffusion induced by random thermal motion. Diffusion results in the charge spreading out according to a Gaussian distribution over its drift duration towards the electrodes. The width of the distribution is given by [21]:

$$\sigma = \sqrt{2Dt_c}, \quad (3.5)$$

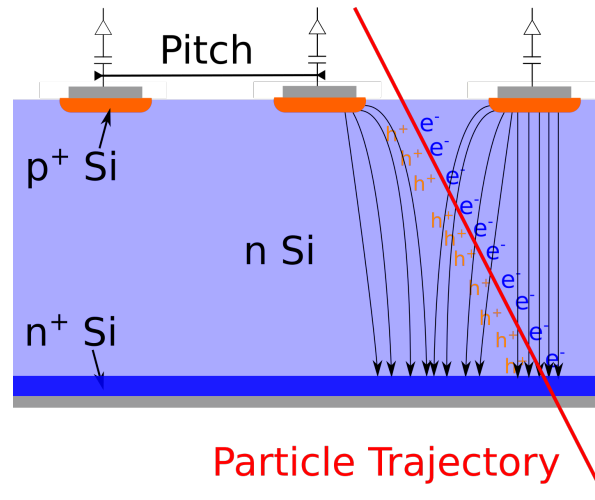
where  $t_c$  is the charge collection time and  $D$  is the material dependent diffusion constant of the electrons/holes. As the diffusion constant is proportional to the mobility and the collection time is anti-proportional to the mobility, the particle spread of the charge is the same for both electrons/holes and is given by:

$$\sigma = \sqrt{2 \frac{k_B T}{e} \frac{w^2}{V} \ln\left(\frac{V_b + V_{\text{dep}}}{V_b - V_{\text{dep}}}\right)}. \quad (3.6)$$

$k$  is the Boltzmann constant,  $e$  the elementary charge and  $T$  is the temperature of the system. For the aforementioned system at room temperature (300 K) this results in a maximum diffusion induced charge spread of  $12.7 \mu\text{m}$  at the readout electrodes.

### 3.1.5 Segmented Collection Electrodes for Position Sensing

The position of ionizing particles within a silicon sensor can be determined by segmenting the readout electrodes. This is typically achieved by implanting high concentration donor/acceptor material into a bulk of the opposite doping. Figure 3.4 sketches the segmentation of the top electrode resulting in multiple independent electrodes. The collected charge on each electrode depends on their proximity to the primary charge deposition [24]. Depending on the type of segmentation the resulting silicon sensor is referred to as strip- or pixel sensors:



**Figure 3.4** – Silicon sensor with segmented readout electrodes in the form of high concentration  $p^+$ -doped acceptor implanted silicon within the  $n$ -doped bulk. When getting closer to the electrodes the field lines, depicted as the black arrows pointing down, stop being parallel and funnel the charge to the closest electrodes.

- **Strip sensors:** Their readout electrodes are segmented in one direction. This segmentation provides one-dimensional measurements per sensor.
- **Pixel sensors:** Their readout electrodes are segmented in both directions. This segmentation provides two-dimensional measurements per sensor at the cost of a large increase in the amount of readout channels.

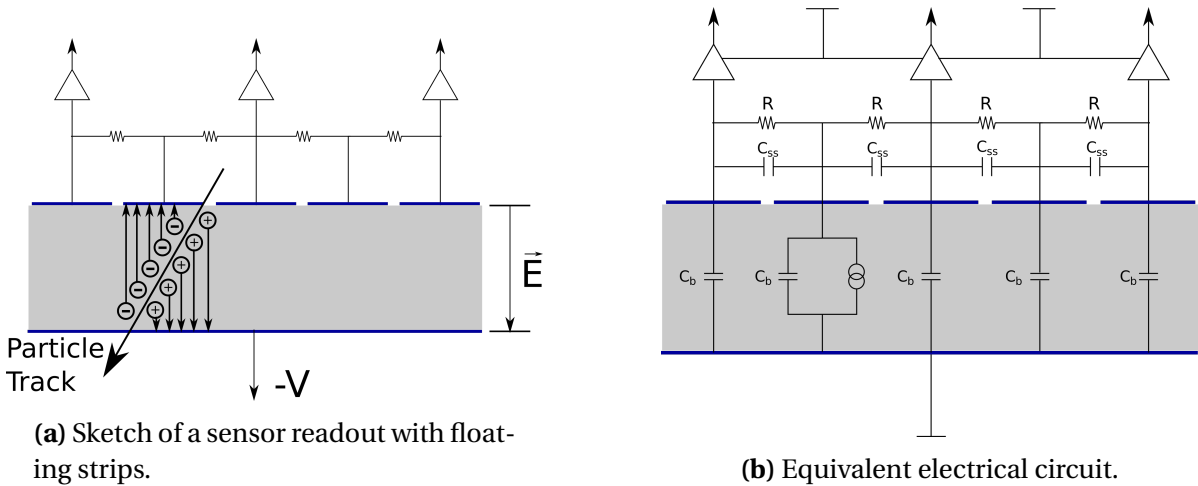
The exact resolution of strip-/pixel sensors depends on both the readout method and the pitch  $p$  of the readout electrodes. For a binary readout system in which an electrode measures the existence/absence of signal the resolution of the system is given by [3]:

$$\sigma_{\text{pos}} = \frac{p}{\sqrt{12}}. \quad (3.7)$$

### Improving the resolution

Improvements to this binary resolution can be achieved through measurement of the amount of deposited charge. As a result of the charge diffusion in the bulk, the charge can spread over multiple electrodes, resulting in charge sharing by a group of electrodes which is referred to as a charge *cluster*. A more precise location of the particle trajectory can be determined based on the charge weighted center of gravity of the *cluster*<sup>1</sup>. Hence

<sup>1</sup>Even for a binary system readout charge shared over multiple electrodes can be used to improve the resolution of the system.



**Figure 3.5** – The floating strips are capacitively coupled to the adjacent readout strips as a result of their inter-strip capacitance as a result of their parallel path through the sensor. When signal is registered on the "floating" strip a signal is induced in the adjacent strips based on the ratio of the inter-strip capacitance  $C_{ss}$  to the strip-to-backplane capacitance  $C_b$ . Pictures adapted from [21]

the presence of diffusion in the system improves the resolution of the system if the pitch of the electrodes is small enough to induce multiple electrode clusters as a result of diffusion. Depending on the thickness and charge collection time of the sensor this can require an extremely small readout pitch which increases the complexity and cost of a sensor.

Another method is to improve the charge sharing of the sensor without reducing the readout pitch. This can for example be achieved through implantation of differently doped intermediate layers into the bulk of the sensor that spread out the charge via Enhanced Lateral Drift (ELAD) [25].

Another method is the use of *floating* electrodes/strips [21]. A sketch of such a system setup where each readout strip is followed by a *floating* strip is given in Figure 3.5. Each strip is capacitively coupled via what is referred to as the inter-strip capacitance  $C_{ss}$  to their adjacent strip. The bias resistors ensure that all strips are on the same potential though each *floating* strip can change individually as a response to signal charge due to the large time constant formed by the bias resistance and the inter-strip capacitance. This requires that the charge sensitive amplifier connected to the readout strips is fast compared to the time constant of the CR circuit to the *floating* strip. When signal is induced in a *floating* strip, adjacent readout strips register signal as a result of their capacitive coupling.

In addition to the coupling between strips, each strip has a coupling capacitance to the

back-plane in which charge is also induced. The total deposited charge  $Q_{\text{tot}}$  is split into:

$$Q_{\text{tot}} = 2 \cdot Q_s + Q_b. \quad (3.8)$$

The charge of the a readout strip is  $Q_s$  and the charge of the back-plane is  $Q_b$ . The charge on the back-plane is lost. The fraction of the total charge registered by one of the adjacent strips of the system  $Q_s/Q_{\text{tot}}$  depends on the ratio of the inter-strip capacitance  $C_{ss}$  to the strip-to-back-plane capacitance  $C_b$ . The exact relation is given by [21]:

$$\frac{Q_s}{Q_{\text{tot}}} = \frac{1}{1 + 2(C_b/C_{ss}) + \frac{1}{2}(C_b/C_{ss})^2} \stackrel{C_{ss} \gg C_b}{\approx} \frac{1}{2} \cdot \frac{1}{1 + 2(C_b/C_{ss})}. \quad (3.9)$$

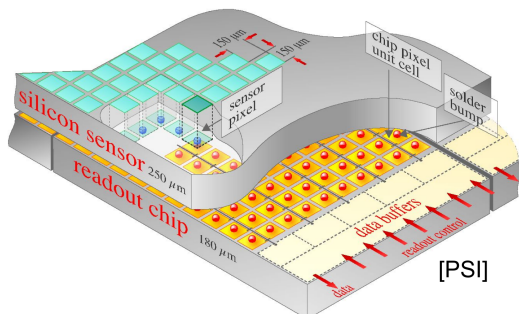
For a ratio of  $C_b/C_{ss} = 0.1$  the amount of charge registered in one strip is 41.7% resulting in a loss of 16.7% to the back-plane making a high inter-strip capacitance important for such a system to function without significant charge losses.

## 3.2 Silicon Tracking Detectors

Silicon detectors have been implemented in a large variety of segmentations, ranging from strips to pixels. The readout electronics of a silicon sensor can be either implemented directly in the sensor (Monolithic Active Pixel Sensor (MAPS)) or on a second dedicated silicon readout chip layer connected to the sensor (hybrid). Their basic concept, advantages and disadvantages differ significantly and are described briefly below.

### 3.2.1 Hybrid Sensors

Hybrid sensors consist of two separate layers, an active sensor layer which generates the charge signal once a particle deposits energy within its depletion zone and a readout chip layer which is responsible for the signal processing. Hybrid sensors exist for both strip and pixel configurations. In a pixel configuration the readout chip cell size is adjusted to the cell size of the silicon sensor in order to connect the readout chip to the silicon sensor surface via bump-bonds (see Figure 3.6a). Figure 3.6b shows the Timepix3 sensor, a pixel detector that is used in this thesis as a reference (see section 8.3.2). For strip sensors no such adjustments are made as the readout chip is usually not directly bump bonded onto the sensor. Instead, each strip signal is transferred to the readout chip that is typically placed on top of a printed circuit board and connected via wire-bonds. Advantages of hybrid sensors are that:



(a) Sketch of the design of the CMS hybrid pixel sensor [26].



(b) Picture of the Timepix3 readout chip [27].

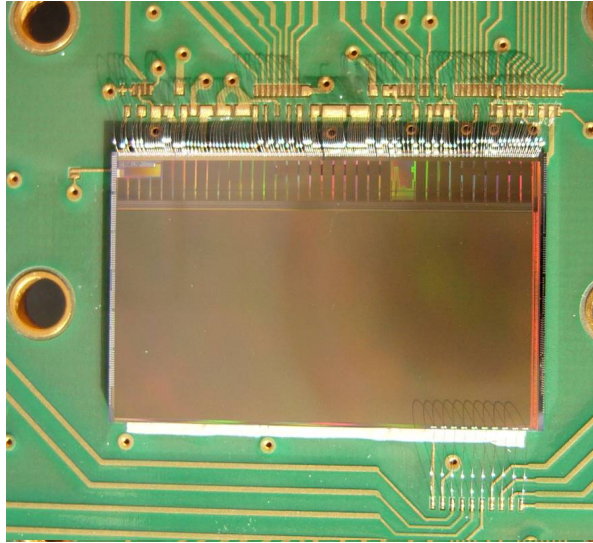
**Figure 3.6** – Example of a hybrid chip and sketch of the connection method.

- The sensor and readout chip layer can be developed/ optimized independently of one another.
- The readout chip layer can be used for a more generalized application where no silicon sensor is required [28] or with different types of silicon sensors [29].
- The sensor layer of hybrids can be biased with high voltage resulting in full depletion of the sensor even for thicker sensors (larger signal) and low charge collection times (radiation hardness).

The disadvantages of the technology are:

- Bump-bonding processes are not commonly used in industry and are relatively expensive.
- The pitch of the sensor is limited by the size of the bump-/wire-bonds.
- The separation of the readout and sensor layer generally result in a thicker module with increased material inducing more multiple scattering.
- It is also possible to pick up noise within the bump-/wire-bonds.

Hybrids have been the most common type of silicon detector in the last decades and have been in use for most vertex detectors over the last 30 years [30].



**Figure 3.7** – Picture of the Mimosa26 pixel sensor on its carrier board as used at the DESY II Test Beam Facility [31].

### 3.2.2 Monolithic Active Pixel Sensors

The base design for a MAPS is that both sensor and readout are integrated within the same silicon wafer. Standard MAPS suffer from a low fill factor<sup>2</sup> as a result of charge being lost when it diffuses into the electronics instead of the electrodes. As normal MAPS sensors are operated with only small depletion zones, most of the charge collection is a result of diffusion which is significantly slower, making charge loss due to recombination and trapping an issue which reduces the radiation hardness of the sensor. A larger depletion of standard MAPS is not possible as they cannot sustain high voltage bias that is required to deplete the low resistivity substrate which they are produced with.

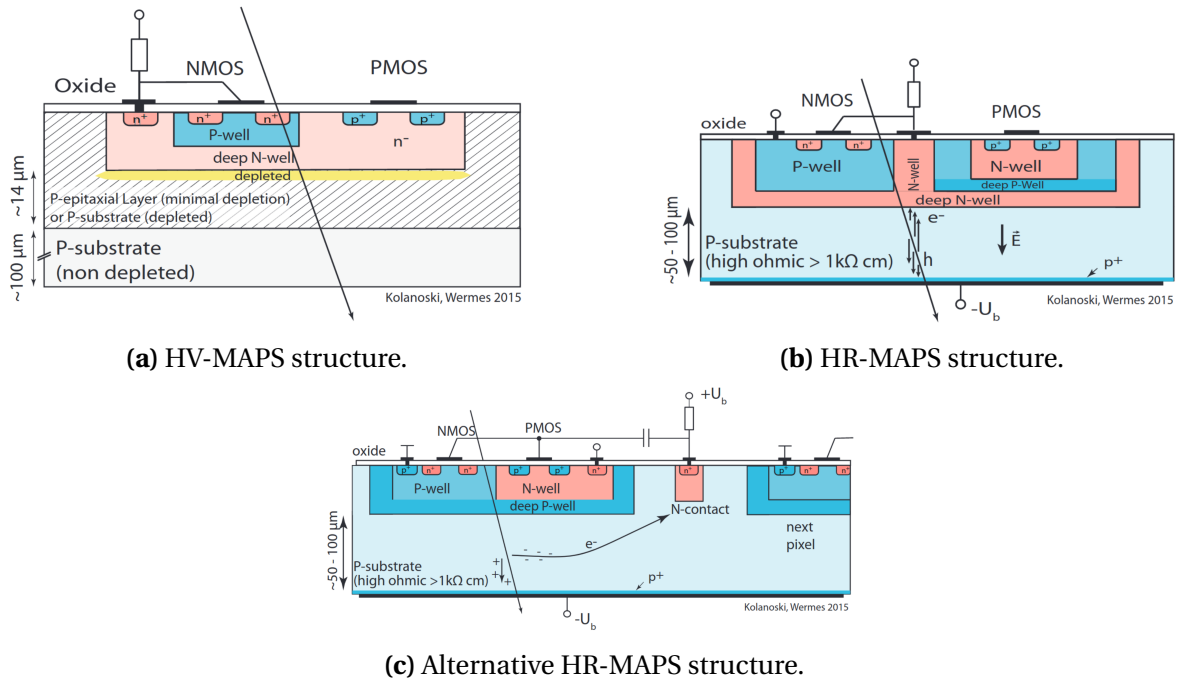
An example for a classical MAPS sensor is the Mimosa26 pictured in Figure 3.7 that is used as a reference in this thesis (see section 5.3). In the Mimosa26, the electronics are moved to a periphery at the side of the sensor to ensure the pixels themselves do not have any dead areas.

The problem of insufficient radiation hardness and insufficient fill factor was resolved through the use of modern Complementary Metal-Oxide-Semiconductor technology (CMOS) processes that allow the implantation of deep n-/p-wells which are highly doped regions within the bulk of opposite doping. The electronics are embedded into these wells, shielding them from the deposited charge that can then only diffuse to the readout electrodes.

---

<sup>2</sup>fill factor describes the percentage of the pixel area that is sensitive to charge deposition





**Figure 3.8** – Structure of modern CMOS based MAPS [23].

One differentiates between two technologies for modern CMOS based MAPS, High-Voltage-CMOS (HV-CMOS) and High-Resistivity-CMOS (HR-CMOS).

In HV-CMOS (HV-MAPS) all electronics, including the readout electrode is placed inside the deep n-well resulting in a large collection well with high capacitance but fairly uniform drift lengths. High voltage can be applied to the low resistivity substrate to deplete it (see Figure 3.8a).

In HR-CMOS (HR-MAPS) the electronics can either all be placed within a deep well (see Figure 3.8b) or everything but the electrode is placed within the deep well which results in a smaller capacitance but larger drift path (see Figure 3.8c). The substrate of a HR-CMOS has a much higher resistivity and low voltages are sufficient to deplete it. The depletion zones for these sensors can reach between  $15\mu\text{m}$  for HV-MAPS [32] to  $100\mu\text{m}$  for HR-CMOS MAPS [23]. The HV-/HR-MAPS can be thinned down to thicknesses of around  $50\mu\text{m}$  without expected charge loss resulting in significantly less material at the cost of lower charge yield and larger charge fluctuations (see section 2.1.3) when compared to thick hybrids. The introduction of charge collection via drift significantly improves the charge collection time resulting radiation hardness compared to normal MAPS. The increased depletion zone also results in a lowered capacitance to the back-plane. The pixel pitch of MAPS is not limited to connection processes such as bump-bonding, only by CMOS production

capabilities which are continuously improving. While HV-/HR-CMOS processes have significantly improved the radiation hardness of MAPS they are not yet on the same level as hybrid sensors.

# Chapter 4

## Particle Track Reconstruction

Detectors in particle physics provide local measurements of the position of a particle when passing through the sensor. The combination of multiple seemingly independent measurements on different layers into trajectories that accurately describe the path of the particle is referred to as particle track reconstruction which includes track finding, track fitting and alignment that are described in detail below.

### 4.1 Track Finding and Fitting

In particle physics experiments, tracking detectors are used to measure the trajectory of the particle. In the presence of a magnetic field one can further determine the momentum of charged particles  $P$  based on the radius of their trajectory  $r$  within the magnetic field  $\vec{B}$ . The relation is given by [3]:

$$\begin{aligned} F_{\text{cent}}^{\vec{}} &= \vec{F}_B \\ \frac{mv^2}{r} \vec{e}_r &= q\vec{v} \times \vec{B} \\ \frac{Pv}{r} \vec{e}_r &= qv\vec{e}_v \times \vec{B} \\ \frac{P}{r} \vec{e}_r &= q\vec{e}_v \times \vec{B} \\ \Rightarrow P &= qrB \sin(\alpha). \end{aligned} \tag{4.1}$$

Which says that the centripetal force  $F_{\text{cent}}^{\vec{}}$  bending particles on a curved trajectory within a magnetic field is given by the strength applied onto the particle by the magnetic field  $\vec{F}_B$ . The mass of the particle is given by  $m$  and the direction of the force is along the radial vector

$\vec{e}_r$ . The electric charge of the particle is  $q$  and  $\vec{v}$  is the particles velocity vector. The angle between the magnetic field vector and the particle velocity vector is  $\alpha$ .

Precise knowledge of the particle trajectory allows the reconstruction of the particles point of origin (vertex) which helps in determining the particle type. If the particle resulted from the decay of a short lived intermediate particle then the vertex does not align with the interaction point. As a result of this, tracking detectors are an essential component of modern particle physics detectors (see chapter 3).

The reconstruction of particle tracks based on measurements on different layers can be split into two categories, track finding and track fitting. Track finding uses different hits on different layers and combines them into what is referred to as a track candidate. Only if a track candidate passes certain quality cuts are they referred to as tracks in this thesis. The fact that any two hits can be combined into a track candidate means that the number of track candidates  $n_{tc}$  is given by:

$$n_{tc} = \prod_{i=0}^N n_i, \quad (4.2)$$

for  $N$  numbers of layers where each layer  $i$  has a number of hits  $n_i$ . This quickly results in a large amount of track candidates if the hit multiplicity on the layers is high. To reduce the amount of combinations the problem can be approached based on an initial particle trajectory assumption, a seeded approach. In a seeded approach the trajectory is propagated from layer to layer where only hits that are within the propagation uncertainty are accepted. When no initial trajectory is assumed then it is an unseeded approach.

Ambiguities exist in the cases that the track multiplicity is larger than one or that noise hits are present on the layers. Either can result in the wrong assignment of hits and subsequently the incorrect reconstruction of the particles vertex or momentum. Track candidates are typically selected based on the  $\chi^2$  of the fit.

Many different methods of track finding exist such as:

- Hough transformation [33].
- Combinatorial Kalman filter [34].
- *Triplet finder* [35].
- *Road search* [35].

and similarly, different methods of track fitting exist that take into account multiple scattering in object such as:

- Kalman filter [34].

- General Broken Lines (GBL) [36].

All track finding in this thesis is based on the *triplet finder* and *road search* from *EUTelpy* with variations for one-dimensional measurements. All track fits performed in this thesis use the GBL framework.

## 4.2 Particle Reconstruction at Test Beams

All particle track reconstruction performed in this thesis is used to reconstruct data obtained from test beam measurements. For the purpose of particle track reconstruction this means that generally the particles initial momentum and trajectory are fairly well known and the tracking layers used to reconstruct the particles trajectory are typically staggered one after another in a straight line. This arrangement of tracking layers is referred to as a telescope which is a commonly used reference tracking device at test beams used to investigate the performance of other Devices Under Test (DUTs). The knowledge of the particles initial momentum, position and angle simplify the problem of track reconstruction significantly.

### 4.2.1 Global and Local Coordinate Systems

In order to combine the local measurements from multiple sensors into a combined track, the precise relation between their measurements need to be know. Local measurements on a sensor layer are given by:

$$\vec{q} = \begin{pmatrix} u & v & w \end{pmatrix}^T, \quad (4.3)$$

which are defined as the movement along the row ( $v$ ) and along the column ( $u$ ) of the sensor. The  $w$  axis is the normal vector to this plane.

The global coordinates are given by:

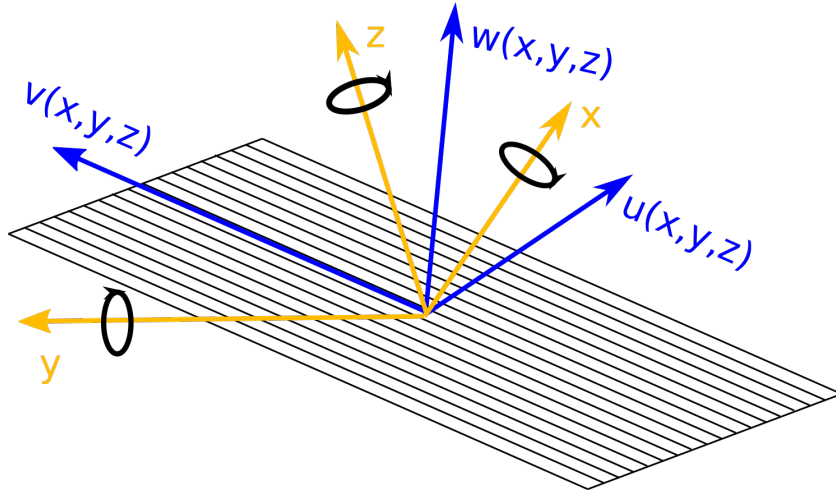
$$\vec{p} = \begin{pmatrix} x & y & z \end{pmatrix}^T. \quad (4.4)$$

In the global coordinate system the  $z$ -axis is defined by the beam particle direction with movement along positive  $z$  going parallel to the beam. The  $y$ -axis is defined along row movement and the  $x$ -axis is defined along column movement of the first pixel layer. The

position

$$\begin{pmatrix} x \\ y \end{pmatrix} = \begin{pmatrix} 0 \\ 0 \end{pmatrix} \quad (4.5)$$

is defined as the center of the first tracking layer with  $z = 0$  being in the center between the two outermost sensitive layers. A sketch of the relation between the global and local coordinate is depicted in Figure 4.1.



**Figure 4.1** – Local coordinate system for the sensor. Depending on angles to the beam the local coordinates can depend on all three global parameters.

A transformation from local parameters to global parameters can be performed via a rotation and translation of the local coordinate system around and along the global axes as given by:

$$\vec{p} = \mathbf{R}\vec{q} + \vec{t}, \quad (4.6)$$

with the rotation matrix around the global coordinate axes  $\mathbf{R}$  and the translation vector  $\vec{t}$ . They are given by:

$$\mathbf{R} = R_y \cdot R_x \cdot R_z = \begin{pmatrix} \cos(\gamma) & 0 & \sin(\beta) \\ 0 & 1 & 0 \\ -\sin(\beta) & 0 & \cos(\beta) \end{pmatrix} \cdot \begin{pmatrix} 1 & 0 & 0 \\ 0 & \cos(\alpha) & -\sin(\alpha) \\ 0 & \sin(\alpha) & \cos(\alpha) \end{pmatrix} \cdot \begin{pmatrix} \cos(\gamma) & -\sin(\gamma) & 0 \\ \sin(\gamma) & \cos(\gamma) & 0 \\ 0 & 0 & 1 \end{pmatrix}, \quad (4.7)$$

and

$$\vec{t} = \begin{pmatrix} \Delta x \\ \Delta y \\ \Delta z \end{pmatrix}. \quad (4.8)$$

The angles of the sensors in the global coordinate system around the  $x$ ,  $y$  and  $z$  axis are given by  $\alpha$ ,  $\beta$  and  $\gamma$ . The local position of the sensors relative to the origin of the global coordinate system in global coordinate  $x$ ,  $y$ , and  $z$  are  $\Delta x$ ,  $\Delta y$  and  $\Delta z$ .

A transformation from the global to the local coordinate system is achieved by taking the inverse transformation:

$$\vec{q} = \mathbf{R}^{-1} \vec{p} - \mathbf{R}^{-1} \vec{t}. \quad (4.9)$$

### 4.2.2 Track Model

All track finding methods described below use a straight line track model in their algorithm which is given by :

$$\vec{f}(z) = \vec{a} + \vec{s} \cdot z, \quad (4.10)$$

where  $z$  denotes the position along the  $z$ -axis of the global coordinate system  $\vec{a}$  is the initial position in the global  $x$ -/ $y$ -plane at  $z = 0$  and  $\vec{s}$  is the slope.

Measurements performed within a magnetic field require a modification of the straight line using the relation of the centripetal force bending particles on a curved trajectory within a magnetic field  $\vec{B} = (B_x \ B_y \ B_z)^T$  as described in (4.1). The particle velocity is by design parallel to the  $z$ -axis of our global coordinate system so that:

$$\vec{e}_v = \vec{e}_z = \begin{pmatrix} 0 \\ 0 \\ 1 \end{pmatrix}, \quad (4.11)$$

from which the curvature  $\vec{\kappa}$  within the magnetic field can be calculated as:

$$\vec{\kappa} = \frac{1}{r} \vec{e}_r = \frac{q}{P} \times \begin{pmatrix} -B_y \\ B_x \\ 0 \end{pmatrix}. \quad (4.12)$$

The initial value of the momentum is taken as the energy chosen during the test beam but

can be refined using the track fitting in order to iteratively improve upon the result. The quality of a track is determined using the  $\chi^2$  of the fit. The fit  $\chi^2$  is described as the sum over the residual between the predicted particle hit position  $v_{ip}(\tau_j, \mathbf{p})$  and the measured particle hit position  $v_{im}$  divided by the measurement uncertainty  $\sigma_i$ :

$$\chi^2 = \sum_j \sum_i z_{ij}(\tau_j, \mathbf{p}) = \sum_j \sum_i \left( \frac{v_{im} - v_{ip}(\tau_j, \mathbf{p})}{\sigma_i} \right)^2. \quad (4.13)$$

$i, j$  are the indices for all hits and tracks respectively while  $\tau_j, \mathbf{p}$  are the track parameters and parameters based on which the hit prediction is performed.

### 4.2.3 Track Finding

The track finding approach for pixelated measurement layers in *EUTelpy* can be split into two different methods named *road search* and *triplet finder* which differ in their approach.

- The *triplet finder* separates the telescope into its two arms each with three sensor layers. It starts by finding all possible combinations of hits between the first and the last sensor within an arm and performs the construction of a *doublet* by combining the two hits via the track model. A search for hits in the middle layer that are within a distance  $\Delta(x/y)_{dbl}$  relative to the projected position of the *doublet* in both  $x$  and  $y$  is then conducted.

In the case that the double uniqueness<sup>1</sup> is fulfilled, the new object including all three hits is called a *triplet*. This is done for each telescope arm separately after which an extrapolation of all *triplets* to the center between the sensors is performed using the track model. A matching of the *triplets* is conducted by requiring that matched *triplets* have a projected central hit within  $\Delta(x/y)_{trp}$  of each other in both  $x$  and  $y$  as well as an a small angle deviation below  $\Delta\theta_x/\Delta\theta_y$  for each *triplet*. Double unique *triplet* combinations between the two arms are combined into a valid track candidate.

- The *road search* starts by finding all possible hit combinations in all sensor layers starting with hits that are furthest apart from each other along the  $z$ -axis. The outermost layers, referred to as *seed layers*, are used to construct a *road* via the track

---

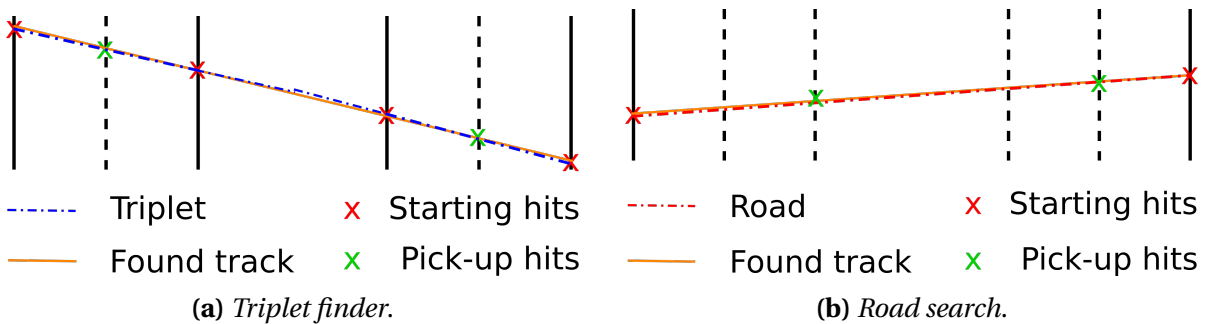
<sup>1</sup>Only one-to-one relations are accepted - one-to-many or many-to-many are not accepted. This means that for two objects -e.g. a hit and a track or two tracks- each hit has exactly one track it can be associated with and each track has only this specific hit -or one other track- it can be associated with. For hits this is only limited to hits in the same layer.



model. The track is then projected to all layers between the *seed layers*. If the position difference to the projected *road* position is below  $\Delta x/\Delta y$  then the hit is assigned to the track. As before, double uniqueness between *road* and hit per layer is required. Only in the case that the *road* has found hits in at least two more sensor layers is it considered a valid track candidate.

Both approaches are applied iteratively on all available hits until no more track candidates are found. Due to the more strict requirement to the number of hits in the *triplet finder*, the track finding is focused on high purity. The *road search* however can find tracks that do not fulfill the *triplet finder* requirements leading to a higher efficiency. In order to find both high purity tracks in addition to as many tracks as possible the *triplet finder* is performed first until no more tracks are found. Only then is the *road search* performed to gather all remaining tracks that were not found before.

Figure 4.2 depicts sketches explaining the two track finding algorithms.



**Figure 4.2** – Sketch explaining the *triplet finder* and *road search* track finding algorithms. The black vertical lines are the measurement layers. The solid lines are the starting layers from which the algorithm starts and the dashed lines are used for pickup of further hits.

### Track Finding for One-Dimensional Measurements

A strip telescope only provides one-dimensional local information per layer. This necessitates the existence of different angular rotations around the sensors  $w$  axis in order to reconstruct the coordinate in both directions. The configuration in this thesis has two arms of three strip sensors each. The final orientation for this setup is  $+ - 00 - +$  where  $+$  means the layer has a positive stereo angle,  $-$  means the layer has a negative stereo angle and  $0$  means the layer is without stereo angle and is an axial layer (see section 6.3).

The track finding for the one-dimensional measurements is performed with an adapted *road search* and *triplet finder*. For a strip telescope a minimum of four hits is required in or-

der to determine the four track parameters of a straight line which are the  $x_0$  and  $y_0$  offsets as well as the slopes  $dx/dz$  and  $dy/dz$  of the track. In addition, because of the ambiguity stemming from one dimensional measurements, a layer is only considered valid when its number of *clusters* is below a cut value in order to avoid noisy event layers blowing up the combinatorics. A detailed mathematical description of the two track finding methods can be found in section J. The most important aspects of the two are mentioned below:

- For the *strip road search* with six layers, each providing one-dimensional measurements, a minimum of four layers (*seed layers*) are required for a track candidate to define a line in space. The four stereo layers are preferred *seed layers* candidates assuming they are not considered busy. If they are, one of the axial layers is used as a *seed layer* instead. Axial layers not used as *seed layers* are used for testing of the track candidate similar to the *road search* and the *strip road search* requires a minimum of five layers, four *seed layers* and one additional axial layer, to generate a valid track candidate.
- The problem of the three layers per arm is even more pronounced for the *S-triplet finder*. With only three measurements per *triplet*, the complete set of four track parameters can't be determined. Instead, a two dimensional position and one distance to this position can be measured. The slopes along  $x/y$  are required to propagate the measurement to a common position along the  $z$ -axis as the three layers are at different positions along the  $z$ -axis. These are provided externally from knowledge of the beam direction at the test beam with modifications via bending in a magnetic field. Alternatively, the three measurements can be used to define a position in 2D and a slope in one dimension which is referred to as a *S-triplet*. Those parameters are then used for the matching of *S-triplets* between the two arms similar to the *triplet finder*.

#### 4.2.4 Track Fitting using GBL

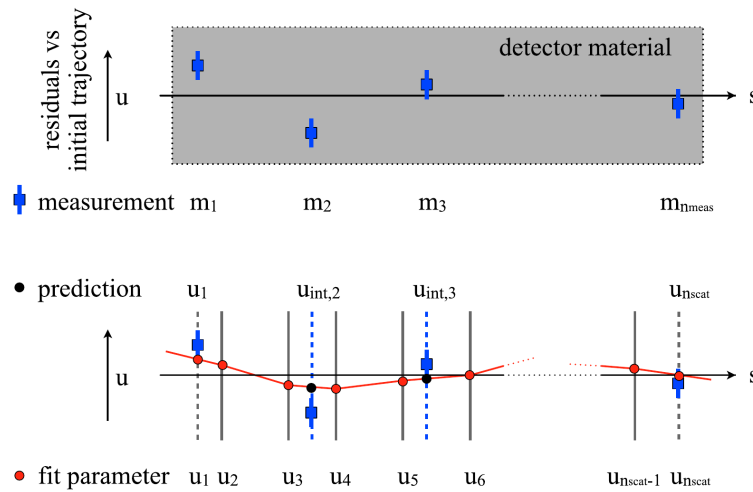
The track fitting approach used in this thesis is based on the General Broken Lines (GBL) framework [36] which is a local seeded approach. GBL takes uncertainties from multiple scattering at the sensor layers as well as measurement uncertainties from finite pixel sizes into account. It requires the existence of a seed trajectory upon which it iteratively performs linearized corrections. At each scatterer, which is any type of material within the beam path including air, the particle is deflected. In GBL the minimization problem is therefore the minimization of the sum of the  $\chi_m^2$  of the measurement offsets and of the  $\chi_K^2$

of the deflection angles (kinks) [36]:

$$\chi^2 = \chi_m^2 + \chi_K^2 = \sum_{i=1}^{n_{\text{meas}}} m_i^T V_{m,i}^{-1} m_i + \sum_{i=2}^{n_{\text{scatt}}-1} k_i^T V_{k,i}^{-1} k_i. \quad (4.14)$$

$V_{m,i}$  is the covariance matrix of the measurements and  $m_i$  are the residuals between the extrapolation and the measurement for perpendicular tracks in the curvilinear system<sup>2</sup>.  $V_{k,i}$  is the covariance matrix of the kinks and  $k_i$  are the kinks at a scatterer. Corrections based on this refit are propagated along the reference track and for each layer  $u_i$  the correction depends only on the layers before  $u_{i-1}$  and after  $u_{i+1}$ .

Figure 4.3 depicts a sketch of a track fit based on an initial straight line which ignores scattering layers and the effects of the GBL refit on the particle trajectory (red) and the fit prediction points. A more detailed mathematical description and comparison of the GBL track fitting to other methods can be found in [36] [37].

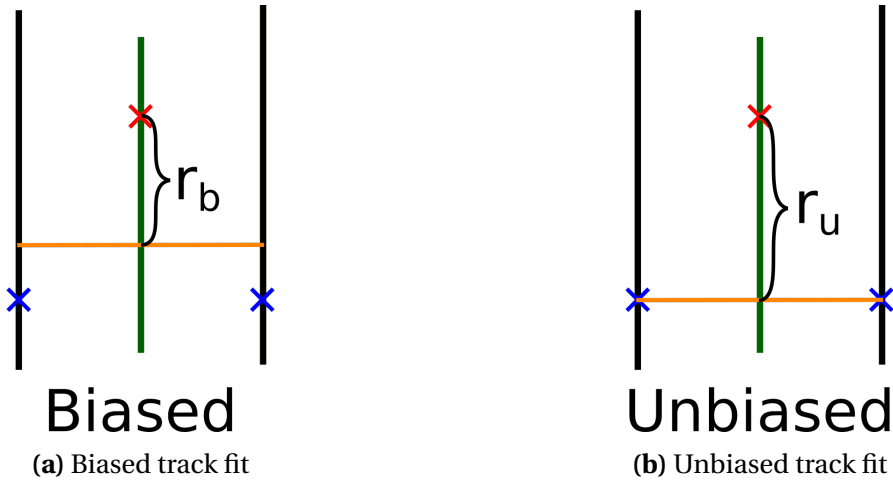


**Figure 4.3** – Sketch explaining the effect of the GBL refit [38].

### Biased and Unbiased Track Fits

For the investigation of a DUT, two different approaches exist for the track refit. The hits on the DUT can either be added to the track refit which results in what is referred to as a biased track or in an unbiased track when the DUT hits are not taken into account. For biased track fits this results in a reduced distance between the track fit and the hit on the

<sup>2</sup>a curvilinear system is a cartesian coordinate system that travels along the particle trajectory meaning that the z axis is always parallel to the particle trajectory



**Figure 4.4** – Biased and unbiased residual of the projected track hit to the cluster position for S43.

DUT compared to unbiased track fits as the hit itself is taken into account in the minimization of the fit. Figure 4.4 shows, as an example, a simplified explanation of the difference between a biased and unbiased straight line fit without GBL.

To determine the true single point resolution of the DUT, the geometric mean of the residual between track and hit are taken for both the biased and the unbiased track fit [39]:

$$\sigma_{\text{SinglePoint}} = \sqrt{\sigma_{\text{unbiased}} \cdot \sigma_{\text{biased}}}. \quad (4.15)$$

### 4.3 Alignment

In order to reach the highest measurement accuracy, precise knowledge of the sensor position is required. Typically no external tools are available to determine the position and angles of the sensors to an accuracy which is similar to that of the sensor resolution. It can, however, be determined using track based alignment.

Displacements between layers increase the  $\chi^2$  of the track fit whereas distortions common to all layers such as rotations or displacements of the entire setup relative to the beam can be absorbed into the track parameters and do not change the  $\chi^2$ . As such, the precise determination of the sensor positions and rotations relative to one another can be achieved by using tracks generated by the particle beam through minimization of the track  $\chi^2$  (4.13).

In order to perform track based alignment, the track parameters need to be overconstrained to allow a variation of the positions and angles of singular layers in order to min-

imize this  $\chi^2$ . The method by which this  $\chi^2$  is minimized in this thesis is the Millepede-II algorithm [38] which performs a linearization of the  $\chi^2$ .

For this the results gathered from GBL are fed into the Millepede-II framework which performs the minimization of the  $\chi^2$  and gives back the changes that need to be made to the alignment to more accurately reflect the sensors positions relative to the beam and one another. The procedure itself is repeated iteratively multiple times and is only performed with tracks from the *triplet finder*, as high purity is important for a precise alignment. More details to the mathematical methods are found in [38][40].



## **Part III**

### **DESY II and Lycoris**





# Chapter 5

## The DESY II Test Beam Facility

The DESY II Test Beam Facility [41] provides electron/positron beams for testing of particle detectors at a multi-GeV range in order to verify their functionality and performance. Pixel beam telescopes are widely utilized auxiliary devices. They are used to verify the integrity of devices under test at test beam facilities and the design and commissioning of a new telescope based on a novel sensor is the focus of this work.

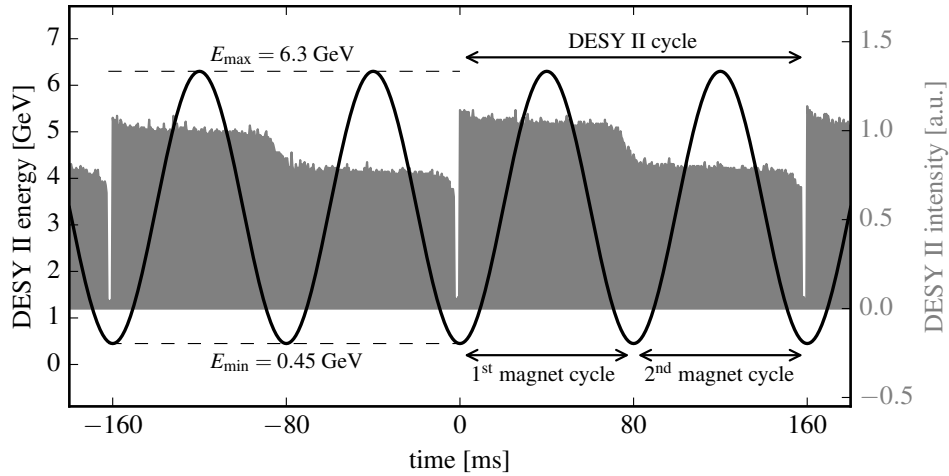
As such, the DESY II Test Beam Facility is both what the sensors are designed to be used at and used to determine the performance of the sensors and is therefore described in more detail below.

### 5.1 The DESY II Synchrotron

The DESY II synchrotron [42][43] is an electron accelerator in operation since 1987 as a component for a multitude of different installations including DORIS, PETRA, HERA and the DESY II Test Beam Facility [41].

The DESY II synchrotron parasitically provides particles for test beam operation which is explained in more detail in section 5.1.1. It has a circumference of  $U = 292.8\text{m}$  with an average radius of 46.6m. The synchrotron consists of dipole magnets, quadrupole and sextupole magnets as well as two High Frequency (HF) systems made up of klystrons and cavities. The dipole magnets are used to bend the particle on a curved trajectory.

The quadrupole and sextupole magnets are used as Focussing-Defocussing (FODO) cell optics. These arrangements of magnets widen the beam in one direction and focus it in another. The force that focuses the beam depends on the spread within the magnet. Hence, multiple rotated FODO cell optics one after another result in a net reduction of the beam size in both directions.

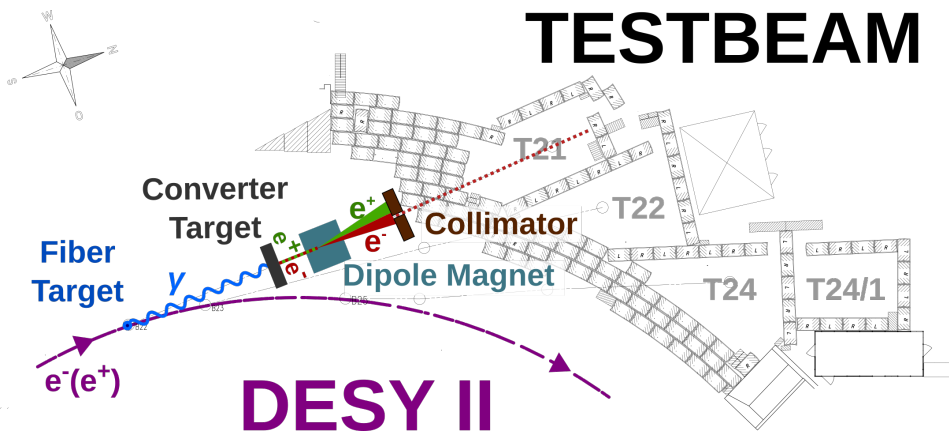


**Figure 5.1** – Measurement of the particle intensity within DESY (grey histogram) and the corresponding particle energy (black line) throughout two DESY injection cycles. [41]

The Klystrons are used to generate High Frequency (HF) electric fields which result in a strong electric field parallel to the particle within the four 500MHz 7-cell PETRA-type cavities. These fields are used for acceleration of the particles.

Standard operation is with a single HF system allowing the electrons to reach an energy of  $E_{\max} = 6.3 \text{ GeV}$  with the option of reaching  $7 \text{ GeV}$  when using both HF systems. As the electrons are highly relativistic, their speed is close to the speed of light which means that the particles take  $0.976 \mu\text{s}$  for a single cycle around the DESY II Synchrotron which is referred to as the DESY II bunch cycle.

The DESY II synchrotron ramps the beam energy up and down following a  $12.5 \text{ Hz}$  sinusoidally oscillating magnet current as the different installations like DORIS and PETRA required different injection energies. To allow the DESY II synchrotron to work as injector for all of them, the energy is constantly ramping up/down and the beam is extracted at the desired energy. This ramping scheme results in a cycle period of  $T_{E_{\min}} = 80 \text{ ms}$ . Every  $160 \text{ ms}$  a new particle bunch of up to  $10^{10}$  electrons/positrons is injected from the LINAC II (LINear ACcelerator) via the PIA (Positron Intensity Accumulator) storage ring into the DESY II synchrotron at an energy of  $E_{\min} = 0.45 \text{ GeV}$ . It then follows the sinusoidally oscillating magnet current and is accelerated up to  $E_{\max}$  and subsequently decelerated again to  $E_{\min}$  which is shown as the black line in Figure 5.1. This is repeated once more before the beam is dumped  $160 \text{ ms}$  after injection with a subsequent injection of a new particle bunch which is visible in Figure 5.1 in the form of the small low intensity gaps at  $-160$ ,  $0$  and  $160 \text{ ms}$  for the grey histogram which represents the particle intensity within the DESY



**Figure 5.2** – Sketch showing the DESY II Test Beam Facility [41].

II synchrotron.

The noticeable reduction in intensity at -80 and 80 ms is an effect of increased scattering at low energies in interactions with the carbon fiber targets used for test beam generation explained in section 5.1.1. The interactions result in an emittance increase due to broadening of the beam via multiple scattering and a subsequent loss of particles [41] as they are no longer within a stable orbit. To ensure that the intensity within DESY II does not drop too low the injection of new particles happens every 160 ms.

### 5.1.1 Test Beam Generation

The test beam is generated with the intention of minimal impact on the DESY II beam stability and lifetime. This is achieved via a double conversion scheme which, in addition, allows the user to choose the test beam energy.

Located behind the DESY II quadrupoles 21, 22 and 24, a target holder is installed within the beam pipe consisting of six 30 mm long and 7  $\mu\text{m}$  thick carbon fiber targets of which one at a time can be moved into the center of the electron beam. Particle interactions with the fiber target produce high energy photons via bremsstrahlung (see section 2.1.4) that are not affected by the magnetic field and exit the synchrotron tangentially via an extraction beam pipe with a thin aluminum exit window [41]. A sketch of the location of the test beam areas T21, T22 and T24 relative to the DESY II synchrotron, including all parts of the transfer path is shown in Figure 5.2.

After traveling for up to 22m the photons hit a converter target consisting of different materials listed in Table 5.1 and produce electron positron pairs via pair production (see section 2.1.4). The main effect of the different converter targets is the different rate of con-

Target No.	T21	T22	T24
1	Cu 5 mm	Cu 5 mm	Cu Wire 1 mm
2	Cu 4 mm	Cu 1 mm	Cu 4 mm
3	Cu 3 mm	Cu 3 mm	Cu 3 mm
4	Al 3 mm	Al 4 mm	Al 3 mm
5	Al 2 mm	Al 3 mm	Al 2 mm
6	Al 1 mm	Al 1 mm	Al 1 mm
7	Cu Wire 1 mm	Cu 10 mm	Cu 1 mm

**Table 5.1** – Different secondary target materials and thickness for the three test beam lines [41]

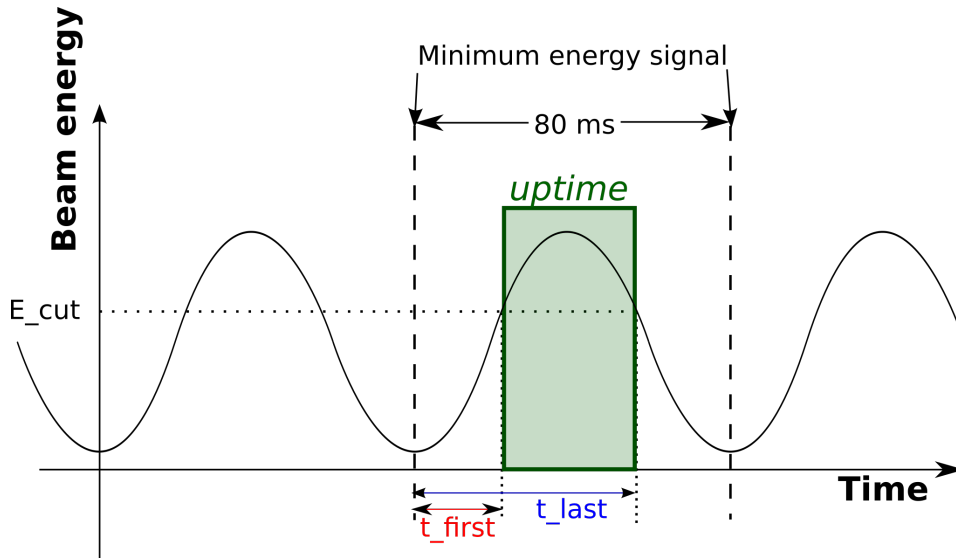
version resulting in an increased or reduced particle rate. The energy of the particles varies between zero and  $E_{\text{DESYII}}$  which is the energy of particles within the DESY II synchrotron at the moment of interaction with the carbon fiber target [41]. Before reaching the test beam area the particles travel through dipoles and pass the primary collimator. The particle type ( $e^+ / e^-$ ) and beam energy  $P_{\text{beam}}$  can be chosen by setting the strength and polarity of the dipole magnet  $B_{\text{dipole}}$  as only particles with a correct bending radius  $r_{\text{open}}$  within the magnetic field will be able to pass through the collimator:

$$r_{\text{open}} = \frac{P_{\text{beam}}}{eB_{\text{dipole}}}, \quad (5.1)$$

assuming no larger angular deviations of the particles.

A shutter is installed behind the primary collimator that, when closed, is able to stop all particles when no beam is needed. The primary collimator opening is adjustable in both directions allowing one to adjust the momentum spread as a trade off to the particle rate. Behind the shutter follows an evacuated beam pipe going to the test beam area where the particle exits via a Kapton foil window, passes through a beam monitor consisting of two coincident  $10 \times 10 \text{ mm}^2$  scintillators and finally passes through a secondary lead collimator with a length of 300 mm which allows for a final adjustment of the beam size and particle rate by varying its opening [41].

As a result of geometric limitations, two dipole magnets have to be used in conjunction for delivery of particles to Area T24. Only one dipole can switch its polarity without requiring any recabling and as a result only electrons are available as beam particles within area T24.



**Figure 5.3** – Sketch of the relation between the *uptime* and the chosen energy for the sinusoidal DESY II energy cycle.

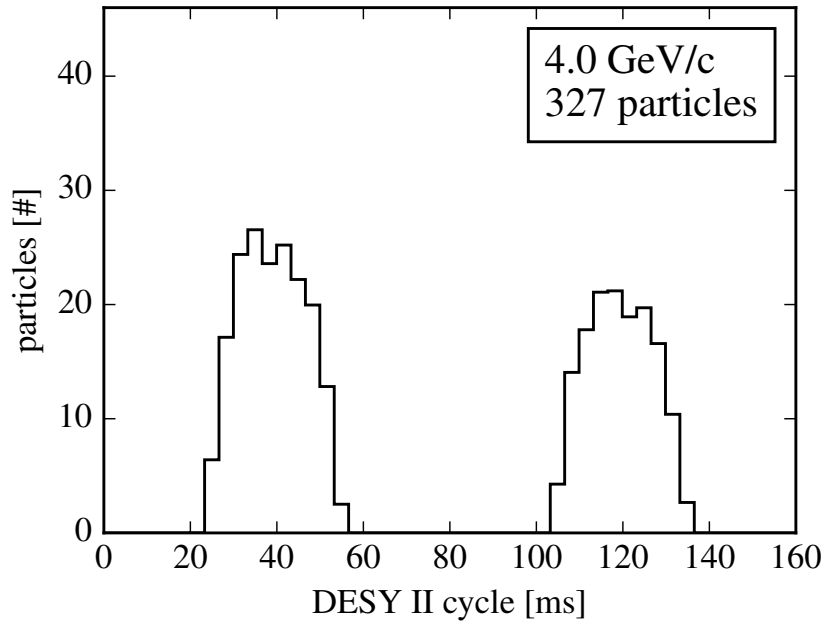
### 5.1.2 Beam characteristics

As a result of the sinusoidal energy cycle of the DESY II synchrotron and the double conversion particle generation, the generated test beam has a distinct time structure. A test beam can only be generated through the aforementioned process if the energy within the DESY II Synchrotron  $E_{\text{DESYII}}$  is higher than the energy chosen by the user  $E_{\text{cut}}$ . As such the start and end of the *uptime*, the time period during which test beam particles are generated, also depends on the chosen energy which is illustrated in Figure 5.3.

Figure 5.4 shows measurements for the time difference between the DESY II injection signal and the appearance of particles for a chosen energy of  $E_{\text{cut}} = 4 \text{ GeV}$  over a 160 ms period recorded in area T24 using the beam monitors as particle counters. The *uptime* is from 23 ms to 58 ms after injection into DESY II resulting in a total *uptime* of  $T_{\text{live}} = 35 \text{ ms}$  [41].

A secondary peak between 106 ms and 138 ms after injection corresponds to the second acceleration of the particles before dumping. The reason for the slight reduction in height compared to the first peak is the result of the reduced number of particles within DESY II after passing through the minimum energy point explained in section 5.1.

A general overview of the *uptime* for different beam momenta can be seen in Figure 5.5. The errorbars show the spread on the start and end times of the particles. The reason for the discontinuity of the spectrum are the extremely low rates at energies below 1 GeV severely

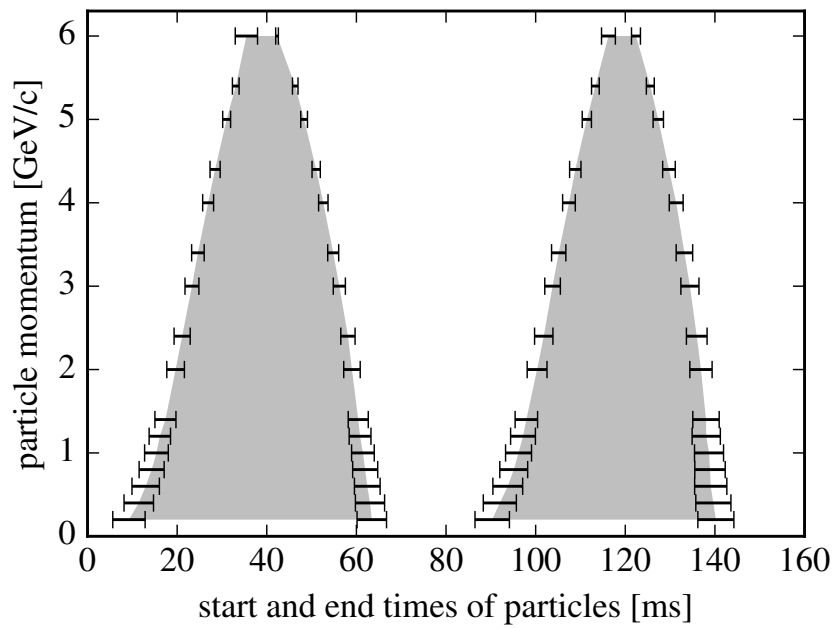


**Figure 5.4** – Time difference between the injection signal at 0 and the appearance of test beam particles in T24 over a whole injection cycle. [41]

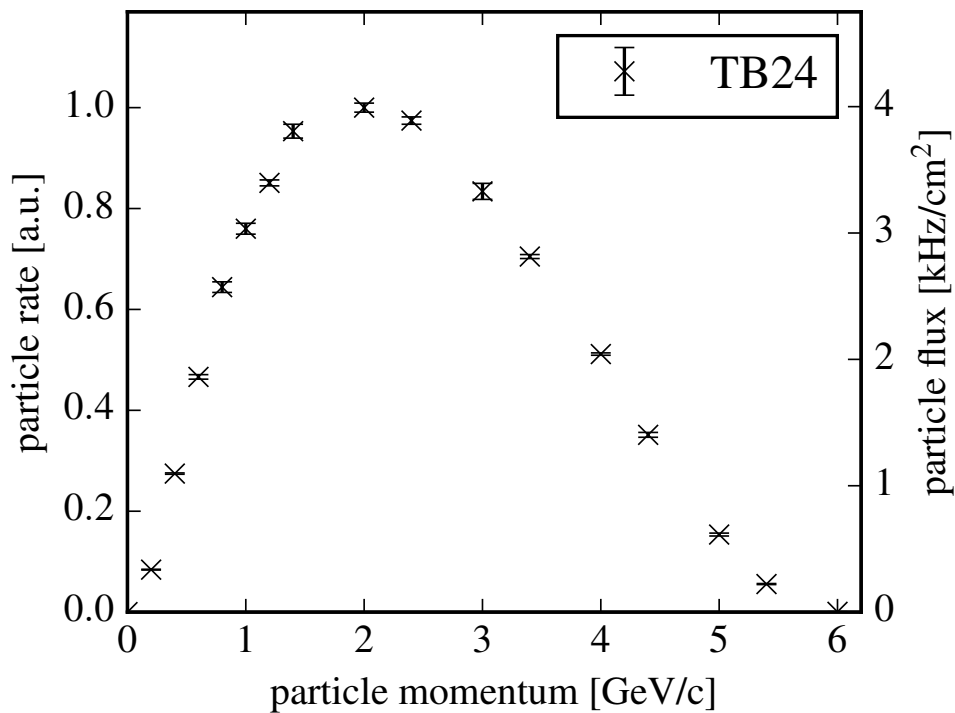
limiting the available statistics. The grey background shows the *uptime*.

The overall particle rate during test beam operation depends on many parameters chosen by the user which includes the exact position of the primary target within the DESY II beam, the secondary target material and thickness, the opening of the primary and secondary collimator, as well as the chosen beam momentum [41].

The relation between particle energy and beam flux is depicted in Figure 5.6. It shows the particle flux measured by the beam monitors located before the secondary collimator for different particle momenta. The distribution has a maximum at 2 GeV/c with a flux of 4 kHz/cm<sup>2</sup>. The reason for the rate reduction at higher energies is a result of the reduced *uptime* at higher energies and the lower available phase space for the production of high energy particles through the double conversion. The reason for the reduced rate at low energies is in part because of increased interactions of low energetic particles with rest gas and other material during the transfer from generation to the area resulting in both absorption of particles as a result of the higher energy loss as well as the increased multiple scattering. In addition, the magnetic field and collimator setup allows only a limited angle of particles to pass through the system. While the rate of particles increases at lower energies, most are not produced in the necessary small angular allowance of the transfer path and are lost as a result of hitting the collimator or pipe wall [41].



**Figure 5.5** – Beginning and end point for the test beam *uptime* for different energies measured via the T24 beam monitors. The grey area is the *uptime*.



**Figure 5.6** – Particle flux measured at the T24 beam monitors before the secondary collimator within the area. [41]

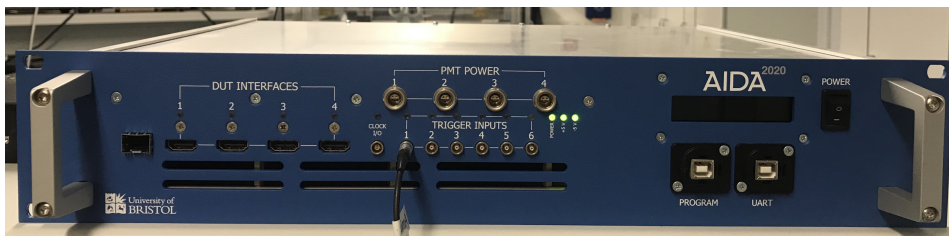
## 5.2 The AIDA Trigger Logic Unit

An infrastructure common to all test beam areas at the DESY II Test Beam Facility are the AIDA Trigger Logic Units (TLU). Trigger logic units are devices used to provide timing and trigger information to different devices used at test beam facilities. This is important as for example some Device Under Test (DUT) are running only externally triggered and/or their particular data readout structure requires the suppression of triggers to synchronize the data between multiple devices. TLUs are important for the combination of data streams from DUTs as well as auxiliary devices used to verify measurements such as silicon telescopes.

The previous generation of TLU at the DESY II Test Beam Facility were built as part of the EUDET [44] project which was a European detector research and development program. The AIDA [45] and AIDA2020 projects [46] are successors of the EUDET project. As part of these projects a new TLU iteration, which is referred to as the AIDA TLU, was designed and built.

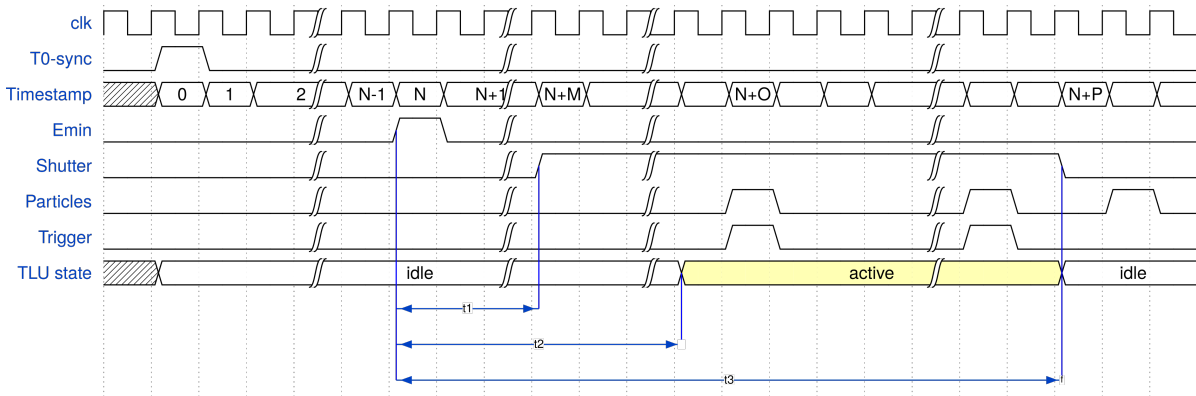
The AIDA TLU exists as both a tabletop and a rack unit. A picture of the rack unit, which was used in this thesis, is shown in Figure 5.7. The AIDA TLU can receive up to six asynchronous trigger inputs via single pole LEMO connectors, visible in the center of the TLU. The input is connected to fast discriminators with a threshold range between  $[-1.3, +1.3]$  V and any logical *AND/OR* combination for the six inputs can be used to generate a flexible global output for up to four Devices Under Test (DUT) via standard size High Definition Multimedia Interface (HDMI) connectors [47]. The HDMI connectors are used to send out trigger, clock and synchronization signals and a detailed pin out is shown in Table 6.

The TLU is also capable of receiving/sending out an external clock via a 2-pin LEMO connector which is located next to the trigger input connectors based on a 3.3 V Low Voltage Differential Signal (LVDS), as well as providing a 12 V power and control voltage via a power module in order to supply the operational voltage for up to four photomultipliers using



**Figure 5.7** – Picture of the AIDA TLU rack unit.





**Figure 5.8** – AIDA Mode operation for the TLU with synchronization T0 and synchronization to the DESY II *uptime* via the  $E_{\min}$  signal via the use of a shutter. [47]

4-pin LEMO connectors located above the trigger input.

The TLU firmware is operated on an Enclustra AX3 board and can generate any clock frequency between 100Hz and 1028MHz via its clock multipliers and connected jitter attenuators but is commonly operated with a 40MHz clock at the DESY II Test Beam Facility. The discriminated input signals can be stretched and delayed in multiples of the clock period in order to account for different signal delays between devices, for example, due to different cable lengths. For debugging purposes the TLU is capable of generating a periodic internal trigger signal which is referred to as the *auto trigger* [47].

The AIDA TLU offers four different operation modes:

- EUDET Mode: Once a trigger is registered by the TLU, the signal is sent out to the DUT and a busy line is set in order to ignore any further triggers. The busy is reset by the DUT once it is capable of receiving further triggers.
- EUDET Mode with trigger number: In addition to the above mentioned mode, the TLU logs out the trigger number by toggling the DUT clock line while the busy is active.
- AIDA Mode: The TLU and DUT are operated on the same clock and with synchronized time stamps. This is done by sending out a T0/sync signal at the start of the run which is used to reset the time stamp.
- AIDA Mode with trigger number: In addition to the above mentioned mode, the TLU sends out the trigger number on the T0/sync line.

In addition, the AIDA TLU allows the use of what is referred to as a shutter window in which two time periods are defined relative to an input signal. Any triggers that falls outside of

the two time periods are suppressed. The shutter window can be set to, for example, take into account the *uptime* at the DESY II Test Beam Facility, or the operational window of devices, even when they are incapable of sending back a busy to the TLU. The details of this operation mode are shown in Figure 5.8.

The different lines, described from top to bottom show the following [47]:

1. The continuous 40 MHz clock of the TLU.
2. The T0-sync signal which is used to tell all devices to start data taking.
3. The time stamp recorded by the AIDA TLU.
4. The  $E_{\min}$  which is given to the AIDA TLU via one of the lemo connectors. It can be used to synchronize to the DESY II *uptime* and was added explicitly for this thesis.
5. The Shutter which is based on the  $E_{\min}$  and can be adjusted by setting delays (t1, t2 and t3).
6. The particle occurrences in the input line.
7. The trigger line output based on the delay, coincidence and shutter settings.
8. The status of the TLU.

The TLU can be configured via configuration files and the following parameters can be adjusted[47]:

- Logical trigger combinations.
- Trigger delays.
- Coincidence window openings.
- Trigger output window openings.
- Signal input thresholds.
- Signal shutter windows.

### 5.3 The EUDET Type Silicon Telescopes

A key infrastructure at the DESY II Test Beam Facility are the EUDET type silicon telescopes[48]. At the time of writing, three separate telescopes are available called DATURA, DURANTA and AZALEA which are located in the areas T21, T22 and T24 respectively [49].

The EUDET type silicon telescopes consist of six silicon pixel planes which are based on the Mimosa26 [50] Monolithic Active Pixel Sensor (MAPS) (see section 3.2.2). The sensor has a pixel pitch of  $18.4 \mu\text{m}$  and is split into 1152 columns and 576 rows resulting in an active area of about  $21.2 \text{mm} \times 10.6 \text{mm}$ . A picture of the chip is shown in Figure 3.7.

Each sensor is about  $(54.5 \pm 3.6) \mu\text{m}$  thick and achieves a binary resolution of  $\sigma_{\text{res}} = \frac{18.4 \mu\text{m}}{\sqrt{12}} = 5.3 \mu\text{m}$ . Amplification and correlated double sampling is integrated in each pixel allowing for in-pixel zero suppression. The chip is operated with a 80 MHz clock and every column is read out in parallel using a rolling shutter. The rolling-shutter takes 16 clock cycles to read out each row which equates to a time of  $115.2 \mu\text{s}$  to read out the whole chip. After the rolling shutter has read out the last row it starts anew from the first [51]. The threshold above which the pixel responds to input can be set via JTAG files with the threshold being in multiples of the RMS noise of the chip. In this thesis the threshold was set to four times the RMS noise for all measurements.

The Mimosa26 is housed within an aluminum jig on its carrier PCB. Each jig is 15 mm thick, 180 mm long and 194 mm high with a small cutout in the middle for the Mimosa26 chip. The cutout is covered with  $25 \mu\text{m}$  thick Kapton CB foils located at the entrance and the exit in order to ensure the sensor is not exposed to light. The total material budget for the entire telescope system consisting of six such layers consists of  $\approx 300 \mu\text{m}$  of silicon and Kapton each resulting in a total radiation length of  $X = X_{\text{kapton}} + X_{\text{silicon}} \approx (1.0 + 3.2) \cdot 10^{-3} \approx 0.42 \% X_0$ .

Each jig can be connected to water tubes in order to water cool the Mimosa26 during operation using a Huber mini chiller which is capable of keeping the sensors at a stable temperature and are typically operated at a temperature of 15 to  $20^\circ\text{C}$ . Three of these jigs are each placed on top of a guiding rail with a length of 300 mm which allow the change of individual distances between the planes. In addition, the guiding rails can be moved together in order to not disturb any alignment and to adjust the distance to the DUT. The two guiding rails are placed on a common rotating frame allowing the change of the inclination angle of the system to the beam.

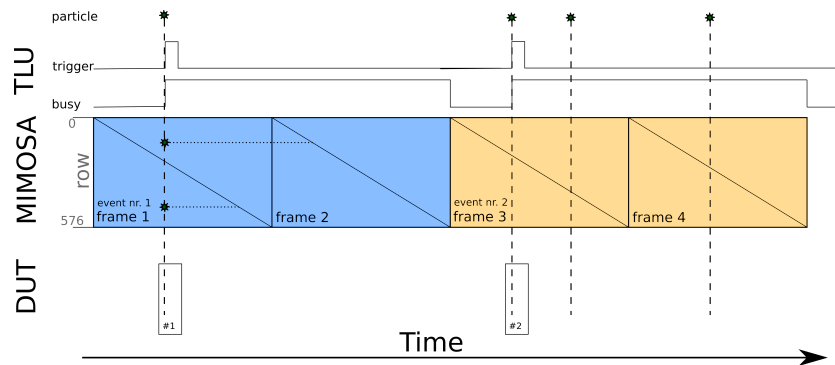
Four scintillators, grouped into two x-/y-orientations are placed before and after the telescope with an overlapping area of about  $10 \text{mm} \times 20 \text{mm}$ . They are run in coincidence using the AIDA TLU to provide trigger signals for telescope operation.

Figure 5.9 shows the full telescope setup within Area T24 at the DESY II Test Beam Facility. Using an analysis based on GBL (see section 4.2.4) [36] to take into account multiple scattering, the telescopes are able to achieve a track resolution down to  $2 \mu\text{m}$  depending on the beam energy, DUT thickness and plane distances [48].



**Figure 5.9** – Picture of the EUDET Type telescope within testbeam area T24 [31].

There is a chance that the rolling shutter has already read out the row the particle passed through before its arrival, as the data of the Mimosa26 is readout sequentially row by row. This particle is then only registered after the rolling shutter has completed the second frame readout. As each frame is only written to disk if a trigger signal is received during the frame this results in the particle not being recorded as the trigger arrived in the first frame. To avoid such a scenario, a Mimosa event consists of two readout frames as shown in Figure 5.10. This doubles the readout time for a single event to  $T_{FA} = 230.4 \mu\text{s}$ , increasing the multiplicity per event and degrading the time resolution.



**Figure 5.10** – Sketch showing the workings of the EUDET telescope readout. The readout is split into frames each of which take  $115.2 \mu\text{s}$  to readout. Two of them are combined into an event shown by the two colors. The diagonal line running through the frame signals the rolling shutter readout position with the time shown on x axis. A particle could be located in a row that has already been read out by the rolling shutter as such it is only read out once the rolling shutter once more reads out the row in question signified by the dotted line connecting the particle location to the diagonal line. The second event shows that nothing will be read out in the case that no trigger arrives with a particle.

## 5.4 The PCMAG 1T Solenoid

In order to verify the detector performance in a scenario as similar as possible to many particle physics detectors, tests in a magnetic field are crucial. In order to facilitate such tests, a superconducting solenoid magnet, called PCMAG (Persistent Current MAGnet) is located in test beam area T24/1 (see Figure 5.11).

The operational central magnetic field strength of the PCMAG is up to 1 T. The magnet bore has an opening diameter of 85 cm and a length of 130 cm. The magnet possesses no return yoke as it was originally designed for a balloon experiment for which a yoke would have introduced too much weight and material [52][53]. As a result, the electrons only have to pass through the magnet wall itself which contributes 20% of a radiation length  $X_0$ . Operation without a yoke results in a less homogeneous magnetic field. The inhomogeneity of the field increases closer to the edge of the coil and the magnet has stray fields affecting the entire T24/1 area. The exact field of the solenoid was mapped with very high precision in a dedicated study [54].

The PCMAG is mounted on a movable stage, constructed as part of the EUDET project [44]. The stage allows the PCMAG to be moved perpendicular to the beam, horizontally and vertically, with a precision of 0.3 mm. Additionally, the PCMAG can be rotated up to  $45^\circ$  in both directions around the vertical axis to introduce an inclination angle between





**Figure 5.11** – Picture of the PCMAG superconducting solenoid located in Area T24/1 without the four additional rails used for the Lycoris telescope.

the magnet and the beam with a precision of  $0.1^\circ$ . Two rails are installed within the PC-MAG to allow the mounting of different devices such as the EUDET-type telescopes within the PCMAG. Four more rails have been installed within the PCMAG in order to house the Lycoris telescope which is described in more detail in the following chapter, which was

# Chapter 6

## The Lycoris Strip Telescope

The Lycoris strip telescope is the newest addition to the beam telescopes for the DESY II Test Beam Facility. The system is designed to improve the capabilities of the DESY II Test Beam Facility by providing a new telescope with a focus on a large active area and minimal support structure while providing comparable spatial resolution to the existing telescopes.

The system consists of six layers of a large area silicon strip sensor with a strip pitch of 25  $\mu\text{m}$ . The sensor has a novel readout in which the strip signal is routed through extra metal layers to a bump-bonded integrated readout ASIC. Three layers each are housed in an aluminum cassette in which they are mounted in the correct orientations and protected from the environment. The requirements, resulting choice of sensor and the final hardware components of the telescope are described in this chapter.

### 6.1 Project Requirements

The design of the Lycoris telescope has been largely influenced by the Linear Collider Time Projection Chamber (LCTPC) collaboration's effort to building a high precision Time Project Chamber (TPC) for the International Linear Collider (ILC). As part of this effort, a small scale prototype of the ILC TPC field cage was built which has a diameter of 77 cm and a length of 61 cm.

Measurements of the prototype field cage are performed within the PCMAG superconducting solenoid which has an inner diameter of 85 cm [55]. The coordinate system within the PCMAG is defined as follows:

- The  $z$ -axis is defined by the beam particle direction with movement along positive  $z$  going parallel to the beam,

Parameter	Value
Resolution $x$	1 mm
Resolution $y$	80 $\mu\text{m}$
Resolution $q/P$	$4.584 \times 10^{-6} \text{ MeV}^{-1}$

**Table 6.1** – Design performance of the LCTPC prototype [56].

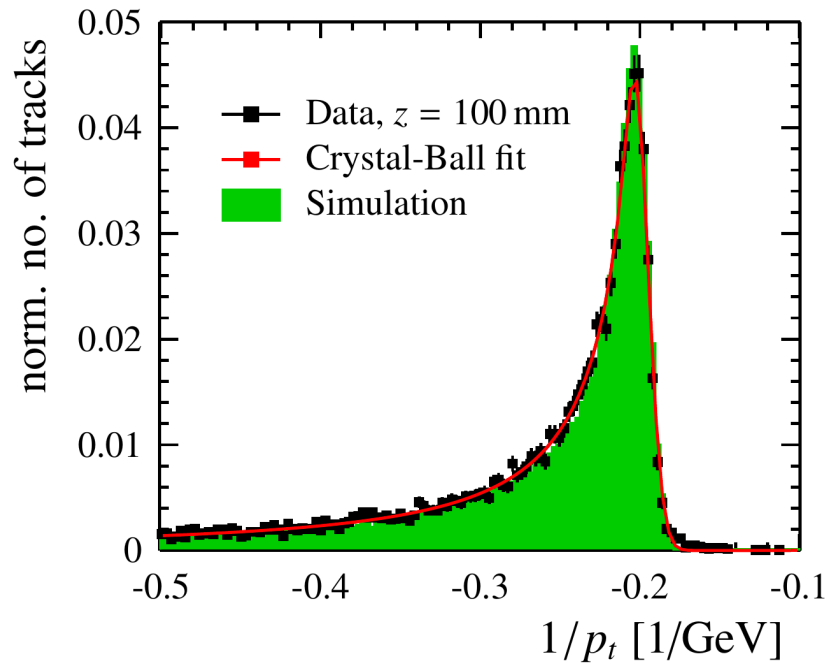
- the  $x$ -axis is parallel to the magnetic field line within the PCMAG solenoid,
- the  $y$ -axis is perpendicular to the other two axis and spans a right handed cartesian coordinate system.

As is typical for a DUT, it is necessary to confirm the DUTs performance which is tabled in Table 6.1. The verification of this performance cannot be done with the currently existing EUDET type telescopes because of their size. It is not possible to install more than one layer of the AZALEA telescope in the gaps in front and behind the prototype field cage within the PCMAG, due to the large size of the EUDET type telescope layer sizes [49].

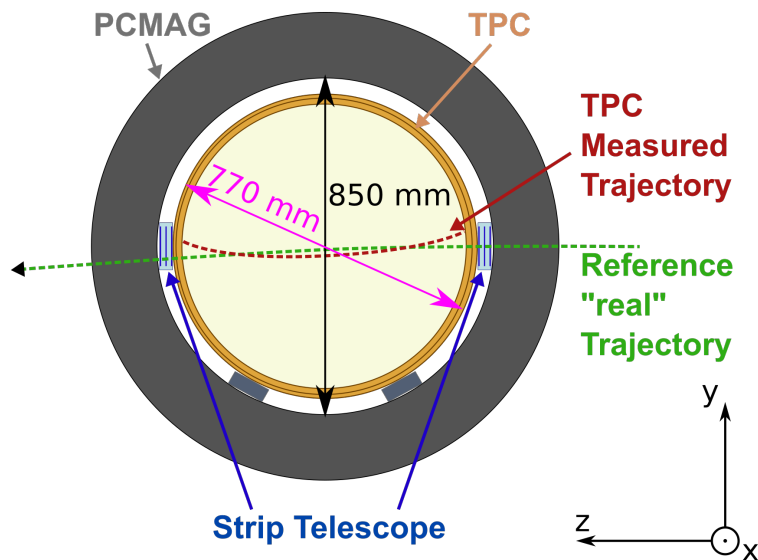
While it is possible to install the full system outside of the PCMAG, this would not be useful to determine the performance of the LCTPC prototype. As mentioned in section 5.4, the electron beam has to pass through the magnet coil to enter the magnet. Interactions with the magnet wall not only result in a deviation from the measured track parameters by the telescope through multiple scattering, energy loss in the interaction with the magnet wall reduces the particle momentum and affects its bending. The exact effect of the interaction with the magnet wall onto the particle momentum was determined in a simulation which is shown in Figure 6.1. It is not possible to determine the momentum within the PCMAG to an accuracy better than the width of the peak in the distribution of  $1.9 \text{ MeV}^{-1}$  [57]. This is far below the theoretically achievable momentum resolution of the LCTPC prototype of  $4 \times 10^{-6} \text{ MeV}^{-1}$  [57]. In addition, an independent measurement of the particle trajectory through the prototype field cage allows the measurement of potential field distortions of the electric drift field present inside the field cage which can skew the measured trajectory by the TPC.

The Lycoris system needs to provide as good or better performance in all parameters than the LCTPC prototype. To achieve this, it needs to be installed together with the LCTPC prototype field cage within the PCMAG, resulting in strong constraints on the available space. Figure 6.2 shows a sketch of the principle of the setup. The red curve within the sketch is an exaggerated example in which the TPC measures a trajectory that is different from the true particle trajectory because of field distortions. The requirements to the point





**Figure 6.1** – Particle momentum distribution after interaction with magnet wall through Data in black and simulation in green [57].



**Figure 6.2** – Sketch showing the functionality of an external reference within the PCMAG to determine correct momentum resolution and the used coordinate system.

		Telescope arm size			
		4 cm	3 cm	2 cm	1 cm
Sensor resolution	2.5 $\mu\text{m}$	2.85	2.90	3.00	3.68
	5 $\mu\text{m}$	3.05	3.21	3.63	5.52
	7.5 $\mu\text{m}$	3.37	3.65	4.43	7.92
	10 $\mu\text{m}$	3.68	4.16	5.33	9.90
	15 $\mu\text{m}$	4.49	5.36	7.53	14.3

**Table 6.2** – *GEANT4* momentum resolution in units of  $1 \times 10^{-6} \text{MeV}^{-1}$  for different configurations of the sensors spatial resolution and the distance between outermost layers within an arm based on a system with 4 layers [56].

resolution in x and y of the LCTPC prototype are easily achievable by commonly available silicon sensor systems. The momentum resolution on the other hand improves with the number of measurement points  $N$  in which the TPC excels. The relation between the momentum resolution and the number of measurement points is given by the Glueckstern formula [58][3]:

$$\frac{\sigma_p}{p} \propto \sqrt{\frac{720}{N+4}}. \quad (6.1)$$

The telescope needs a much better single point resolution in direction of the bending of the magnetic field than the TPC to achieve a similar momentum resolution. In order to investigate the required performance of the sensors, a *GEANT4* [59] simulation was performed to verify the required number of layers, active area coverage, single point resolution, sensor spacing and material budget to achieve the necessary momentum resolution. The simulation includes the magnet with its wall, the silicon layers with a standardized thickness of  $250 \mu\text{m}$  as well as the TPC prototype field cage. 100000 electrons with an energy of  $4.4 \text{GeV}$ , a beam size of  $1 \text{mm}$  and a beam spread of  $2 \text{mrad}$  are used in the simulation. Based on the results from the *GEANT4* simulation (see Table 6.2), sensors with a single point resolution of less than  $10 \mu\text{m}$  are required to achieve a momentum resolution better than  $4.584 \times 10^{-6} \text{MeV}^{-1}$  with the available space per arm of less than  $4 \text{cm}$ .

Figure 6.3a shows the simulated particle spread after arriving inside of the PCMAG before the beam has been influenced by the magnetic field. Figure 6.3b on the other hand shows the same distribution before the beam leaves the inside of the magnet after all particles were influenced by the magnetic field. While the entry position is mostly given by the starting parameters, the exit distribution shows the beam spot is about  $30 \text{mm}$  lower in accordance with the particle bending in the magnetic field described by (4.1). In addition

to the shift to lower  $y$  values, a larger tail in the exit distribution is shown which is a result of the energy loss of particles through interaction with the magnet wall getting bent further down as a result of their lowered momentum. For a good efficiency, the detector should be able to record as much of the tail as possible. An active coverage area of about  $10 \times 10 \text{ cm}^2$  is chosen which allows to record close to 95% of all particles [56].

Using the intended height of the system, the maximum available space within the PC-MAG next to the prototype field cage (see Figure 6.4) can be determined. Due to the curvature of the TPC and magnet wall, the available space along the beam direction reduces with increasing height of the sensor. For a coverage of 100 mm in  $y$ , this limits our available spacing of the sensors to:

$$\begin{aligned} a &= b - r_1 \\ b^2 &= r_2^2 - y^2 \\ \Rightarrow a &= \sqrt{r_2^2 - y^2} - r_1 \approx 37 \text{ mm}. \end{aligned} \tag{6.2}$$

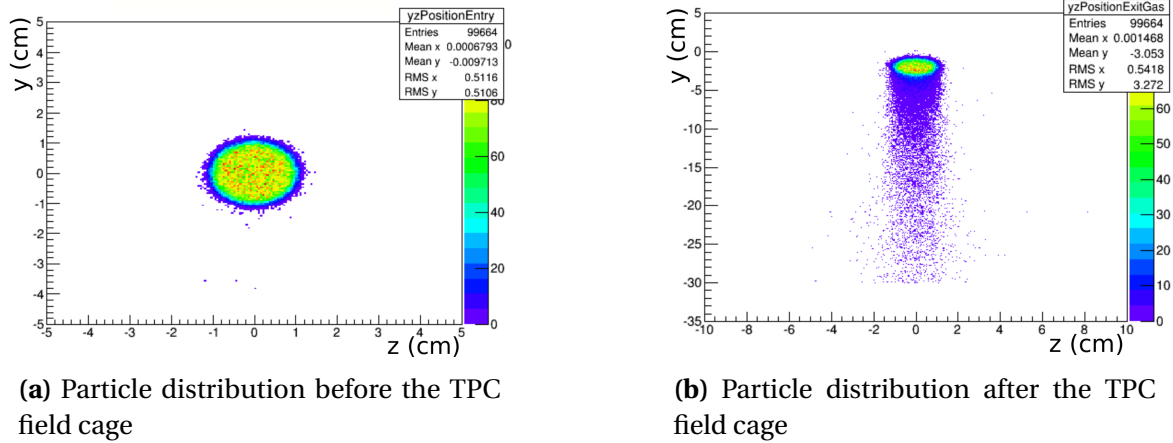
There are no inherent constraints on the size of the telescope along the  $x$ -axis except that it needs to fit within the 1.3 m long PCMAG opening. The effect of the material budget was simulated and is required to be below  $2.1 \times 10^{-2} X/X_0$  [60] to reduce multiple scattering induced smearing of the momentum resolution. The simulation was performed under the assumption that the sensors have a distance of about 3 cm between the first and last sensor within an arm and a spatial resolution of  $10 \mu\text{m}$ . This limits the number of layers that can be installed per arm and any further material that could be part of the support structure.

As the movement of the particles within the TPC is described by a helix, a minimum of five independent measurements is required to constrain the fit. Pixel layers provide two-dimensional measurements meaning that three layers are sufficient. Strip layers provide only one-dimensional measurements meaning at least five strip layers are required. The requirements on the sensors and the telescope as a whole are summarized in Table 6.3.

Since the telescope system is intended as a general infrastructure upgrade of the DESY II Test Beam Facility, the telescope system should be easy to use for non-expert users. This means that it has to be easy to un-/install, allowing easy access to all necessary mechanical and electrical connections and ensuring high protection for the sensors in every-day operation.

Different sensors have been considered for the project:

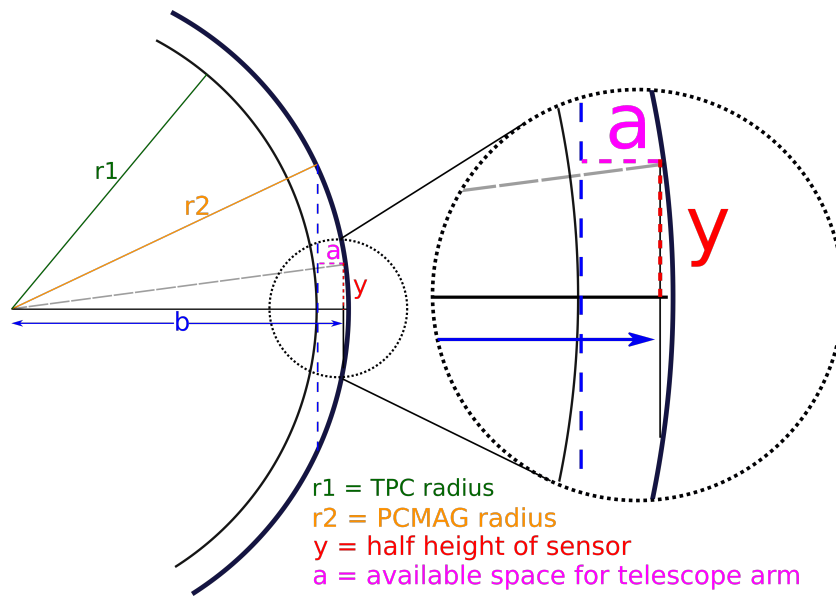
- Current ATLAS and CMS sensors were considered but deemed unfeasible as they do not achieve the necessary single point resolution [61][62].



**Figure 6.3** – *GEANT4* simulation result for the particle hit location at the entry and exit of the PCMAG [56].

Parameter	Requirement
Area A	$\approx 10 \times 10 \text{ cm}^2$
Thickness d	$\leq 37 \text{ mm}$
Length L	$\leq 1300 \text{ mm}$
$\sigma_y$	$\leq 10 \mu\text{m}$
$\sigma_x$	$\leq 1 \text{ mm}$
Nr. of layers	$\geq 3/5$ (Pixels/Strips)
Total Radiation Length per arm $X/X_0$	$\leq 2.1 \%$

**Table 6.3** – Final requirements to the telescope system [60].



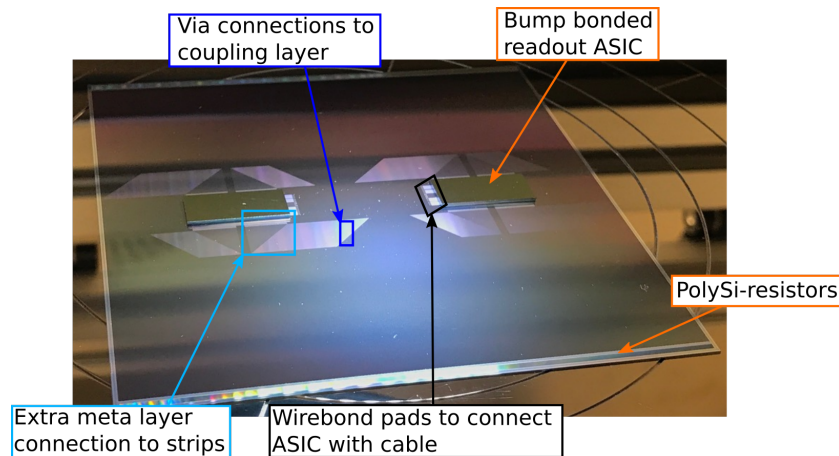
**Figure 6.4** – Sketch showing relation between sensor height  $y$  and available space  $a$ .

- The Mimosa26 chip used in the EUDET type telescopes (see section 5.3) within a different housing was considered, but to achieve the required large active area would have required funding above what the project allowed and cooling was considered an issue.
- The sensors from the former Zeus vertex tracker [63] would have achieved the necessary resolution but could not be used as there is no existing support and hardware for the DAQ.
- The SiLC strip sensor [64] was also under consideration. It provides a large active area, though the single point resolution was at the edge of what was necessary and the expected support was lower than for the sensor which was chosen.

The final choice fell on a system consisting of the SiD outer tracker strip sensor [1] with the KPiX [29][65] readout chip both of which are explained in detail below.

## 6.2 The SiD Sensor and Readout

The SiD sensor is intended to be used as the main sensor instrumenting the whole barrel of the SiD detector concept [1]. The KPiX Application Specific Integrated Circuit (ASIC) [29] is the readout chip intended to be used for signal processing from the silicon sensors



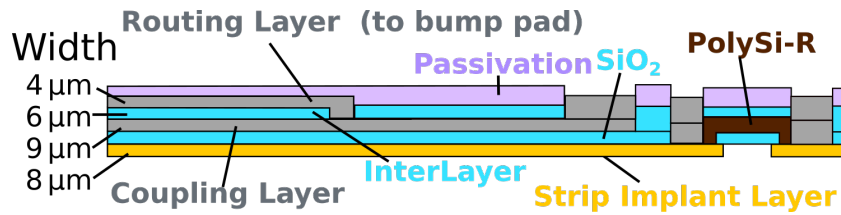
**Figure 6.5** – Picture of an SiD strip sensor with flip chip bonded ASICs- The three squares are regions of the sensor shown in microscopic pictures in Figure 6.8a (azure), Figure 6.8b (black) and Figure 6.10 (blue).

which includes the SiD tracking sensor [1] and silicon based SiD electromagnetic calorimeter sensor [66]. A picture of the SiD tracking sensor which is referred to as the SiD sensor is shown in Figure 6.5. The two objects visible on top are the flip-chip bonded KPIX readout ASICs.

### 6.2.1 SiD Sensor

The SiD strip sensor is a  $320\ \mu\text{m}$  thick hybrid silicon sensor designed by SLAC for the SiD detector concept. The sensor is made up of n-type silicon with  $p^+$  strip implants and an  $n^+$  back plane. They are produced by Hamamatsu [67] Photonics, have a total size of  $93.53 \times 93.53\ \text{mm}^2$  and consist of 3679 strips with a pitch of  $25\ \mu\text{m}$  and a length of 92 mm resulting in a total active area of  $92 \times 92\ \text{mm}^2$ . The active area is surrounded by three ring structures consisting of the inner bias ring, the central guard ring and the outer ring connected to the negative substrate (nsub) of the sensor.

The SiD strip sensor has a novel readout method for the strips compared to normal hybrid strip sensors (see section 3.2.1). Instead of reading out the strips through wire-bonds at the edge of the sensor, additional metalization layers are added to the top of the sensor which route the signal from the strip to pads on the topside allowing for much smaller strip pitch than is conventionally supported. This design is referred to as a *hybrid-less* sensor design by SLAC as it eliminates the need for a carrier PCB to house the readout ASIC and compared to normal hybrid pixel sensors the readout ASIC can be of much smaller size



**Figure 6.6** – Sketch of the readout layers of the SiD sensor

than the sensor reducing the average material budget.

Because of this, the silicon sensor is split into multiple layers with some layers unique to the makeup of the sensor and depicted in Figure 6.6. Charge deposited in the sensor bulk drifts to the strip implants which have a width  $8\ \mu\text{m}$  and are shown in yellow in the sketch.

These strip implants are mirrored by what is described as the *coupling layer* from which they are separated by a silicon oxide layer for the entire routing structure on top of the sensor shown in blue.

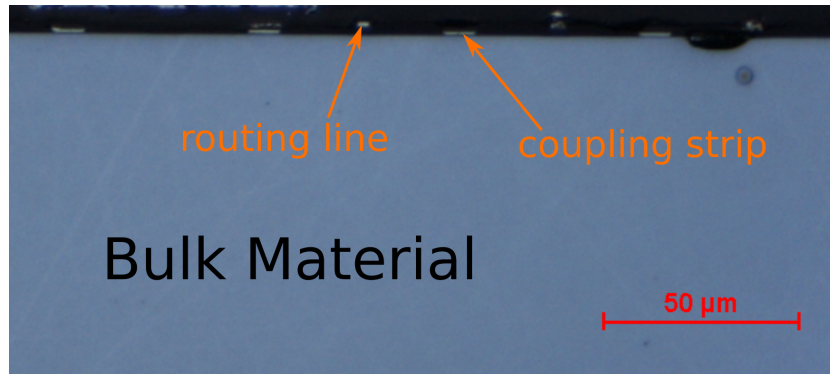
The *coupling layer* layer is made up of  $9\ \mu\text{m}$  wide aluminum strips, running in parallel to the strip implant, capacitively coupling the two layers. This layer is shown as the grey line parallel to the implant layer.

The *coupling layer* is connected through vias to what is referred to as the *routing layer*.

The *routing layer* layer is made of  $4\ \mu\text{m}$  wide aluminum and is located between the passivation which is shown in violet on top of the sensor and an additional silicon oxide layer, referred to as the *InterLayer* with a width of about  $6\ \mu\text{m}$  also shown in blue. The *routing layer* is used to provide a direct electric connection to the bump-bond pads which are located on the surface of the sensor to be readout by the readout ASIC.

The sensor surface has 33 rows of 32 bump pads per side with an under bump metalization consisting of Ti/Ni/Au which has been applied by Hamamatsu during production. Most of the pads from the 32 outermost rows of bump pads are connected to the *coupling layer* via the method described above and are used to transfer signal induced on the *coupling layer* to the surface where they can be read out. The *routing layers* are the visible structures inside the sensor next to the KPiX ASICs in Figure 6.5. The innermost row of the 33 bump pad rows of the sensor halves are connected to wire-bond pads via a separate *routing layer*. Exact specifications of the thicknesses of the non bulk material have not been made available by Hamamatsu, but a rough value could be inferred from a microscopic picture of a sensor cross section shown in Figure 6.7.

The values of the different layers are listed in Table 6.4. The picture shows that the *routing layer* appears to vary in thickness. This is the case when the cross section is at a



**Figure 6.7** – Microscope picture of the cross section of a SiD sensor.

Layer	Thickness
Total	≈ 320 μm
Bulk	≈ 314 μm
Non-Bulk	≈ 6 μm
<i>Coupling layer</i>	≈ 1 μm
<i>Routing layers</i>	≈ 1 μm
<i>Interlayers</i>	≈ 1 μm
Oxide layers	≈ 3 μm

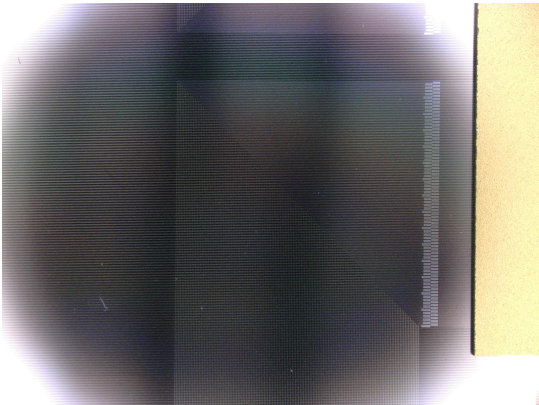
**Table 6.4** – SiD layer thickness

point where a via of the *routing layer* is located resulting in a seemingly thicker *routing layer*. The area between two metal dots in the picture is described as the *InterLayer* which separates the implant from the strip see Figure 6.6.

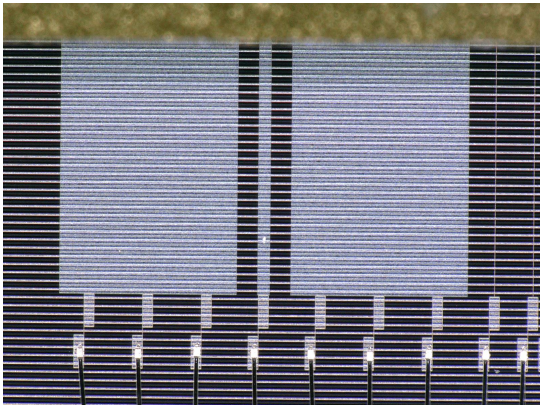
Figure 6.8a to Figure 6.9 show microscopic pictures of three specific connection regions of the extra metal layers to different points such as the ASIC, the wirebond pads and the *coupling layer* on the sensor. The relation of the pictures to the whole sensor structure are given by the rectangular highlights in Section 6.2.1. Figure 6.8 shows pictures taken with a microscope camera looking, from the top, directly at the *routing layers* connecting the KPiX, which is the golden structure visible in the picture. Figure 6.8a shows the routing from the strips to the KPiX, while Figure 6.8b shows the routing from the KPiX to its connection wire-bond pads.

Depicted in Figure 6.9 is a close up of the via that connects the *coupling layer* to the *routing layer*. The silver lines are the metal layers of the *coupling layer* and *routing layer*. Only every second of the 3679 strips has a *coupling layer* and is read out, resulting in 1840



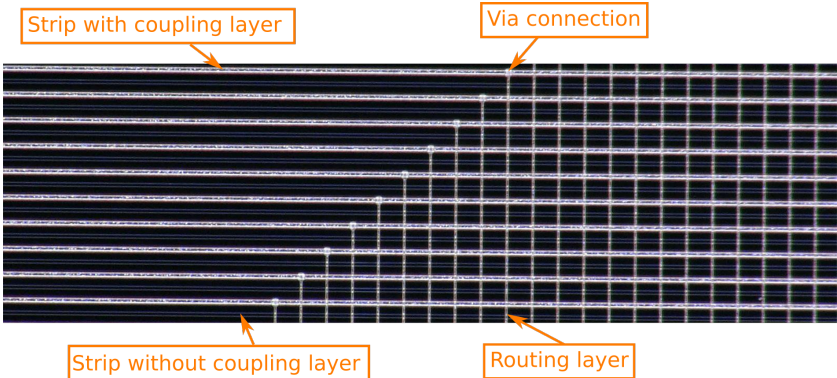


(a) Picture of the routing layer connecting a strip to the KPiX

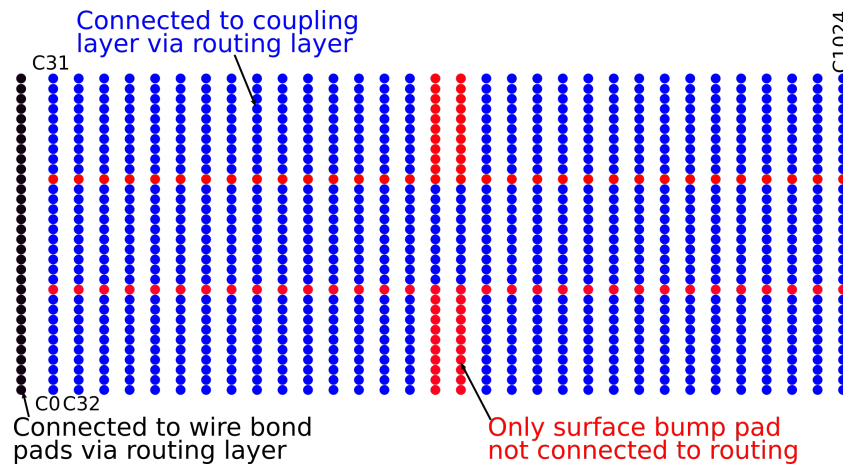


(b) Picture of the routing layer connecting the KPiX to the wirebond pads

**Figure 6.8** – Microscope pictures of the SiD sensor routing layers.



**Figure 6.9** – Microscope picture showing the via connection from the *coupling layer* to the *routing layer* which transfers signal to the ASIC.

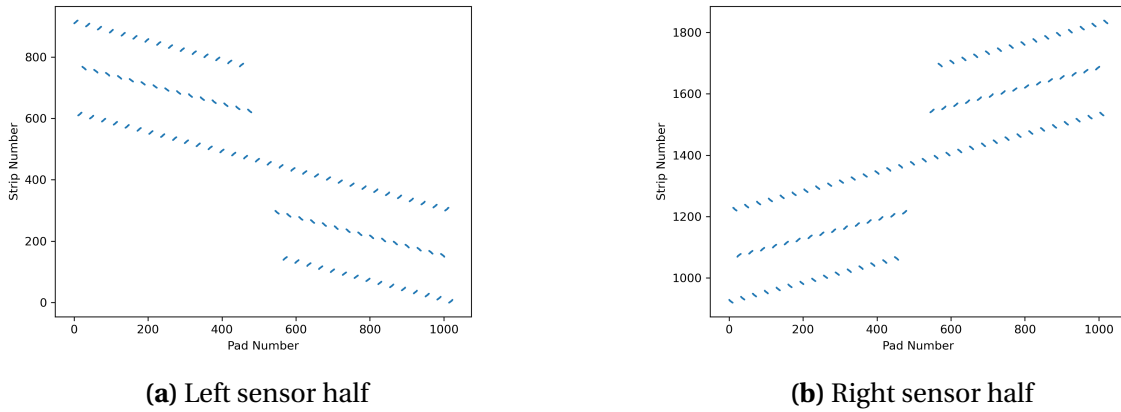


**Figure 6.10** – Sketch of the locations of the different connections of the bump-bond pads to the wire-bond pads and *coupling layer*. The names C0 to C1024 is based on the name of the corresponding KPiX channel which is connected to this bump-bond pad.

readout strips with a pitch of  $50\ \mu\text{m}$ . Interspersed between the two metal strips of the *coupling layer* is another darker strip. These are *floating* strips which are not read out and are used to improve the point resolution of the sensor via charge sharing as explained in section 3.1.5.

The 1840 readout strips are split into two blocks of 920 strips that are connected to surface readout pads. Figure 6.10 is a sketch of the bump-bond pads on the surface of the sensor with a description what the different pads are connected to on the sensor. The naming of the pads such as C0 to C1024 refers to the corresponding channel number of the KPiX ASIC. Ten bump pads per row are referred to as a block of pads which are connected to ten strips adjacent to one another meaning that an increase in channel number by 1 results in a change in strip number by 1. The next group of ten connected bump pads are once more connected to a block of strips but, because of the routing, two adjacent bump pad blocks do not translate to adjacent strip blocks. By defining strip zero to be the strip closest to the edge, strip 920 to be in the center of the sensor and strip 1840 to be at the opposite edge, a pad to strip mapping with the pad numbering scheme shown in Figure 6.10 can be produced. The result of this mapping is shown in Figure 6.11 which is given for both halves of the sensor separately as each half is a rotated version of the other.

The sensor is designed to deplete with a voltage of  $V_{\text{dep}} = +50\text{V}$  and have dark currents in the order of  $\mu\text{A}$ . The sensor has pads on the sensor surface through which it can be probed. Each strip implant can be connected to via an AC pad located in front of the resistors. The resistors consist of poly-crystalline silicon (Poly-SiR) and connect the *coupling*



**Figure 6.11** – Plot showing the relation between the pad number on the x axis and the corresponding strip number on the y axis for the two sensor halves.

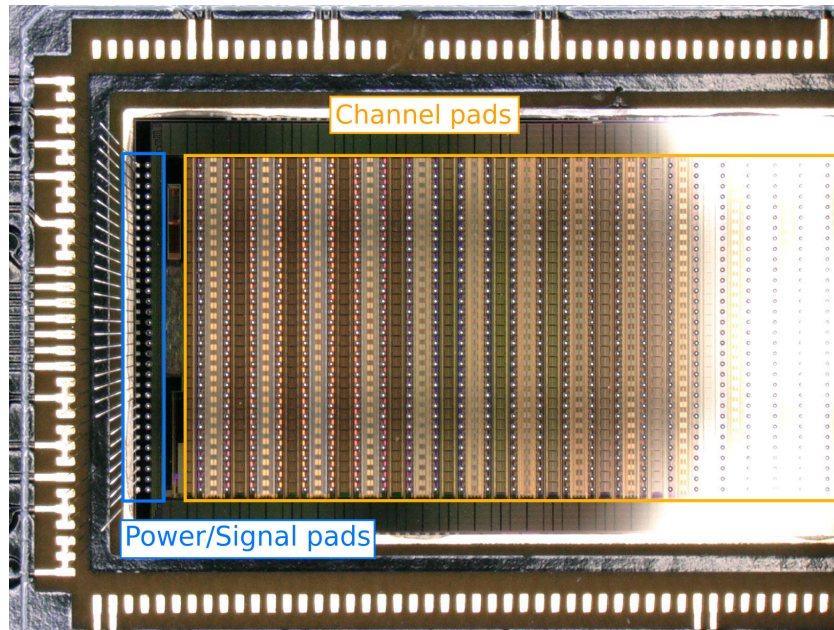
PAD name	Size ( $\mu\text{m}^2$ )
AC	$30 \times 40$
DC	$60 \times 200$
Bias Ring	$170 \times 430$
Guard Ring	$70 \times 430$
Nsub	$280 \times 430$
Readout	$60 \times 200$

**Table 6.5** – Probe pads of the SiD sensor

layer of each readout strip to the bias ring. Each *coupling layer* can be connected to via a DC pad located next to the AC pads. Each of the three rings surrounding the sensitive areas has multiple pads located all around the sensor to connect to them. This is used to determine the electrical properties of the sensor (see section 7.2). Pads connecting to the routing metal layer are located close to the bump-bond pads. The sizes of the different probe pads are tabled in Table 6.5.

## 6.2.2 KPiX ASIC

The KPiX ASIC is  $250 \mu\text{m}$  thick and based on a  $250 \text{ nm}$  mixed-mode CMOS process from Taiwan Semiconductor (TSMC) [68]. The chip consists of 1024 channels with a fully digital 13-bit ADC readout. It provides both timing and temperature information and is typically operated with an analog voltage of  $2.5 \text{ V}$  and a digital voltage of  $2.0 \text{ V}$ . Signals are measured



**Figure 6.12** – Microscopic picture of the bottom side of a bare KPiX ASIC which in the picture is flipped over and connected to via wirebonds.

as negative pulses relative to the 2.5V analog operational voltage. The chip is designed for power pulsing operation at the ILC which has what is referred to as a train of bunches with spacing of 524 ns between bunches which lasts for 0.727 ms that is repeated every 200 ms [69]. As such there is a long time during which no particles are expected and during which the analog front-end of the ASIC is powered down in order reduce power consumption and thereby the heat generated by the system [65].

Depicted in Figure 6.12 is a microscopic picture of the bottom side of the KPiX ASIC. In the picture, the chip is read out via wire-bonds. To the right of the wire-bonds, some of the 32 rows each consisting of 32 channels which are normally connected to the sensor via bump-bonds are shown. The wire-bonds in the picture are connected to the outermost row which is used to connect the KPiX to the wire-bond pads through the *routing layer* depicted in Figure 6.8b. A simplified block diagram of a single KPiX readout channel is shown in Figure 6.13 and the KPiX can be separated into four different components:

- Calibration circuit,
- Amplification circuit,
- Trigger circuit,
- Digitization circuit.





range ranging from about 5% of the charge deposition of a Minimum Ionizing Particle (MIP) in  $300\ \mu\text{m}$  of silicon to the deposition of up to 2000 MIP simultaneously. During normal gain operation, a charge deposition of 1 fC results in a voltage amplitude of 2.5 mV whereas in high gain operation it results in a voltage amplitude of 10 mV because of the different input capacitances. The amplifier circuitry is connected to an active reset that is used to discharge all capacitors in the amplifier [29].

The amplified signal is transferred to the trigger circuitry. The KPiX system can be operated in internal triggering operation and in external triggering operation. During internal triggering, an event is recorded when the signal is above a voltage threshold adjustable via an 8-bit DAC ranging from zero to 2.5V with the same translation as described in (6.3). The thresholds cannot be adjusted for each channel individually, though the system can compensate a possible non uniform pixel response to a certain extent by allowing two different triggering thresholds. These thresholds are referred to as thresholds A/B and are set for each KPiX separately. In internal triggering, the signal first passes a shaper with adjustable integration time constants of  $0.5\ \mu\text{s}$  or  $0.2\ \mu\text{s}$  and differentiation time constant of  $15\ \mu\text{s}$ ,  $7.5\ \mu\text{s}$ ,  $5\ \mu\text{s}$  or  $3.75\ \mu\text{s}$  before being compared to the threshold. In standard operation, the time constants are set to  $\tau_{diff} = 7.5\ \mu\text{s}$  and  $\tau_{int} = 0.5\ \mu\text{s}$  which results in a peak signal strength of [21]:

$$V_{\text{peak}} = 0.82 V_{\text{in}} \cdot A, \quad (6.4)$$

where A is the amplification factor of the amplifier embedded within the shaper which is  $A = C_1/C_2 = 1\ \text{pF}/33\ \text{fF} = 30$ , resulting in a peak amplitude of:

$$V_{\text{peak}} \approx 24.7 V_{\text{in}}. \quad (6.5)$$

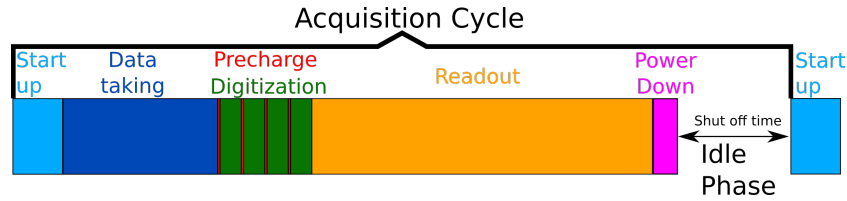
As KPiX measures negative pulses relative to  $V_{\text{analog}} = 2.5\ \text{V}$ , a high DAC threshold value, which is equal to a large voltage level, equates to a low effective threshold. The threshold can be set between

$$\text{Threshold} = 255\ \text{DAC} = 0\ \text{fC} \quad (6.6)$$

and

$$\text{Threshold}_{\text{NormalGain/HighGain}} = 0\ \text{DAC} = 40.48\ \text{fC}/10.12\ \text{fC}. \quad (6.7)$$

In external triggering operation each channel stores the currently recorded charge independent of any threshold levels upon receiving an external trigger signal and the shaper, which is only used to shape the signal for triggering, is bypassed. When a trigger is sent out, the amplified signal is stored on up to four 1 pF storage capacitors which are hence-



**Figure 6.14** – Sketch of the KPiX power pulsing acquisition cycle.

forth referred to as *buckets* zero to three (b0..3). These *buckets* are digitized via a Wilkinson ADC with 13-bit resolution. The conversion via a Wilkinson ADC is done by connecting a current source to the capacitors in order to linearly discharge them. At the point when the discharge starts, a gate pulse is set that stays on until the capacitor is fully discharged. The time duration for which the gate pulse is set to high is stored via a Gray code counter which ensures that the time counting is done in only single bit changes. This is done to decrease the load on the digital electronics which could otherwise introduce cross-talk in the analog circuitry and to ensure minimal sampling errors. An example of Gray code values is given in Table 5. Due to the linear discharge, a direct relation between the time it takes to discharge the capacitor  $t_C$  and the stored charge  $Q = C \cdot U$  is given by [21]:

$$t_C = C \frac{U - U_{BL}}{I_R}, \quad (6.8)$$

where  $U$  is the voltage applied on the capacitor,  $C$  is its capacitance,  $U_{BL}$  is the baseline voltage level below which the capacitor is considered fully discharged and  $I_R$  is the current of the current source. After digitization, the data is sent out to the DAQ system.

### KPiX operation

The KPiX power pulsing operation ensures that the KPiX is active only for a short time frame and is otherwise operated with significantly reduced load in *idle-phases*. This reduces the power consumption and subsequent heat generation. A full cycle of the power pulsing operation is referred to as an *acquisition cycle*. A sketch of this cycle is depicted in Figure 6.14. It shows that KPiX uses a sequential instead of a continuous data readout which requires the presence of the *buckets* to store data in analog form before digitization. The operational temperature of the KPiX is recorded at the start of each *acquisition cycle* in an 8-bit register.

The setting of the different phases of the *acquisition cycle* can be adjusted as integer multiples of the system clock  $T_{\text{system}}$ . There exists a minimum period of 50 ns for all KPiX

Clock	Value (ns)
$T_{\text{system}}$	5
$T_{\text{acquisition}}$	320
$T_{\text{digitization}}$	50
$T_{\text{pre-charge}}$	6000
$T_{\text{idle}}$	200
$T_{\text{readout}}$	200

**Table 6.6** – Standard KPiX clock periods

clock values which can then be increased in values of  $T_{\text{system}}$ . The clock values used for the studies presented in this thesis are represented by as periods of

$$T_x = \frac{1}{f_x}, \quad (6.9)$$

to signify that they are characteristic time periods which defines the operation of KPiX based on the internal clock frequency. The values represented with a  $t_x$  signify that these are values for the total amount of time the KPiX stays in the corresponding operational phase and is typically given by multiplying the corresponding time period  $T_x$  with a constant that indicates the amount of cycles the system operates in the corresponding phase. The standard values for the time periods of the different phases are listed in Table 6.6 which corresponds to the phases depicted in Figure 6.14.

The clock periods are important for the KPiX operation as they define the length of the different phases of the *acquisition cycle*. Both the length of the data acquisition phase during which the system is able to record data and the time granularity of the system are dependant on the clock periods. Studies have also shown that adjusting the clock periods impacts the overall performance of the system (see section 10.2). The relation between the clock periods and the exact operational time of KPiX is given below:

- The start-up phase of KPiX begins after receiving a start signal. During this phase, KPiX operates using the acquisition clock  $T_{\text{acquisition}}$  and is configurable via the delay DAC value to last for:

$$t_{\text{Start-up}} = T_{\text{acquisition}} \cdot DAC_{\text{delay}}. \quad (6.10)$$

During start-up, the KPiX ramps up both the analog and digital currents to operational values and resets the internal KPiX registers and the Gray counter.

- During the data acquisition, the analog data is recorded and stored in the *buckets*.



Each channel is capable of storing up to four events, limited by the number of *buckets*. KPiX operates with the acquisition clock  $T_{\text{acquisition}}$  and stores the time information of the trigger via a 13-bit counter. This is referred to as the *BunchClockCount* (BCC) which increments by one every eight clock pulses and is reset to zero before the start of a new cycle.

The data taking phase is limited to the range of the 13-bit counter but can be shortened via the  $DAC_{BCC}$  setting. The data acquisition phase lasts for:

$$t_{\text{acquisition}} = DAC_{BCC} \cdot BCC = DAC_{BCC} \cdot 8 \cdot T_{\text{acquisition}}. \quad (6.11)$$

An additional DAC value, the trigger inhibition  $DAC_{TIB}$ , can be adjusted in order to suppress any system triggers within the first  $DAC_{TIB}$  BCC. The frame readout-time of a triggered channel in the acquisition phase can be adjusted. The time is related to the acquisition clock and can range from  $t_{FK} = 1 \cdot BCC$  to  $8 \cdot BCC$ .

- The digitization phase is split into two subcategories, the pre-charge phase and digitization phase, which are both repeated once for each of the four *buckets*. The pre-charge phase uses the pre-charge clock  $T_{\text{pre-charge}}$  and lasts for:

$$t_{\text{pre-charge}} = 2 \cdot T_{\text{pre-charge}}, \quad (6.12)$$

during which the analog bus is charged to a known level. This bus is connecting the storage capacitors to the Wilkinson ADC and carries some charge from previous events. During the digitization phase the current source is enabled and the analog charge stored in a *bucket* is digitized using the Wilkinson ADC. This phase uses the digitization clock  $T_{\text{digitization}}$  and lasts for:

$$t_{\text{digitization}} = (8192 + 18) \cdot T_{\text{digitization}}, \quad (6.13)$$

meaning that for all four buckets to be digitized the system needs a time of:

$$t_{\text{full-digi}} = 4 \cdot (t_{\text{pre-charge}} + t_{\text{digitization}}). \quad (6.14)$$

- After the digitization phase, the KPiX data, including Temperature, one time stamp and one ADC value per *bucket* is read out sequentially row by row using the readout clock  $T_{\text{readout}}$ .

The readout phase lasts for:

$$t_{\text{readout}} = 215728 \cdot T_{\text{readout}}. \quad (6.15)$$

- After the data readout the analog KPiX current is reduced to low levels the time of which can be fully customized.

The currents drawn by KPiX during operation differs between the different operation phases and is used in section 10.1 to investigate the chips operational performance. The structure as a whole is depicted in Figure 6.14.

### 6.3 The Sensor Configuration

As the telescope is based on a strip sensor, each layer in the telescope provides only measurements in one dimension. Sensitivity in two dimensions can be achieved by rotating sensors relative to each other along the z-axis. The angle by which they are rotated is referred to as the stereo angle. The different layers are referred to as stereo layers if they are installed at an angle and axial layers if they are installed without an angle. The required stereo angles and the optimal combination of stereo layers and axial layers to achieve the optimal resolution in momentum and in x was determined via simulations using the General Broken Lines (GBL) [36] approach. Particles are moving perpendicular to the sensor layers with an energy of 4.4 GeV within a 1 T magnetic field. The coordinate system is the same as described in section 6.1 and depicted in Figure 6.2.

The movement of a charged particle within a uniform magnetic field, pointing in the x direction, can be described by a helix. A helix can be split into two components, the circular movement requiring three parameters to define it as well as the linear movement along the magnetic field defined by two points. The helix can therefore be described using five parameters. Typically, the parameters are the offsets ( $x_0, y_0$ ), the slopes ( $dx/dz, dy/dz$ ) and the curvature ( $\kappa$ ). The helix parameter values are determined in mm for offsets,  $\text{mm}^{-1}$  for the curvature and radian for the slopes. The ability of the system to determine these parameters, specifically the resolution of the curvature  $\kappa$  and the resolution for the position parallel to the magnetic field  $x_0$  are important.

A minimum of five sensors is required to constrain the helix and a sixth hit can be used to filter out fake combinations, which are present in a real system with noise. Therefore, the system has a minimum requirement of six layers which can be split into two arms of three layers each. For these simulations, a single point resolution of  $10 \mu\text{m}$  is assumed for

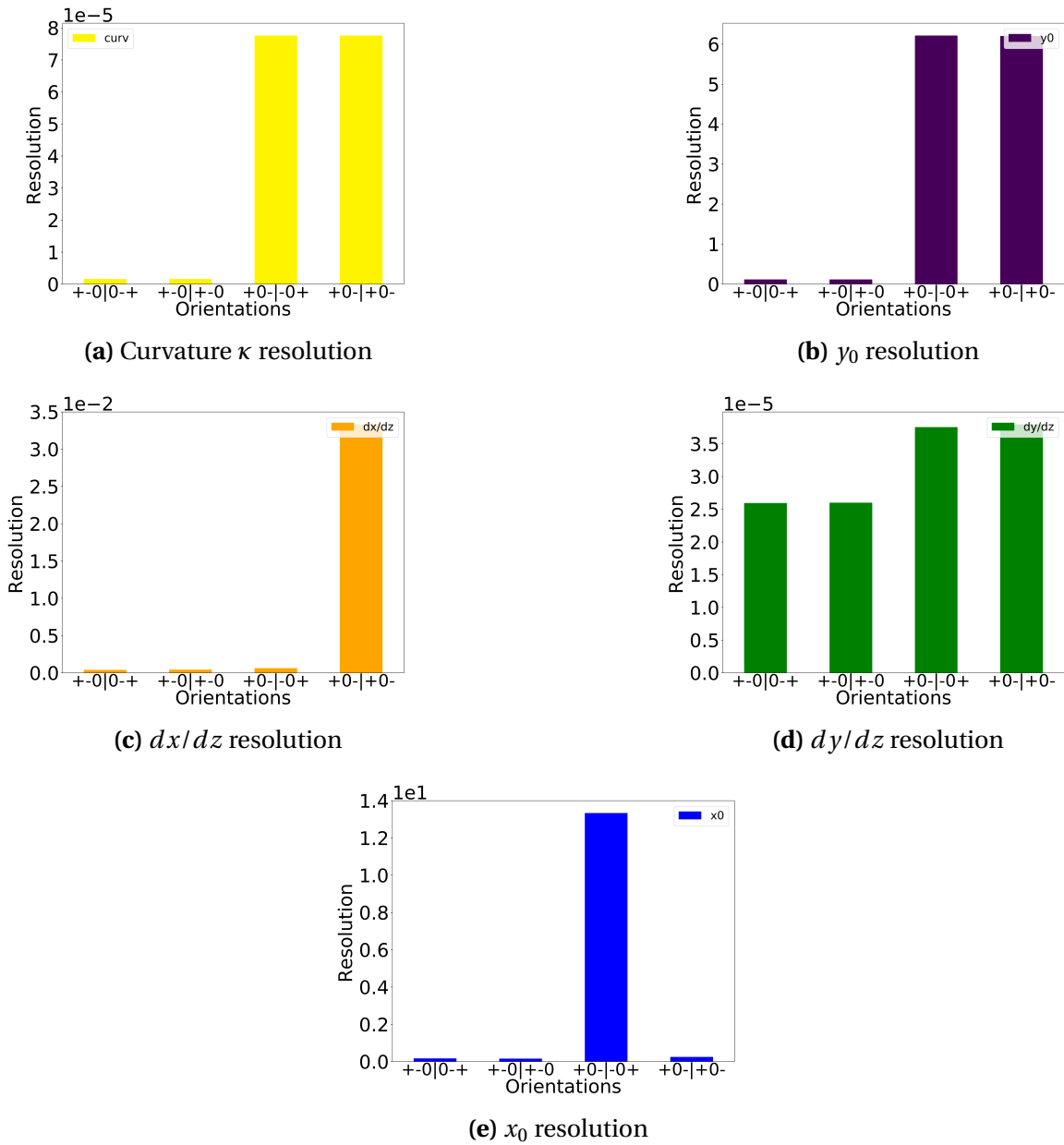
the sensors perpendicular to the strips with an equidistant spacing between sensors within the same arm of 15 mm and a distance of 830 mm between the two arms. The thickness of the sensor planes is set to 320  $\mu\text{m}$  to take into account multiple scattering in the GBL framework. This is explained in more detail in Section 4.2.4.

Both the choice of orientations, which layer is rotated in what direction, and choice of the value of the stereo angle were determined iteratively. The effect of different orientations is exemplified here using a  $2^\circ$  angle for the stereo layers. The results of these studies are shown in Figure 6.15. The x axis of the plots gives the different orientations of the sensors within an arm and the y axis gives the resolutions depicted in the parameters. + means that the sensor is rotated by  $+2^\circ$ , - means that the sensor is rotated by  $-2^\circ$  and 0 means that the sensor is installed as an axial layer without an angle.

The first two entries show positions where the axial layers are placed at the edge of the cassette with the stereo layers next to each other and the last two entries show positions where the axial layers are placed in between the stereo layers. The resolution of every parameter worsens when the axial layer is placed between the stereo layers with a trade-off between the  $x_0$  and  $dx/dz$  resolution depending on the orientation of the stereo layers.

The reason for this decrease in resolution becomes apparent when looking at the correlations between the different parameters for the orientations. This is shown in Figure 6.16. The first two show the orientations with the axial layers at the edges, which show an almost full correlation between the curvature and the offset in y (orange) as well as minor correlations which, depending on the orientations of the stereo layers, are between  $\kappa$ - $x_0$ ,  $dy/dz$ - $dx/dz$  and  $y_0$ - $x_0$  or between  $\kappa$ - $dx/dz$ ,  $dy/dz$ - $x_0$  and  $dx/dz$ - $y_0$ . In comparison, when placing the axial layer between the two stereo layers, the same correlations are present but now all parameters are almost fully correlated except for  $dy/dz$ - $dx/dz$  in +0-0+ and  $dy/dz$ - $x_0$  in -0+-0+ which show a correlation of 0.8. As such changes in one parameter can be compensated by a change in another parameter. When the two stereo layers are placed one after another they produce a pseudo double layer which removes that correlation to a large extent though not completely as the sensors have a small offset along the z-axis. An orientation of + - 00 - + was chosen for ease of installation, as in this scheme one arm is simply a rotated version of the other (see Table 6.7).

To investigate the impact of larger angles on the track parameters, the six sensors were distributed in the pattern shown in Table 6.7 and the angles were varied from  $2^\circ$  to  $64^\circ$  (see Figure 6.17). Figure 6.17a depicts only a minor impact of the stereo angle to the curvature resolution which only degrades once the stereo angle becomes large. This is similar for  $y_0$  depicted in Figure 6.17b. The  $dy/dz$  resolution depicted in Figure 6.17d is insensitive to



**Figure 6.15** – Helix track parameter resolutions dependent on the size of the stereo angles in relation to the previously mentioned PCMAG coordinate system.

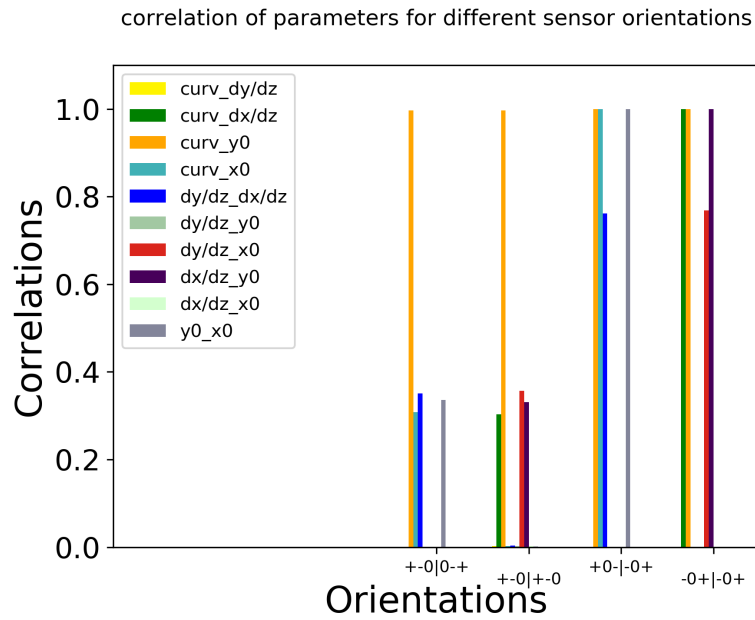


Figure 6.16 – Correlations from the GBL simulation between the different parameters.

layer	Orientation s
First	Positive stereo angle(+)
Second	Negative stereo angle(-)
Third	Axial(0)
Fourth	Axial(0)
Fifth	Negative stereo angle(-)
Sixth	Positive stereo angle(+)

Table 6.7 – Sensor orientations as seen by beam particles

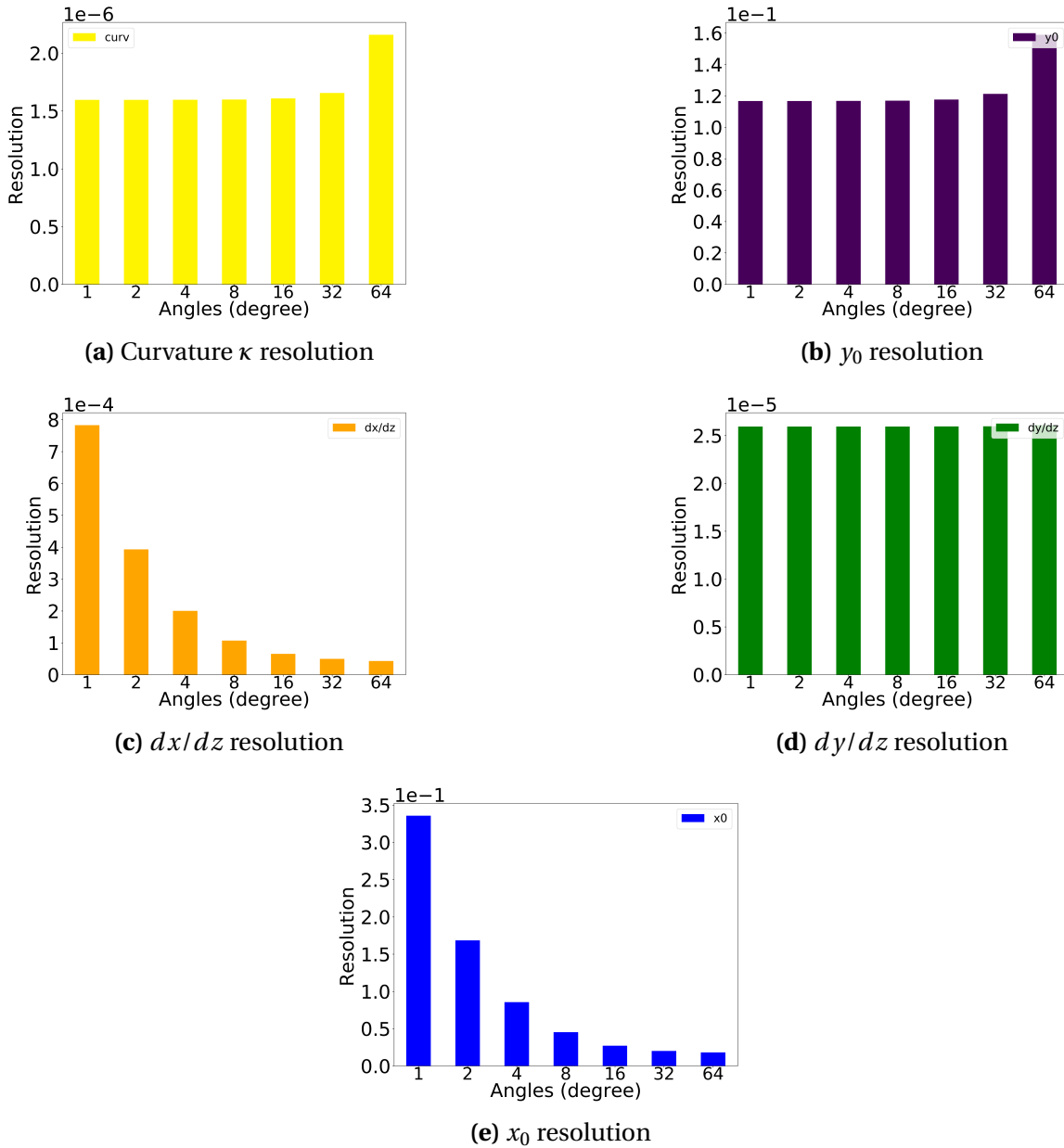
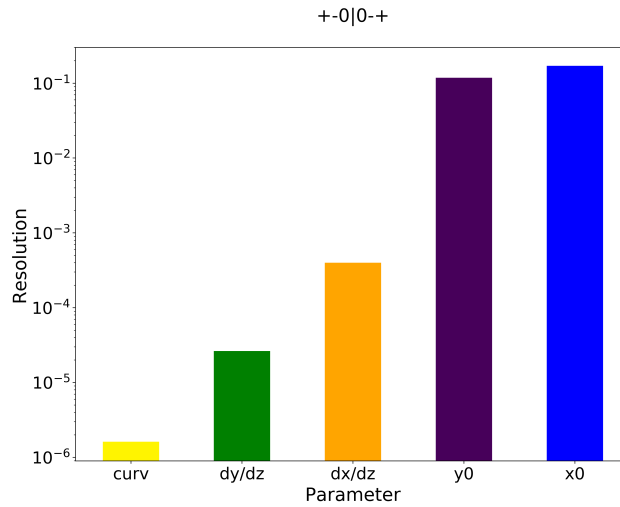


Figure 6.17 – Helix track parameter resolution dependency on the stereo angle.



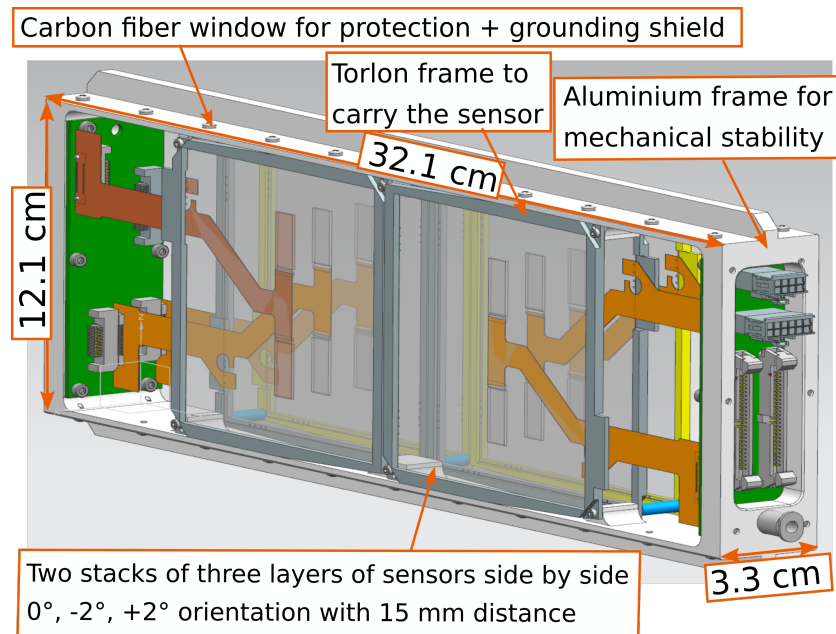
**Figure 6.18** – Expected parameter resolution for a helical fit within PCMAG using Lycoris sensors in a 0, -2, +2, +2, -2, 0 degree orientation.

the angle of the stereo layers while the resolution of  $dx/dz$  depicted in Figure 6.17c and  $x_0$  depicted in Figure 6.17e show a massive improvement, even with small angle increases. Unfortunately, due to the spatial constraints presented in section 6.1, angles larger than 2° are not feasible within the PCMAG system, as the placement within the curved solenoid limits, besides the width, also the height of the system and therefore the angle of the sensors orientation.

The achievable resolution for the five parameters of the helix with the + - 00 - + orientation and 2° angle is shown in Figure 6.18. All test beam measurements are performed in this configuration.

## 6.4 Mechanics

Custom made sensor housings and support structures have been designed and built to fulfill the project requirements posed in section 6.1. Basis of this custom design is the sensor housing which is referred to as the telescope cassette. It houses up to two stacks of three sensors side by side with each cassette representing one full arm of a telescope system. A design similar to the one of the AZALEA system, in which each sensor is housed individually, is not possible due to the spatial constraints inside the magnet. To mount the cassettes, a custom made rail system was designed, built and installed within the PCMAG. This allows for free movement of the cassette within the PCMAG independent of the proto-



**Figure 6.19** – CAD drawing of a Lycoris cassette which are used to house the sensors for telescope operations[71].

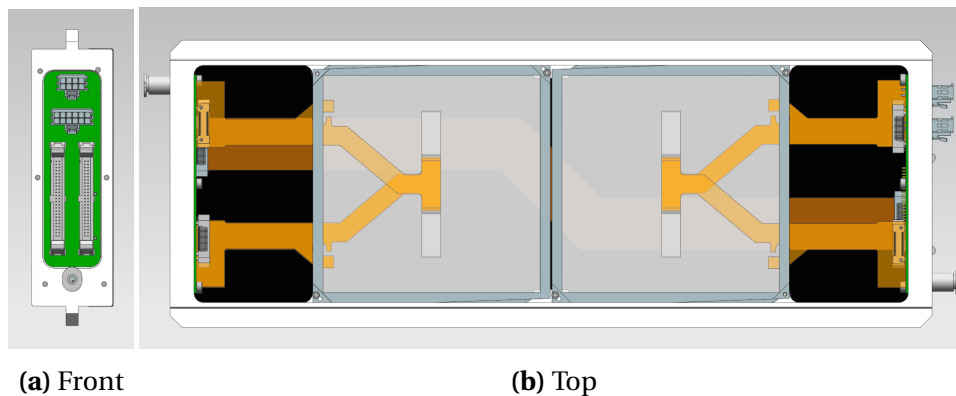
type field cage.

### 6.4.1 Telescope Cassette

The telescope cassettes are aluminum housings for the sensors. A drawing of the housings with the different sizes and other key aspects is depicted in Figure 6.19. As shown in the drawing, each cassette is capable of housing two pairs of three silicon sensors resulting in a maximum active area of close to  $10 \times 20 \text{ cm}^2$  for the telescope. The two stacks are identical to one another. The only difference is, that the sensors are rotated  $180^\circ$  along their normal to allow them to be connected to the backside of the cassette. While the mechanical support allows for two stacks to be installed, the system is only operated with a single stack of three sensors within a cassette in this thesis.

Figure 6.20a and Figure 6.20b depict what is, in the following, referred to as the front and top of the cassette respectively. The dimensions of a cassette are  $33 \text{ mm} \times 121 \text{ mm} \times 321 \text{ mm}$ . The sides of the cassette are milled out and replaced with an aluminum foil reinforced carbon fiber window to provide a beam window with a radiation length of about  $1.2 \times 10^{-3} X/X_0$  that is light tight, conductive, and able to protect the sensor from the environment. The front side the of cassette has a large opening window for what is referred to as





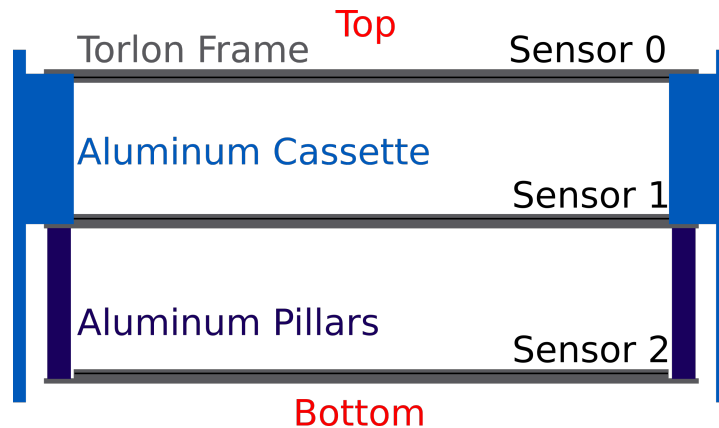
**Figure 6.20** – CAD drawing of the Lycoris cassette that is used to house the sensors of the telescope [71].

the cassette master board that is described in section 6.5.1. Both, the front- and backside, of the cassette have holes with an M5 screw thread to screw in a 6 mm Festo® [72] connector to flush the cassette with dry gas if desired to reduce the humidity the sensors are exposed to. The configuration with two cassettes including the readout described in section 6.5.1 is referred to as the Lycoris telescope in the following. For installation of the sensor into the cassette, each sensor is glued into a plastic frame, which is screwed to the cassette frame.

Sensors zero and one, named for their electrical connection socket, are located on the top and the center of the cassette and their frames are screwed directly to small protrusions within the cassette with a spacing of 13.84 mm. The middle layer (sensor one) is screwed into the cassette with aluminum pillars which have an outer screw thread on one side and an internal screw thread on the other. Sensor two is mounted onto these pillars to optimally use the available space, resulting in a spacing of 14.34 mm between sensor one and sensor two. The internal arrangement showing the installation method of the three sensor layers is depicted in Figure 6.21. To access sensor one, sensor two has to be uninstalled beforehand.

### Sensor Frames

The frames which hold the sensors are hollow squares with a size of  $100 \times 100 \text{ mm}^2$ , a wall strength of 4.5 mm and a thickness of 3 mm. The inner wall has a cutout that carries the sensor on a 1.25 mm wide ledge on each side. The remaining central region is empty, ensuring minimal material within the beam path. The frames are made of Torlon® 4301 for its high tensile strength ensuring that the frame does not bend easily, reducing potential



**Figure 6.21** – Sketch of the installation of sensors within the Cassette.

stress on the sensor while being non-conductive. The frame material has a significantly different Coefficient of Thermal Expansion (CTE) of 25.2 ppm/K compared to that of Silicon 2.6 ppm/K though the system is not foreseen to be under high thermal load and as such this should not be overly relevant. The frames have two opposite edges slanted with a  $2^\circ$  angle which allows each sensor to be tilted during installation. This was done in order to allow any sensor to be installed at either stereo or axial position in order to have a large pool of spares for operation at the DESY II Test Beam Facility. A stress relief is added to the frame which is used to press the readout cable described in section 6.5.1 to the frame to ensure that any force to the cable does not translate to the glue used to hold the cable on the sensor or the wire-bonds connecting the sensor to the cable. A picture of a sensor installed within the Torlon<sup>®</sup> frame is shown in Figure 6.22.

### 6.4.2 Rail System

For mounting within the PCMAG, the cassettes are installed within a specially designed rail system shown in Figure 6.23. This system consists of four Rose-Krieger profiles with a Drylin<sup>®</sup> T guide rail, upon which a concentrically curved aluminum cart, which is used to hold the telescope cassette within the PCMAG, is installed between the upper and lower rails with two fixed and one loose bearing. The cassette is installed in the cart using two aluminum holders that can be screwed to the cassette and that each have six wheel bearings. This allows the cassette to be moved up and down along the cart with a pin fixing the angular position in  $5^\circ$  steps.

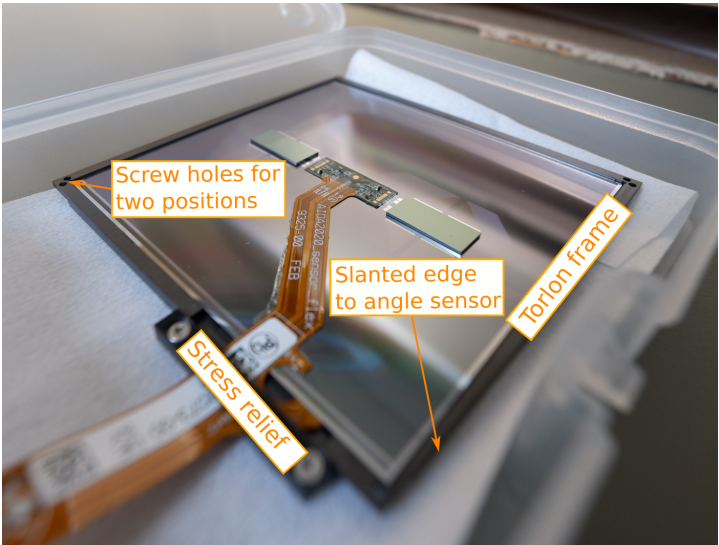


Figure 6.22 – Picture of an SiD sensor installed in the Torlon frame.

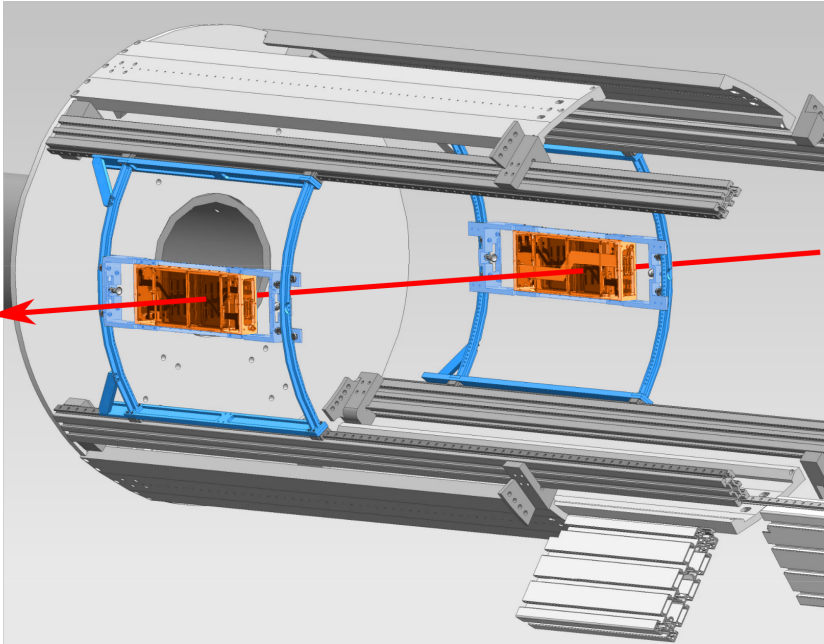


Figure 6.23 – CAD drawing of the rail system that holds the two cassettes within the PCMAG[71]. The aluminum cart is depicted in light blue and the cassette is depicted in orange. The red arrow depicts the electron path.

## 6.5 The Data Acquisition System

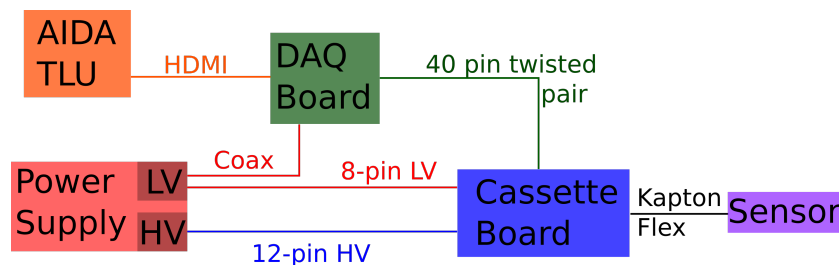
The Data Acquisition (DAQ) system is used both to configure and to operate the KPiX chip. The DAQ system controls the start and end point of what constitutes a run and receives the data and writes it in a common format to the readout PC. The readout PC runs the software and communicates between the different devices that constitute the measurement setup. The DAQ System of the Lycoris telescope consists of commercial and custom hardware, custom software and Field Programmable Gate Array (FPGA) firmware based on the Rogue [73] framework which are all connected to one another.

### 6.5.1 Hardware

The hardware can be split into five main components. The Power Supply (PS), the DAQ board, the cassette boards which are the master and the slave cassette board, *Kapton Flex Cable* and AIDA TLU which is described in section 5.2. Figure 6.24 shows the electronic connections between these components.

#### Power Supply

The Power Supply (PS) consists of a Wiener MPOD Mini MQA4E240000T crate [74], capable of housing up to four different modules. The crate houses both Low Voltage (LV) and High Voltage (HV) modules with a maximum power output of 3kW for LV modules and 0.6kW for HV modules. The LV module is an MPV8016I [74] with eight floating channels split into two 37 pin Sub-D connectors. Each channel is capable of supplying a voltage of 15V and a maximum current of 5A. The maximum power is 50W per channel with a voltage ripple of less than  $2\text{mV}_{\text{pp}}$ . The HV module is an EHS F205p\_106 [74] with 16 common floating channels split into 16 SHV connectors, capable of providing a maximum voltage



**Figure 6.24** – Block diagram showing the electronic connections between the different devices required for the Lycoris telescope.

of 500V and a maximum current of 10 mA with a voltage ripple of less than 5 mV<sub>pp</sub>. The LV and HV modules are connected to the DAQ board and the Master cassette board via custom made cables explained in more detail in section G.

### DAQ board

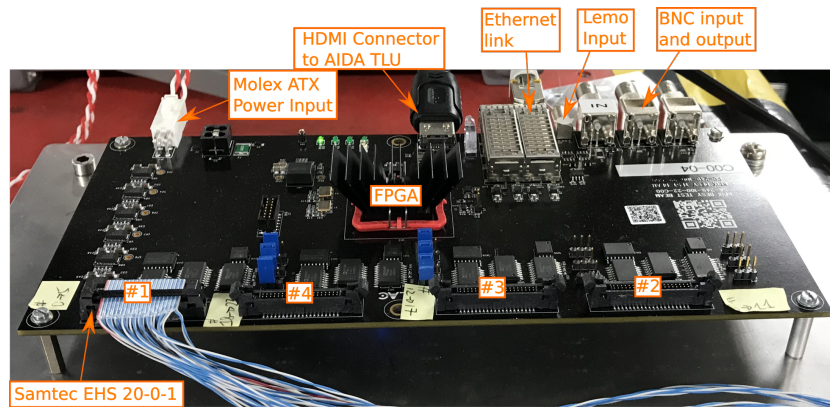
The DAQ board is a custom made Printed Circuit Board (PCB) made by SLAC, housing a Xilinx Kintex 7 Field Programmable Gate Array (FPGA) used to run the data acquisition firmware. The board consists of 8 layers, is 245.1 mm long and 127.0 mm wide (see Figure 6.25). The DAQ board has four Samtec 1.27 mm pitch shrouded IDC headers with ejectors [75], with two rows of 20 pins each used to connect the communication lines from the FPGA to the master cassette board.

Each line is paired with their corresponding partner in case of low voltage differential signals or with the cassette ground in the case of non-differential signals. Lines that are common to all KPiX such as the trigger lines (TRIG) and clock lines (CLK) are transferred only once and fanned-out on the cassette board. In addition to the signal lines, 2.5V and 2.0V power are sent back to the DAQ board via three lines each in order to power the optoisolators on the DAQ board. They are designed to separate the DAQ circuitry from the cassette board circuitry to avoid noise being transferred over the lines into the KPiX system.

The DAQ board is connected to the Run PC via a 1 GBit Ethernet link which is generated using Small Form-factor Pluggable (SFP) fiber-based Ethernet converters and is capable of connecting to the AIDA TLU via an HDMI connector. The DAQ board can receive trigger signals, as well as an outside clock via the HDMI connector from which the baseline clock can be generated. Trigger signals can also be received via BNC and Lemo connectors. The FPGA on the DAQ board uses 12V supplied via a four pin ATX Molex connector [76] from which it generates its on board voltages to control the FPGA via DC-to-DC converters. The existence of coils in both the 1 GBit Ethernet link as well as in the DC-to-DC converters requires that the board is kept outside of strong magnetic fields during operation.

### Cassette Boards

The cassette boards are the interface between the sensors and the DAQ board and two different types of boards were designed: A master cassette board and a slave cassette board. The master cassette board is a 13 layer high density PCB to be used as the interface between the DAQ board and power supply to the sensors and KPiX. It has a length of 92 mm and a width of 32 mm. The board has components installed on both sides of the board, which



**Figure 6.25** – Picture of the KPiX DAQ Board.

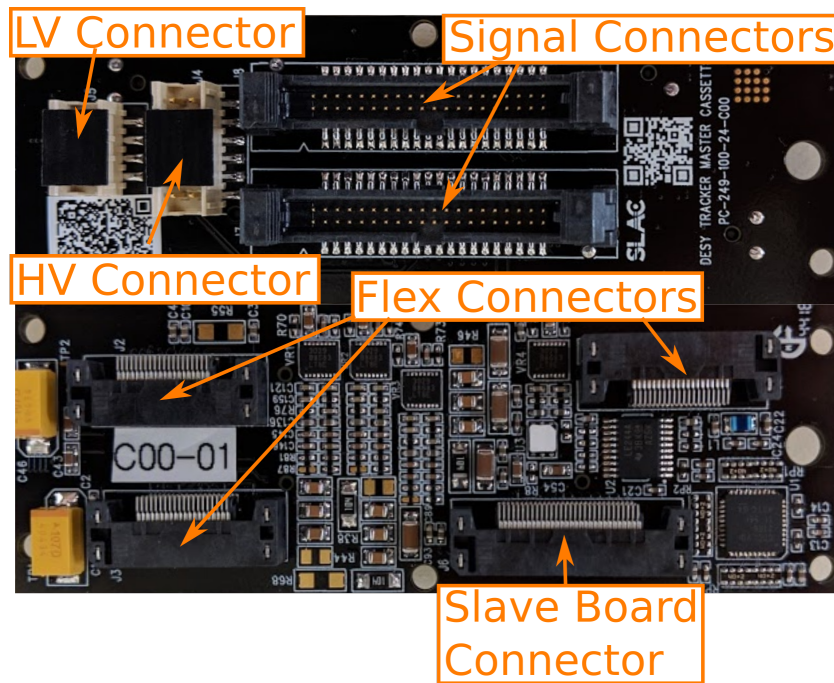
are shown in Figure 6.26. The front side shown in the top half of the picture consists of the aforementioned Amphenol 12 and eight pin connectors [77] used for connection to the HV and LV modules of the PS as well as two signal connectors, each of which is used to connect a stack of three SiD sensors to the KPiX DAQ board. The lower half of the picture shows the back of the cassette master board. Some of the key components of the board are:

- The three Samtec ERF5-20-01 board-to-board connectors [78] used to connect to the sensor and KPiX via the *Kapton Flex Cable* described below,
- a humidity and temperature sensor,
- linear regulators operated at 3V in order to generate the analog voltage of 2.5V and the digital voltage of 2.0V required for KPiX operation on the board,
- a Samtec ERF5-30-01 connector is used to connect the master cassette board with the slave cassette board,
- different noise filtering components for the different voltages and signals,
- clock and trigger fan-outs.

The high voltage, as opposed to the low voltage, is not generated on the board and is fed directly to the different sensors.

The cassette slave board is designed to fulfill the same function as the master cassette board with only the back side being equipped with components. Instead of receiving and sending signal to and from an external connection, the slave cassette board is designed to receive power and transmit signals via the Samtec ERF5-30-01 connector using a custom made flexible PCB. The cassette slave board and the flexible connection PCB were, as of the





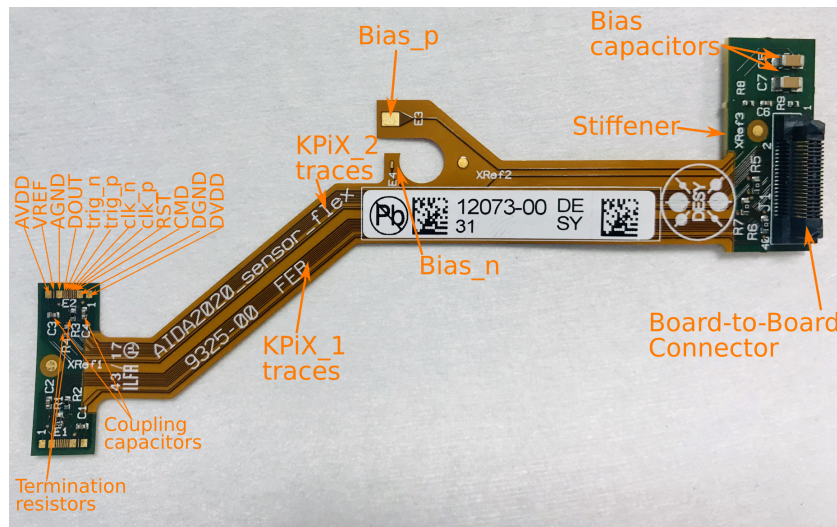
**Figure 6.26** – Picture of front (top) and back (bottom) of the KPiX Cassette Master Board.

writing of this thesis, not yet produced. They are only needed to operate a second stack of sensors within the cassette which was not done in the studies presented in this thesis.

### Kapton Flex Cable

The custom made Kapton based flexible PCB used to connect the sensor and ASIC to the cassette board is referred to as the *Kapton Flex Cable*. The *Kapton Flex Cable*, which is shown in Figure 6.27, is 103 mm long. The design is based on a design from the University of New Mexico with some changes to lay-outing, form and materials that have been done at DESY. The changes have been done to ensure that the spatial constraints for the telescope within the PCMag are fulfilled. The original cable would have routed the signal to the top of the cassette instead of the front. The bottom part consists of a 1 mm thick stiffener with an area of  $28 \times 12 \text{ mm}^2$ . This houses the ERM5-20-01 board-to-board connectors used to connect to the cassette board [79], as well as multiple resistors and coupling capacitors connected to the bias lines.

The two analog- and the two digital voltages are connected together on the *Kapton Flex Cable* to one combined analog and one combined digital voltage. The reason for this could not be clarified and is later shown to impact the performance of the system (see sec-



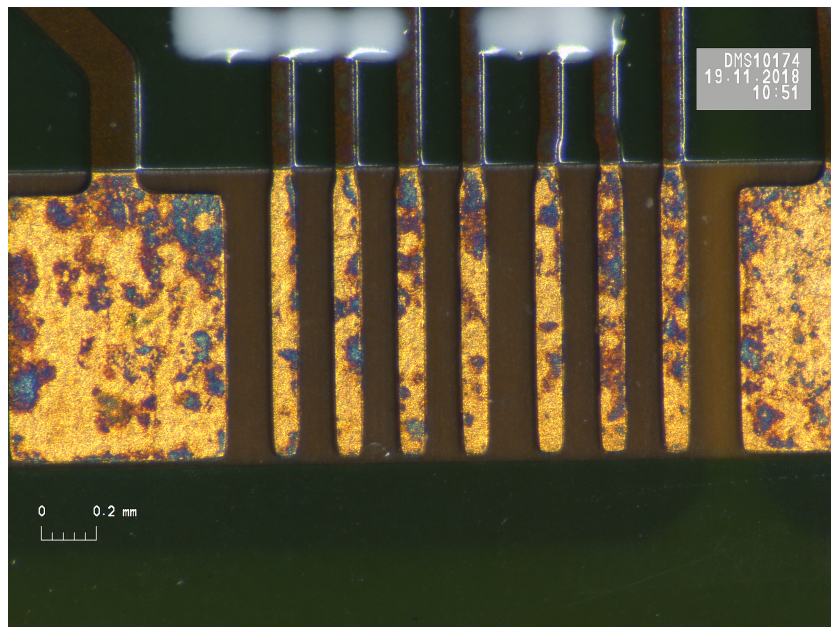
**Figure 6.27** – Picture of a *Kapton Flex Cable*.

tion 10.3.1). It is not known why this was chosen by the original designers of the *Kapton Flex Cable* at the University of New Mexico. All ground connections are combined into a single global ground (GND). While the lines are combined, each KPiX has its own copper traces along the flex print going from the stiffener to the wire-bond pads. The two voltage traces are wider than those used for signals. They have a line resistance from the connector to the bump-bond pad of less than  $0.5\Omega$  to ensure that no significant voltage drop is seen because of the significantly different current that appears during the power pulsing, which is difficult to compensate. In addition, an extra metal layer, split into four segments each, is connected to GND and runs beneath the traces as a shielding layer.

All signal traces move through the entire cable length to the top where each trace has its own gold plated Cu/Ni/Au wire-bond pad. The gold plating ensures that the copper does not oxidize and the nickel in between slows down the diffusion of the copper into the gold. The left and right half of the pads at the top of the cable possess rotational symmetry, like the sensors. The high voltage traces go to a little ear halfway along the cable where the positive bias connects to a large area bond pad. This is connected to the backside and the negative bias connects to a small wire-bond pad. They have the same composition as the bond pads used for the signal lines described above.

The Low Voltage Differential Signals (LVDS) that are used to transport both the trigger and clock lines are terminated with a  $100\Omega$  resistor near the wire-bond pads and the low voltage signals are coupled to their respective ground with  $10\mu\text{F}$  capacitors to provide noise filtering close to the ASIC. All bias lines are coupled to the analog voltage line and





**Figure 6.28** – Picture of oxidized *Kapton Flex Cable* pads.

each other via the same  $10\ \mu\text{F}$  capacitors. Additionally, two  $1\ \text{M}\Omega$  resistors are placed on both the positive and negative bias lines on the *Kapton Flex Cable*.

During assembly, it was found, that for some cables no connections could be made to the bump-bond pads. While the nickel placed between the gold and copper on the wire-bond pads slow down the diffusion of copper into the gold layer it does not stop it completely. Once the copper diffuses to the surface it oxidizes and no connections can be made to the pads (see Figure 6.28). Hence the wire-bond pads have a shelf life of eight to 12 months depending on how they are stored.

As a result of this, a second batch of *Kapton Flex Cables* had to be produced. The only difference between the two is that the old *Kapton Flex Cables* use a  $10\ \text{nF}$  coupling capacitors instead of  $10\ \mu\text{F}$  capacitors. One functional sensor was wire-bonded with the old *Kapton Flex Cable*.

### 6.5.2 Firmware and Software

The KPiX DAQ system software and firmware were built for this project by SLAC. The firmware controls all aspects of the KPiX operation, including configuration, acquisition, and readout. The FPGA also contains a virtual KPiX that runs in lockstep with the KPiX ASICs on the sensors. This enables the firmware to track the state of the KPiX throughout an

acquisition cycle, so that it knows when to change the clock frequency and when to expect readout data. The firmware assembles the raw KPiX data into a custom binary format which is then transferred to the Run PC.

The software is based on Rogue[73], which is a Python and C++ based modular hardware abstraction and DAQ software platform. While Rogue in principle allows the DAQ to be based fully on Python code as for example the Device Tree, time critical operations such as the data processing, are written in C++ within the KPiX DAQ[80].

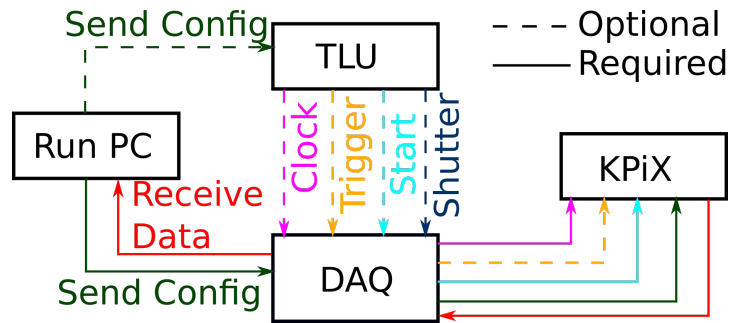
It consists of the following pieces:

- An abstraction layer that allows a configuration to be loaded from a YAML (Yet Another Mark-up Language) file and in addition allows to register values to be viewed and adjusted in a GUI or via a Python script. The different options within the YAML file and their explanation are listed in section H.
- A data writer which receives acquisition data frames from the FPGA and writes them to disk in a custom data class.
- A run coordinator that is responsible for starting and stopping the data taking from the system as well as the setting of parameters for each run.

Reliable UDP (RUDP) is used for communication between the software and the FPGA firmware. An implementation of this protocol is included within Rogue and is also implemented in the firmware on the FPGA. In addition to logging the data received by the KPiX, the DAQ also records the data from the temperature and humidity sensors that are located on both the DAQ and cassette board.

The KPiX DAQ system can operate in what is referred to as a software controlled run. In such a run the system performs acquisitions either with a user set frequency or starts a new *acquisition cycle* as soon as the previous cycle has finished. For example, if the run rate is set to 5 Hz and an acquisition takes KPiX 80 ms then there will be an *idle-phase* with duration of 120 ms between acquisitions (see section 6.2.2). When running without limit there is no *idle-phase*.

In addition to the software controlled run, the runtime operation can also be controlled via external inputs received through the HDMI, BNC and Lemo input ports shown in Figure 6.25. The HDMI pin layout is adapted to the AIDA TLU pin layout listed in Table 6 with a different internal naming scheme. The trigger and clock signals are referred to as *TluClk* and *TluTrigger*. Spare is *TluStart* and Control is *TluSpill*. The BNC connection is referred to as *BncTrig* and the lemo connections are referred to as *Lemo0* and *Lemo1*. The 200 MHz baseline clock can be both generated internally as well as externally using a different clock



**Figure 6.29** – Control and data flow to and from the different DAQ system objects. The dashed lines are optional as the system can be operated in a mode without them. In the case that a dashed line becomes a solid line, like with the clock lines, it means that the DAQ in-between decides whether to use the optional input or not, based on the configuration that was sent.

as input signal such as the 40MHz clock generated by the AIDA TLU given via *TluClk*. Except for *TluClk* all other signal lines are interchangeable for what they are used internally, though the signals are typically used as follows:

- *TluStart* is a signal issued upon which the system starts operation,
- *TluSpill* is used to set the start of an acquisition cycle which is required in order to synchronize with for example the *uptime* of the DESY II Test Beam Facility,
- *TluTrigger* is used to issue trigger signals for the external time stamp and external triggering operation,
- Any of *BncTrig*, *Lemo0* and *Lemo1* can fulfill the same use as any of *TluTrigger*, *TluSpill* and *TluStart*.

The control and data flow is sketched in Figure 6.29.

The common data format of the DAQ includes both the binary data sent out by KPiX as well as clear text data which includes all YAML settings, all environmental data provided by the DAQ board and cassette boards, as well as meta data concerning the status of the KPiX in use. For example, during calibration the meta data is used to know which channel was injected with what DAC value and is used in the analysis to dynamically handle the different settings. An example for meta data within the KPiX binary during calibration is shown in Figure 6.30. The beginning of this block shows the KPiX binary data followed by the clear text data describing the charge injection of channel zero with a DAC value of 229 first for KPiX zero then for KPiX one.

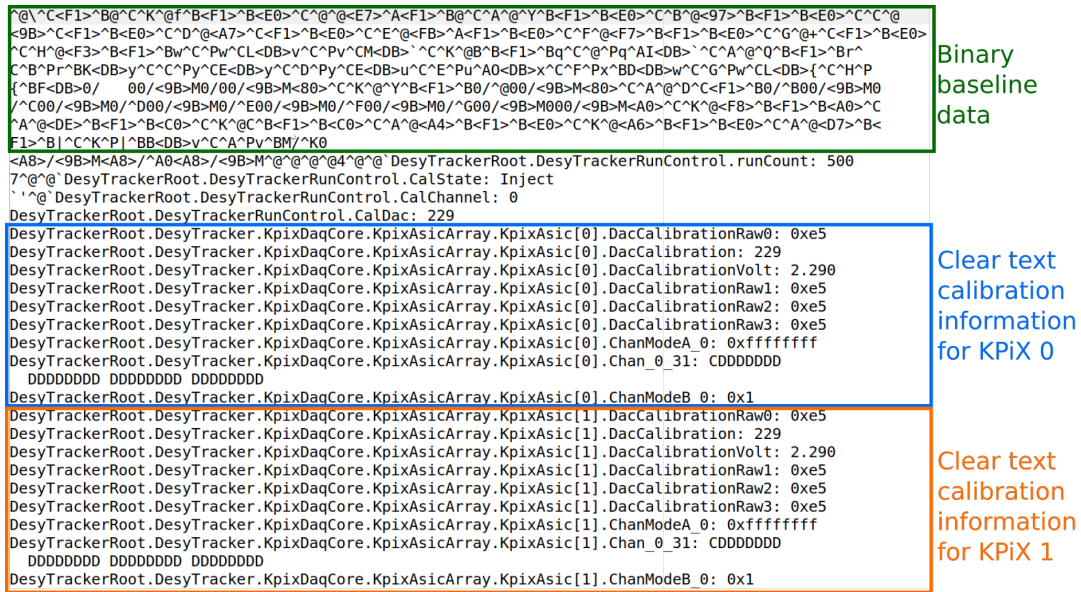


Figure 6.30 – Example of clear text meta data from a calibration run.

Work towards an easier user operation has also been made by integration of the system into the EUDAQ2 [81] framework which is explained in more detail in section C.

# Chapter 7

## Module Assembly

What is throughout the thesis referred to as a Lycoris module consists of the aforementioned SiD sensor module to which, two KPiX readout ASICs have been bump bonded to, a *Kapton Flex Cable* has been glued to, all wire-bond connections have been set and which has been glued into the mechanical support frame.

The SiD sensors are produced by Hamamatsu Photonics and the bump-bonding was performed by Fraunhofer IZM. Assembly and wire-bonding are done at DESY.

Of the 29 available sensor modules produced by Hamamatsu, one sensor has been used to investigate the bump quality and has been grinded down for a cross section picture. Two sensors have been damaged during assembly as a result of high pressure during the gluing process. Two sensors could not be wire-bonded due to aging of the Kapton Flex bond pads. Finally, two sensors are not fully assembled in order to allow assembly with a new Kapton Flex design which is under consideration. 22 sensors have been assembled successfully. All sensors are referred to using their internal Hamamatsu number.<sup>1</sup> Furthermore, based on the electric connection points the KPiX on the sensors are addressed as SXX-1 for the KPiX recording the signals of strip zero to 919 and as SXX-2 for the KPiX recording the signals of strip 920 to 1839.

The chapter includes all permanent procedures performed on the SiD strip sensor modules described in section 6.2.1. This includes the bump-bonding of the KPiX chip, the gluing of the *Kapton Flex Cable*, the wire-bonding connections between the *Kapton Flex Cable* and the sensor, as well as the gluing into the support frame. The sensors are tested for their electrical properties after every major change by performing IV and CV measurements using the clean room probe station described in section 7.2. The results of this are shown

---

<sup>1</sup>The numbering scheme of the sensors stems from Hamamatsu which results in the sensor numbering starting at 31 and ending at 59.

in section 7.2.2 with inter-strip capacitance results gathered from the Detector Assembly Facility (DAF) probe station shown in section 7.2.3.

## 7.1 Assembly

### 7.1.1 ASIC Assembly

For the Lycoris modules, a readout ASIC is, similar to hybrid-pixel detectors, directly connected to the system using a process referred to as bump-bonding. For bump-bonding, solder balls (bump bonds) are attached to every connection that is required to be made between the ASIC and the sensor. The chip is then flipped over so the solder balls are facing the connectors on the sensor and the two objects are aligned against one another. The chip is then pressed onto the sensor with light force. While still under pressure, the bump bonds are remelted which is typically done using a hot air flow.

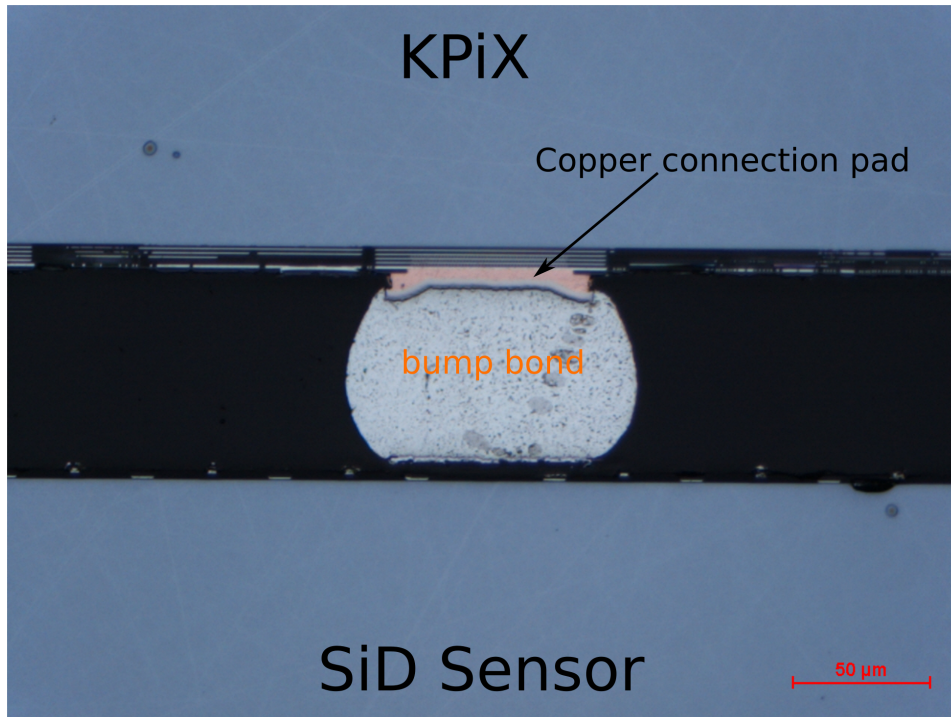
For the bump-bonding, all bare sensors were sent to Fraunhofer IZM together with multiple wafers of undiced KPiX ASICs. Fraunhofer IZM was chosen because of their prior experience of working with the KPiX readout chip as they have bump bonded the KPiX to the SiD silicon pixel ECAL [66]. The bump material is eutectic SnPb which has been pre-applied to the KPiX wafer. The wafer has been diced by Fraunhofer IZM. The Under Bump Metalization (UBM), which is the material of the corresponding bump bond pad on the sensor, is made of Ti/Ni/Au and has been pre-applied on the sensor by Hamamatsu.

One sensor has been grinded down to the bump bonds in order to gather a cross section to inspect the bump bonds. A picture of a cross section of a Lycoris module is depicted in Figure 7.1 with the KPiX visible on the top side and the SiD sensor visible on the bottom side of the picture. In the picture, the solder ball is not exactly halved as the via from the sensor to the lower layers is not visible. The darkened part between the bump bond and the bulk of the SiD sensor consists of the coupling and routing layers mentioned in section 6.2.1. The differently colored object connected to the bump bond on the top side is the UBM of the KPiX pad to which the bump bond was pre-applied. The UBM of the sensor is not visible simply because the picture is not exactly halved and the sensor UBM is thinner than that of the KPiX.

### 7.1.2 Kapton Flex Cable Gluing

After confirming the sensor functionality post bump-bonding, the module is assembled. This means that the *Kapton Flex Cable* (see section 6.5.1) is glued to the sensor sensor





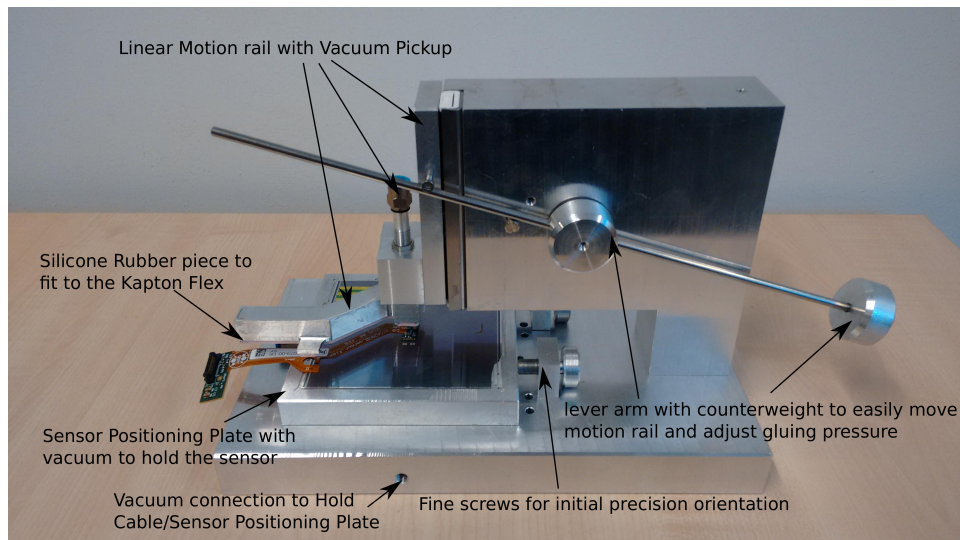
**Figure 7.1** – Microscope picture of the cross section of a Lycoris module at the bump bond.

surface. The glue chosen for this procedure is Araldite 2011 [82], a two component adhesive used by both the CMS and ATLAS groups for assembly of LHC sensors as the glue is shown not to attack the silicon or oxide layer while providing excellent stiffness and requiring no baking at higher temperatures for hardening. The two components are mixed 1:1 by volume and 1:0.8 by weight. The mixed glue requires a cure time of  $T_{\text{cure}}^{\text{Ara-2011}} \approx 10\text{h}$  at  $20^\circ\text{C}$  to reach a lap shear strength above 145psi and the objects must be kept from moving during curing.

The bias pad is attached to the backside after the cable is glued to the sensor surface via the use of the silver epoxy 8331 from MG chemicals [83]. The two component silver epoxy is mixed at a 1:1 weight ratio, has an electric resistivity of  $\rho_{\text{MG-8331}} = 7\text{m}\Omega\text{cm}$  and a cure time of  $T_{\text{cure}}^{\text{MG-8331}} = 24\text{h}$  at  $\approx 20^\circ\text{C}$ .

To verify that the glue does not damage the sensor, test structures have been covered with glue at different spots in order to measure their impact on the sensor performance (see section 7.2).

The first three sensors have been assembled by hand which resulted in damage to two sensor modules. The rest of the sensors have been assembled using a tool that has been built in order to ensure reproducibility of the procedure and to avoid damaging the sensors

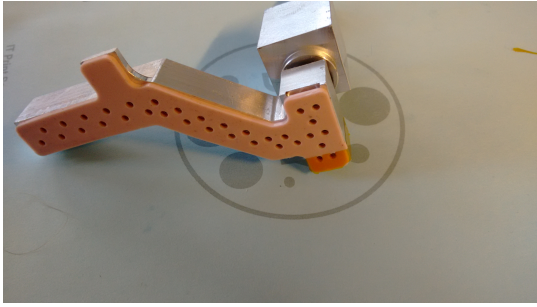


**Figure 7.2** – Picture of the gluing tool used for the gluing of the *Kapton Flex Cable* onto the SiD tracker sensors. Based on the tool used by the University of Hamburg CMS pixel group for the assembly of their modules [84].

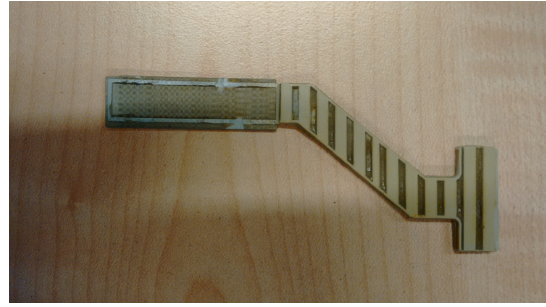
during the assembly. This tool, which is shown in Figure 7.2, is an adapted version of the tool used by the University of Hamburg CMS pixel group for the assembly of their modules [84]. The tool consists of an aluminum platform, a small aluminum head with a vacuum pick-up tool attached a linear motion rail and two positioning plates. One of the positioning plates has a cutout for the *Kapton Flex Cable* and the other has a cutout for the sensors. All objects are hollowed out and have holes drilled into their top sides. For the platform this is used to keep the positioning plates in place during operation. For the positioning plates this is used to keep the sensor or *Kapton Flex Cable* in place during gluing or pick-up.

The position of the positioning plates relative to the vacuum pick-up can be aligned using three fine thread screws. The vacuum pick-up tool consists of a hollowed out aluminum piece in the form of the *Kapton Flex Cable*. It is used both to apply the glue to the sensor surface using a custom made rubber stamp and to place the *Kapton Flex Cable* on top of the sensor. A silicone piece is attached to the bottom side of the pick-up tool. This is done so the vacuum pick-up tool fits to the form of the Kapton flex to ensure no vacuum escapes to the sides. A picture of the rubber stamp and silicone piece on the bottom side of the pick-up tool are shown in fig. 7.3a and fig. 7.3b. The weight by which the vacuum pick-up tool presses onto the sensor is controlled by a counter lever arm. The gluing of the bias pad is done by hand and no issues have been encountered. A step by step of the gluing procedure is described in section I.





(a) Custom made vacuum pick-up tool formed like the *Kapton Flex Cable*, the silicone is used to ensure no vacuum is lost to the sides.



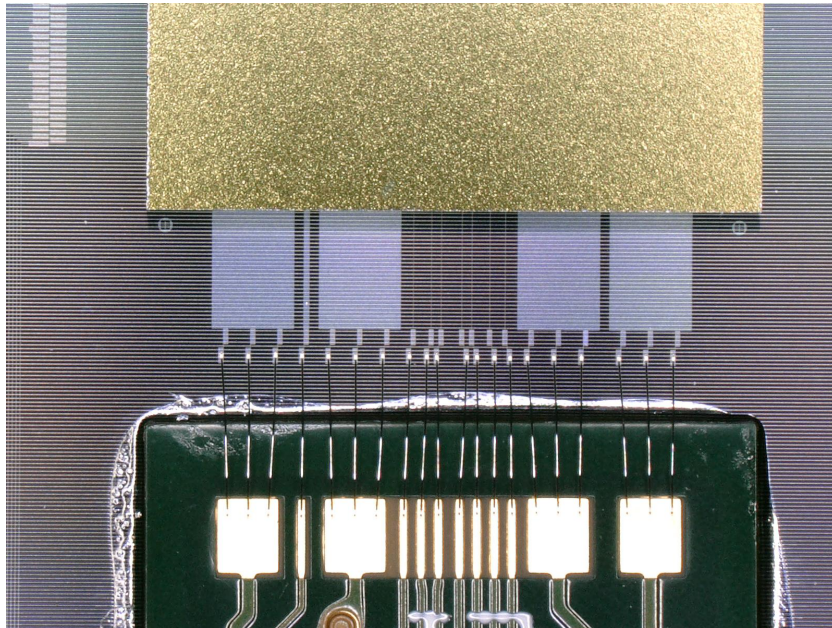
(b) Custom made rubber stamp for glue application, the cutouts are to ensure not too much glue is applied to the sensor.

**Figure 7.3** – Custom made vacuum pick-up tool and rubber stamp.

### 7.1.3 Wire-Bonding

After sensor assembly, they are sent to the DESY ZE group for wire-bonding of the *Kapton Flex Cable* to the sensor. In the procedure a wire is placed onto a dedicated wire-bond pads located on both the sensor and the Kapton Flex. The wire is pressed onto the pad where it and the pad are melted together through what is referred to as thermosonic bonding in which both the pad and the wire are heated up through vibration. Wire-bonds have diameters on the order of a few tens of microns and wire-bonds are used in situations where typical connection methods are not possible.

Figure 7.4 shows a microscope picture of the wire-bonds connecting from the LV and signal pads to the sensor bond pads which are connected to the KPIX ASIC visible as the golden object via the internal sensor routing layers. The LV pads have three wire-bonds each to reduce the resistance while the HV pad connected to the bias ring is set with two wire-bonds. While the current through the HV bias is low, the second wire-bond is placed as an additional safety means. The wire material is AlSi1 consisting of 99% aluminum and 1% silicon with a wire thickness of  $25\ \mu\text{m}$  from Heraeus [85] which has a typical breaking load of 11-16 cN and a resistance of  $61.1\ \Omega\text{m}^{-1}$ . The wire-bonds are pressed onto the bond pads with a force of 25 cN and have a typical length of 2.5 mm which results in wire-bond resistance of  $R_{\text{wire-bond}} \approx 0.15\ \Omega$ . As mentioned in section 6.5.1, two sensors could not be wire-bonded due to bond-pad aging which was found to be present only after the cable was glued to the sensors. Of the 22 assembled sensors, one functional sensor (S59) was assembled with the first *Kapton Flex Cable* using the 10 nF coupling capacitors. After wire-bonding, the sensors are fully assembled and ready for testing.



**Figure 7.4** – Microscope picture of the wire-bonds connecting the *Kapton Flex Cable* to the KPIX chip via the sensor *routing layer*.

#### 7.1.4 Frame Gluing

To be used at the DESY II Test Beam Facility, the sensors have to be installed into the Torlon<sup>®</sup> frames mentioned in section 6.4. The sensors are glued into the frame using Araldite2011. The glue is applied to the frame via a glue dispenser allowing the use of well defined air pressure in order to ensure the glue is pressed out of the syringe uniformly. The cannula used for the gluing has a metal tip with a Teflon insertion resulting in an inner diameter of 0.15mm to ensure that the glue line on the frame is small enough to avoid glue spills into the milled out area or onto the top of the sensor surface. As a result of time constraints, this gluing has been performed by hand. Because of the high viscosity of the adhesive and the small cannula diameter the pressure of the syringe is set close to the maximum of 90 psi and the speed by which the syringe was moved was adjusted to ensure an even application of the glue onto the surface. Glue is applied to all parts of the frame except where the cutout for the Kapton flex is located. The sensor is placed into the frame using a vacuum pincer to hold it and to ensure that no glue is spilled onto the sensor during placement into the frame. After placement within the frame for 10 hours, to allow the epoxy to harden, the final assembly step for the Lycoris modules is complete.

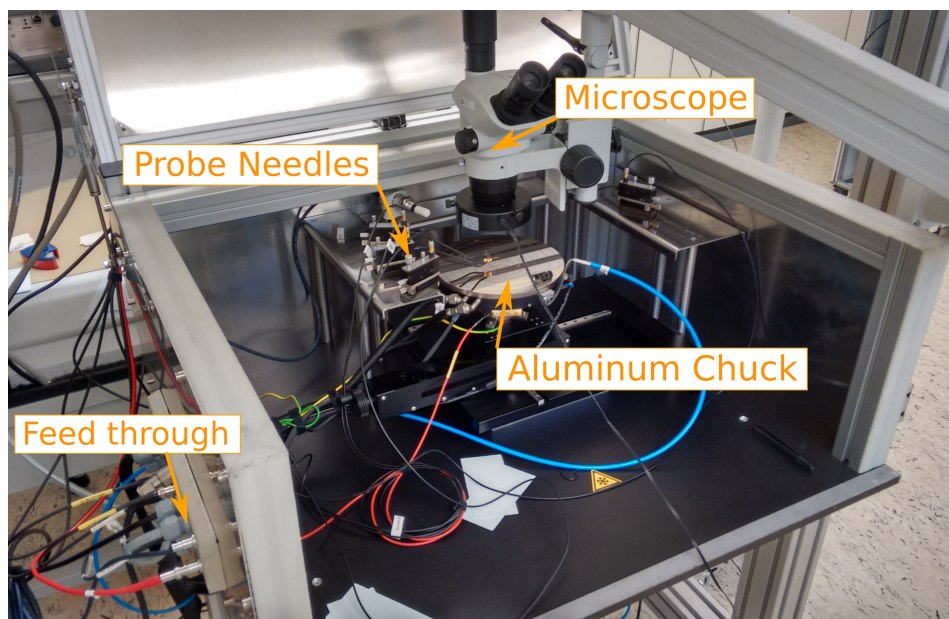


Figure 7.5 – Picture of the opened probe station dark box.

## 7.2 IV/CV and Inter-strip using the Probe Station

Measurements performed at the probe stations can be split into two categories. Measurements of the sensors IV/CV performance are conducted at every assembly step in the FH electronics laboratory clean room. This is done as quality control of the sensors and to ensure that potential problems arising from the module assembly are identified and addressed quickly.

The inter-strip capacitance measurements are performed in the Detector Assembly Facility (DAF) at DESY and are used to determine the charge sharing values of floating strips. They are later compared with results gathered at the DESY II Test Beam Facility. Both setups use the same devices for the measurements and the general system setup is the same. The only difference between the two probe stations is that the one in the DAF is an improved version of the E-Lab probe station which allows for more precise placement of the needles which is beneficial due to the small size of the DC pads of  $A_{DC} = 40 \times 30 \mu\text{m}^2$  that need to be probed for inter-strip measurements.

### 7.2.1 Probe Station Setup

A picture of the probe station in the E-Lab is depicted in Figure 7.5. Both probe stations consist of a Keithley 6517B [86] used as a voltage source and to measure the DUT currents,

an Agilent E4980 LCR meter [87] used for capacitance measurements which is connected to a CV/IV switch box shown in Figure 7 which allows easy switching between connections for the different probe measurements such as IV, CV and inter-strip capacitance and the Keithley 6485 [88] used for guard ring IV measurements.

The devices are connected to the read-out computer via a GPIB-to-USB connector and are operated using Windows 7 (FH E-Lab) and Windows 10 (DAF) via a python readout script that is part of the probe station. All other elements of the two probe stations have the same purpose but are implemented with slightly changed systems not relevant for the measurements.

To measure the electrical properties of the sensors, they are placed onto a milled aluminum chuck with holes connected to a vacuum pump. The vacuum ensures a good connection between the sensor and the chuck. It also ensures that the sensor does not accidentally move when placing the needles. The exact configuration and their purpose depends on the type of measurement performed which are explained in detail below.

### IV measurement

IV measurements are the measurement of the current ( $I$ ) flowing through the sensor at different levels of reverse bias ( $V$ ). The current measurement is performed as a direct measurement of the power supply via:

$$I_{\text{DUT}} = \frac{V_{\text{DUT}}}{R}. \quad (7.1)$$

With  $I_{\text{DUT}}$  and  $V_{\text{DUT}}$  being current flowing through- and voltage applied to the DUT. The DUT resistance is  $R$ . The ground connection of the voltage source is connected to a probe needle which is placed onto the bias pad (see Table 6.5) to deplete the sensor and measure its dark current. The LCR meter is disconnected from the setup using the CV/IV switch box.

### CV measurement

CV measurements are the measurement of the capacitance of the sensor ( $C$ ) at different levels of reverse bias ( $V$ ). The LCR meter is set up to measure the equivalent electrical circuit of a capacitance which is parallel to a resistance. For Direct Currents (DC) the capacitance is effectively an infinite resistor. For Alternating Currents (AC) the capacitance



has an effective resistance which is given by:

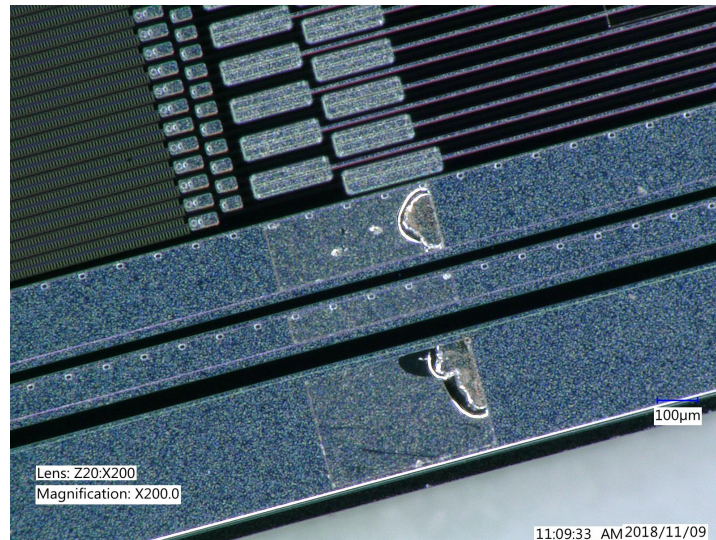
$$C_{\text{DUT}} = \frac{I_{\text{DUT}}}{2\pi\nu V_{\text{AC}}}, \quad (7.2)$$

where  $I_{\text{DUT}}$  is the current flowing through the DUT,  $\nu$  is the AC frequency and  $V_{\text{AC}}$  is the magnitude and phase angle of the measured AC voltage. Increasing the DC component of the power supply slowly increases the depletion zone until full depletion. This reduces the capacitance (see section 3.1.3) which is measured using the AC component via the LCR meter. Similar to the IV measurement the needle is placed onto the bias pad to deplete the sensor. The necessary connections to the LCR meter are performed using the CV/IV switch box which is set to CV to connect the needle to the LCR meter. The same switch also applies the modulating AC over the DC bias supplied by the Keithley 6517B. The frequency of the AC is set to  $\nu = 1$  kHz and an amplitude of  $V_{\text{AC}} = 1$  V is applied.

Typically, an open measurement is performed in order to subtract the capacitance offset of the LCR meter. Open measurements are performed with an open ended connection on the needle. The Agilent E4980 is able to perform such a measurement internally and subsequently automatically subtracts the result from every following measurement. The open measurements could not be performed for many of the later CV measurements. The probe station software and hardware had undergone an overhaul in between some of the measurements after which the appearance of destructive discharges after open measurements with the LCR meter were observed. Multiple test structures have been lost due to destructive discharges (see Figure 7.6) and it has been deemed too dangerous to perform an open measurement as the general usability of the sensor and its depletion voltage can be established even without knowing the absolute capacitance value by looking at the relation between the capacitance and the bias voltage.

### Inter-strip capacitance measurement

The measurement principle behind the inter-strip capacitance measurement is the same as for the CV measurement. The difference comes from the addition of two needles that are placed on adjacent DC pads of the sensor which are connected to the  $p^+$  implant. The necessary connections to the LCR meter of the different needles are performed using the CV/IV box. The box is set to CV+C/R. This means that the current needle is routed to the LCR meter and a modulated AC is applied to the chuck using the same amplitude and frequency as before. In addition, one of the two additional needles supplies an AC to the strip implant with the other measuring the resulting potential and current on an adjacent strip via



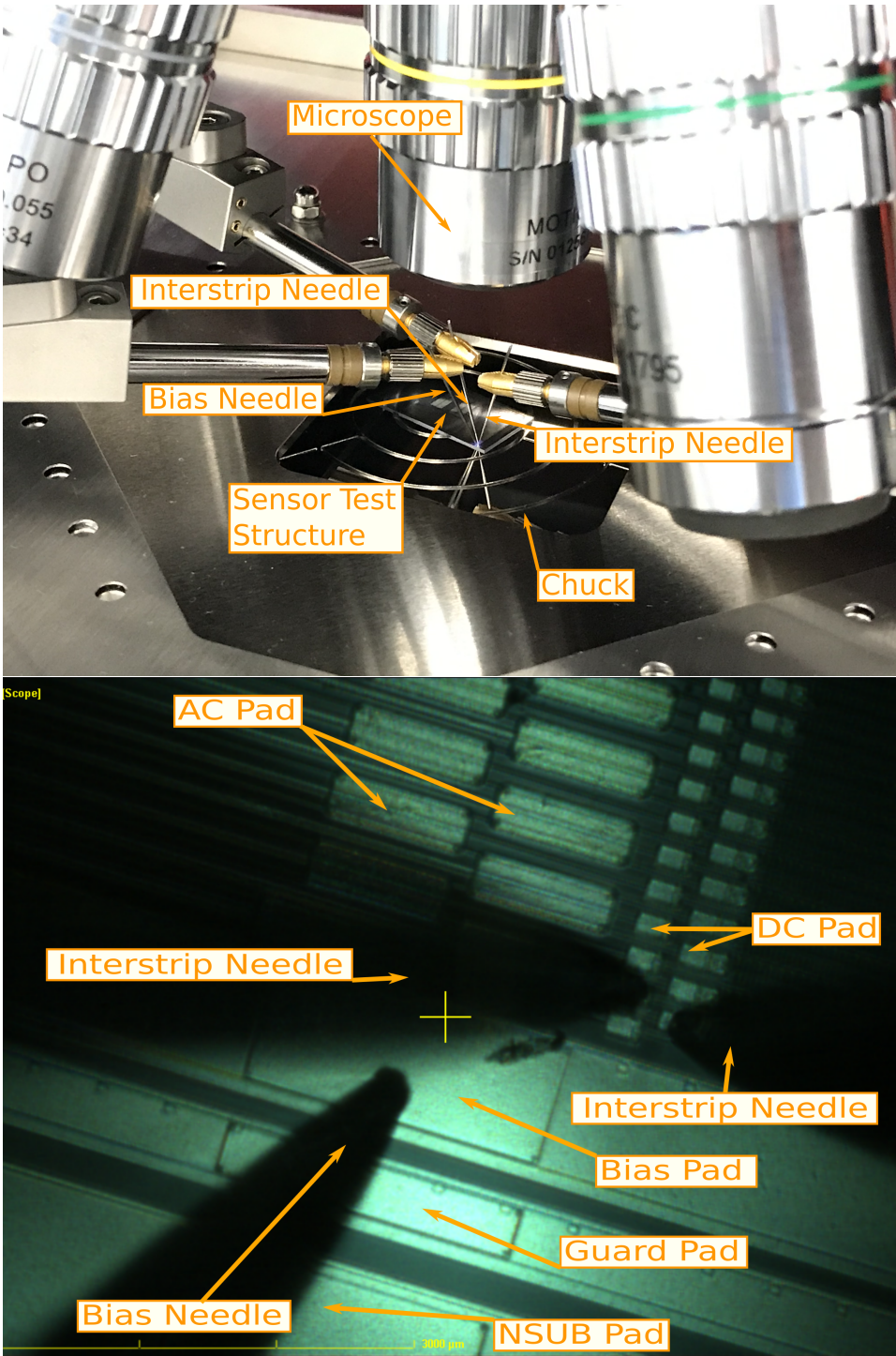
**Figure 7.6** – Picture of a test structure pad after destructive discharge.

the same LCR meter in order to determine the capacitance between the two strips. This is done for the strip on both sides of the supplying needle. A picture of the setup in the DAF with needles placed on the DC pad and the corresponding microscopic picture are shown in Figure 7.7.

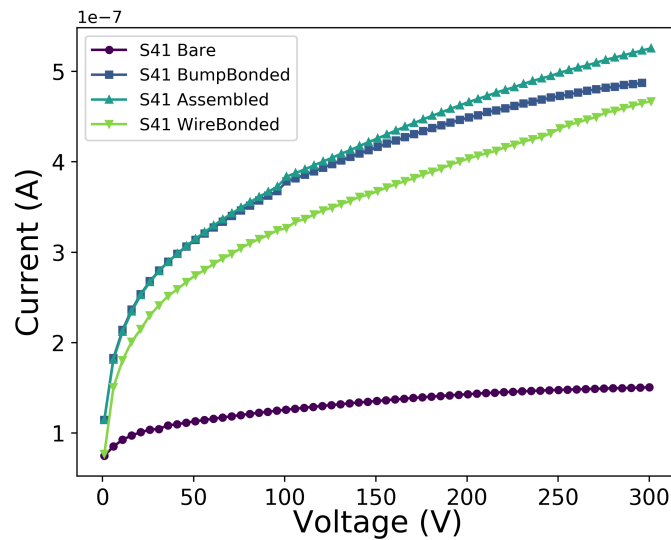
### 7.2.2 IV/CV Measurement Results

As mentioned in chapter 7, IV and CV measurements are performed after each major change to the SiD sensor. The different states the sensors are tested at are referred to as *Bare*, *BumpBonded*, *Assembled* and *WireBonded*.

- *Bare*: The sensor is tested right after arrival at DESY in a state just as after production at Hamamatsu.
- *BumpBonded*: The KPiX ASIC is bump-bonded to the sensor.
- *Assembled*: The *Kapton Flex Cable* is glued to the sensor as described in Section 7.1.
- *WireBonded*: The wire-bond connections between the ASIC, the Sensor and the *Kapton Flex* are completed. CV measurements are no longer feasible at this point as with the connection of the wire-bond to the bias ring, measurements of the capacitance result in the measurement of the 10  $\mu$ F capacitor that connects the two bias lines on the *Kapton Flex Cable*.



**Figure 7.7** – (Top) Picture of an SiD test structure on the DAF probe station for inter-strip measurements. (Bottom) Microscopic view of the same test structure with the needle placement.



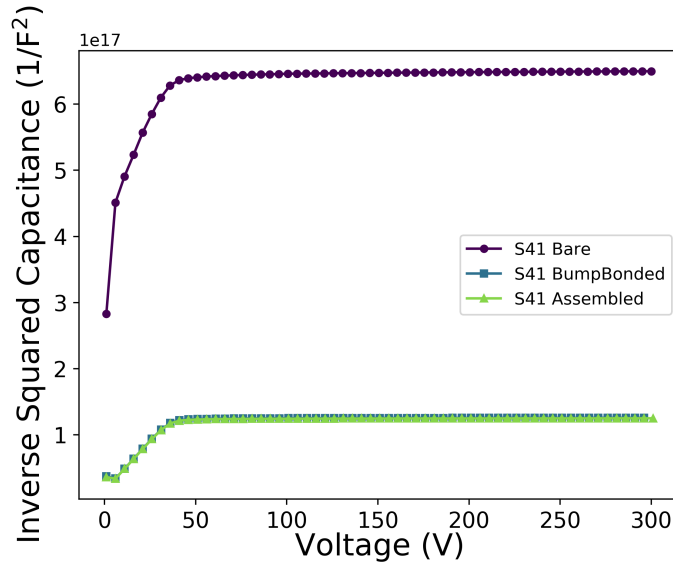
**Figure 7.8** – Current measurements of the SiD sensor for different bias voltages before and after major steps. The different stages are highlighted in the legend.

Representative, the development is shown in Figure 7.8 for the IV measurements and in Figure 7.9 for the CV measurement of S41 which shows a fairly typical development.

The IV curve shown in Figure 7.8 shows a large increase in the dark current comparing the measurements before and after bump-bonding. This is expected to be a result of treatment of the sensor surface during the bump-bonding procedure introducing impurities into the system. The decrease in dark current between the *Assembled* curve and *WireBonded* system can be explained by the exposure of sensors to humidity. All sensors are stored in a nitrogen cabinet to reduce the exposure to oxygen, the nitrogen in the cabinet is enriched with water to keep humidity at around 35% Relative Humidity (RH) to avoid build up of static charge. As such the sensors are exposed to humidity during storage which can attach to the surface. After wire-bonding the sensors are stored in a dry cabinet resulting in less water attached to the sensor surface resulting in a lowered dark current.

The  $C^{-2}V$  curve shown in Figure 7.9 depicts the measured capacitance for the different steps in the assembly. The curves of the three measurements show in general the same behavior with increasing bias voltage. Their inverse squared capacitance rises sharply and subsequently flattens out after around 40V is reached. They do show a large difference in the absolute values. The reason for this difference is the aforementioned changes to the ProbeStation software and hardware. This changed the standard AC frequency used for CV measurements from 10kHz to 1kHz which went unnoticed for a long time. For consistency





**Figure 7.9** – Capacitance measurements of the SiD sensor for different bias voltages before and after major steps. The different stages are highlighted in the legend.

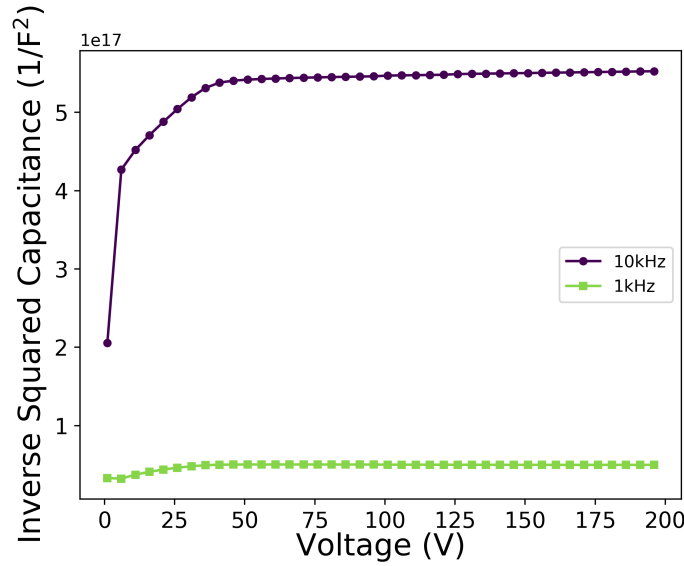
purposes between measurements of bump bonded, assembled and wire-bonded sensors, all later measurements have been performed with an AC frequency of 1 kHz. A back to back measurement of S56 with 10 kHz and 1 kHz AC frequency shown in Figure 7.10 shows the clear decrease of the measured capacitance with increased AC frequency which is expected based on the relation of the impedance used to measure the capacitance to the frequency. Minor changes between capacitance measurements are the result of the missing open measurements mentioned previously in Section 7.2.

In order to determine the depletion voltage, two linear regressions are fitted to the data showing the inverse squared capacitance against the bias voltage. One regression is fit to the early part where the capacitance drops quickly with increasing bias voltage ranging from 5 V to 35 V and another regression is fit to the flattened part ranging from 60 V to 300 V as shown in Figure 7.11 which results in two linear regressions with

$$C_{\text{rise}}^{-2} = 6.37 \times 10^{15} \text{ F}^{-2} \text{ V}^{-1} \cdot V_{\text{bias}} + 4.19 \times 10^{17} \text{ F}^{-2} \quad (7.3)$$

and

$$C_{\text{flat}}^{-2} = 2.48 \times 10^{13} \text{ F}^{-2} \text{ V}^{-1} \cdot V_{\text{bias}} + 6.43 \times 10^{17} \text{ F}^{-2}. \quad (7.4)$$



**Figure 7.10** – Capacitance measurements of the SiD sensor for a 1 kHz and 10 kHz AC frequency. The measurement accurately reflects the effect of the increased frequency based on (7.2).

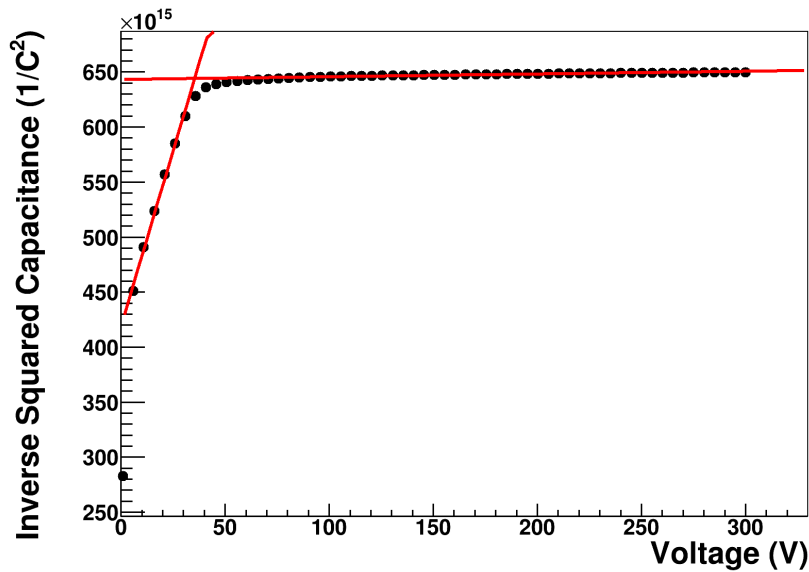
The intersection point of the two regressions is at

$$0 = C_{rise}^{-2} - C_{flat}^{-2} = 6.35 \times 10^{15} \text{ F}^{-2} \text{ V}^{-1} \cdot V_{dep} - 2.23 \times 10^{17} \text{ F}^{-2} \quad (7.5)$$

resulting in a depletion voltage of

$$\Rightarrow V_{dep} \approx 35.4 \text{ V}. \quad (7.6)$$

Figure 7.12 shows the IV curves for all 29 sensors before bump-bonding. Four of the 29 sensors show abnormal behavior. S34 shows a jitter in the measured current and an overall higher current value which would be explained by an issue with the connection of the probe needle to the sensor pad. In addition, S42 and S43 show an accelerated increase in dark current with increasing bias voltage indicating the start of a breakdown at around 150V. S48 also shows an accelerated increase in dark current though at a higher bias voltage of around 280V. Similarly, Figure 7.13 (left) shows the  $C^{-2}V$  curves for all 29 *Bare* sensors showing an overall similar behavior between all sensors and a similar depletion voltage the distribution of which is shown in Figure 7.13 (right). As the depletion voltage of all sensors is around  $V_{dep} = 40 \text{ V}$  all sensors are typically operated with a voltage of 70V on the power supplies which, after passing through the two 1 MOhm resistors on the Kapton Flex cable,



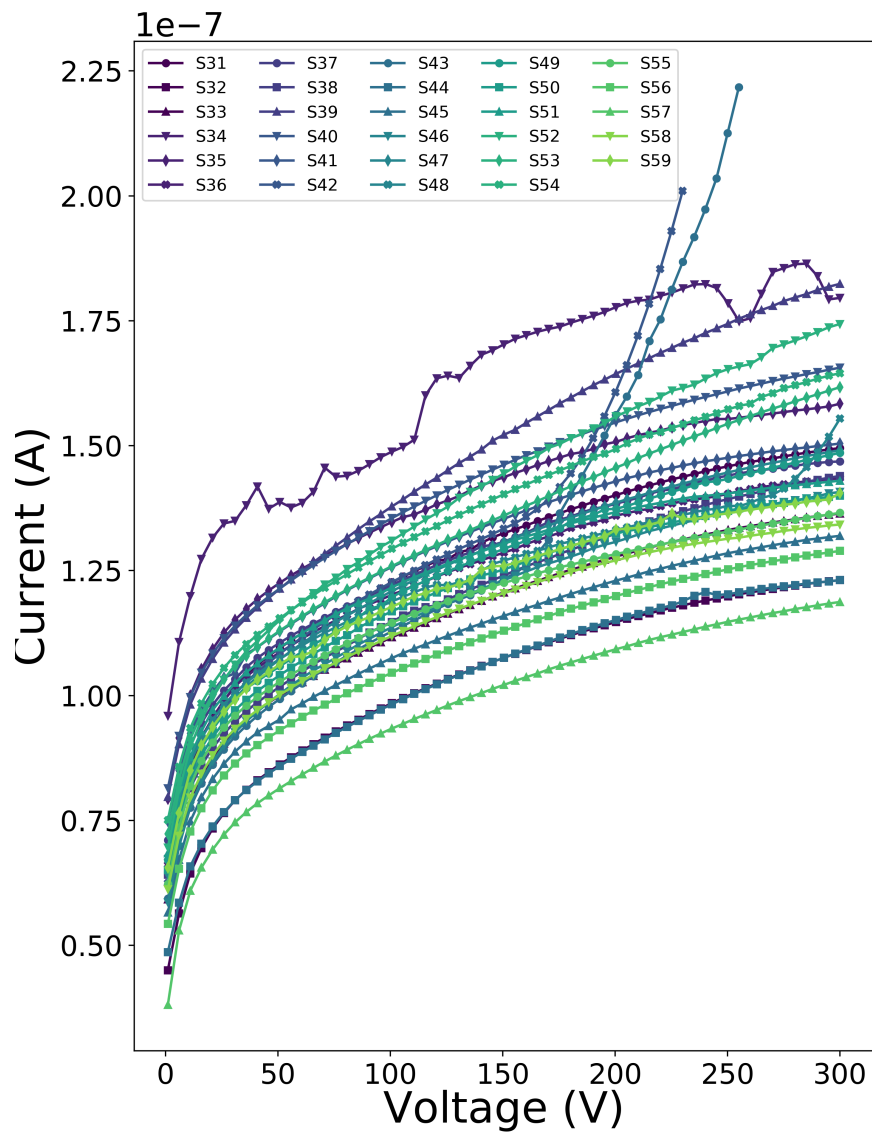
**Figure 7.11** – Inverse square capacitance value versus bias voltage for S41 with linear regressions to the flattened part and the early rise.

results in an applied voltage of 63V on the sensor which is slightly above the depletion voltage of all sensors.

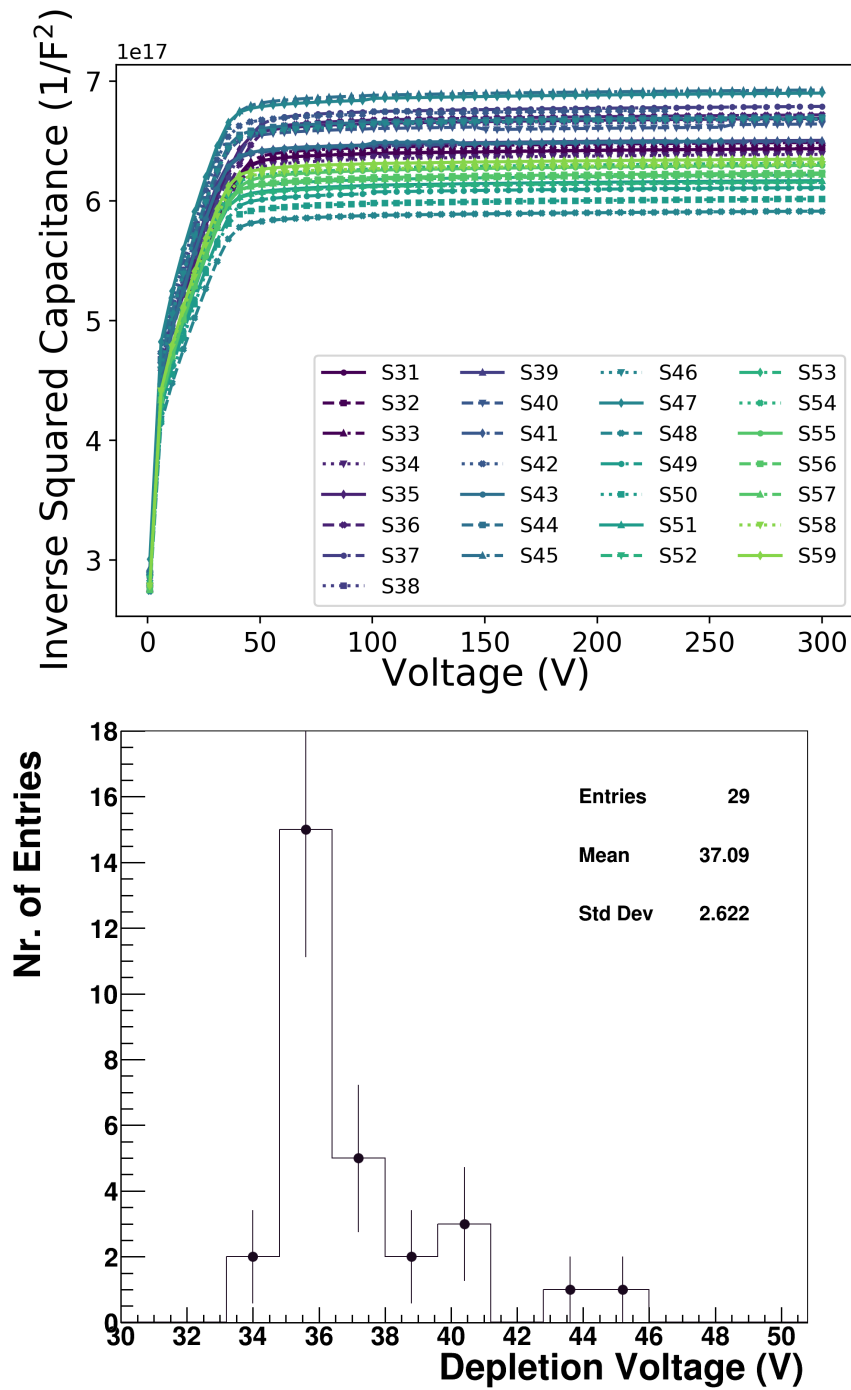
While S41 shows the typical behavior for the sensors, not all sensors perform as well after wire-bonding as their *Bare* counterpart. Some sensors show a breakdown that was not previously seen and such effects could appear after the assembly step. IV measurements for four *wired* sensors are chosen that represent the different effects of the assembly in Figure 7.14. It shows that S43 still has the start of the breakdown at 150V while now S55 and S32 show a massive increase in dark current once a certain voltage level has been surpassed which is not the case for the *Bare* sensors. In detail, looking at the behavior of S55 between the different steps (see Figure 7.15) shows that the breakdown at lower voltages was introduced by the assembly procedure during which the *Kapton Flex Cable* is glued to the top of the sensor. As such, the potential impact of the application of the glue has been studied in more detail.

### Glue impact on performance

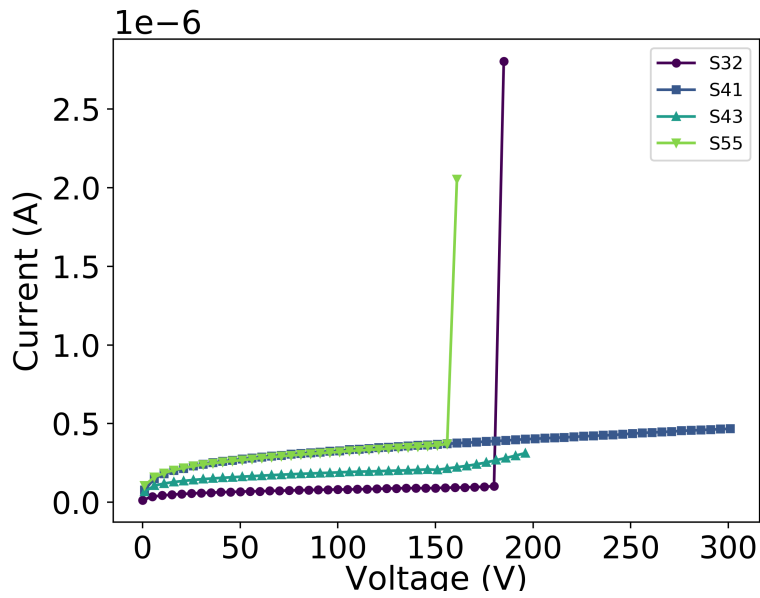
Tests of the impact of the glue on the sensor performance have been conducted using test structures made from the same wafers as the silicon sensors. These test structures are tested once in a pristine condition and once with glue pollution on different parts of the structure both directly after glue application and after curing. The spots where glue was



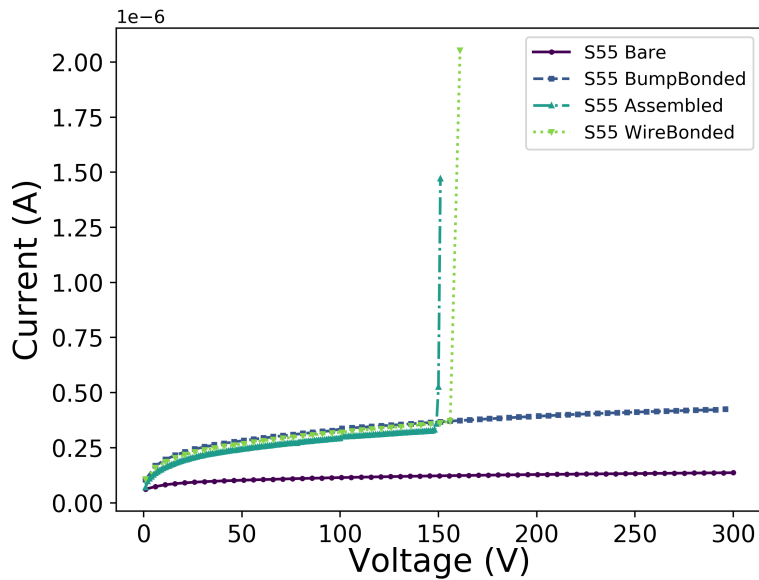
**Figure 7.12** – IV curves for all 29 *Bare* sensors.



**Figure 7.13** –  $C^{-2}V$  curves for all 29 *Bare* sensors (top) and the corresponding distribution for their depletion voltages (bottom).



**Figure 7.14** – IV curves for some of the *WireBonded* SiD sensors. S41 and S43 are representative for all sensors which show no change in their behavior. S32 and S55 on the other hand show a very sudden large increase in the dark current which indicates a full breakdown which was not present for the *Bare* sensors.



**Figure 7.15** – Current measurements of the SiD sensor S55 for different bias voltages before and after major steps. The different stages are highlighted in the legend.

placed deliberately are:

- the center of the sensor structure where there are no coverable pads or anything to determine whether the glue attacks the sensor surface,
- the ring structure at the edge of the sensor,
- the Poly-SiR close to the edge.

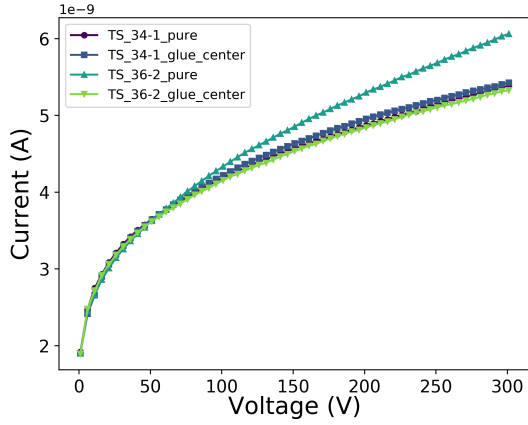
All of these regions are close to the *Kapton Flex Cable* and inaccurate application of glue can result in glue being applied on these structures. The results of these tests are:

- Test structures with glue in the center show no large difference in the IV curve before and after gluing as shown in Figure 7.16.
- Test structures with glue placed over the ring structure show an early breakdown as shown in Figure 7.17.
- Test structure with glue freshly applied on top of both the edge and over the Poly-SiR structure shows a resistor like behavior (see Figure 7.18). After curing this changes into an early breakdown similar to the one shown in Figure 7.17.

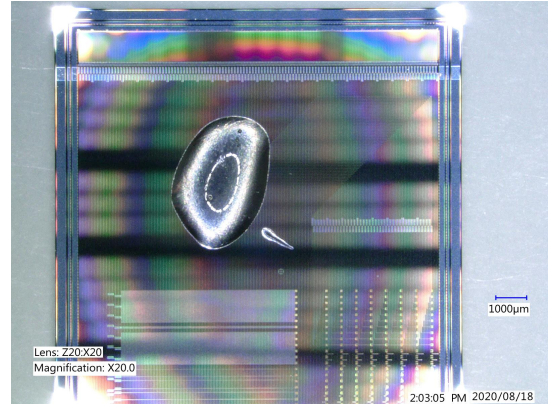
The parts beneath the *Kapton Flex Cable* cannot be inspected for potential pollution. It is therefore possible that small amounts of glue produce a connection between the different ring structures, resulting in an early breakdown of the sensors as is shown in Figure 7.14 for S55 and S32. This is considered not to be an issue for sensor operation as the breakdown happens at around 150V while for all sensors their depletion voltage is around 37V. The sensors are not operated in a high radiation environment and an increase of the operational bias voltage far beyond the depletion voltage is not foreseen.

### 7.2.3 Inter-strip measurement

The inter-strip capacitance is important for determination of the expected charge loss as result of the floating strips losing charge to the back-plane (see section 3.1.5). The measurements are performed as described above and the measured inter-strip capacitance for both the left and right strip adjacent to a readout strip is depicted in Figure 7.19a. While the distribution shows the expected early development similar to a normal CV measurement, after a certain bias level is reached, the capacitance once again starts an accelerated decrease with increasing bias voltages. It is not entirely clear what the reason is for this result. Some ideas are:

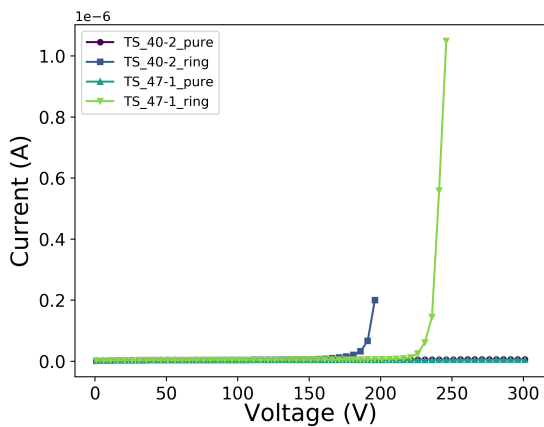


(a) IV measurement.

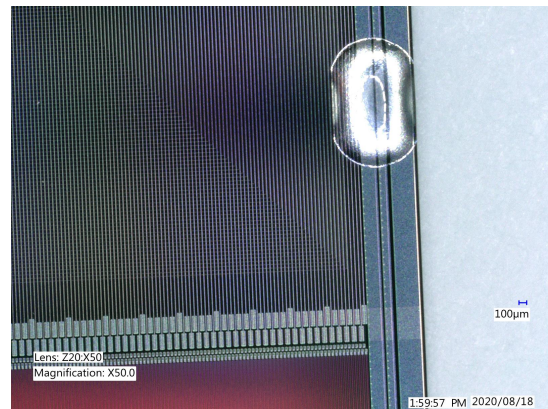


(b) Microscope picture.

**Figure 7.16** – IV measurement for SiD test structure in a pristine condition and after glue was applied to the center of the structure as shown in the microscope picture.



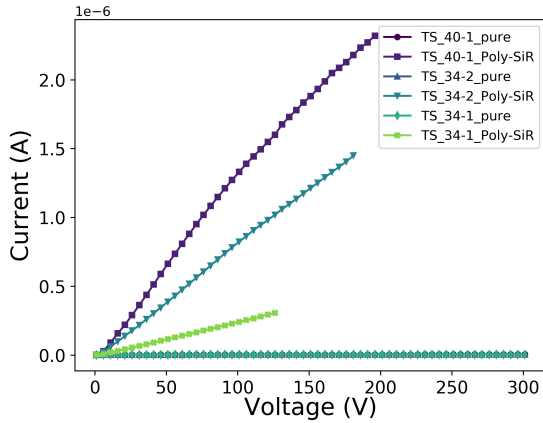
(a) IV measurement.



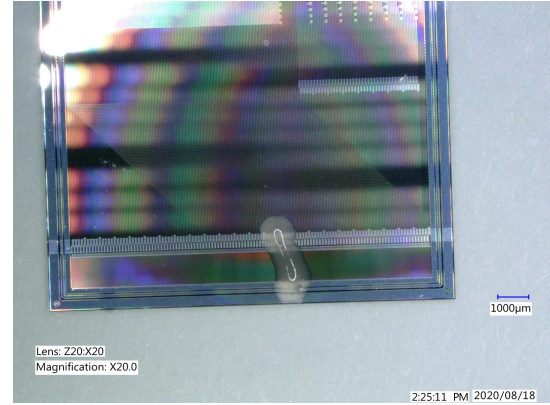
(b) Microscope picture.

**Figure 7.17** – IV measurement for SiD test structure in a pristine condition and after glue was applied to the ring surrounding the structure as shown in the microscope picture.





(a) IV measurement.



(b) Microscope picture.

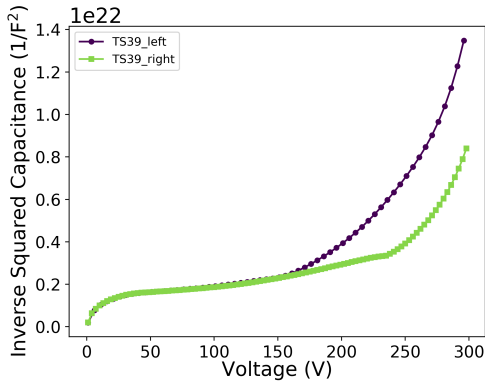
**Figure 7.18** – IV measurement for SiD test structure in a pristine condition and after glue was applied to over the Poly-SiR including the ring structure and pads as shown in the microscope picture.

- Crossings of the strips with the *routing layer* can impact the measurement and as such the measurements should be repeated at an area where fewer crossings are expected,
- the measurement has been performed using a two needle setup, the strip opposite of the central readout strip is not on a controlled level resulting in an incorrect measurement of the inter-strip capacitance. At the time of this thesis the setup at the DAF does not allow for a three needle inter-strip setup.

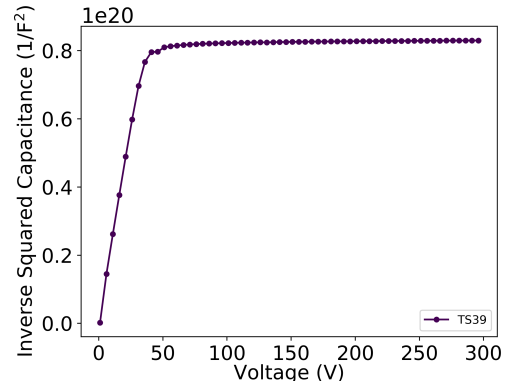
Under the assumption that the capacitance at the flattened out area represents the true inter-strip capacitance this results in a value of  $C_{ss} = 2.42 \times 10^{-11}$  F. The capacitance to the back-plane is calculated from the results of a standard CV measurement based on the equivalent circuit shown in Figure 3.5b. The total capacitance measured during a CV measurement is the sum of all capacitances that are set in parallel and in series. For a sensor with only three strips in parallel as shown in the sketch in Figure 7.20 the total capacitance of the system is given by

$$C_{tot} = 2 \cdot \frac{1}{1/C_b + 1/C_{ss}} + C_b \stackrel{C_{ss} \gg C_b}{\approx} 3 \cdot C_b. \quad (7.7)$$

We therefore calculate the capacitance of a single strip to the back-plane using the capacitance from CV measurements after full depletion by dividing it by the number of strips



(a) CU measurements of the two strips adjacent to the readout needle for a test structure.



(b) CU measurements of the test structure used for the interstrip measurements.

Figure 7.19 – Inter-strip and normal CV measurement of the SiD test structure 39.

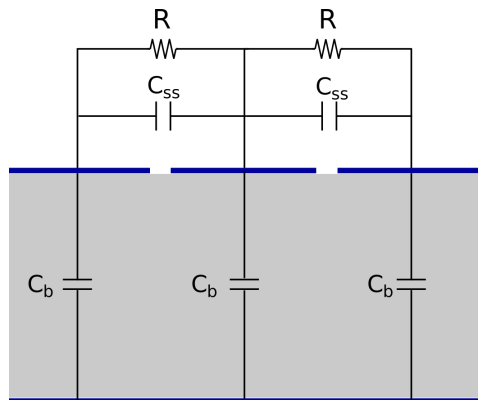


Figure 7.20 – Sketch of a three strip silicon sensor electronic circuit equivalence.

which, for a test structure, is equal to 479 strips. The CV measurement is shown in Figure 7.19b which results in a strip-to-back-plane capacitance of  $C_b = 2.31 \times 10^{-13}$  F.

Using the formula for the charge loss (see (3.9)) the fraction of charge spread to the adjacent readout strips is calculated as to be  $Q_r/Q_{tot} = 0.49$ . This results in a total charge loss of 2% to the back-plane. This value is later compared with the results gathered from the investigation into the sensor as a DUT presented in section 10.5.1 but is significantly below the expected value of about 20% [89].

## **Part IV**

# **Data Analysis**



# Chapter 8

## Lycoris Telescope Setup at the DESY II Test Beam Facility

Measurements have been performed at the DESY II Test Beam Facility (see chapter 5) to investigate the performance of the Lycoris modules and to validate the design of the Lycoris telescope system. The Lycoris system was installed both within area T24 where it was investigated as a DUT within the AZALEA telescope and within the PCMAG area T24/1 in which the system has been tested for its functionality as a telescope designed for use inside the PCMAG. The data taking methods and the types of data taken are described at the end.

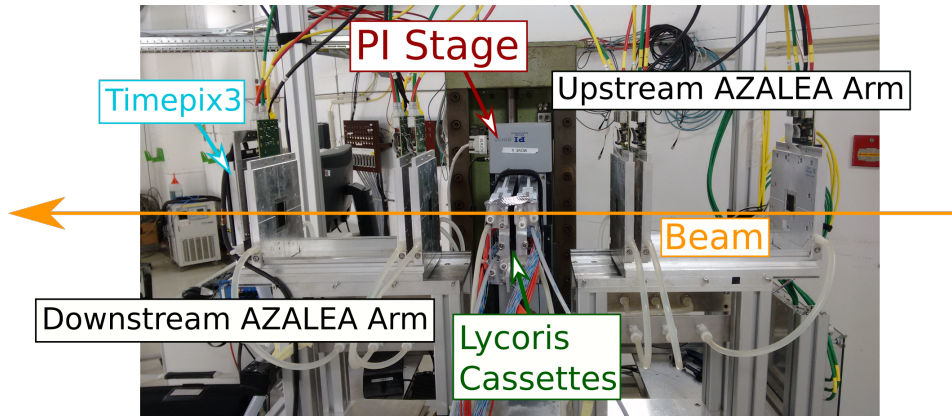
### 8.1 Lycoris as a DUT

In order to investigate the performance of the Lycoris module the system was installed within the test beam area T24 between the AZALEA telescope arms to use the tracks generated by the AZALEA telescope to investigate the performance and efficiency of the Lycoris modules.

The T24 test beam setup can be split into four components. The electronics, the setup of AZALEA relative to the Lycoris cassette, the internal Lycoris cassette layout and the components impacting the beam traversal.

The beam path through the area begins where the description of the beam generation stopped in section 5.1.1 as the setup within the area depends on the measurement performed.

After traversing the beam monitors, the electron beam enters the secondary collimator which was chosen to have an opening of  $20 \times 10 \text{ mm}^2$  to match the active area covered by

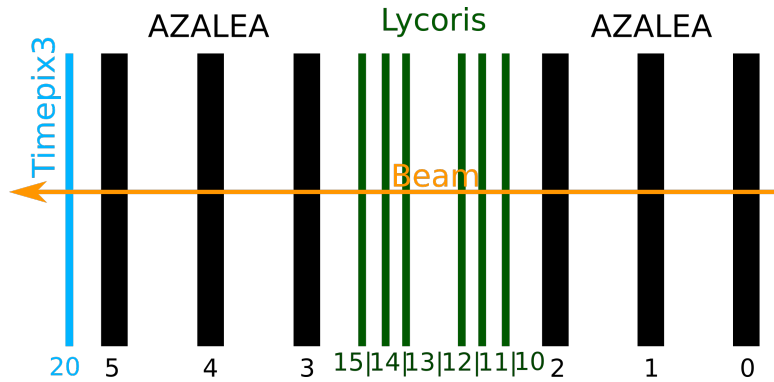


**Figure 8.1** – T24 setup during operation with three AZALEA layers in front and behind two Lycoris cassettes. The Timepix3 was located on the leftmost layer located after the last AZALEA layer.

the AZALEA telescope described in section 5.3. The beam hits a scintillator cross installed before the first AZALEA layer that was used to generate fast trigger pulses for the systems. The particles then enter the first three layers of the AZALEA telescope followed by both Lycoris cassettes each of which houses three Lycoris modules with the orientations described in section 6.3. This is followed thereafter by three more layers of the AZALEA telescope. The Lycoris system was placed between the AZALEA system as the error incurred by interpolation is smaller than the error incurred by extrapolation resulting in a higher accuracy. In one case an additional pixel layer in the form of the Timepix3 sensor was placed behind the last AZALEA layer as an additional timing layer. The naming scheme for the different layers is based on the order in which they are hit by the beam and is described by:

$$\text{Beam} \rightarrow \overbrace{l_0 \rightarrow l_1 \rightarrow l_2}^{\text{AZALEA}} \rightarrow \overbrace{l_{10} \rightarrow l_{11} \rightarrow l_{12} \rightarrow l_{13} \rightarrow l_{14} \rightarrow l_{15}}^{\text{Lycoris}} \rightarrow \overbrace{l_3 \rightarrow l_4 \rightarrow l_5}^{\text{AZALEA}} \rightarrow \overbrace{l_{20}}^{\text{Timepix3}} \rightarrow \text{Beam}.$$

For this setup the Lycoris telescope was installed on a xy stage from "Physik Instrumente" (PI). The setup in area T24 is shown in Figure 8.1. Not visible in the picture are the electronic components described in section 6.5.1 and the AZALEA DAQ (section 5.3) which are placed in close proximity to the setup. During test beams the system was flushed with boiled off nitrogen to keep humidity within the cassette at low levels (see section 10.2.1). The PI stage consists of two rails to allow for movement along the x and y axis of the Lycoris telescope. The movement range of the stage is 10 cm along x and 20 cm along y. A sketch of the distances along the beam axis z between the different active layers is shown in Fig-

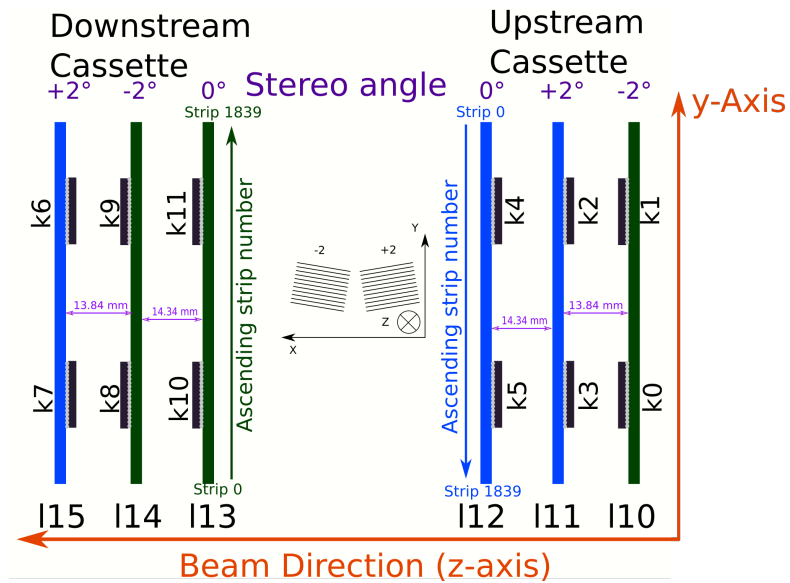


**Figure 8.2** – Sketch showing the layer numbering between the different sensor layers in area T24. Lycoris layers are shown in green, AZALEA layers in black and the Timepix3 layer in azure. The beam direction is indicated by the orange arrow.

ure 8.2. Unless otherwise noted, all sensor layers are kept perpendicular to the beam axis. Each layer of the AZALEA telescope has the same initial angle around the plane normal before track based alignment. The same assumption was made for the Lycoris cassettes though the internal configuration is described in section 6.3.

A description of the lay-outing within the cassettes is sketched in Figure 8.3. For layers l10, l13 and l14 an ascending strip number is equal to an increase in the global y coordinate while for layers l11, l12 and l15 it is the opposite, meaning that an ascending strip number equals a decrease in the global y coordinate.

The sensors used during the test beam campaigns and their positions along the z-axis are listed in Table 8.1. The system does not need to be symmetric as long as the actual distances between layers are known to a precision of a centimeter. This knowledge is then used as initial parameters for the track based alignment of the system described in section 4.3. To reduce the combinatorics and to achieve an accurate timestamp for each track, a Timepix3 [90] ASIC was installed behind the last AZALEA plane in the most recent test beam campaign in August 2020.



**Figure 8.3** – Sketch showing the angles and orientation of the Lycoris layers within their cassettes.

Layer	Lycoris module	z-position March2020 (mm)	z-position August2020 (mm)
0	AZALEA 0	-307.5	-380.0
1	AZALEA 1	-195.2	-119.1
2	AZALEA 2	-81.6	-92.2
3	AZALEA 3	44.5	47.4
4	AZALEA 4	174.9	77.3
5	AZALEA 5	307.5	393.7
10	Lycoris S59	-52.5	-57.4
11	Lycoris S40	-39.7	-44.9
12	Lycoris S43	-25.4	-30.3
13	Lycoris S48	-9.1	-14.1
14	Lycoris S47	5.8	-0.9
15	Lycoris S46	19.5	14.4
20	Timepix3	-	399.5

**Table 8.1** – Layer configuration with name of which sensors were used in the setup as well as their corresponding position along the z axis.



## 8.2 Lycoris within the PCMAG to determine the resolution of the helix

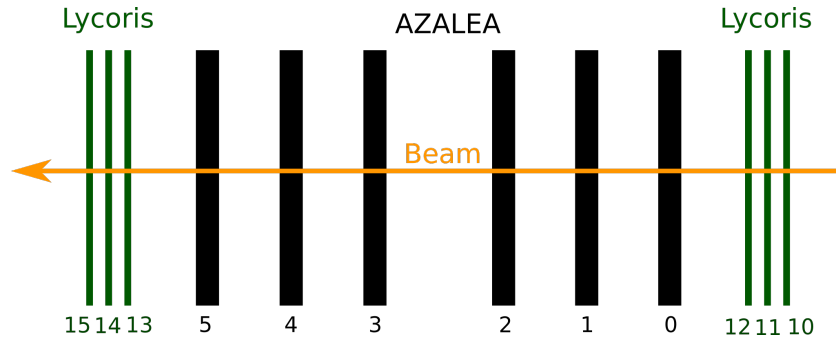
The Lycoris telescope has also been operated within the PCMAG superconducting solenoid within Area T24/1. The purpose of these measurements are to verify the design of the Lycoris support structure, to show the functionality of the system within the magnetic field and to determine the achievable momentum resolution of the system. The area T24/1 setup can also be split into the beam traversal, the AZALEA setup, the Lycoris setup and the PCMAG. The beam particles pass through area T24 which, for these measurements, has all objects removed from the beam path. The secondary collimator insertion in T24 was also removed to reach the highest possible rates. The beam size was limited via the T24/1 secondary collimator which is located within the wall separating areas T24 and T24/1. Once the shutter located in Area T24 is opened, the beam can traverse through the secondary collimator within the wall with an opening of  $12 \times 12 \text{ mm}^2$ . A trigger finger setup consisting of up to four scintillator fingers with a maximum overlap area of about  $20 \times 20 \text{ mm}^2$  is located behind the collimator.

The beam then passes through the wall of the PCMAG (section 5.4) after which the beam hits the silicon sensors that were placed within the solenoid. The naming scheme is the same as previously though the beam now first hits the Lycoris layers which surround the AZALEA layers within the magnet. The order of sensors is given by:

$$\text{Beam} \rightarrow \overbrace{l_{10} \rightarrow l_{11} \rightarrow l_{12}}^{\text{LYCORIS}} \rightarrow \overbrace{l_0 \rightarrow l_1 \rightarrow l_2 \rightarrow l_3 \rightarrow l_4 \rightarrow l_5}^{\text{AZALEA}} \rightarrow \overbrace{l_{13} \rightarrow l_{14} \rightarrow l_{15}}^{\text{LYCORIS}} \rightarrow \text{Beam}.$$

The layout is sketched in Figure 8.4 with the distances measured via external tools listed in Table 8.2 that are used as input for the track based alignment (see section 4.3). For the installation within the T24/1 PCMAG, the Lycoris telescope was installed within the rail system described in section 6.4. The AZALEA telescope was installed in the PCMAG using a cart affixed onto the two central rails installed in the PCMAG described in section 5.4. The cart itself uses the same rails for holding the aluminum jigs mentioned in section 5.3 and allows for movement of the single jigs along the  $z$ -axis as well as movement of the whole system along the  $x$ -axis and the shifting of single arms along the  $y$ -axis. The AZALEA layers are adjusted to have the same  $x$  and  $y$  position. The Lycoris modules were moved around them.

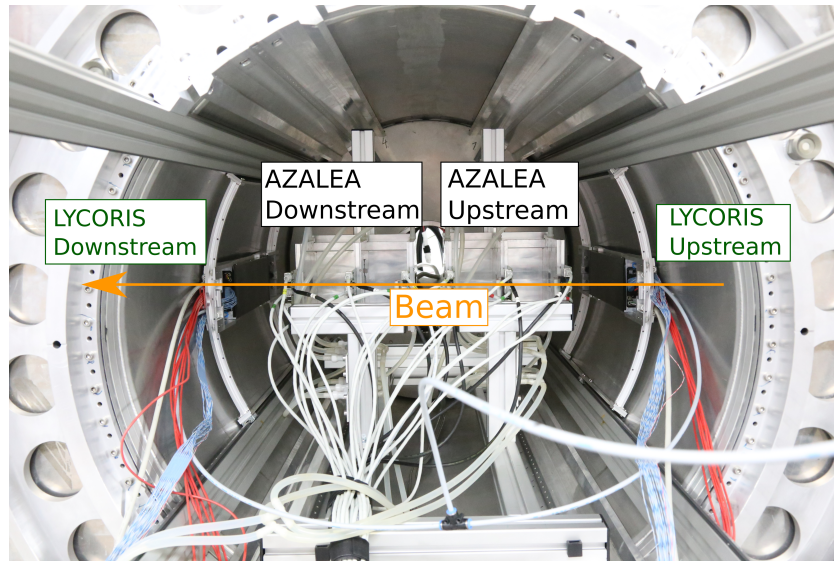
The rail system of the Lycoris telescope enforces a static position along  $z$  with a dis-



**Figure 8.4** – Sketch showing the layer numbering between the different sensor layers in area T24. Lycoris layers are shown in green, AZALEA layers in black. The beam direction is indicated by the orange arrow.

Layer	Lycoris module	z-position (mm)
0	AZALEA 0	-250.2
1	AZALEA 1	-154.4
2	AZALEA 2	-61.4
3	AZALEA 3	38.5
4	AZALEA 4	150.9
5	AZALEA 5	264.7
10	Lycoris S59	-415.8
11	Lycoris S43	-404.0
12	Lycoris S40	-390
13	Lycoris S48	390
14	Lycoris S47	404.9
15	Lycoris S46	418.3

**Table 8.2** – Layer configuration with name of which sensors were used in the setup as well as their corresponding position along the z axis.

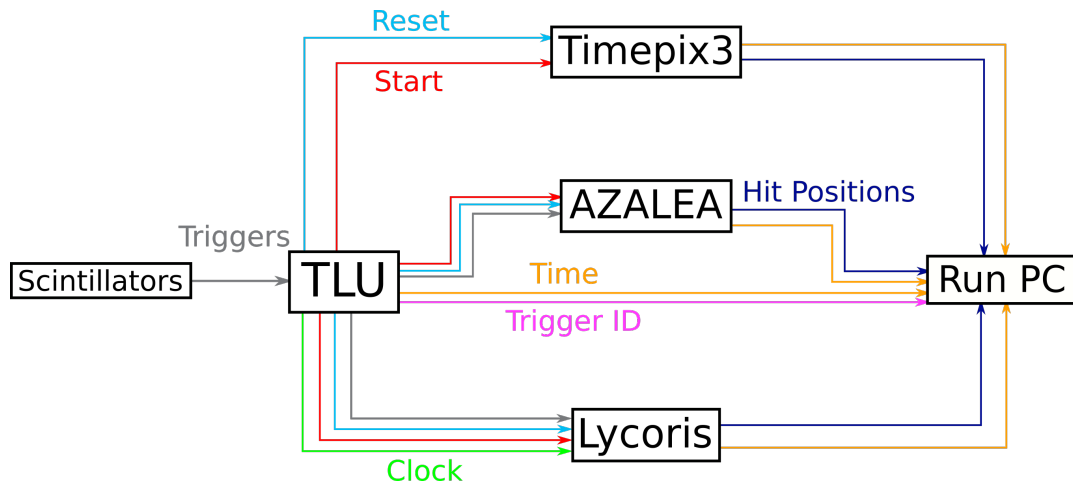


**Figure 8.5** – T24/1 setup during operation with six AZALEA layers located between two Lycoris cassettes.

tance of  $\approx 780$  mm between the two innermost layers if they are not angled to each other as the TPC prototype field cage mentioned in section 6.1 needs to fit in between them. The internal orientation and layout is the same as during the T24 testbeam shown in Figure 8.3.

A picture of the setup within the PCMAG solenoid can be seen in Figure 8.5 showing the front side view of the PCMAG solenoid with the two Lycoris cassettes within the rail system close to the left and right magnet wall and the AZALEA telescope located in the center.

As the PCMAG does not possess any magnet yoke, its stray field radiates into the whole area. This required that the DAQ board was installed at a distance of 1 m above the magnet opening in order to avoid interference from the stray magnetic field. The field of the magnet was also limited to 0.9T as instabilities have been shown to exist during operation at 1 T. All other components are the same as used within area T24 with them being placed at a distance of 4 m to avoid the magnetic field pulling the electronics towards the magnet. The readout PC uses a Hard Disk Drive (HDD) that is sensitive to magnetic fields and as such the readout PC was placed within the hut and connected to the different devices via the LAN patch panels in area T24/1.



**Figure 8.6** – Sketch of the data/signal flow between the different devices used at the test beam setups

## 8.3 Data Taking

Test beam operation includes the operation of all devices mentioned in the area description though with a large focus on the settings needed to operate the Lycoris system as the device under test. A description of the necessary steps of operation of the other devices such as the Timepix3 and AZALEA system is given with a focus on the steps taken in order to ensure a synchronous operation between the different devices as well as the electron beam *uptime* mentioned in section 5.1.2. A sketch of the signals and data transferred to and from the different devices is shown in Figure 8.6.

### 8.3.1 Operation Modes

During test beam, several operation modes were studied. Most of the data presented in this thesis were gathered in what is referred to as the standard operation of the Lycoris telescope which is described below.

In standard operation, the KP*i*X is operated with an acquisition clock period of 320 ns resulting in an event readout time which is equivalent to eight BCC or 20.46  $\mu$ s. The data taking period can be limited to a window ranging from 0 to anywhere within 8191 BCC. An inhibition of triggers can in addition be set anywhere between 0 and 8191 BCC to adjust the starting point of the data taking. The data taking start point and end point are adjusted based on the noise recorded within the system to achieve the best performance. This is explained in more detail in Section 10.4.1.1 though for standard operation the window is

set to start from 4000 BCC and lasts until 8191 BCC resulting in a window of 10.75 ms (see (6.11)) as it has shown to provide the best results in terms of noise with a sufficiently long data taking window.

The system performance was studied in both high gain and normal gain as well as in both external and internal triggering operation. The different triggering and gain modes are described in more detail in section 6.2.2. In both internal triggering and external triggering operation the system records the trigger received from the TLU as an external timestamp for debugging purposes. In external triggering it is used as the trigger signal.

In addition to this, in internal triggering operation, channels which have abnormal behavior or are not connected to a sensor strip are actively disabled before data taking as to reduce potential cross-talk.

### 8.3.2 Synchronization

#### Beam synchronization

The beam structure of the DESY II Test Beam Facility (see section 5.1) *uptime* as well as the *acquisition cycle* operation of KPiX (see section 6.2.2) requires the synchronization of the acquisition window to the *uptime* of the DESY II accelerator. The point in time when the energy within the DESY II synchrotron is at their minimum  $S_{E_{\min}}$  is provided at the test beam facility and the energy within the synchrotron can be described relative to the point of minimum Energy as

$$E = \frac{E_{\max} + E_{\min}}{2} + \frac{E_{\max} - E_{\min}}{2} \sin(2\pi\nu t + \pi/2). \quad (8.1)$$

$E_{\min} = 0.45 \text{ GeV}$  is the minimum energy of electrons within the DESY II synchrotron,  $E_{\max} = 6.3 \text{ GeV}$  is the maximum energy of electrons in the DESY II synchrotron.  $\nu = 1/(T_{E_{\min}}) = 1/80 \text{ ms}$  is the DESY magnet ramp frequency (see section 5.1).

The start of the *uptime* ( $E > E_{\text{cut}}$ ) relative to the  $S_{E_{\min}}$  can therefore be calculated as:

$$\begin{aligned} E_{\text{cut}} &= \frac{E_{\max} + E_{\min}}{2} + \frac{E_{\max} - E_{\min}}{2} \sin(2\pi\nu t + \pi/2) \\ \frac{2E_{\text{cut}} - E_{\max} - E_{\min}}{E_{\max} - E_{\min}} &= \sin\left(2\pi \frac{1}{T_{E_{\min}}} t + \pi/2\right) \\ t &= \frac{T_{E_{\min}}}{4} + \frac{T_{E_{\min}}}{2\pi} \arcsin\left(\frac{2E_{\text{cut}} - E_{\max} - E_{\min}}{E_{\max} - E_{\min}}\right). \end{aligned} \quad (8.2)$$

When taking into account the start-up time  $t_{\text{Start-up}}$  and the trigger inhibition time  $t_{\text{TrigInhibit}}$

of KPix described in section 6.2.2 this leads to:

$$t_{\text{delay}} = \frac{T_{E_{\text{min}}}}{4} + \frac{T_{E_{\text{min}}}}{2\pi} \arcsin\left(\frac{2E_{\text{cut}} - E_{\text{max}} + E_{\text{min}}}{E_{\text{max}} - E_{\text{min}}}\right) - t_{\text{Start-up}} - t_{\text{TrigInhibit}}. \quad (8.3)$$

For the test beam setup the start-up time is typically set to  $t_{\text{Start-up}} = 3000 \cdot T_{\text{acquisition}} = 0.96 \text{ ms}$  or  $t_{\text{Start-up}} = 9000 \cdot T_{\text{acquisition}} = 2.88 \text{ ms}$ . For a chosen beam energy of  $E_{\text{cut}} = 4.4 \text{ GeV}$  this results in a minimum delay, which is performed within the AIDA TLU, of:

$$t_{\text{delay}} \approx 21.28 \text{ ms}, \quad (8.4)$$

before the signal is sent out to the KPix DAQ as the acquisition signal.

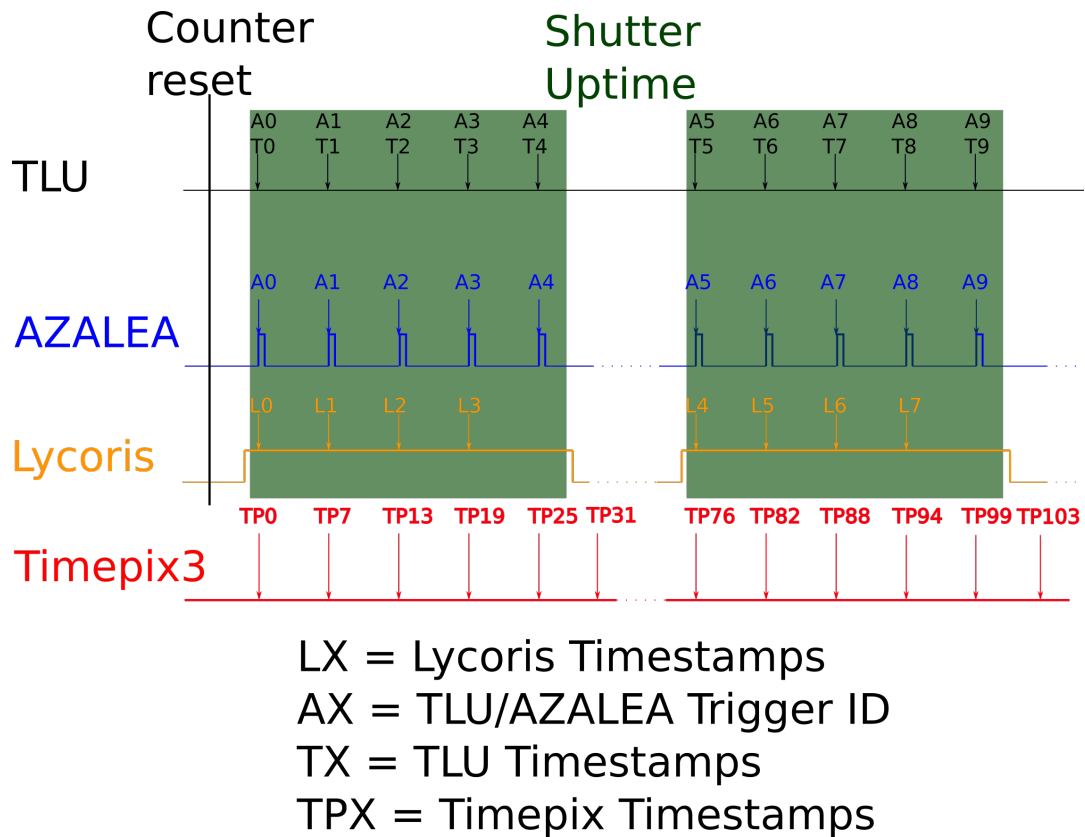
### AZALEA synchronization

As mentioned in section 5.3, the AZALEA telescope possesses a continuous readout with an event readout time of  $t_{\text{FA}} = 230.6 \mu\text{s}$  (see section 5.3) compared to the Lycoris pulsed readout with an event readout time of  $t_{\text{FL}} = 20.48 \mu\text{s}$  (see section 6.2.2).

The KPix system is incapable of reporting back the status of its operation to the TLU meaning that triggers in one system do not immediately result in a trigger in the other system. As such the AIDA TLU ability to assign both trigger ID and timestamp to devices was used to perform an offline synchronization of the two data streams. The methodology of the synchronization is shown in the sketch in Figure 8.7. The TLU receives the triggers from the scintillator crosses of which both the ID and time are stored within TLU data when operated in AIDA Mode (see section 5.2).

The KPix DAQ uses a 64-bit run-time counter that increments based on its 200 MHz system clock which, to avoid asynchronicity, is in lockstep to the 40 MHz clock of the TLU to log every time a new *TLU spill* signal is registered by the DAQ to signify the start of the Lycoris data taking. Whenever a trigger signal is received by the KPix DAQ from the TLU (*TLU trigger*) the value of the 64-bit run-time counter is logged within the event as the trigger time stamp. The data from AZALEA and Lycoris are then matched by using the TLU trigger ID times with the KPix times. As the trigger IDs are the same as the ones stored within the AZALEA DAQ a simply trigger ID number matching is sufficient to combine the two data streams.

All registers are reset to zero at the same time using the TLU  $T_0$  signal which is sent out when starting the data taking operation to ensure that there are no large offsets in the time and trigger ID registers. Furthermore, the synchronicity of the two systems data is ensured



**Figure 8.7** – Sketch of the data synchronization between Lycoris and AZALEA . The TLU records the Trigger ID similar to the AZALEA system while also recording the timestamp of the trigger. The times of the TLU triggers can be compared with the list of trigger times received from Lycoris in order to perform an event by event matching. The Timepix3 operates via internal triggers at a much higher precision and is not limited by external shutters.

by using the TLU shutter to limit the triggers sent out to within the Lycoris data readout. An example of how the matching works can be seen in Table 8.3 .

TriggerID (TLU)	TriggerID (AZALEA)	Time stamp (TLU)	Time stamp (KPiX)	
0	0	A		
1	1	B		
2		C	C	
3	3	D		
4	4	E		
5	5	F	F	<b>Match</b>
6		G	G	
7		H	H	
8	8	I	I	<b>Match</b>
9	9	J	J	<b>Match</b>

**Table 8.3** – Event synchronization between AZALEA and Lycoris via the TLU.

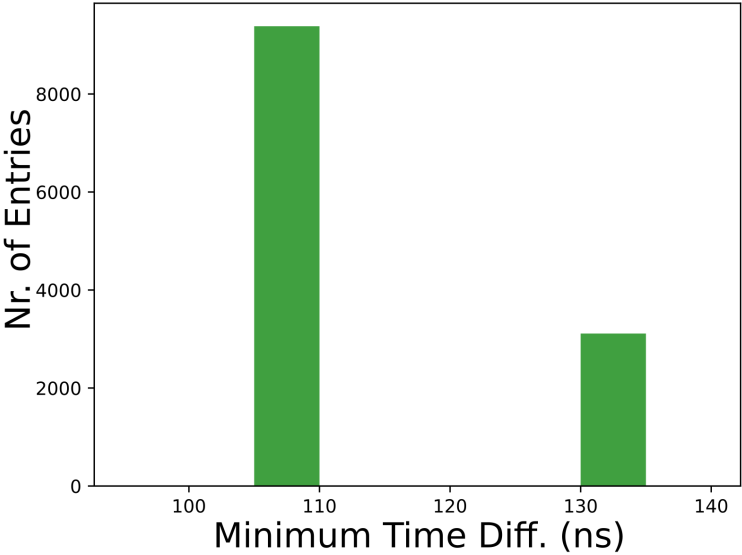
Using this method allows to resolve the time between events of the two systems down to a 25 ns accuracy. This is limited by the clock speed of the TLU which is shown for one data sample in Figure 8.8. The reason that the distribution is not centered at zero is a result of different signal delays which originates from different cable lengths between systems. All events which cannot be matched this way are, as a precaution to avoid introducing a shift in the event matching, omitted from the analysis.

### Timepix3 synchronization

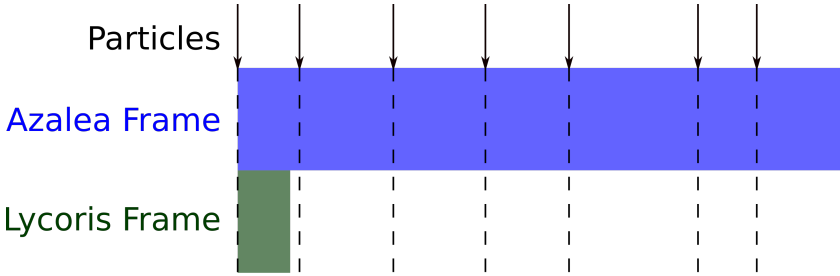
The reason for using the Timepix3 system within the setup stems from the significantly different frame readout times between AZALEA (230  $\mu$ s) and Lycoris (20.48  $\mu$ s) resulting in multiple tracks per event within the AZALEA system. The first particle results in both the AZALEA and the Lycoris system recording the event. While the events can be synchronized, the significantly longer frame readout time of the AZALEA system results in an average amount six particles found within the event. As both of them are only matched on an event by event basis it is not possible to know with certainty whether a track found within the AZALEA system can be found in the Lycoris system. This effect is sketched in Figure 8.9.

The data gathered by the Timepix3 sensor possesses a time resolution of about 1.56 ns based on its operational clock frequency of 640 MHz that can be improved further with

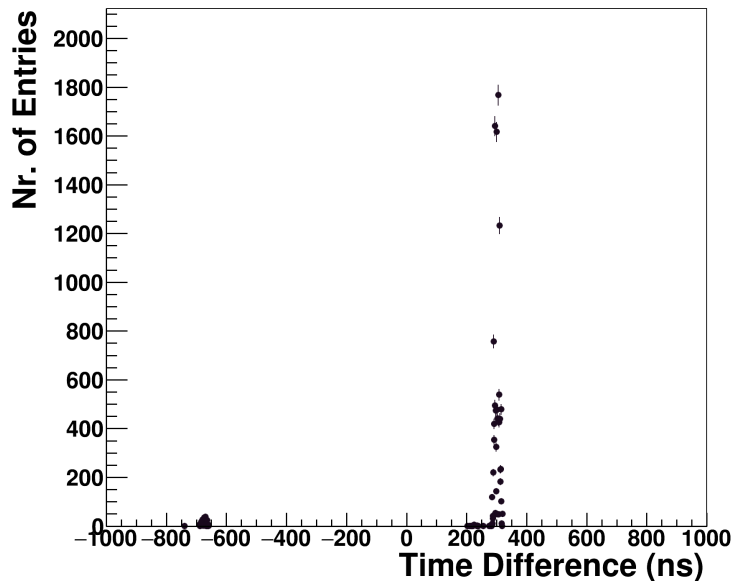




**Figure 8.8** – Minimum time difference between the TLU timestamp and the KPiX timestamp after synchronization.



**Figure 8.9** – Sketch explaining the different number of recorded tracks within the AZALEA system compared to the Lycoris system.



**Figure 8.10** – Time difference between events recorded by the Timepix3 system relative to events recorded by the Lycoris system.

optimized settings [90] which were deemed not necessary for the purpose of assigning the Timepix3 timestamp to the data gathered by AZALEA through spatial matching of AZALEA track with Timepix3 hits [90]. After searching for all AZALEA tracks containing both spatially matched Timepix3 and Lycoris hits, their time difference is determined. The result of this is shown in Figure 8.10. A large peak is visible at around 300 ns. The peak is not at zero due to the differences in cable length and the triggering logic between the two DAQ systems. The secondary peak at around  $-670$  ns is a result of a secondary particle being generated after the electron beam within the DESY II synchrotron has performed one turnaround which takes 976 ns (see Section 5.1).

Not all data samples are available with Timepix3 data and while it improves the clarity of the results the overall message is often not changed. Only in cases where the Timepix3 data is necessary (see section 10.5.4) to achieve a reasonable result is it used.

### 8.3.3 Available Data samples

Data taken at the test beam includes internal triggering data as well as external triggering data. The operational settings of the KPiX impact both the calibration performance and the data taking performance. Typically the same settings used for a data run are used to perform a calibration and the settings were chosen to optimize both the calibration per-

formance and the data taking performance.

The internal triggering data analyzed includes:

- Threshold scan without beam
- Beam data taken with the AZALEA system

fewer runs were taken in internal triggering operation compared to external triggering operation as a result of the systems performance which is explored further in section 10.3.

The external triggering data analyzed in this thesis includes:

- High and normal gain comparisons at noise optimized settings,
- adjustments of the data taking window to investigate impact on noise,
- data with repetitive *auto triggers* without beam to validate the analysis decisions,
- beam data taken with both AZALEA and Timepix3 to determine the inner structure of the Lycoris module and its efficiency,
- beam data taken to investigate the performance of the dedicated track finding and fitting algorithm,
- measurements with a 0.9 T magnetic field to verify the functionality of the system,
- bias scan ranging from 0 V to 150 V to cross check depletion voltage results and investigate impact of bias voltage onto cluster size.

While measurements were performed within the magnetic field of the PCMAG, the data could not be used to verify the expected curvature resolution. At the time of the measurements, the performance of the Lycoris modules was considered insufficient to perform tracking.

The investigation into the Lycoris modules noise performance is presented in section 10.4 with a detailed description of efficiency and resolution based on the measurements with Lycoris as a DUT presented in section 10.5. The results gathered from the standalone track finding and fitting on used to determine the telescope performance are presented in chapter 11.



# Chapter 9

## Event Reconstruction

Multiple different systems are used in the analysis of the Lycoris telescope performance. As a result of the different types of data provided by the different systems each requires its own conversion. In this chapter, the different analysis parts are introduced in section 9.1. The analysis of the Timepix3 and the AZALEA data are based on two generalized frameworks, Corryvreckan[91] and EU Telescope[92]. The analysis for the Lycoris data is tailored for this system and based on programs written in both, C++ and Python, using the ROOT6 data analysis framework [93] and is described in detail in section 9.2. The combination of multiple independent measurements into a common particle track and subsequent alignment of the system using these measurements is explained in detail in chapter 4.

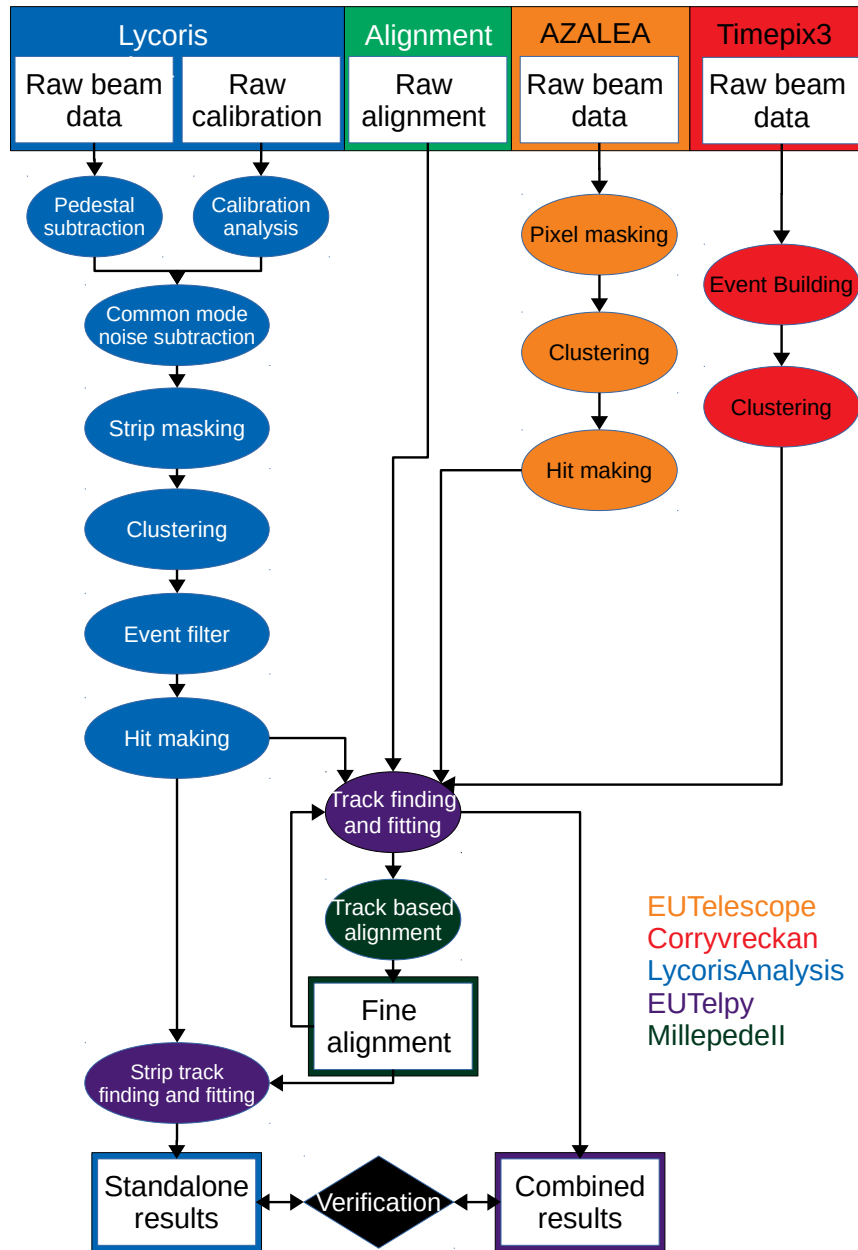
### 9.1 Reconstruction overview

A full analysis of a test beam data set requires multiple steps to get to a final result. These steps depend on the devices and are shown as a flow diagram in Figure 9.1.

The Lycoris data analysis requires two data sets. The run data storing the raw ADC hits recorded in the KPIX channels and the calibration data which is used to convert the ADC values back into physical charge values. In order to extract the ADC to charge conversion, the injected charge and its corresponding ADC response are analyzed in order to know the conversion rate from ADC to fC for the run data. For the run data itself, a pedestal subtraction is performed through which the ADC offset for each channel is determined. This is done in order to take out a potential offset between the different channel ADC values.

Combining the pedestal subtracted run data and the ADC to charge conversion allows a common mode subtraction which is used to remove a cycle based charge offset.

In the next step a strip mask is applied based on how often a single channel is above a



**Figure 9.1** – Flowchart showing a step by step of the analysis for the data sets gathered by the different detectors used during a test beam analysis.

threshold. This threshold is applied in the triggering during internal triggering operation and after data collection during the data analysis for external triggering operation.

Finally, a strip clustering is performed in order to take into account charge shared between multiple strips to improve the resolution. The cluster results are used to perform an event filter to get rid of events with high amounts of noise clusters and lastly perform what is referred to as *hit making* in which the cluster parameters and the local hit parameters are calculated taking into account the Lycoris module orientations to generate global hit coordinates. All correlated clusters are used as Lycoris track input.

The AZALEA system provides zero-suppressed binary hit information. The analysis of the AZALEA data is performed using the standard EUTelescope analysis framework which is explained in more detail in [92]. EUTelescope starts by masking noisy pixels that are, similarly to the noisy strips, defined as pixels that appear above the set threshold of  $S/N_{AZALEA} \geq 4$  more often than:

$$\frac{n_{\text{trigger}}}{n_{\text{event}}} > 0.001. \quad (9.1)$$

After the masking of noisy pixels a pixel clustering which starting from a pixel sums up adjacent pixels into a cluster requiring that the pixels are not masked and are connected to one another via the edge without any specific threshold as the data is zero suppressed.

As a last step a hit making on all reconstructed clusters, to more accurately reflect the local particle hit position, is conducted where the new cluster location:

$$c_{(x,y)} = \frac{1}{N_{\text{pixel}}} \cdot \sum_0^{N_{\text{pixel}}} p_{(x,y)}, \quad (9.2)$$

is the center of gravity of the locations  $p_{(x,y)}$  of all pixels in the cluster. This result is then transformed into global coordinates using the transformations mentioned in section 4.2.1 and are used as AZALEA track input.

Data gathered by the seventh silicon pixel layer, the Timepix3, is used optionally in order to improve time resolution of the different AZALEA tracks beyond the readout frame time of the Mimoso26 as mentioned in section 8.3.2. The Timepix3 data is analyzed using the Corryvreckan analysis framework [91]. The Timepix3 is operated in an internal triggering operation and the synchronization between the data gathered by the Timepix3 and the AZALEA telescope is done by an *event building* in which, using the TLU timestamps, events are build whose start, length and end match the Mimoso26 frame readout time while retaining the timestamp of each trigger. This ensures, that there is no wrong assignment of spatially matched tracks to Timepix3 hits that cannot be part of the same event. The

Timepix3 data is then clustered together and hits are made to be used in the track finding and fitting.

Combining the two data streams using the raw alignment measurements, performed via external tools, allows a combined track finding and fitting using *EUTelpy* [35] which uses the General Broken Lines (GBL) [36] framework. The tracks are then used in order to perform a track based alignment of the sensors using Millepede-II [94]. The new fine alignment is then used to improve the track finding and fitting and a subsequent finer alignment.

When using Timepix3 data, the tracks found by *EUTelpy* for the AZALEA are projected onto the Timepix3 layer where the local track projection is spatially compared to the track. The hit with the smallest distance to the projected track hit is assigned to the track assuming the distance between the Timepix3 hit position  $r_{\text{tpx3}}$  and the projected track position  $r_{\text{track}}$  is below

$$d = |r_{\text{track}} - r_{\text{tpx3}}| < r_{250\mu\text{m}}, \quad (9.3)$$

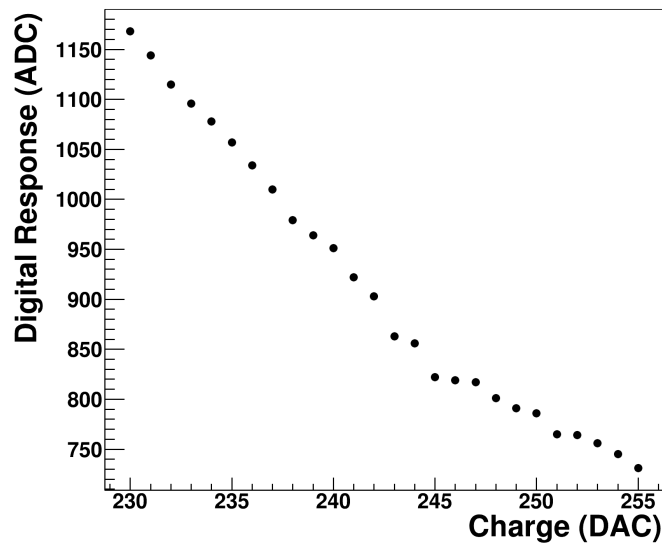
in order to generate a timestamp for the tracks. If no hit within that window is found then the track is discarded.

After multiple iterations of the alignment, the results of the combined track finding and fitting are used in order to determine the performance of the Lycoris modules. The fine alignment is also used as input for the standalone strip tracking with the Lycoris telescope which is used to determine the achievable performance of the telescope as a whole. The results from the two tracking methods are used to verify each others methods.

## 9.2 Lycoris Data Analysis

The Lycoris modules, described in chapter 6, have a 13-bit ADC charge readout and can operate in internal triggering and external triggering (see section 6.2.2). For each of the three different data sets (external, internal and calibration) a dedicated analysis is used. In internal triggering only channels above a set DAC value are recorded as opposed to the external triggering in which all channels save the recorded charge independent of the value. The advantages and disadvantages of the mode and subsequent operational procedures are described in the following sub-sections. Furthermore, calibration results are used in order to determine the performance of individual channels. In the case that the performance of a channel does not meet pre-defined quality criteria, the channel is disabled for the data taking in internal triggering or filtered out of the analysis in external triggering.





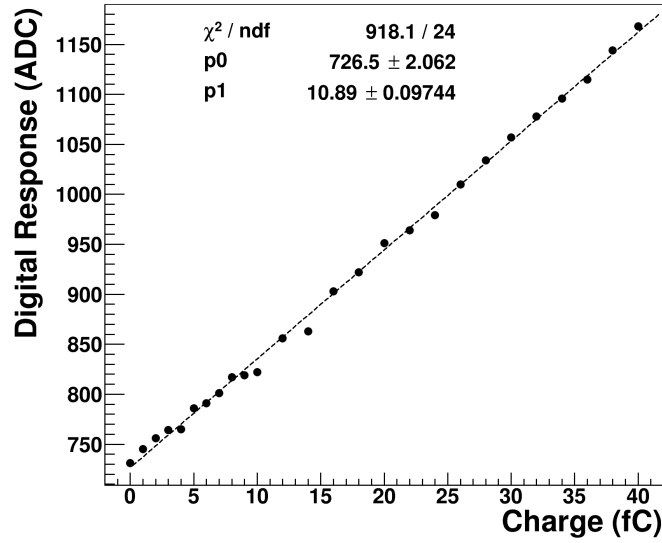
**Figure 9.2** – Single channel charge calibration result in ADC vs DAC. The visible kink at 246 DAC is a result of an internal DAC to voltage conversion that transitions from one method to another. The linear regression does not take this into account and therefore results in a bad fit. It is used to more accurately show the difference between DAC value and fC value.

### 9.2.1 Charge Calibration

Using the calibration circuitry described in section 6.2.2, different charge values are injected into the KPiX channel to look at the ADC response. The calibration is performed separately for every single KPiX, channel and *bucket*. A charge injection range from 255 DAC (0 fC) to 229 DAC (40 fC) is chosen as it covers far into the tail of the distribution of the expected deposited charge. The amount of repeats of each charge injection and the step size between two injections can be chosen. The step size was set to one DAC to be less sensitive to fluctuations during a single injection. No repeats are performed on the data to investigate potential issues with certain DAC injection values that could be masked by repeats in which the mean value is taken. The result of the charge response for a single channel at different DAC injection values is shown in Figure 9.2.

The kink present in the distribution is a result of a change in the *DAC* to voltage conversion within the KPiX control software when moving below a *DAC* value of 246 as described in (6.3). After conversion from *DAC* to charge using the capacitor size of 200 fF and the *DAC* to voltage conversion described in (6.3) this transforms into the digital response to the injected charge shown in Figure 9.3 that no longer has any kinks.

A linear regression is fit to the measurement points in order to convert the measured



**Figure 9.3** – Single channel charge calibration result in ADC vs fC.

charge in ( $Q(ADC)$ ) to coulomb ( $Q(C)$ ) using the slope of the regression

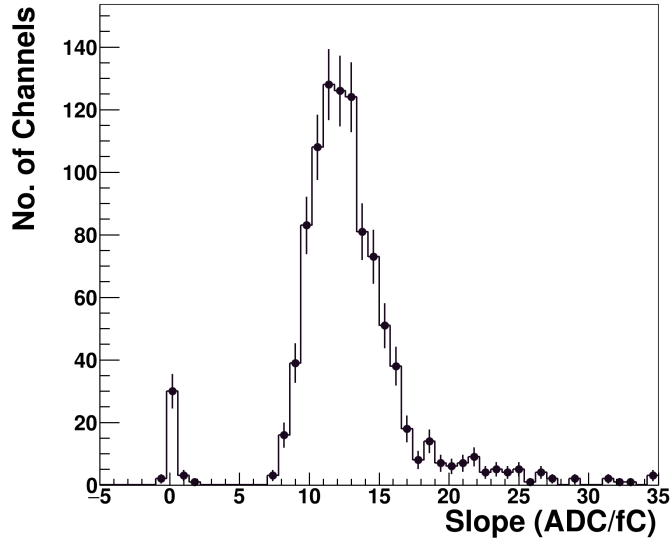
$$Q(C) = \frac{Q(ADC)}{\text{slope}}. \quad (9.4)$$

This is performed for each KPiX , channel and *bucket*. A distribution of slopes for a single KPiX with only *bucket* zero is shown in Figure 9.4. In an ideal scenario the calibration slopes for a single KPiX follow a Gaussian distribution with a mean of around 12–16ADC/fC for high gain and 3–4ADC/fC for normal gain operation which can be attributed to the four times higher capacitance during normal gain operation compared to high gain operation. The distribution shows some outliers which can be the result of incorrect ADC to charge response which is an indicator of faulty channels.

The quality of a channel is defined by the value of the slope as well as the Pearson Correlation Coefficient (*PCC*) which is a measure of the linear correlation between two variables. The coefficient is a number between plus and minus one with a perfect linear correlation showing a coefficient of +1 and a perfect anti correlation at -1. When there is no linear correlation between the two variables the *PCC* will evaluate to zero. In the case that for all X values Y evaluates to the same value then the *PCC* is not defined as both numerator and denominator evaluate to zero.

It is calculated as:

$$\rho_{X,Y} = \frac{E[(X - \mu_X)(Y - \mu_Y)]}{\sigma_X \sigma_Y}, \quad (9.5)$$

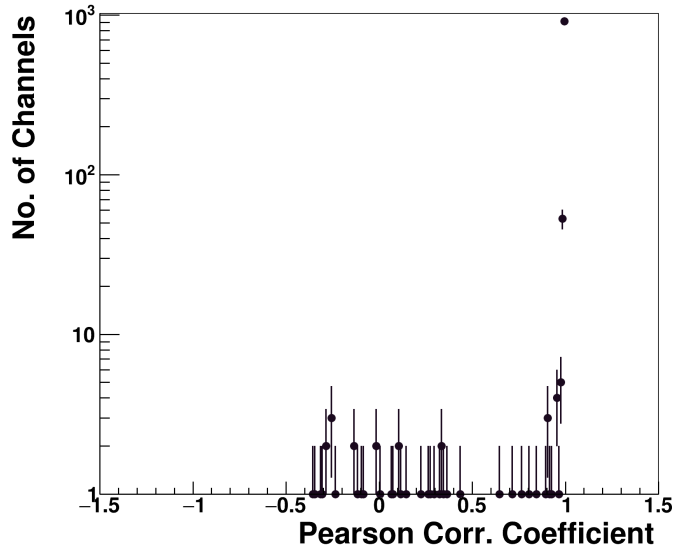


**Figure 9.4** – Slope distribution of *bucket* zero calibrations for all channels in a single KPiX

where  $\mu_{X/Y}$  are the mean and  $\sigma_{X/Y}$  are the standard deviation of  $X/Y$  while  $E$  denotes that the numerator is the expectation of the expression within the parenthesis. A *PCC* distribution for the above slope distribution is visible in Figure 9.5. It shows a large peak at one for 900 channels with a small tail down to 0.95. A cutoff for good channels is chosen as  $PCC \geq 0.9$  as even small fluctuations can impact the *PCC* without having a large effect on the slope. An additional cut is set to slope  $\geq 6.5$  ADC/fC for high gain and slope  $\geq 2$  ADC/fC for normal gain operation. These cuts are used to ensure that in further analysis faulty calibrations are not misinterpreted as potential evidence for signal. For well performing KPiX this results in about a dozen channels being disabled. In the case of internal triggering operation, channels that are below cutoff are disabled during data taking in order to avoid any cross talk between faulty channels and adjacent channels.

## 9.2.2 External Trigger Data Analysis

In external triggering operation the KPiX registers all recorded charge at the time where the DAQ system has received a trigger signal. The system records a large amount of channels which are not expected to carry any signal. The frame read out time of  $T_{FL} = 8 \cdot 2.56 \mu\text{s} = 20.48 \mu\text{s}$  in combination with the recorded particle rate of  $\approx 8$  kHz at the DESY II Test Beam Facility means that for every external trigger signal generated by the triggering scintillators, a particle multiplicity of about one to two is expected to pass through the Lycoris modules



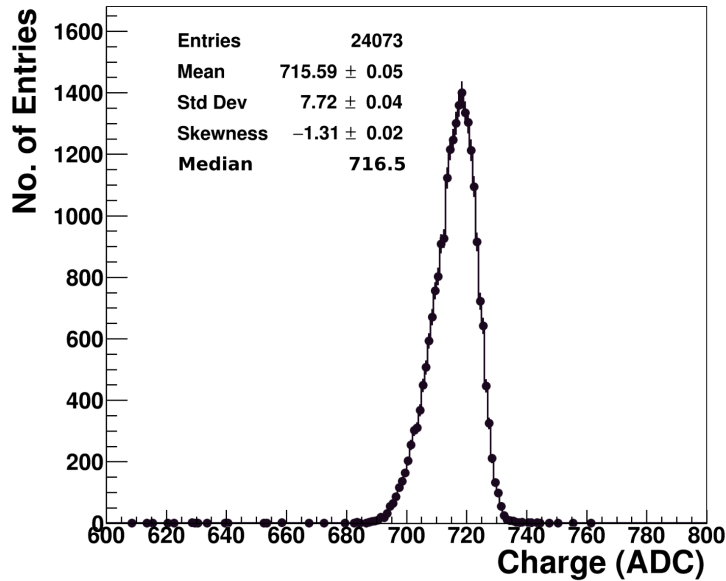
**Figure 9.5** – Distribution of the pearson correlation coefficient for all *bucket zero* calibration results of a single KPiX .

in each readout frame. Each Lycoris module therefore records on average only a few strips with signal with most strips recording only noise. To filter out the noise from the signal multiple analysis steps are needed. They include a pedestal subtraction, common mode subtraction, a hit clustering, as well as the track finding and fitting using the external AZALEA telescope. All measurements presented were taken in either area T24 or T24/1 at the DESY II Test Beam Facility which are described in section 8.1 and section 8.2 respectively.

### 9.2.2.1 Pedestal and common mode subtraction

The raw signal recorded by each KPiX channel is shown in Figure 9.6. For a simple noise distribution the peak is expected to be centered around zero. However, a baseline needs to be subtracted which is referred to as the pedestal. The reason for the pedestal is, that during operation a small dark current is flowing through each channel which is integrated and appears as a charge offset in the output. The asymmetry of the distribution is due to what is referred to as a pedestal drift. This drift is a result of the charge being stored as an analog value before digitization. The drift is compensated for in the following analysis. To determine the pedestal, the median of all raw ADC values ( $ADC_i$ ) is calculated for a given KPiX , channel and bucket

$$Pedestal = median(ADC_i). \quad (9.6)$$



**Figure 9.6** – Raw baseline distribution for channel 290 of S47-2. The pedestal is asymmetric with a tail to lower ADC values which is due to leakage of capacitors resulting in a pedestal drift.

The median is taken instead of the mean as it produces a result that is less sensitive to outliers and more accurately reflects the peak of the distribution but is equal to the mean for a perfect gaussian. The pedestal distribution shown in Figure 9.6 has a skewness of -1.31 which is a result of the aforementioned pedestal drift that is explained below.

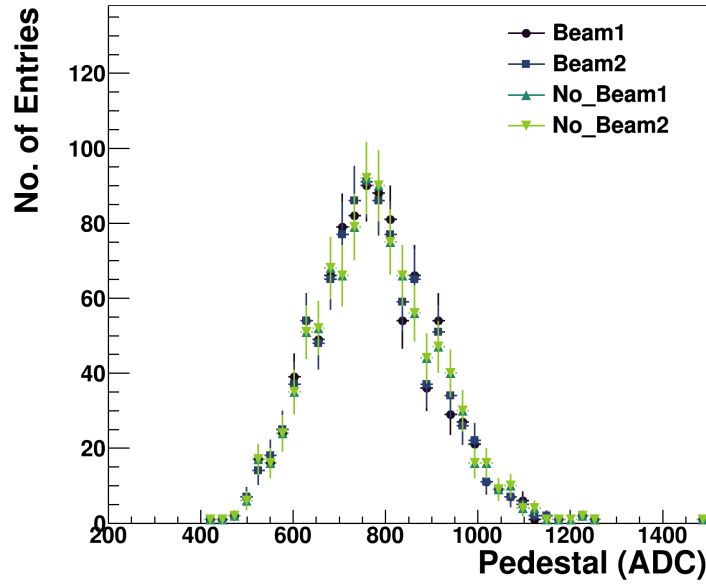
Typically a dedicated pedestal run is taken with dummy triggers and without any signal to avoid skewing the calculated pedestal to higher values. In the measurements taken at DESY II Test Beam Facility, because of the low multiplicity, the pedestal is not affected by channels with beam deposited charge as these are singular outliers and do not skew the median calculated pedestal (see Figure 9.7). As a result, the pedestal is calculated directly from a beam run in the analysis.

In addition to the pedestal itself, the Median Absolute Deviation (*MAD*) of the raw values is calculated which is given by:

$$MAD = \text{median}(|ADC_i - Pedestal|). \quad (9.7)$$

In the case that the *MAD* of a channel is 0, the channel is ignored in the further analysis as its behavior is considered erroneous.

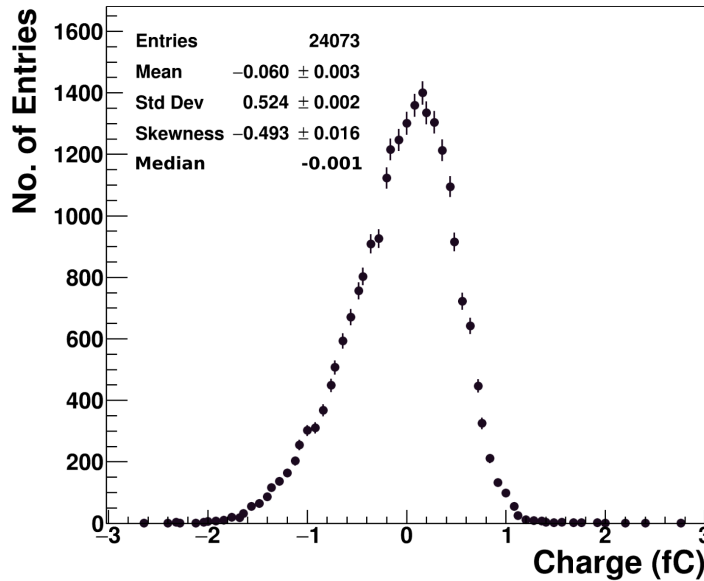
It is found that the charge recorded on the buffer capacitors drift depending on how



**Figure 9.7** – Pedestal comparison for S47-2 for four different runs, two with and two without any beam passing through the Lycoris module. Each entry represents one of the 1024 channels of the KPiX ASIC.

Graph	Mean	RMS
Beam1	$773 \pm 4.1$	$129 \pm 2.9$
Beam2	$775 \pm 4.1$	$130 \pm 2.9$
No_Beam1	$779 \pm 4.1$	$133 \pm 2.9$
No_Beam2	$779 \pm 4.1$	$132 \pm 2.9$

**Table 9.1** – Mean and RMS of the beam and no beam runs of Figure 9.7



**Figure 9.8** – Distribution of all recorded charge after pedestal subtraction and calibration conversion for channel 290 of S47-2.

long the charge is stored before readout. This is an unwanted feature of the current iteration of the KPiX ASIC and as a result, the true pedestal also depends on when the trigger was recorded. Two methods can be used to compensate for this time dependence which would otherwise increase the noise in the system. One can either generate time dependent pedestals by calculating the pedestal for certain time ranges in order to compensate for this drift instead of a single pedestal or, in the case of external triggers, the common mode calculation explained below naturally compensates for the pedestal drift.

After subtracting the pedestal of each channel, the distribution is centered around zero and a conversion from ADC to Coulomb using the calibration results shown in section 9.2.1 is performed.

$$Q_i = \frac{ADC_i - Pedestal}{slope}. \quad (9.8)$$

This results in the charge distribution for all events in a single channel after subtraction of a static pedestal and conversion to Coulomb shown in Figure 9.8. The distribution is also skewed to negative values resulting in a mean which is slightly offset from zero. The median value which is used to calculate the pedestal however is located almost exactly at zero. The width of the distribution is a measure of the noise within the system. In the example here it is shown to be about  $\sigma = 0.5$  fC.

Two contributions are present in this case, the pedestal drift which is due to small leak-

Graph	Mean	RMS
Beam Trigger	$-0.07 \pm -0.003$	$0.47 \pm 0.002$
Forced Trigger	$0.009 \pm 0.001$	$0.15 \pm 0.001$

**Table 9.2** – Statistics for the two different common modes based on the different triggering schemes shown in Figure 9.9.

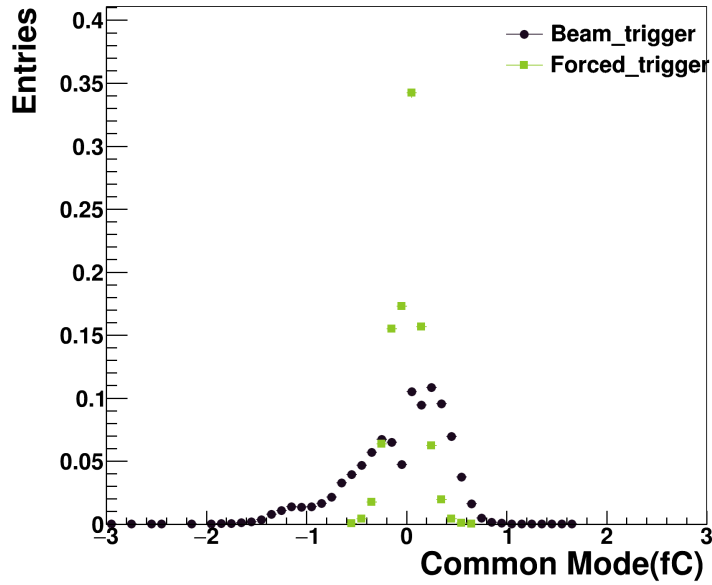
age of the capacitors between charge recording and digitization and the so called called Common Mode (*CM*) noise. The *CM* is an offset that is not specific to each channel like the pedestal but is noise influencing the power line and therefore all channels in the same direction. As a result of the power pulsing the common mode can shift between different *acquisition cycle* and needs to be subtracted separately for each cycle. In external triggering the common mode and pedestal drift affect each channel the same way whereas in internal triggering due to the different triggering times of the channels the pedestal drift differs between channels as the charge is stored for different amounts of time. For the same reasons as before, the *CM* is calculated as the median of all charge  $Q$  for all channels within a given *acquisition cycle* after pedestal subtraction and charge conversion:

$$CM = \text{median}(Q[\text{cycle}]). \quad (9.9)$$

The channels that record beam deposited charge do not have a large impact on the *CM* as the median is not sensitive to single outliers similar to the pedestal calculation and as such is insensitive to the beam deposition due to the low occupancy of beam particles of a single channel.

As all channels trigger at the same time within the *acquisition cycle* in external triggering operation, the drift for each channel is the same which simply results in a change of the *CM*. This is exemplified in the the plots shown in Figure 9.9. Figure 9.9 shows two common mode distributions. The black distribution is data triggered via beam particles using a scintillator. The triggers are random points in time within the *acquisition cycle*. The green distribution are a forced trigger setup in which triggers which are generated internally and are forced to happen at a fixed point in time within the *acquisition cycle*. This means that for forced triggers, the normal calculation of the pedestal already compensates for the pedestal drift as all measurements happen at a fixed point within the *acquisition cycle* resulting in the same amount of drift each time. This is not the case for beam particle and the increased spread of the common mode for beam particles is a result of having to





**Figure 9.9** – Common mode distribution of S47-2 once for beam triggered data with semi random time distribution and once for a forced trigger which results in each channel recording their baseline at the exact same time during the acquisition cycle.

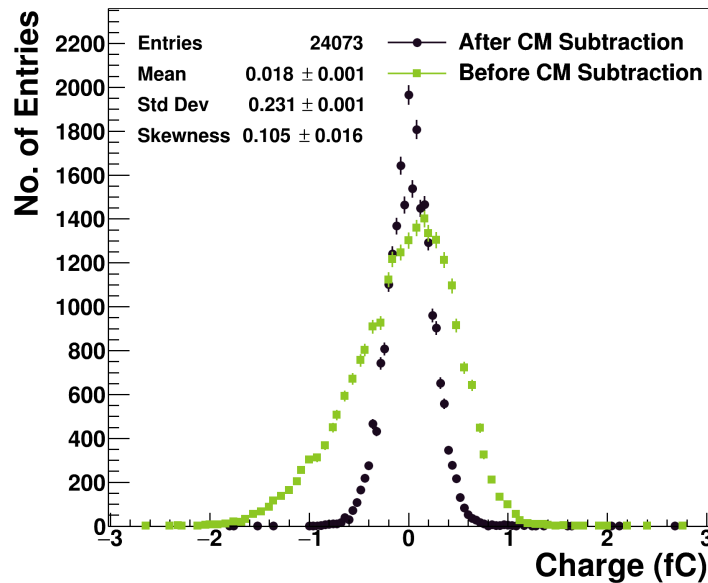
additionally compensate for the pedestal drift.

After subtraction of the  $CM$  of each cycle from the recorded charge, the resulting charge is referred to as the true charge  $Q_i^{\text{true}}$  generated within the Lycoris module which is given by:

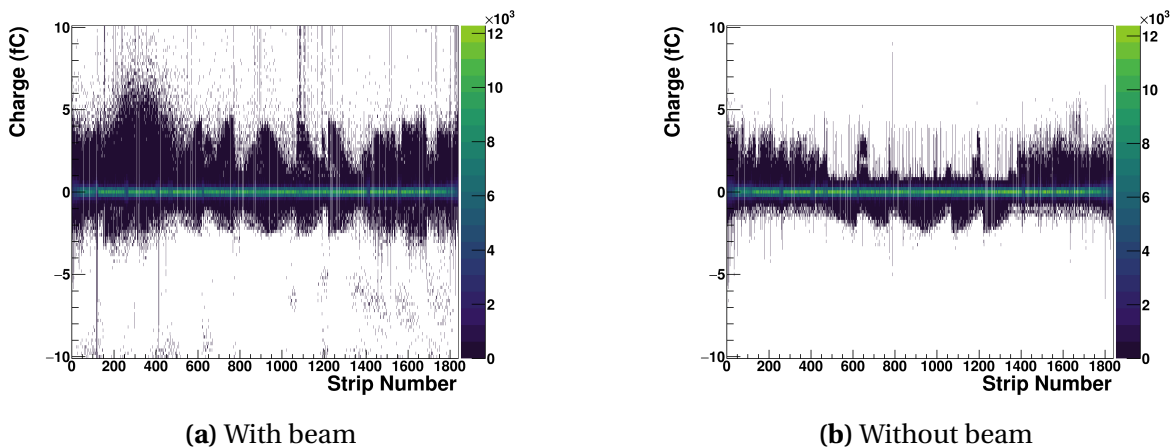
$$Q_i^{\text{true}} = Q_i - CM = \frac{ADC_i - Pedestal}{slope} - CM. \quad (9.10)$$

After  $CM$  subtraction the distribution, shown in Figure 9.10, is significantly less skewed, 0.1 compared to  $-0.49$  previously. In addition the distribution has a significantly reduced width of  $\sigma = 0.22$  fC.

The noise of a channel is calculated in order to determine the Signal over Noise ( $S/N$ ) of each channel as a cut parameter in the hit clustering. The noise of a single channel is calculated as the width of the true charge distribution and is determined by calculating the Median Absolute Deviation ( $MAD$ ) which is related to the sigma of a Gaussian distribution by  $\sigma = MAD \cdot 1.4826$  in order to be less sensitive to potential outliers and to avoid dependence on the fit parameters and fit range.



**Figure 9.10** – Distribution of true charge  $Q^{\text{true}}$  after pedestal subtraction, calibration conversion and common mode subtraction for channel 290 of S47-2. The green curve shows a comparison to the distribution shown in Figure 9.8 before common mode subtraction and the statistics shown here are only for the new black curve with the old stats already shown in Figure 9.8.



**Figure 9.11** – 2D histogram showing the true charge  $Q^{\text{true}}$  recorded versus the sensor strip number once for a run with beam and once for a run without beam.

### 9.2.2.2 Strip Clustering

Figure 9.11 are distributions of the true charge in the case of a high gain measurement recorded in area T24. Figure 9.11a depicts the true charge distribution for a run with beam while Figure 9.11b is the same type of distribution just without any beam passing through the Lycoris module. One can see an excess of charge located around the strips numbered 200 to 400 which is not present in the run without the beam. The other excesses are fluctuations and not visible in different runs. Furthermore, as there are channels in the charge distribution without beam (see fig. 9.11b) that are not perfectly symmetric there must be a source of noise that is not compensated for within the analysis. This is investigated further in section 10.4.1.

While the impact of the beam can already be seen in the plots, in order to perform tracking and determine the Lycoris module performance, a strip clustering is required to correctly reconstruct the particles position. It is important to identify the cases in which charge is split between multiple strips in order to accurately reconstruct the deposited charge and position of the particle. This is done through the clustering algorithm described below.

After calculation of the true charge Signal  $S = Q^{\text{true}}$  and the noise  $N$  for each channel, the strip significance  $(S/N)_{\text{strips}}$ , which is the parameter used to cut on whether a strip is going to be part of the clustering algorithm or not, is calculated. The clustering loops over all strips and searches for the strip with the largest  $S/N$  which is referred to as the *seed*. Starting at the *seed*, the clustering algorithm looks for strips adjacent to the *seed* and adds them to a cluster object. This is continued in both directions until either there are no longer any strips adjacent to the cluster, or the next strip has higher  $S/N$  than the previously added strip. In such a case this strip is expected to be part of a separate cluster as an increase in  $(S/N)_{\text{strip}}$  with increased distance to the *seed* is unexpected.

After finding a cluster, the parameters of its strips are used to calculate the cluster charge

$$Q_{\text{cluster}} = \sum_{i=1}^{N_{\text{strips}}} Q_i, \quad (9.11)$$

the significance

$$(S/N)_{\text{cluster}} = \frac{\sum_{i=1}^{N_{\text{strips}}} Q_i}{\sqrt{\sum_{j=1}^{N_{\text{strips}}} N_j^2}} \quad (9.12)$$

and charge weighted hit position on the Lycoris module

$$v = \frac{\sum_{i=1}^{N_{\text{strips}}} y_i Q_i}{Q_{\text{cluster}}}. \quad (9.13)$$

$N_j$  is the hit noise,  $Q_i$  is the hit charge and  $y_i$  is the local hit position.

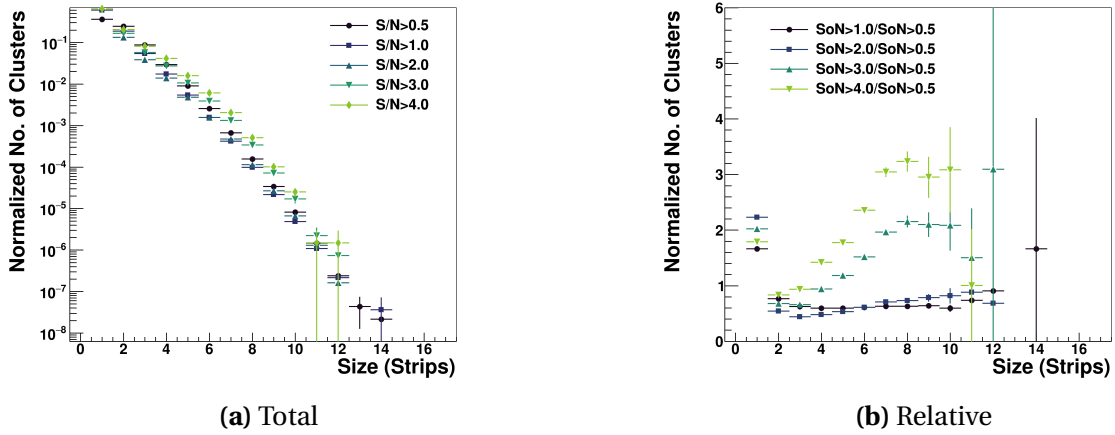
The clustering repeats the procedure with the next most significant strip that is not part of a cluster as *seed* until there are no unassociated strips left. Another significance cut on all clusters  $(S/N)_{\text{cluster}} \geq 4$  is applied to cut out noisy clusters. All clusters that pass this cut are treated as signal in the further analysis and are used as input into the track finding and track fitting algorithm described in detail in section J.

The  $(S/N)_{\text{strip}}$  cut value was determined by looking at the cluster size distribution for different values of  $(S/N)_{\text{strip}}$ . In the case that the cut is set too loose, more noise strips are expected to be reconstructed as clusters. While these are filtered out by the cluster quality cut, an increase in the size of the signal clusters is expected because of the addition of noise strips to the cluster. This shifts the charge weighted measured position away from the true position and decreases the achievable resolution. When the cut is too tight, charge spread via diffusion or the *floating* strips might fall below the cut value. This results in two strip clusters being reconstructed as one strip clusters, also shifting the charge weighted position away from the true position and reducing the resolution.

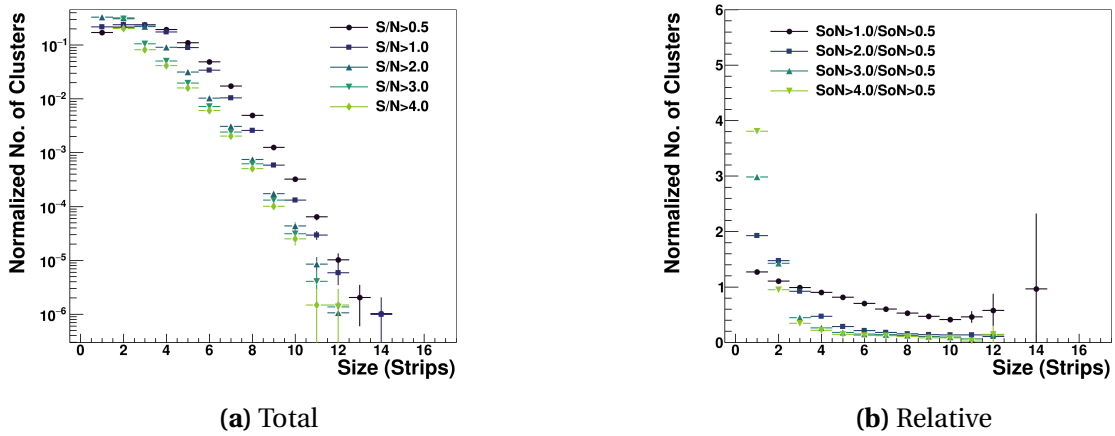
Figure 9.12 shows the distribution for all reconstructed clusters normalized to the total number of entries once in total numbers and once relative to the number of clusters reconstructed for the lowest  $(S/N)_{\text{strip}} > 0.5$  cut. This plot makes it seem that tightening the strip cut value increases the number large clusters relative to the number of small clusters. This is a result of the normalization to the total number of entries, which varies significantly without any cluster cut. The number of entries for different cuts are listed in Table 9.3. When requiring that the reconstructed clusters fulfill the final quality cut of  $(S/N)_{\text{cluster}} \geq 4$ , this results in the distribution shown in Figure 9.13. This shows the expected relation between the cluster size and the strip cut value.

Ignoring cases in which a large angles or delta electrons results in a larger cluster size, a roughly equal amount of single and double strip *signal* is expected, which is given for a  $(S/N)_{\text{strip}} \geq 2$  cut and thus is chosen for the analysis.

Clustering performed using  $S/N_{\text{cluster}} \geq 4$  and  $S/N_{\text{strip}} \geq 2$  on the  $Q^{\text{true}}$  distribution shown in Figure 9.11 results in the cluster distribution depicted in Figure 9.14. The distribution shows the number of clusters versus the local position on the Lycoris module once for a run with beam Figure 9.14a and once for a run without any beam Figure 9.14b. In the



**Figure 9.12** – Number of clusters versus the size of the reconstructed cluster, normalized to the total amount of reconstructed clusters, for different input  $(S/N)_{\text{strip}}$  cut values without any cut on the final reconstructed cluster significance.



**Figure 9.13** – Number of clusters versus the size of the reconstructed cluster, normalized to the total amount of reconstructed clusters, for different input  $S/N_{\text{strip}}$  cut values with a cut on the combined cluster Signal over Noise of  $S/N_{\text{cluster}} \geq 4$ .

Graph	Clusters(All)	Clusters( $S/N_{\text{cluster}} \geq 4$ )
$S/N_{\text{strip}} > 0.5$	$4.63 \cdot 10^7$	$9.81 \cdot 10^5$
$S/N_{\text{strip}} > 1.0$	$2.78 \cdot 10^7$	$1.02 \cdot 10^6$
$S/N_{\text{strip}} > 2.0$	$6.17 \cdot 10^6$	$9.45 \cdot 10^5$
$S/N_{\text{strip}} > 3.0$	$1.36 \cdot 10^6$	$7.38 \cdot 10^5$
$S/N_{\text{strip}} > 4.0$	$6.78 \cdot 10^5$	$6.78 \cdot 10^5$

**Table 9.3** – Number of entries for different strip cuts for the two plots showing the normalized number of entries versus the size of the reconstructed cluster. Once for all reconstructed clusters and once only for clusters with  $S/N_{\text{cluster}} \geq 4$  which is the final quality cut that was chosen.

beam run, a large amount of clusters centered around  $\nu = -30$  mm with a width of 10 mm is present which corresponds to the beam spot location with the width corresponding to the opening of the secondary collimator described in section 8.1.

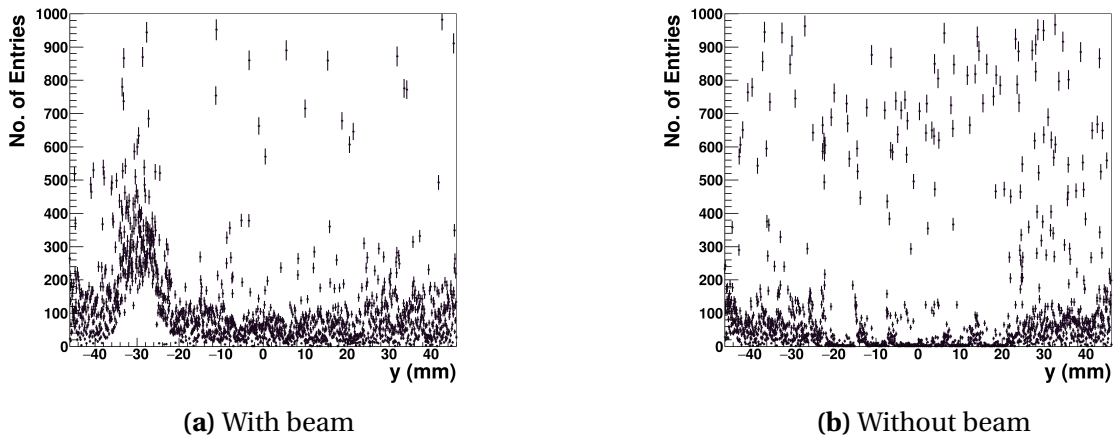
Similarly to Figure 9.11, the edges show large amounts of clusters that do not correspond to any known signal source. They are present in both runs indicating non-Gaussian noise that is not fully filtered out by the  $(S/N)_{\text{strip}} \geq 2$  and  $(S/N)_{\text{cluster}} \geq 4$  cuts. The source of this noise is investigated in more detail in section 10.4.1. This type of noise presents an issue for track reconstruction as the edge noise is present in all Lycoris modules resulting in spatially correlated noise that can result in the reconstruction of fake tracks which is investigated in detail in section 11.2.

### 9.2.3 Internal Trigger Data Analysis

The KPiX internal trigger data analysis is similar to the external triggering analysis once data taking has concluded with only a minor difference in the pedestal subtraction. The largest difference in the analysis stems from the method of data taking focused around issues which are present in the current version of the KPiX ASIC.

If the amplified charge recorded within a channel is above a threshold which can be set via an 8-bit DAC, then the channel stores the charge in the analog buffer capacitor. This allows the system to record only the relevant channels, drastically reducing the amount of noise that is recorded.

Unfortunately, a known flaw of the current version of the KPiX ASIC used for the Lycoris modules is the presence of so called *monster events* [95]. In internal triggering operation,



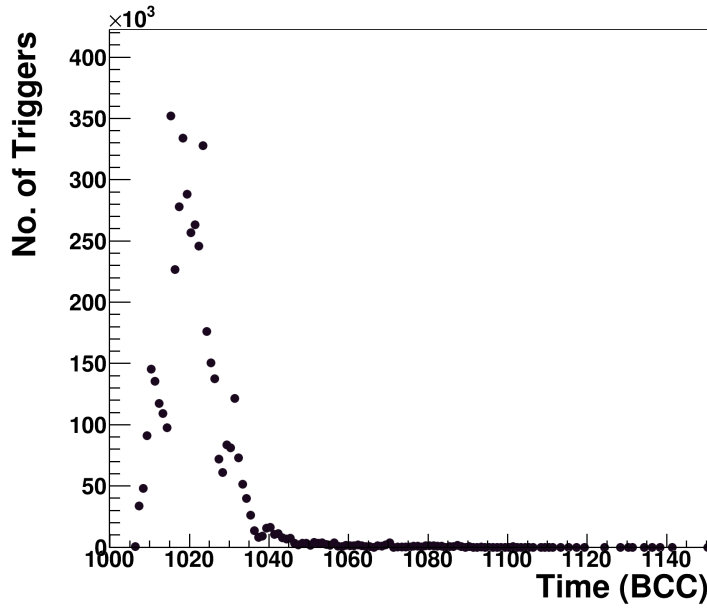
**Figure 9.14** – Histogram showing the position distribution of all clusters with  $S/N_{\text{cluster}} \geq 4$  once for a run with beam and once for a run without beam. The single channels with large amounts of entries are noisy channels which are not masked here.

the reset signal used to discharge the input capacitor and which is issued at the end of integration results in a spurious signal coupled into several adjacent channels. At a low enough threshold these channels will trigger at reset time of the original channel and in turn will cause delayed triggers in more channels. This can cascade out until all channels have triggered. The malfunction is particularly troublesome for the tracker because of the requirement for low thresholds.

A *monster event* is similar to an event in which the internal triggering threshold of the system was set below the noise value of the system and they both have the same effect on the systems performance in that almost all triggers recorded by the system do not correspond to any physical signal. The difference between the two is that *monster events* can occur even at extremely high threshold values.

*Monster events* can result in a situation in which almost every single channel has recorded on average one trigger per acquisition meaning each channel has recorded something without any known input source. Once every channel has triggered at least four times, no further triggers are allowed by the system as the KPiX ASIC is only capable of storing four analog signals which is necessary due to the power pulsing operation of the chip (see section 6.2.2) [29].

Figure 9.15 shows the time distribution of internal triggers within the KPiX when a monster event occurs. No triggers are visible before 1000 BCC because of the trigger inhibition that was set. Shortly after the inhibition drops, a large amount of triggers are recorded in a short time frame of about 40 BCC after which the amount of triggers drop close to zero sim-



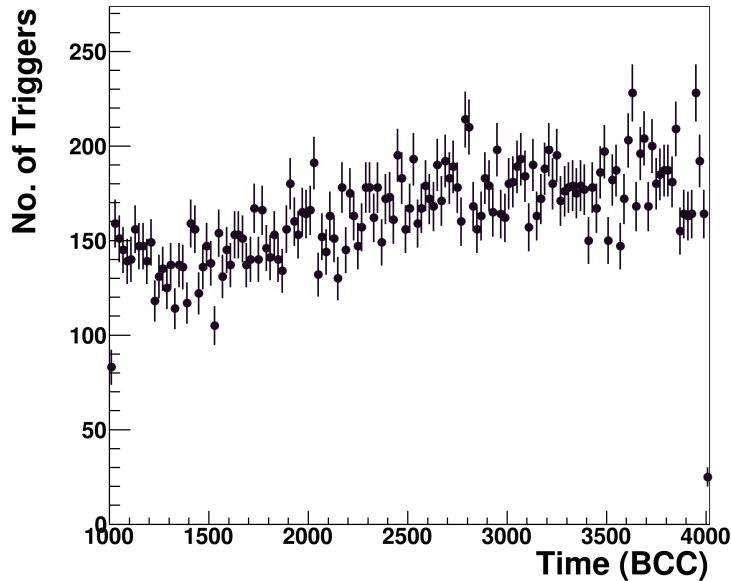
**Figure 9.15** – The time distribution of triggers in an acquisition in units of BCC without beam. A trigger inhibition was set to 1000 BCC resulting in no triggers being registered before that. The peak is a result of a large amount of triggers which only starts lowering because each channel reaches the maximum amount of triggers allowed.

ply because no more triggers can be accepted because almost every channel has already triggered. In an event without monster events and an internal triggering threshold barely above the noise level, the distribution of trigger times is expected to be equally spread over the whole active time of the KPiX as shown in Figure 9.16. For a signal to be visible it has to arrive within  $102.4 \mu\text{s}$  after the system has dropped the trigger inhibition as otherwise the entire system has already reached the maximum trigger capacity in *bucket zero* which is similar for the other *buckets*.

This type of behavior is expected when the trigger threshold for the operation is set below the noise level of the system. The threshold operated during this data sample was set to 230 DAC in normal gain operation which is equivalent to a voltage threshold of  $V_{\text{thresh}} = 2.3\text{V}$  (see (6.3)). As KPiX measures negative pulses relative to  $U_{\text{ana}}$  (see section 6.2.2), this results in a trigger threshold of  $\Delta U = 200\text{mV}$ . The required deposited charge value is calculated using the capacitance in normal gain  $C_{\text{normal}} = 400\text{fF}$  and the shaper amplification  $A = 24.7$  resulting in a required minimum deposited charge value of

$$Q_{\text{dep}} \geq C \cdot \left( \frac{U_{\text{ana}} - U_{\text{thresh}}}{A} \right) = 400\text{fF} \cdot \frac{0.2\text{V}}{24.7} \approx 3.23\text{fC}, \quad (9.14)$$





**Figure 9.16** – The time distribution of triggers in an acquisition in units of BCC with beam and *monster event* suppression. A trigger inhibition was set to 1000 BCC resulting in no triggers being registered before that.

in order to trigger. This value is above the most probable charge deposition of a MIP in  $320\ \mu\text{m}$  silicon which is at around  $3\text{fC}$ .

In order to operate the KPiX in internal triggering operation, either a much higher effective threshold has to be chosen in order to record data reliably which impacts the efficiency of the system, or steps need to be taken by which the induction of *monster events* can be suppressed.

This suppression is done via a so called *channel masking* in which channels that have been identified as potential causes are disabled. The internal triggering threshold of the ASIC is increased until *monster events* are no longer occurring and any channel that still records triggers 10% of the time at such a high threshold is disabled. The threshold is then lowered until a threshold is reached that once more allows the creation of *monster events*. Slightly above that threshold all channels that record triggers in 10% of all acquisitions are disabled and the procedure continues. The procedure can be done until a sufficiently low threshold is reached. For internal triggering operation in a threshold of about  $241\text{DAC} = 1.45\text{fC}$  is required in order for the expected shared charge in a floating strip deposition to be above the threshold. Disabled channels however also negatively affect the system efficiency and spatial resolution by increasing the pitch between active readout channels. A balance

has to be found in which the system can be operated at sufficiently low effective thresholds with enough active channels.

Details of this operation and its results are shown in section 10.3. Once the data has been procured, the analysis procedure is the same as described previously for the external trigger analysis (see section 9.2.2) with two exceptions:

- The common mode subtraction is unable to correct for drifting pedestals as channel triggers are distributed over the entire active time of the system and as such each channel has a different pedestal shift value requiring a time dependent pedestal subtraction.
- The system records both external trigger timestamps as well as internal trigger timestamps allowing the search for the minimal time residual between the two trigger times in order to filter out noise by removing events that cannot be assigned to an external trigger.

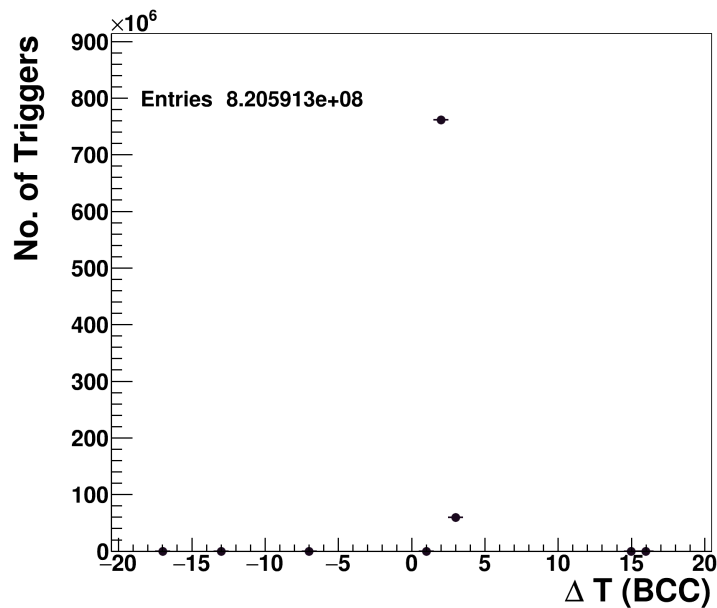
The second item is described in more detail below.

### External trigger comparison

Each internal time stamp is specific to the triggered channel unlike the external time stamps that are stored as a list of times that were received by the DAQ during the acquisition cycle. Each internal timestamp is compared with the whole list of external timestamps for a given cycle, trying to find the minimum time difference given by:

$$\Delta T = \min(t_{\text{external}} - t_{\text{internal}}). \quad (9.15)$$

The correct time assignment is determined based on a  $\Delta T$  distribution for an externally triggered system that is depicted in Figure 9.17. In external triggering an internal timestamp is only recorded when an external timestamp is recorded, resulting in a large peak at 2 to 3 BCC time different. The shift of the peak off zero can be explained by slight differences when in the operation the external time stamp is recorded relative to the internal time stamp. The reason for the two peaks is that depending on where within a cycle the trigger is received the actual recording of the external trigger can fall within the next cycle. There is an offset of about half a BCC meaning that depending on where within the 1 BCC time window the trigger is received it is attributed to one of two BCC values. The times recorded outside of the peak should not be present and indicate a bug within the DAQ system. This is not considered an issue in normal operation as the main peaks have about  $10^8$



**Figure 9.17** – Minimal difference value between the internally record channel trigger time and the externally recorded scintillator trigger signal time in externally triggered beam operation. Except for single triggers, all triggers are located in the two main peaks.

entries. The channels lying outside of the peak are single entries.

Using this information, a cut on all internally recorded triggers is performed in which they are required to be recorded 2 to 3 BCC before an external trigger timestamp is registered. If triggers fall outside this window they are considered noise.

### 9.3 Summary

A full analysis of all test beam data gathered by the different devices is needed to determine the sensor performance. Each of the devices has their own analysis steps which are unique to the data being provided. The analysis of the Timepix3 and AZALEA data are performed in their own dedicated Corryvreckan and EU Telescope analysis frameworks which are described in more detail in [91] and [92].

The analysis of the data gathered by Lycoris on the other hand is made from the ground up and split into three different parts, the charge calibration, the external trigger data analysis and the internal trigger data analysis. In order to convert the the ADC values to physical charge the slope of a dedicated calibration run is extracted and used. As the performance of channels can vary significantly only channels with a slope of around  $12 - 16 \text{ ADC} / fC$

in high gain and  $3 - 4ADC/fC$  in normal gain as well as a pearson correlation coefficient greater than 0.9 are considered to ensure that faulty calibrations are not misinterpreted as potential evidence for signal. All channels not fulfilling these criteria are removed from the analysis. The overall calibration performance of the KPiX chips in different settings and environments are presented in section 10.2.

The analysis of the run data depends on the triggering operation KPiX is operated in. All steps presented in the section 9.2.2 also apply to internal triggering data including a pedestal subtraction, charge conversion and common mode subtraction in order to filter out common mode noise. In the case of external triggering the common mode also compensates for the pedestal drift present within KPiX which requires a dedicated time dependent pedestal subtraction for internal triggering data. It is shown that the beam itself has a negligible impact on the overall results which allows the avoidance of dedicated pedestal runs. The noise that is calculated as  $\sigma = MAD \cdot 1.4826$  of the true charge distribution  $Q^{\text{true}}$  is then used in the strip clustering algorithm as a threshold for the different channels. Once the true charge distribution is determined, all channels are clustered together in order to be used as input for the track finding and fitting algorithm described in Section 4.2. As there is no threshold applied in data taking, the optimal threshold for good clustering efficiency was determined to be  $(S/N)_{\text{strips}} \geq 2$  and  $(S/N)_{\text{clusters}} \geq 4$  as they provide the best clusters in terms of efficiency, fake rate and average cluster size. The results gathered from the external triggering data are presented in section 10.4, section 10.5 and chapter 11.

Data gathered using the internal trigger uses the same steps as the external triggering data, though a known flaw within the KPiX can result in large amounts of noise triggers even at extremely high thresholds in what is referred to as a *monster event* making the system unusable for operation at the test beam. A dedicated *monster event* suppression has to be applied in order to even make the system usable at the test beam which results in the disabling of large amounts of channels in order to lower the effective internal triggering threshold to improve the overall efficiency. Noise hits can further be filtered out through a comparison in the minimal trigger time difference between the internal and external trigger timestamps which, for signal, has to be between 2 and 3BCC. The difficulties and the results when working with internal triggering are presented in section 10.3.

# Chapter 10

## Module Performance

As mentioned in chapter 7, a total of 22 functional Lycoris modules have been assembled at DESY. An overview of their performance is presented here.

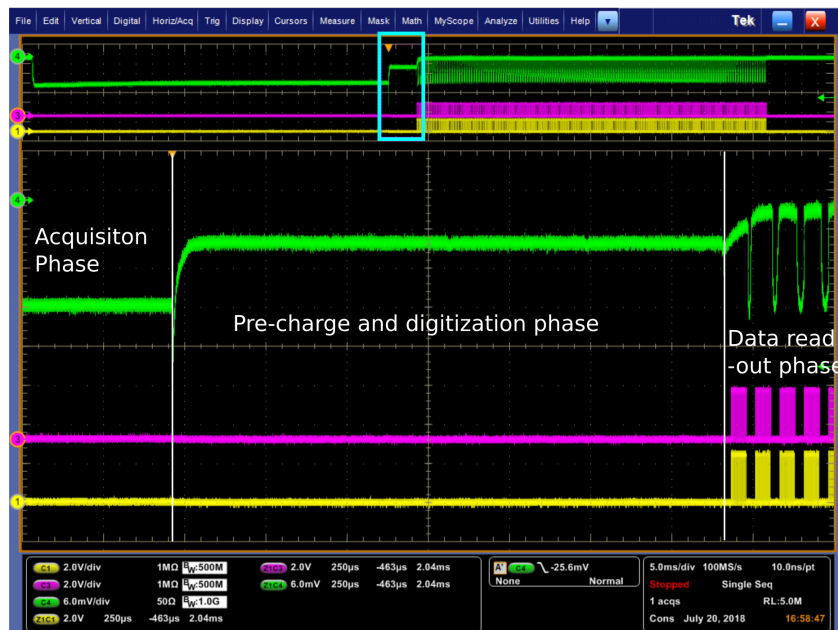
### 10.1 Operational Performance of the KPiX

Each Lycoris module is equipped with two KPiX ASICs which have shown asynchronicity in operation. This manifests itself in an asynchronous data readout from the ASIC. This resulted in crashes in an older version of the DAQ when reading out multiple KPiX ASICs. The behavior was specific to certain KPiX ASICs. Some KPiX can be operated together while some cannot. This issue was not encountered in previous generations of the KPiX ASIC and has been investigated in detail here.

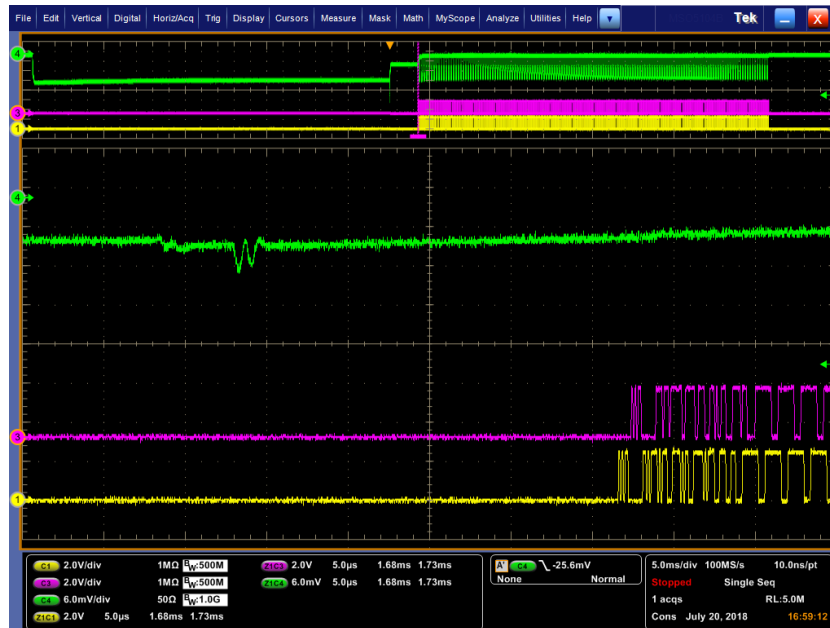
To investigate, oscilloscope probes were connected to the different signal lines of two KPiX which are unable to be operated together. These lines are shown in pink and yellow in the following plots. A current probe is connected to the analog supply line in order to visualize the different KPiX operational states. The analog supply line current is shown in green. A KPiX operation phase switch is visible in that the different changes draw different operational currents.

Anomalies were found for many different KPiX. This is exemplified here by the S59-1 and S59-2 data readout. Shown in Figure 10.1 is one oscilloscope picture with the aforementioned probes attached. No particular asynchronicity is visible on this time scale in none of the signal or supply lines.

A more detailed look, as shown in Figure 10.2, reveals that while both KPiX appear to go through the same phases at the same time, the two systems are not fully synchronous in that the data readout of both KPiX is shifted slightly relative to each other in time. As both



**Figure 10.1** – Probe of the analog current (green) and the data readout lines of KPiX S59-1 (pink) and KPiX S59-2 (yellow) during an *acquisition cycle*. The small box on top of the picture reflects the full *acquisition cycle* with the azure box showing the zoomed area of the *acquisition cycle* that is shown in detail in the larger picture.



**Figure 10.2** – Probe of the analog current (green) and the data readout lines of KPiX S59-1 (pink) and KPiX S59-2 (yellow) during an *acquisition cycle*. The zoom is focused on the end of the digitization phase and the start of the readout phase of the *acquisition cycle*.

KPiX run on the same analog voltage lines (see section 6.5.1) the green line in the figures show the combined current required for both ASICs. A double peak structure is visible in the analog current. The peak signals the end of the digitization phase and start of the data readout phase. The time difference between the two peaks align with the time difference of the two data readout streams meaning that the KPiX end their digitization phase at different points in time.

No further abnormal structures were be observed within the acquisition cycle and the KPiX appear to be synchronous until the end of digitization. This strongly hints to an issue in the pre-charge and digitization phase. Tests with the system showed, that by reducing the software induced delay between the end of acquisition phase and the start of the pre-charge and digitization phase to a value below 16 clock cycles, the asynchronicity of the system could be resolved allowing multiple KPiX to be operated together.

The reason for this behavior is not understood. It is suggested to lie within the digital core of the KPiX ASIC but was not seen in the previous iterations of the KPiX ASIC and no changes in the digital core have been implemented in between the versions. While the problem was solved by reducing the delay between the two phases, an additional safety mechanism was added in which the DAQ can continue running even when data readout

is asynchronous. Such events are flagged by the DAQ and, while not used for any data analysis, can be used to further investigate the cause of this behavior.

## 10.2 Calibration Performance

The digital response to charge injection in calibration is taken in order to determine the quality of a Lycoris module (see section 9.2.1). Typically, calibrations are performed for all four of the *buckets*, the analog storage capacitors (see section 6.2.2), within the KPiX ASIC. During tests of the system it was noticed, that in most cases no *bucket* beyond *bucket zero* showed acceptable calibration performance which was unexpected.

The digital response for different injection values of a single channel of KPiX S59-1 for *bucket zero* and *bucket one* is shown in Figure 10.3a and Figure 10.3b respectively. *Bucket zero* shows the expected linear digital response to the injected charge. *Bucket one* however shows, that not only is there no linear increase with increased injection charge, the digital response is the exact same value for different injection charge. Under normal circumstances slight fluctuations based on noise in the Wilkinson ADC are expected, indicating something is wrong with data writing or reading within the KPiX. This behavior henceforth referred to as *stale data*.

The distribution of all slopes for KPiX S59-1 is depicted in Figure 10.4. It shows that a large amount of channels with slope of zero is present for most higher *bucket* channels making them unusable for data taking. It can be identified whether the issue is the same for all channels by looking at the distribution of the Pearson Correlation Coefficient (PCC (9.5)) which is not defined in the case that for each value of  $x$  the value of  $y$  is the exact same as is the case for *stale data*. The different PCC values are shown in Table 10.1. *Bucket zero* has no channels with *stale data* while the rest of the *buckets* all have more than 700 channels recording *stale data*. This is the same for all other KPiX, indicating that the issue is limited to higher *buckets*.

<i>Bucket</i>	No. of <i>stale data</i> channels
0	0.0%
1	84.8%
2	74.6%
3	77.1%

**Table 10.1** – Pearson correlation entries



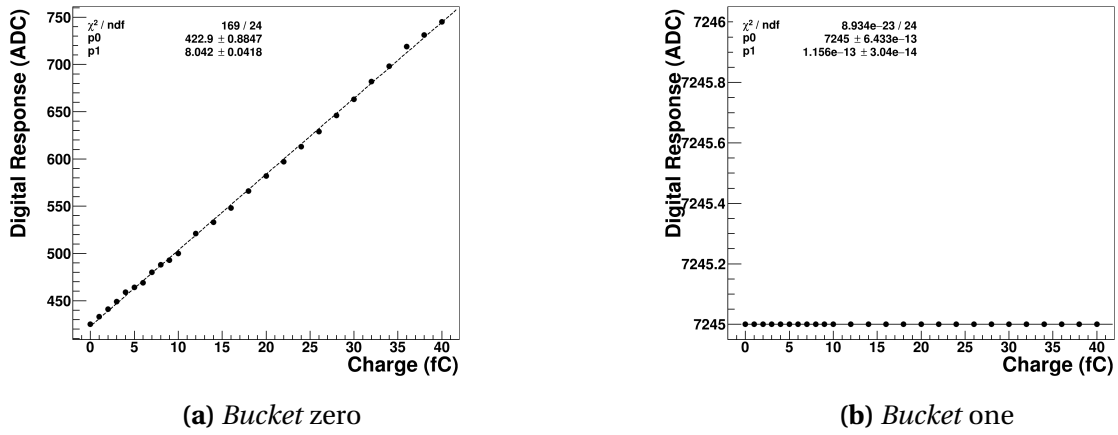


Figure 10.3 – Digital response to injected charge during calibration.

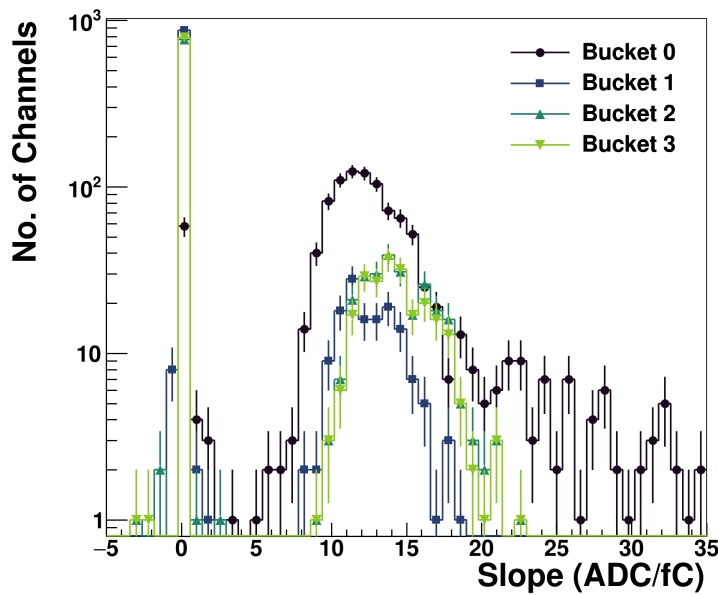
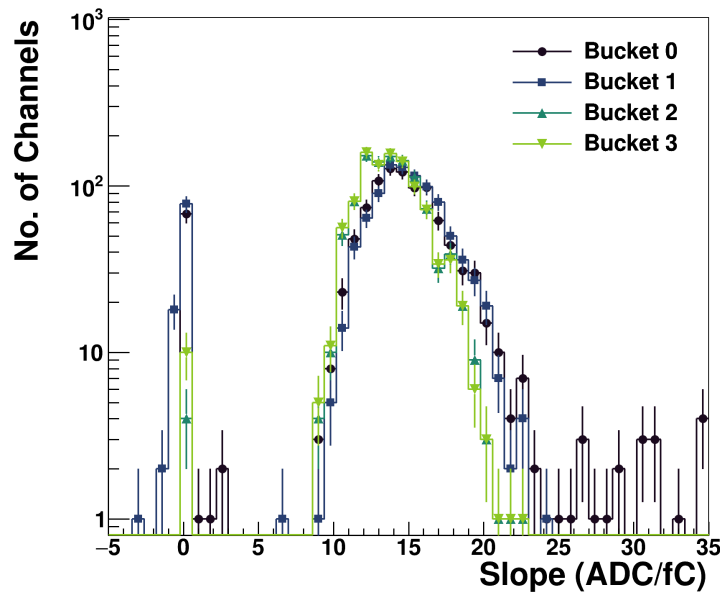


Figure 10.4 – Slope distributions for all 1024 channels of S59-1 for the four different *buckets*.

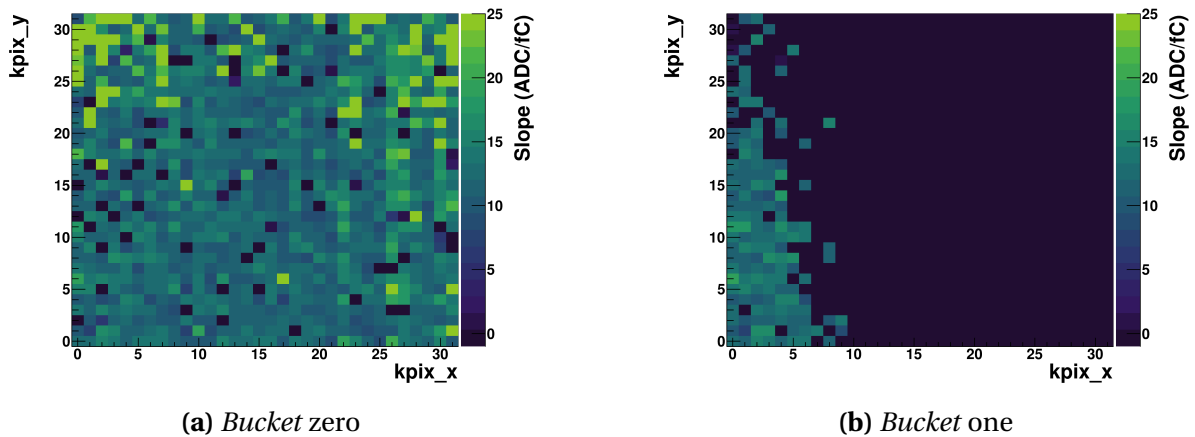


**Figure 10.5** – Slope distributions for all 1024 channels of S42-2 for the four different *buckets*.

As all *buckets* are supposed to be identical within the KPiX, no clear explanation for this behavior could be brought forth. An issue with the DAQ system could be ruled out as, while the DAQ is common, the *stale data* is not present for all KPiX ASICs. As an example, Figure 10.5 shows the slope distributions for a KPiX S42-2 within the same cassette. The slope distributions for this KPiX show only minor differences between the *buckets*. Both data sets were taken at the exact same time and under the same conditions ruling out environmental effects or potential changes in system setup or configuration.

A hint to a possible reason for this behavior was identified when mapping the distribution of slopes onto the KPiX channel space to produce a top down view onto the backside equivalent to the sketch in Figure 6.10. While for *bucket zero* (see Figure 10.6a) the general behavior is fairly random with a few channels located closer to the top edge showing an increased slope, *bucket one* (see Figure 10.6b) shows a clear pattern in that channels located further away from the connection pads are more likely to show *stale data* in calibration. Furthermore, in this projection the analog power input is located closer to the lower half of the distribution which would imply that increased distance to the analog power is responsible for this behavior.

A possible reason for this behavior is that a latch within the KPiX never gets to clear because the amplitude drop off edge is too slow as a result of an insufficient power bus. This latch is responsible to clear the data after the amplitude drops to zero. This clearing of



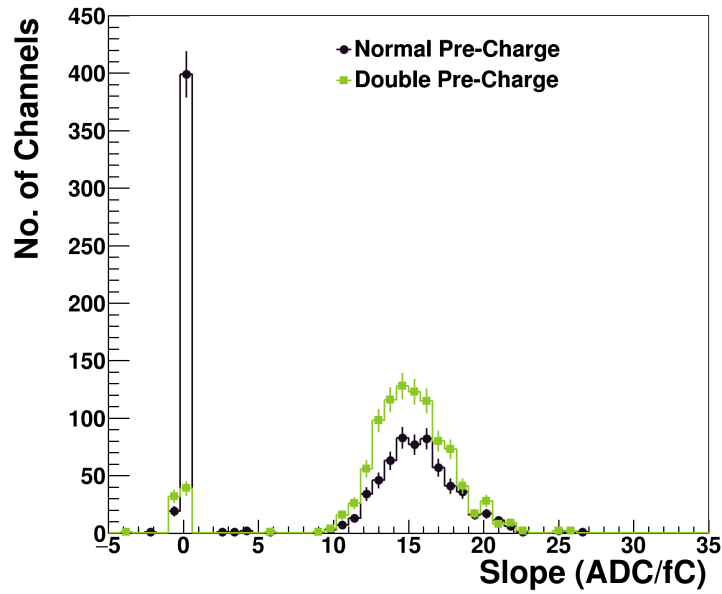
**Figure 10.6** – Slope distributions mapped to the location of the channel on KPiX S59-1 for two different *buckets*.

the data does not happen, resulting in the same data being read out. This is inherent to the KPiX chip and cannot be removed though a potential workaround was identified.

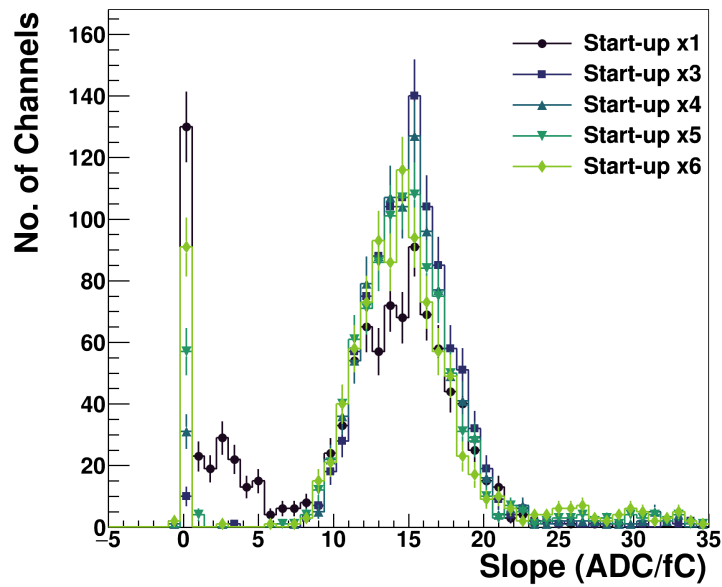
Preliminary tests with some of the Lycoris modules used during the test beam campaigns show a large improvement to the linearity of the digital response to charge injection for many channels when increasing the pre-charge clock period. Figure 10.7 shows the calibration slopes for *bucket one* on S43-2 for the previously used pre-charge clock and for a pre-charge clock period that was doubled. It shows a clear improvement and this could potentially be used to improve the efficiency of the system by allowing multiple particles to be registered within an *acquisition cycle*. This could not be studied more extensively within the time frame of this thesis as the option of increasing the pre-charge clock only became possible due to a recent DAQ firmware change. Hence, all results presented here are focused on the performance of *bucket zero*.

There is also a large discrepancy in the *bucket zero* calibration performance between different Lycoris modules. Of the 22 assembled Lycoris modules, only about 10 show acceptable calibration performance with fewer than 10% faulty channels. Only those Lycoris modules were used during the test beam campaigns.

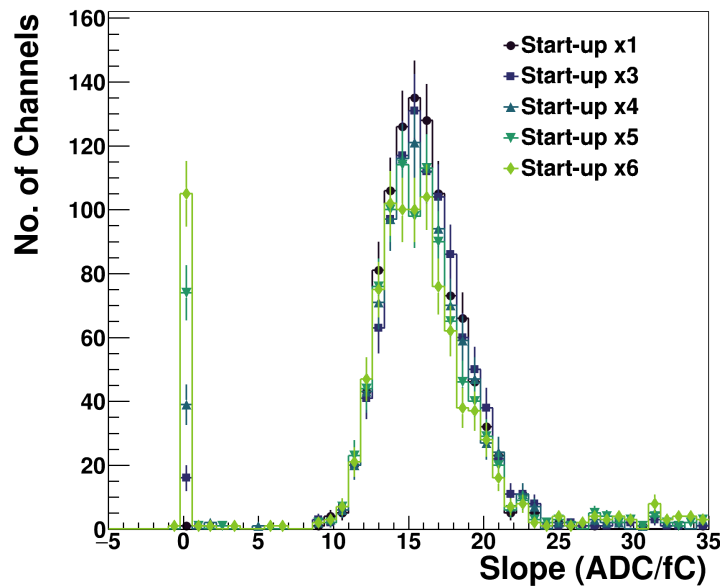
The operational mode of the KPiX, specifically the duration of the start-up phase, was found to impact the performance of the KPiX calibration. Figure 10.8 shows the calibration performance of KPiX S43-1 for different start-up phase durations. The start-up phase is stretched between three to six times the default value. The largest impact is visible when going from the standard time to a time stretched by a factor of three. The number of channels with faulty calibration is reduced by a factor of 25 from 250 to 10 channels. Further



**Figure 10.7** – Calibration slopes for S43-2 bucket 1 for different pre-charge clock values.



**Figure 10.8** – Calibration slopes of S43-1 in high gain operation for different start-up phase durations.

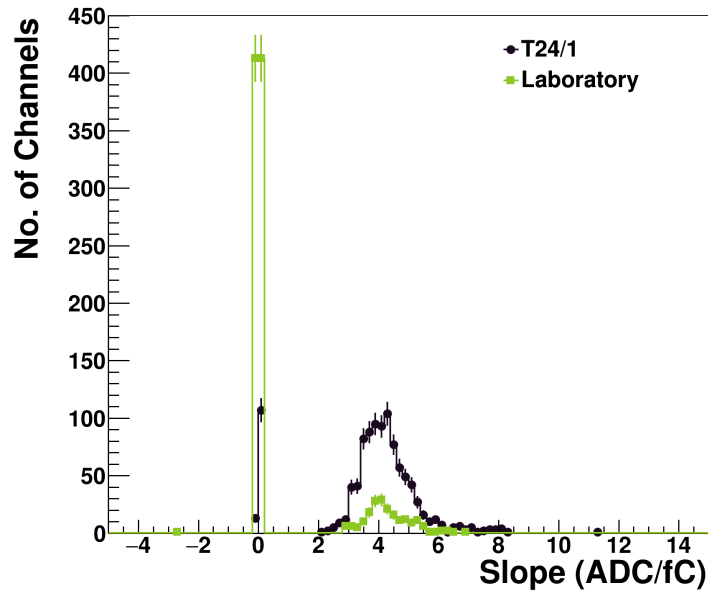


**Figure 10.9** – Calibration slopes of S40-1 in high gain operation for different start-up phase durations.

increase in the start-up phase leads to more faulty channels. By comparison, Figure 10.9 shows the same data with differently stretched start-up phases for KPiX S40-1, that already had a good calibration performance at the standard start-up phase duration. For this KPiX the linearity of the calibration response slowly degrades with increased start-up time phases similar to what S43-1 shows after its improvement when going from the standard duration to the three times stretched start-up. All 12 KPiX tested like this show the same behavior and considering the improvement to S43-1 this could be used to recover the performance of other Lycoris modules that were previously deemed unusable though the tests to that extent could not be conducted within the time frame of this thesis.

### 10.2.1 Humidity Influence

In preparation for a test beam campaign in which the best Lycoris were identified, a large discrepancy in Lycoris module performance was found between measurements performed in the Laboratory and in area T24/1. This can be seen in the calibration slope distribution depicted in Figure 10.10. The KPiX performs significantly better at the test beam compared to the laboratory. After ruling out potential differences in power supplies, shielding or influences from ambient devices, the only noticeable difference between the two measurements was found to be the ambient humidity.

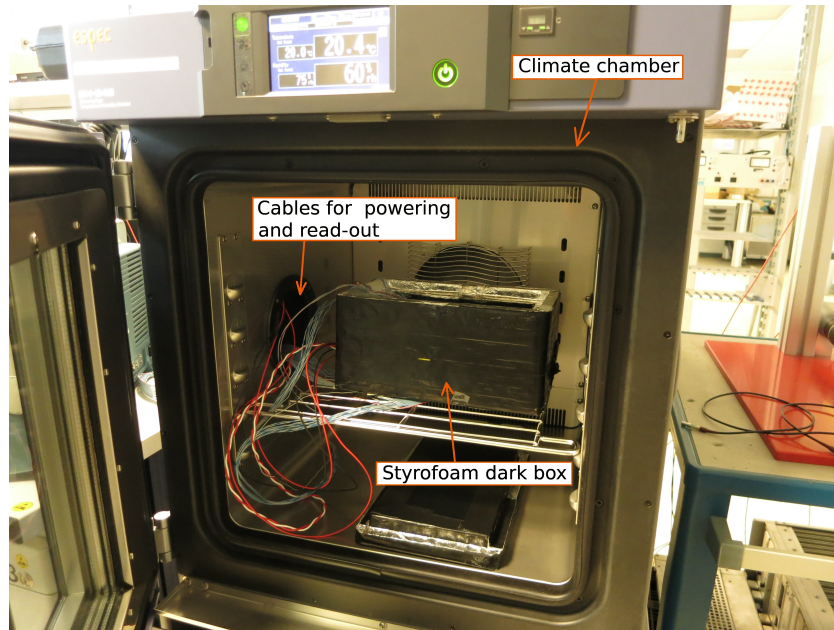


**Figure 10.10** – Calibration slopes of S53-1 in normal gain operation in the laboratory and area T24/1 at the DESY II Test Beam Facility .

The measurements in the laboratory were performed in a non climate controlled room where, later on high humidity levels were noticed. Measurements at the test beam were performed with the system permanently kept dry by flushing the inside of the cassette with boiled off nitrogen. Additionally, fluctuations on the daily performance of the Lycoris module calibration were noted that could not be explained. These fluctuations also disappeared once the system was operated with boiled off nitrogen further indicating that humidity has a noticeable impact on the calibration performance of the system. These observations motivated the following studies into humidity.

### Climate Chamber

To quantify the influence of humidity, measurements were performed using a SH-242 climate chamber from ESPEC [96]. It has inner dimensions of 300 mm × 250 mm × 300 mm and is capable of full temperature control between  $-40^{\circ}\text{C}$  and  $150^{\circ}\text{C}$ . The humidity within the climate chamber can be varied between 30% and 95% relative humidity (RH) which is defined as the partial pressure of water vapor to the equilibrium vapor pressure of water. The equilibrium vapor pressure of water is dependent on the temperature. A picture of the opened climate chamber with the dark box housing the Lycoris module is shown in Figure 10.11. The dark box shields the Lycoris modules from light, which would increase



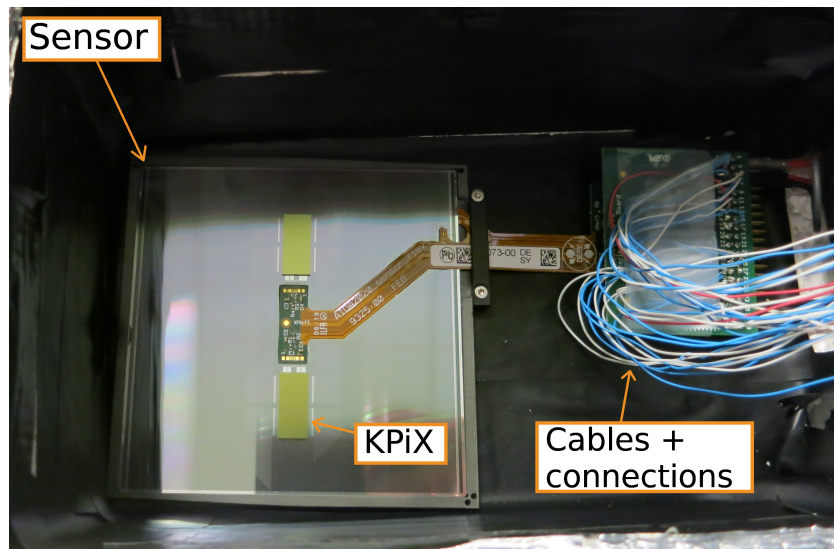
**Figure 10.11** – Picture of the opened climate chamber with the styrofoam dark box which houses the Lycoris module during operation.

the dark current of the Lycoris module and skew the measurement results.

A picture of the opened dark box containing a Lycoris module is shown in Figure 10.12. In contrast to the other measurements, no cassette board is used to connect power and signal, as they had been unavailable at that time. Therefore, the measurements were performed with an adapter board which allows the connection of wires to the *Kapton Flex Cable*. The power and bias are applied without filtering by a TTI [97] and a Keithley [98] source meter. A bias of 70V is set for all measurements.

To ensure that the climate chamber performs as expected, a Fluke 975 AirMeter [99] is placed within the climate chamber outside the dark box at different humidity levels in order to verify that the set humidity is achieved. The relation between the set humidity of the climate chamber and the measurement of the external humidity sensor is shown in Figure 10.13. The expected one to one correspondence is shown in the dashed lines and is not fully reflected by the measurements of the external device. At lower values the measured humidity is higher than the set humidity while at higher values the measured humidity is lower than the set humidity. The humidity within the room was measured to be 55%RH, as such it is possible that the inside and outside of the climate chamber are not perfectly isolated from each other.

As the measured humidity is not far from the set humidity, considering the measure-



**Figure 10.12** – Picture of the inside of the styrofoam darkbox with a single Lycoris module and adapter board which replaces the cassette board in the system setup.

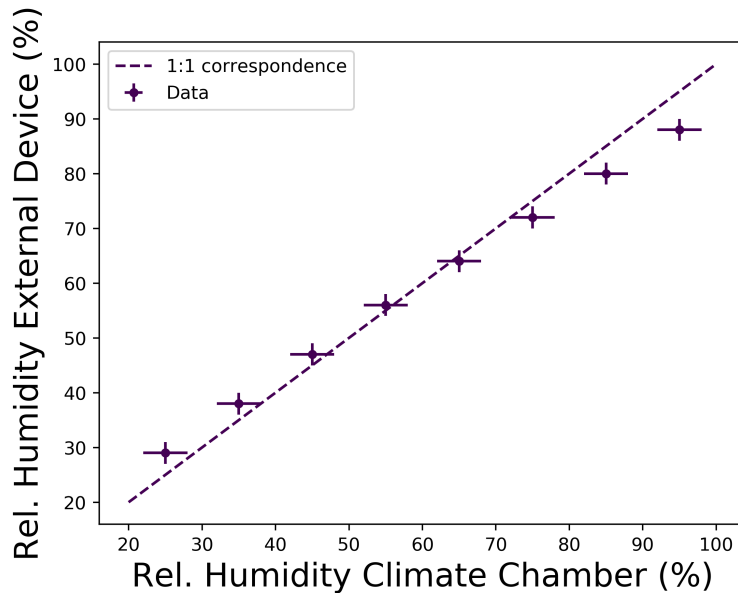
ment accuracy of the devices, the differences were deemed not significant. As such all humidity levels shown in measurements are based on the set humidity of the climate chamber. For all measurements, the dark box is kept open for a duration of one hour after setting a new humidity level to ensure that the humidity within the dark box and the surrounding climate chamber are in equilibrium. The temperature within the climate chamber was kept at a constant 20°C.

### Humidity Results

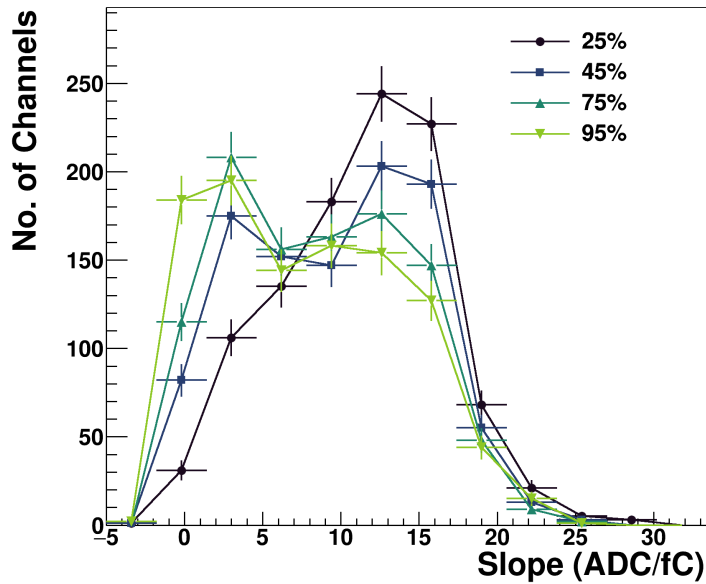
The fits performed in all measurements here are used as one of the two quality criteria mentioned in section 9.2.1, those being the fit slope and the pearson correlation coefficient of the distribution. The overall quality of the fit and its  $\chi^2$  are not important. The fits are simply used as a way to show the impact of the different humidity for a channel and to guide the eye. No results that fall outside of the quality criteria set in section 9.2.1 are used in any further analysis steps and the slope is only used to show the development of the channel performance for different levels of humidity.

Figure 10.14 shows the slope distribution for S41-2 at different levels of humidity, ranging from 25% RH to 95% RH. The overall amount of channels with faulty calibration increases as the humidity increases. Studying the single channel calibrations, three cases become apparent that are highlighted in Figures 10.15 to 10.17. Figure 10.15 depicts a channel

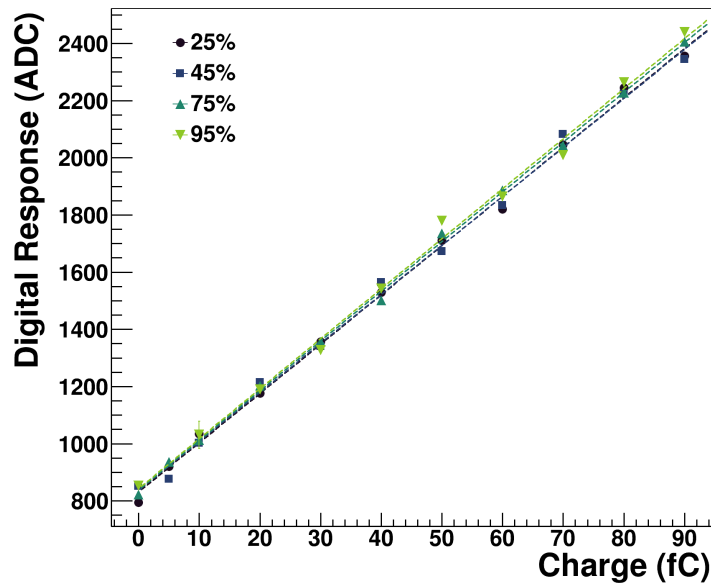




**Figure 10.13** – Relation between the set humidity of the climate chamber and the measured humidity of the external device.



**Figure 10.14** – Calibration slopes for S41-2 for different levels of relative humidity.



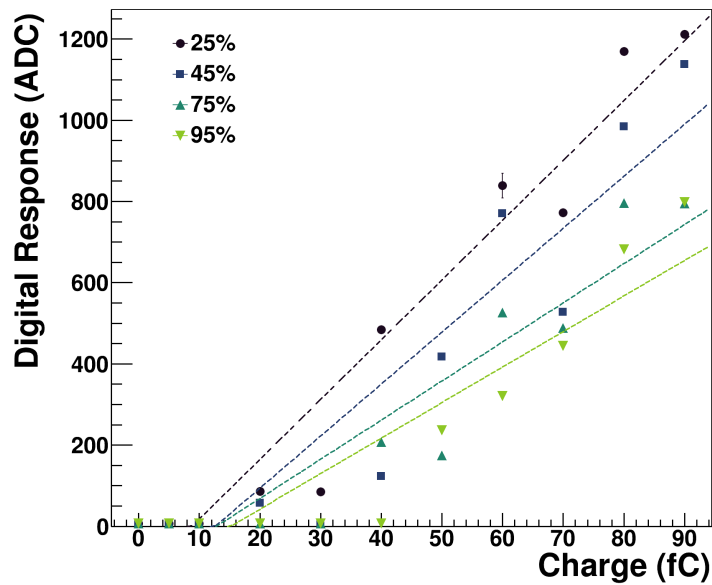
**Figure 10.15** – Calibration of S41-2 channel 557 for different levels of relative humidity. The dashed lines are the linear response fit from which the slope is extracted.

which is undisturbed by the influence of the increased humidity with a similar calibration slope at every level. Figure 10.16 shows a channel with a gradual decrease in the digital response relative to the injection charge with increased humidity levels. Lastly, Figure 10.17 shows heavy fluctuations in the digital response between different injections.

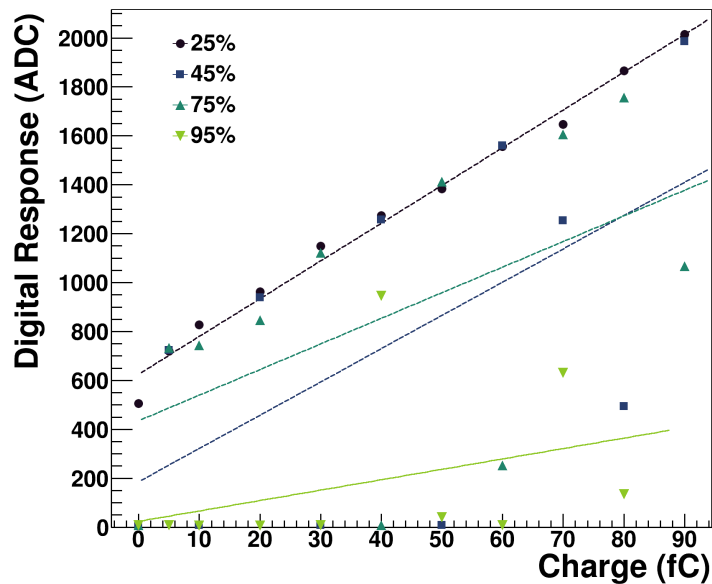
A pattern emerges, when mapping slopes of S41-2 onto the KPiX ASIC as is shown in Figure 10.18a and Figure 10.18b. The pattern is similar to the non connected channels (see Figure 6.10) but differs slightly in details as the central columns do not align perfectly with which channels are connected and which are not. Furthermore, this is not the case for all KPiX. For S41-1, shown in Figure 10.18c and Figure 10.18d, no pattern is present. The degradation of the channels digital response to injected charge is randomly distributed over the whole ASIC.

In addition to the different behavior between the two KPiX on S41, the measurements of the KPiX on S34 show no apparent influence of humidity on their calibration performance as is shown in Figure 10.19. It is unclear why that is the case, though it becomes apparent that channels for which the digital response to injected charge is not perfectly linear at low humidity levels are more easily affected by changes in the humidity. Chips like S34 which show a "better" performance seem to be more robust.

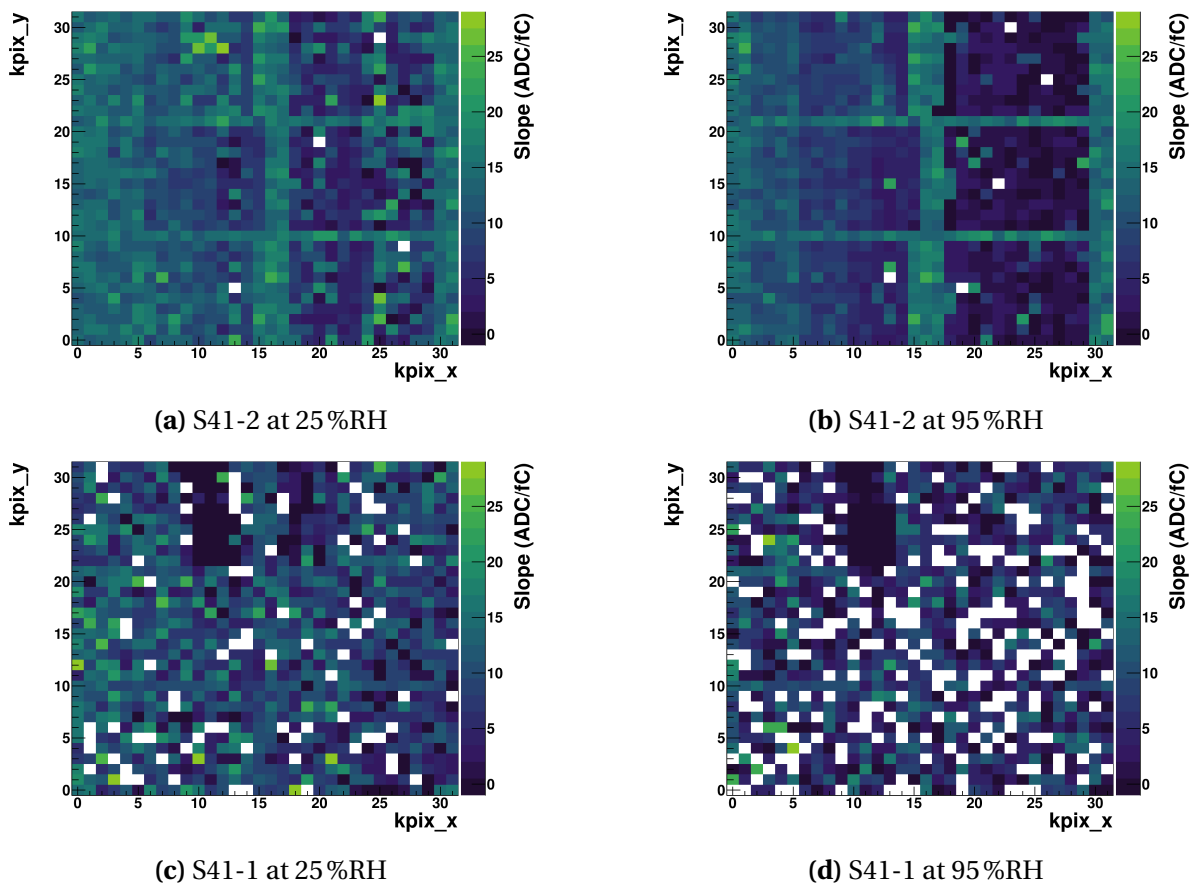
Furthermore, Figure 10.20 shows the slope distribution of S41-2 at 25 %RH, 95 %RH and



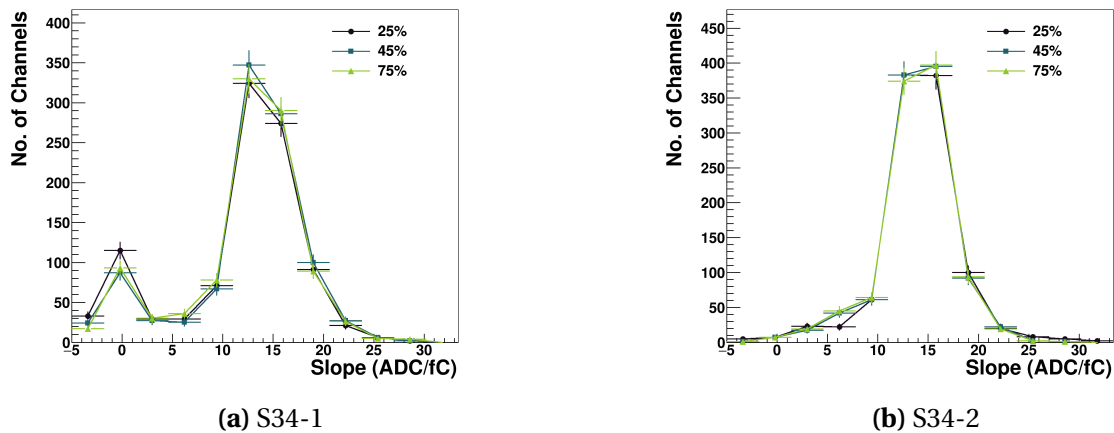
**Figure 10.16** – Calibration of S41-2 channel 200 for different levels of relative humidity. The dashed lines are the linear response fit from which the slope is normally extracted. In this case they are simply there to guide the eye as to the overall development of the digital response for increased humidity



**Figure 10.17** – Calibration of S41-2 channel 898 for different levels of relative humidity. The dashed lines are the linear response fit from which the slope is extracted.



**Figure 10.18** – Calibration slopes mapped onto KPIX space. The white blocks fall outside the z-range and are located at or below zero.



**Figure 10.19** – Calibration slopes for S34 for different levels of relative humidity. The negative slopes are a result where the response to an early charge injection is as expected but at later injections the no response is seen resulting in a negative slope of the linear regression.

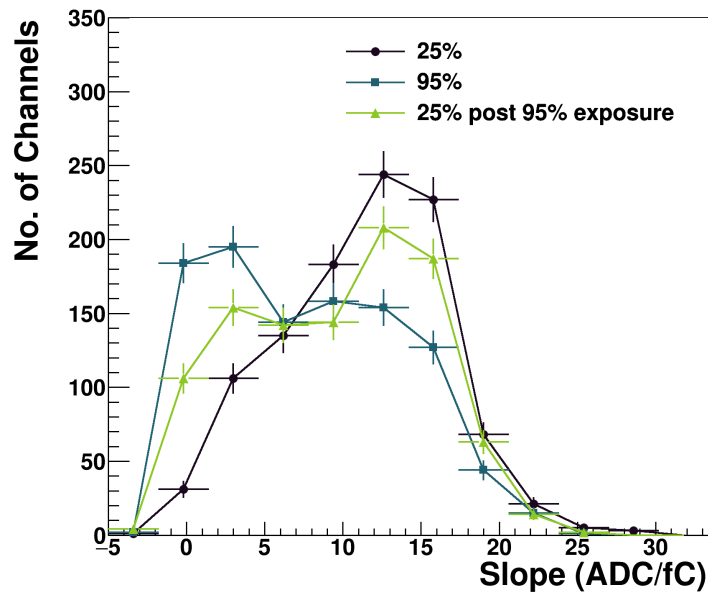
at 25%RH after exposure to the 95%RH environment. It shows that once exposed to a high humidity environment, the Lycoris modules performance is impacted beyond the measurement at high humidity levels. One explanation is water attachment to the surface of the Lycoris module that is not removed once taken out of the high humidity environment meaning, for the best performance, any potential water attached to the sensor surface needs to be removed.

### Module Drying

Lycoris modules are typically stored within a nitrogen environment with a relative humidity of 35%. This value is set to avoid the buildup of static electricity during storage. Studies were conducted during which all Lycoris modules were baked within a vacuum drying oven at 60°C before installation into the cassette system where they are constantly flushed with dry air or boiled off nitrogen. This is done to ensure that no humidity is attached to the Lycoris module.

Similar to the humidity measurements, the Lycoris modules react differently to the baking which is exemplified here by Lycoris module S33.

Figure 10.21 histograms the calibration slopes for all channels of S33 after different stages of baking. Both plots show similar behavior in that the black points show the measurements right after taking the Lycoris module out of storage before any baking. In either case they have close to zero channels with an expected slope distribution. The longer the baking procedure continues the more channels improve to their expected slope values with

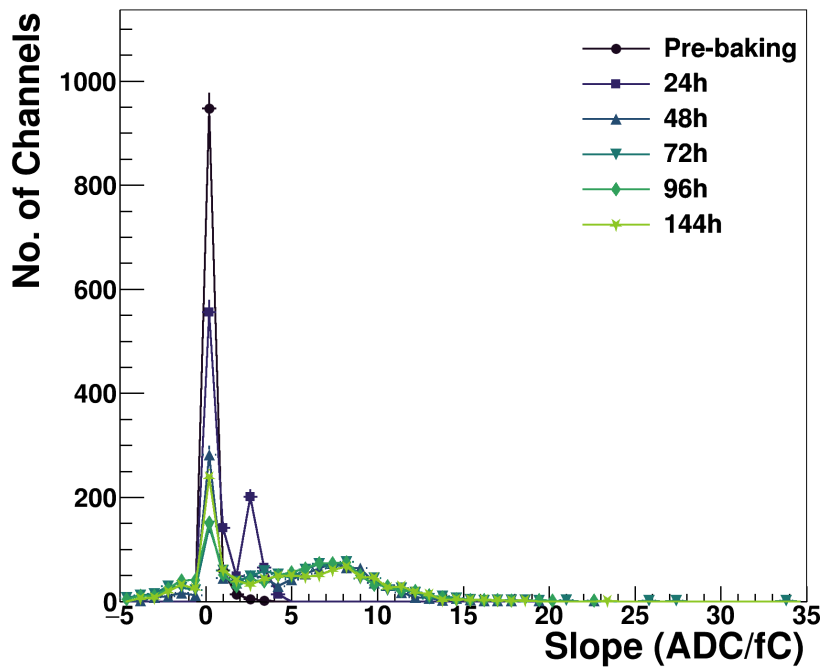


**Figure 10.20** – S41-2 calibration slope distribution at 25 %RH, 95 %RH and at 25 %RH after exposure to the 95% RH environment.

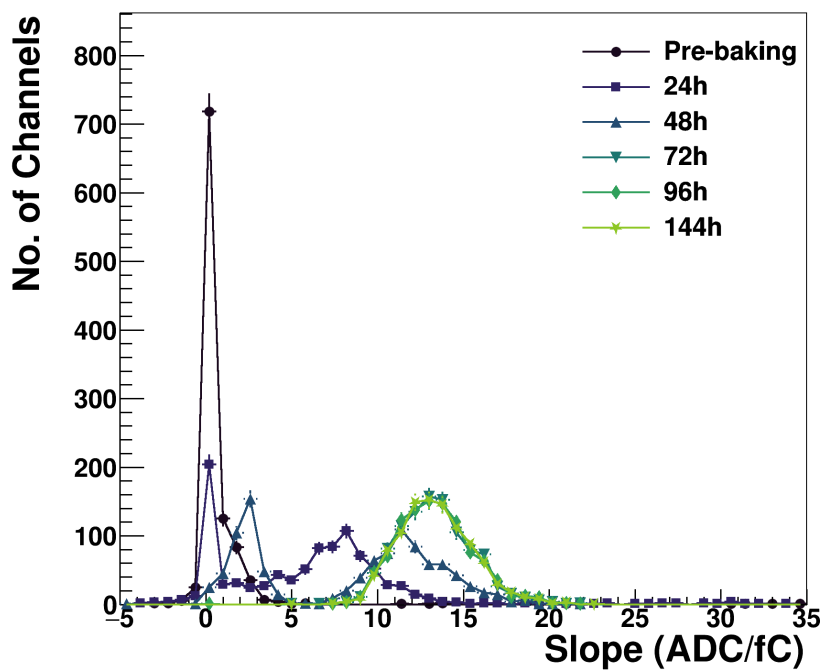
S33-2 recovering close to all channels after 72 hours of baking. S33-1 on the other hand shows only minor improvements during the baking procedure. Barely any channels reach the expected slope value of  $\approx 14$  ADC/fC.

A detailed look at the charge response to the injection for different stages of baking (see Figure 10.22) reveals that the baking recovers not only the linearity between the injected charge and the digital response but also the overall digital response value for lower charge injection values.

A possible explanation for this behavior is that increased humidity results in a reduction of the surface resistance. In other work such as [100] [101] and [102] it was noted that higher ambient humidity values impacts the charge losses as measured from Transient Current Technique (TCT) [103][104] measurements on  $p^+$  in  $n$  sensors. The measurement results are not exactly comparable as the measurement are done to determine how much of the charge generated within the sensor is collected within the integration time whereas in our system the charge is generated on chip and simply transferred to the amplifier. Nonetheless, in [100] the sheet resistivity of the sensor was determined to be a factor 120 higher in the dry environment compared to the humid environment. A study performed by the ATLAS collaboration on the ATLAS12EC and ATLAS17LS sensors shows a similar effect of higher humidity values decreasing the sheet resistivity [105]. It is shown in Figure 6.13 that

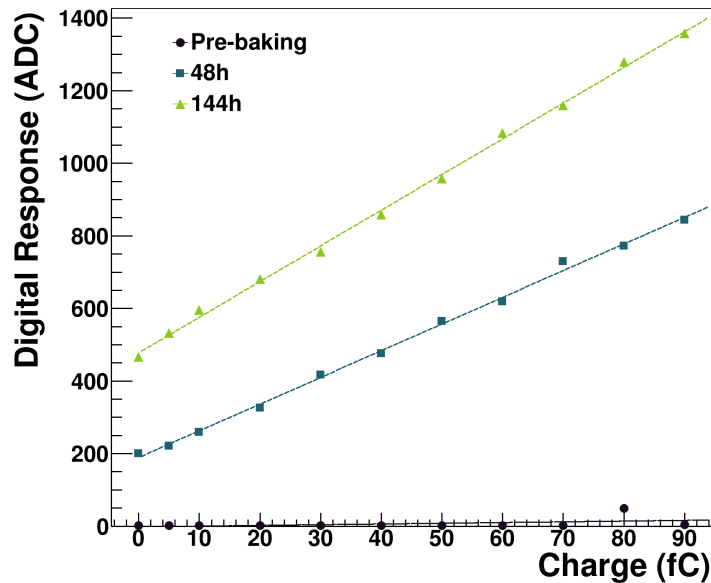


(a) S33-1



(b) S33-2

**Figure 10.21** – Calibration slope distribution for all channels of the KPix on S33 after different levels of baking.



**Figure 10.22** – Calibration slope for channel 557 of S33-2.

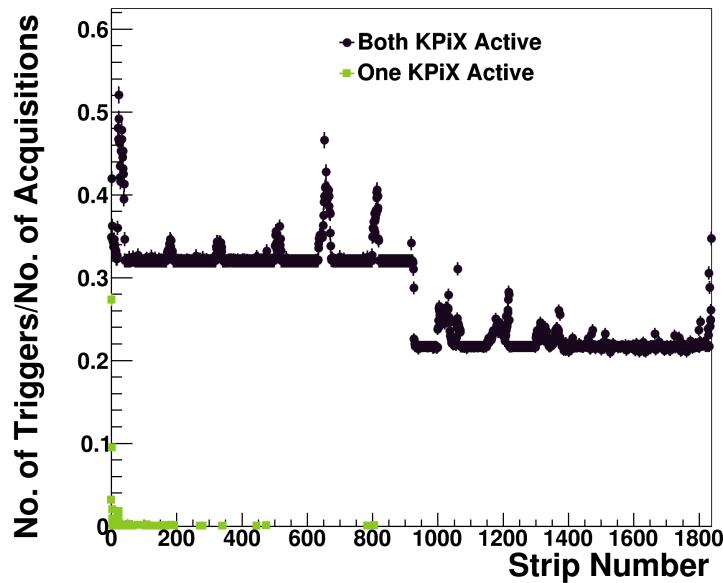
the input line connecting the amplifier to the bump pads and sensor surface is not decoupled during calibration. It is therefore possible that an increase in humidity and subsequent lowering of the sheet resistivity could result in the charge accumulated on the calibration capacitors to leak through this connection resulting in no or lowered charge injected into the amplifier. The different behavior of different KPiX is possibly due to slight differences in the passivation layer sheet resistances. Further studies of this were not possible due to the limited time the climate chamber was available.

Because of the potential negative impact on the performance, all measurements at the test beam are performed in a dry environment. This is achieved by flushing the Lycoris cassette with dry air or boiled off nitrogen.

### 10.3 Internal Triggering Results at the Test Beam

As mentioned in section 9.2.3, the performance of the internal triggering of the system is mostly given as a measure of how low the internal triggering threshold can be set while suppressing the generation of *monster events*. Figure 10.23 shows in black the number of triggers normalized to the number of acquisitions for *bucket zero* of S59. The triggers are mapped against the Lycoris module strip number and a DAC threshold of 200 which is the equivalent of a charge threshold of approximately 8fC. The expected most probable





**Figure 10.23** – Number of triggers normalized to the number of acquisitions for S59 shown against the sensor strip number for a threshold of 200 DAC. The channels with spikes relative to the baseline are primary candidates for channels that cause *monster events*. Only one half of the sensor is activated in the green plot resulting in no triggers for the right half of the plot. The overall lowered amount of triggers even in the left half indicates unwanted cross talk between the two KPiX.

charge deposit of a MIP within the sensor is approximately 3 fC. Using this setup, the system already registers a signal above the threshold in about 25 % of all cases for every single strip which is the result of *monster events* being induced. The difference in the levels between the right and left halves of the Lycoris module are the result of them being read out by different KPiX chips. The spikes present in the normalized number of triggers are most likely the channels which cause the *monster events* as they trigger even in cases where the chip has not caused a monster event. To use the system for track finding, the level of noise triggers, as well as the DAC trigger threshold needs to be reduced significantly. When reducing the threshold to 230 DAC = 3.23 fC the entire system registers a trigger without any input signal making it impossible to use the system for track finding and fitting.

*Monster events* are a known flaw of the KPiX chip used for the Lycoris modules, though in previous use cases the issue was shown to be much less severe with the system being operational at much lower DAC thresholds [95] and strong enhancement of *monster events* must be a result of the way the ASIC is used for the tracker sensor. One difference is that in previous applications each KPiX was on an independent power line. Power consump-

tion is expected to rise sharply during the induction of *monster events* and both KPiX are connected together via their power and ground lines on the Lycoris modules. It is therefore possible that the induction of *monster events* in one KPiX can impact the noise performance in the other KPiX resulting in unwanted noise triggers that can then result in further *monster events*.

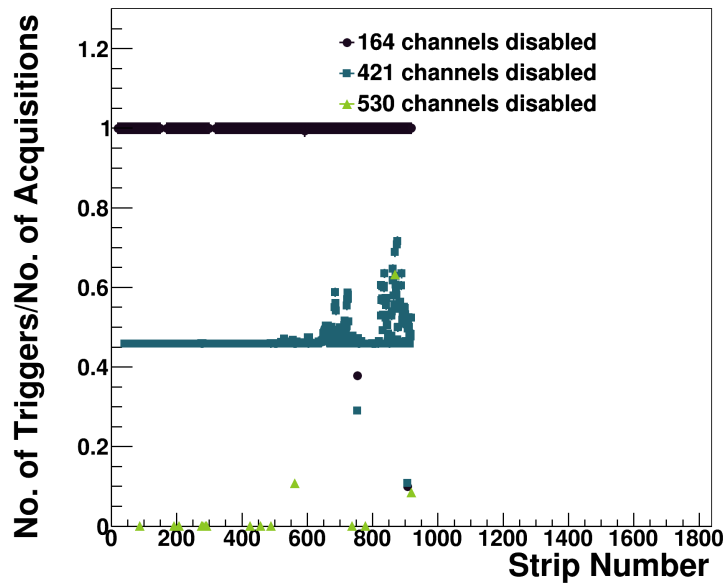
The sensors can be operated with only one of the two KPiX active. This is depicted in the green plot shown in Figure 10.23 for the exact same threshold as before. When only one KPiX is active, the system registers almost no triggers except for a few channels located mostly at the edge. This gives credence to our previous assumption of the KPiX being coupled to one another via the power/ground lines on the *Kapton Flex Cable* increases the noise of the system.

Plans exist for a new *Kapton Flex Cable* which has all power and ground lines separated between the different KPiX. Tests are planned to redo these measurements once a new *Kapton Flex Cable* is produced. This cable is intended to be used to assemble the remaining two Lycoris modules though this was beyond the time frame of this thesis.

### 10.3.1 *Monster Event Suppression*

As mentioned in Section 9.2.3, a *monster event* can be induced by any of the channels reset current. The exact mechanism behind the *monster events* has not been proven at the point of writing and as such the level at which a channel can cause *monster events* is not well understood. Channels showing a large amount of triggers at very high thresholds, indicating high noise, are disabled as they are deemed the most likely candidate for the induction of monster events. In order to determine these channels a gradual disabling is performed though the disabling scheme which has to be adjusted iteratively and depends on the results gathered in each step shown here. The process steps are:

1. Disabling of all channels not connected to a strip (104) per KPiX as well as any channels with a calibration slope  $\leq 3 \text{ ADC/fC}$  and/or a PCC below 0.9 (see section 9.2.1).
2. Setting DAC threshold to a high level during which the system is not triggering for every acquisition. The actual level at which this is achieved depends on the KPiX noise performance and must be determined ad hoc via a gradual increase.
3. Determining channels which trigger more than 10% of the time. These channels are then disabled.



**Figure 10.24** – Number of triggers normalized to the number of acquisitions for S59-1 shown against the sensor strip number for a threshold of 230 DAC = 3.23 fC for three different channel disabling maps.

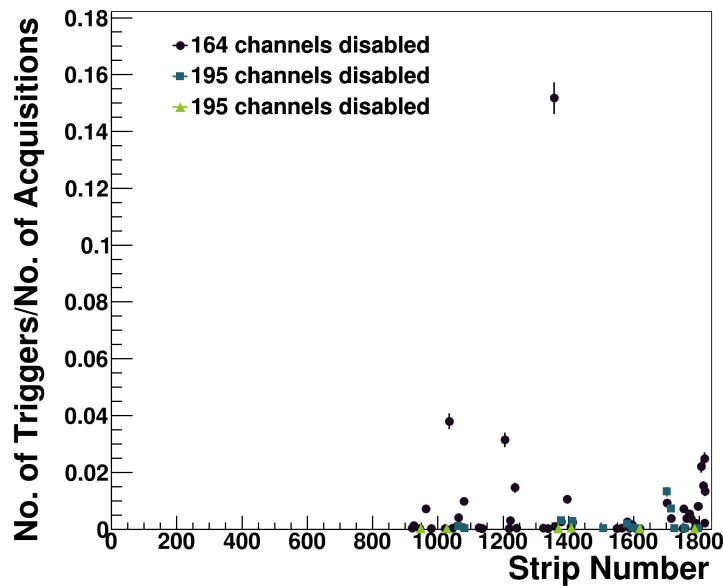
4. Raising of the DAC threshold level until once more channels with more than 10% of triggers appear which are once more disabled.

This is repeated until either, a reasonable threshold level is achieved, or a significant portion of all channels is disabled. Unfortunately both an increase in thresholds as well as an increase in the number of disabled channels negatively affects the performance of the system and a compromise has to be made.

The effect of the disabling of channels can be seen in Figure 10.24. It shows the number of triggers normalized to the number of acquisitions for distribution with increasing amounts of channels disabled. The amount of triggers reduces drastically from an average trigger rate of close to 1.0<sup>1</sup> down 0.0. The performance differs significantly between different Lycoris modules which can be seen in Figure 10.25 for S43-2 which shows a significantly better trigger rate with only 195 channels disabled already reaching a trigger rate of close to 0.0 for all channels. This is similar for all of the other four Lycoris modules tested via this method.

Ideally, a balance would have to be struck in which the system can be operated at a threshold of 241 DAC  $\approx$  1.48 fC without too many channels being disabled. This was found

<sup>1</sup>meaning that every channel triggers once per acquisition



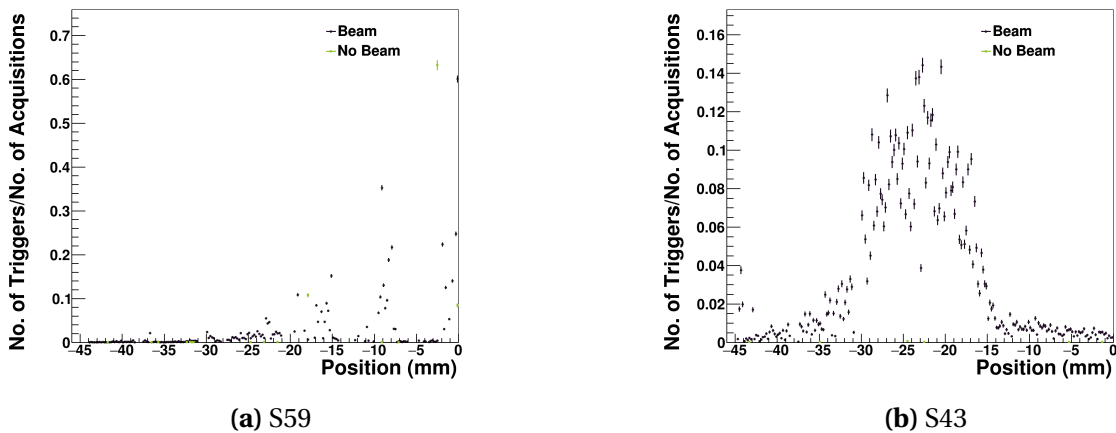
**Figure 10.25** – Number of noise triggers normalized to the number of acquisitions for S43-2 shown against the sensor strip number for a threshold of  $230 \text{ DAC} = 3.23 \text{ fC}$  for three different channel disabling maps.

to not be possible without requiring at least 50% of all channels to be disabled in all KPiX, making internal triggering operation for the telescope impossible as either way the overall efficiency and spatial resolution of the telescope would be below the requirements set in section 6.1.

The system was tested within the electron beam with only one half of all KPiX active and the significantly reduced active number of channels at a threshold of 230 DAC in order to determine whether the system is at all responsive to the beam in internal triggering and to determine what efficiency could be reached.

### 10.3.2 Beam Test

Figure 10.26a depicts the number of triggers within S59 once with beam particles passing through the Lycoris module and once without. The x-axis was changed from the strip number to the local hit position to make it easier to compare results between different Lycoris modules as for flipped modules the higher strip numbers correspond to the same local position as the lower strip numbers of unflipped modules (see section 8.1). The distribution with beam particles shows significantly more triggers, though a beam spot is not visible in the results gathered by S59.



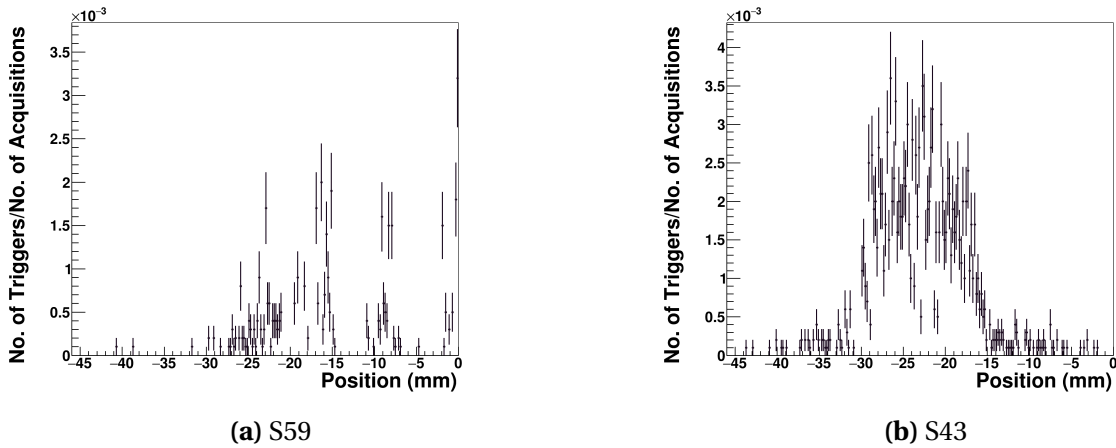
**Figure 10.26** – Number of triggers normalized to the number of acquisitions for two Lycoris modules shown against the local Lycoris module position for a threshold of 230 DAC = 3.23 fC with beam in black and without beam in green.

By comparison, Figure 10.26b shows a clearly visible peak located at around  $-23$  mm in the run with beam which is not present in the run without any beam. The distributions without beam are the same as the green distributions shown in Figure 10.24 and Figure 10.25 which are simply used to show at a glance the impact of the beam. Both KPIX show a significant increase in the amount of triggers in the run with beam relative to the run without beam. This proves that the system is responsive to signal in internal triggering operation.

While the amount of triggers is significantly higher, this does not mean that all recorded triggers are necessarily generated directly by charge deposition from the beam. When a channel triggers due to the beam it is possible that the reset of this channel also triggers monster events which are slightly shifted in time to the initial trigger. In order to determine the systems efficiency these hits need to be removed. This is done by filtering out all triggers that are not correlated in time to the externally recorded trigger time (see section 9.2.3).

Using this cut transforms the distributions of of Figure 10.26a and Figure 10.26b to the distributions shown in Figure 10.27a and Figure 10.27b. The plots show the triggers which are coincident with an externally received trigger indicating a particle passing through. This has a large impact on the statistics of the plot and while the overall form of Figure 10.27b is close to unchanged, for Figure 10.27a it results in a distribution which more closely resembles the expected structure compared to before.

For simplicity, every hit that was filtered out is considered noise, while every hit that is left over is considered signal. With that assumption, a rough upper limit of the system



**Figure 10.27** – Number of triggers normalized to the number of acquisitions with the requirement that an external trigger was recorded two to three BCC after the internal trigger for Lycoris modules shown against the local Lycoris module coordinate for a threshold of  $230 \text{ DAC} = 3.23 \text{ fC}$ .

Lycoris module	Entries
59	408
43	1453
40	491
46	465
47	467
48	683

**Table 10.2** – Timed internal trigger entries for the six different Lycoris modules.

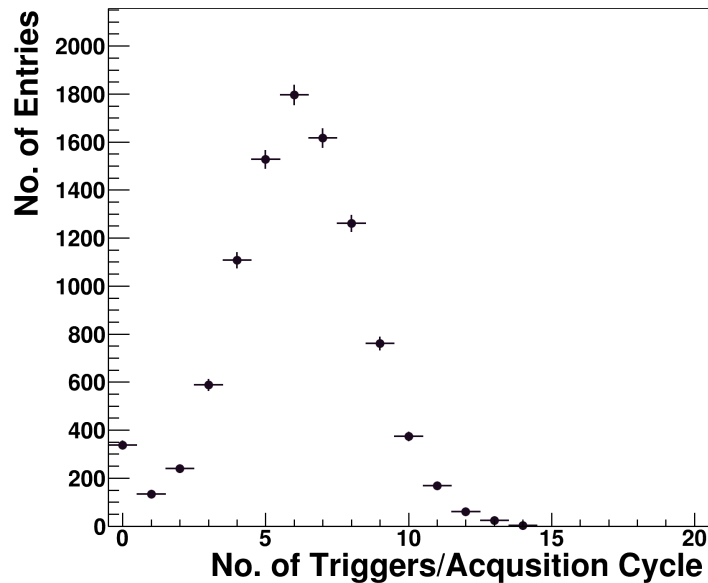
efficiency in internal triggering operation can be determined by comparing the number of registered particles listed in table 10.2, with the expected number of registered particles.

The expected number of registered particle is determined based on the number of registered external triggers per acquisition that is portrayed in Figure 10.28. The distribution of externally received triggers per acquisition has a mean value of about 6 which means that a fully efficient system would record a total of:

$$N_{100\%} \approx 6 \cdot N_{\text{acq.cycles}} \approx 60000, \quad (10.1)$$

particles in each Lycoris module.

Assuming that all triggers recorded after the time quality cut are valid triggers gives an efficiency in internal triggering of 0.68% to 2.42%. To reconstruct a single track with low ef-



**Figure 10.28** – Number of how often a certain amount of external triggers were recorded within a single acquisition cycle

iciencies as given here would require about  $10^{10}$  tracks proving that the system is unusable without significantly lower thresholds.

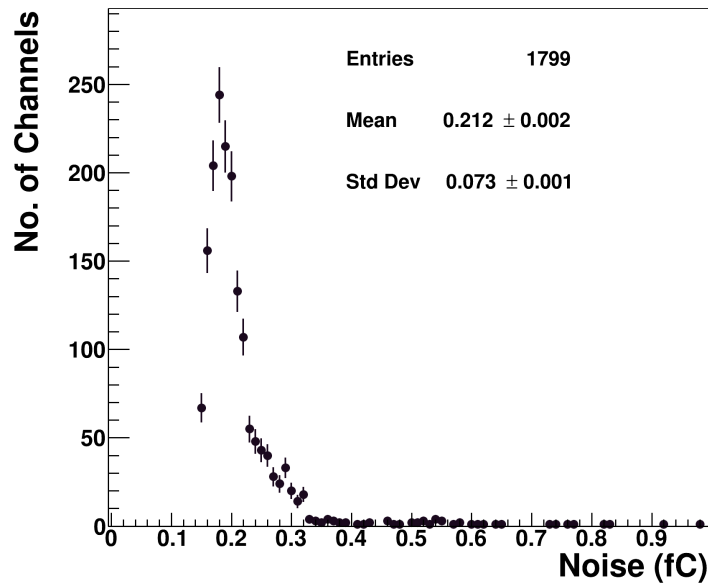
The system needs to be able to be operated at a much lower effective threshold <sup>2</sup> in order to increase the efficiency. This would require a new chip design which inhibits the induction of *monster events* and any track finding and fitting with the current system in internal triggering operation is unfeasible.

As this is not so much an issue of the sensor but more of the ASIC, conclusions on the sensor performance are instead drawn from the external triggering performance which, because a trigger is only recorded once an external device has sent out such a trigger, is unaffected by *monster events* unless coincidentally a trigger is acquired at the exact moment the reset current from the previous trigger is active which is exceedingly unlikely.

## 10.4 External Triggering Performance

The external trigger operation is the main user operation for the system due to the presence of *monster events* in internal triggering. As such, characterizing this operational mode

<sup>2</sup>The threshold given in DAC values is relative to a 2.5V baseline and as such a lowered DAC threshold results in a higher effective threshold to the charge deposition.



**Figure 10.29** – Distribution of 1840 noise values for the strips of sensor S47 recorded during the July 2019 Test beam campaign in Area T24/1. The value of noise for each strip is given by  $\sigma = MAD \cdot 1.4826$  of the true charge distribution.

is the central study in this thesis.

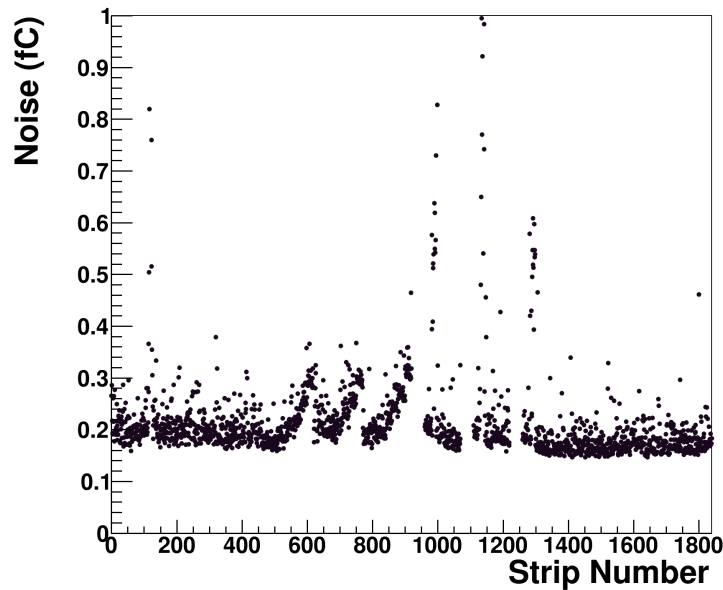
### 10.4.1 Noise Study

During external triggering, signal is differentiated from noise via an elaborate analysis as opposed to the on-chip-based noise-filtering threshold of the internal triggering operation. For an external triggering operation the system noise is determined by the width of the pedestal after ADC to charge conversion, pedestal subtraction and common mode subtraction. It is calculated via  $\sigma = MAD \cdot 1.4826$  through use of the Median Absolute Deviation (MAD) (see section 9.2.2).

Figure 10.29 shows the noise distribution calculated via the MAD (9.7) of the pedestal for wire-bonded sensors that are not yet glued into the frames, at high gain, in standard operation, at the DESY II Test Beam Facility. Most channels have a noise value close to  $N = 0.2$  fC. The distribution of noise for all 1024 channels shows a tail to larger noise values. This is true for all of the sensors operated at the DESY II Test Beam Facility, with variations in the extension of the tail and position of the peak.

Figure 10.30 shows the noise of the the sensors mapped to the sensor space such that strip 0 and 1840 are at opposite edges of the sensor. Multiple noise peaks are found in

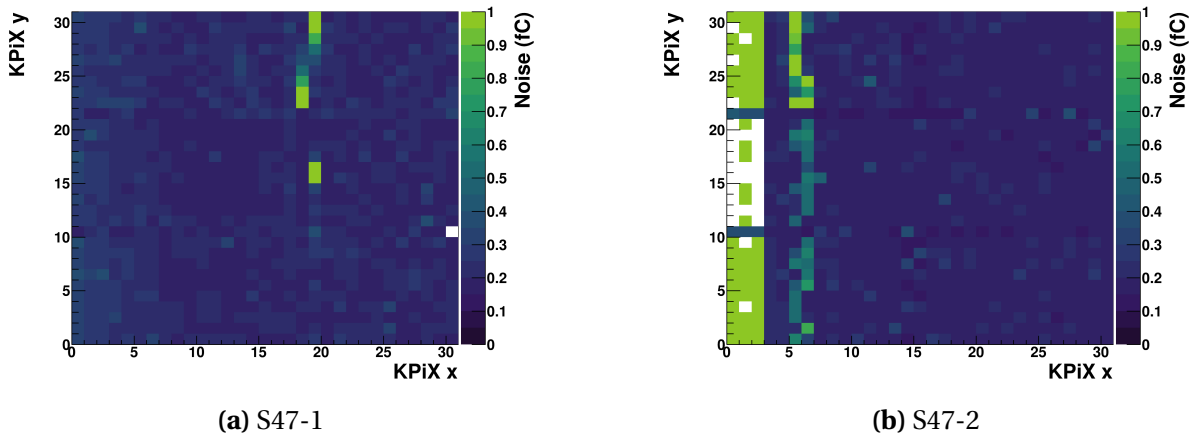




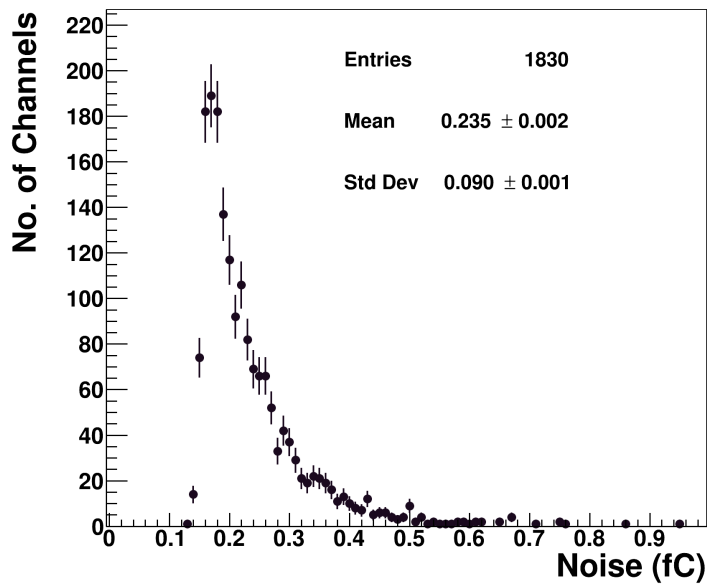
**Figure 10.30** – Noise values of channels mapped to the sensor strip numbers for S47 recorded during the July 2019 Test beam campaign in Area T24/1

the central region of the sensors. Mapping the channel noise to the channel locations in KPiX space, a clear connection between the different noisy channels becomes apparent (see Figure 10.31). All channels with increased noise are located close to the power and signal pads in KPiX space indicating noise induced by either the power lines or the signal lines. The LVDS amplitude of the clock and trigger lines have been reduced as a result to avoid noise induction. It cannot be ruled out that the noise is a result of cross talk between the two KPiX via their analog and digital power lines as was shown to be present in internal triggering operation (see section 10.3.1).

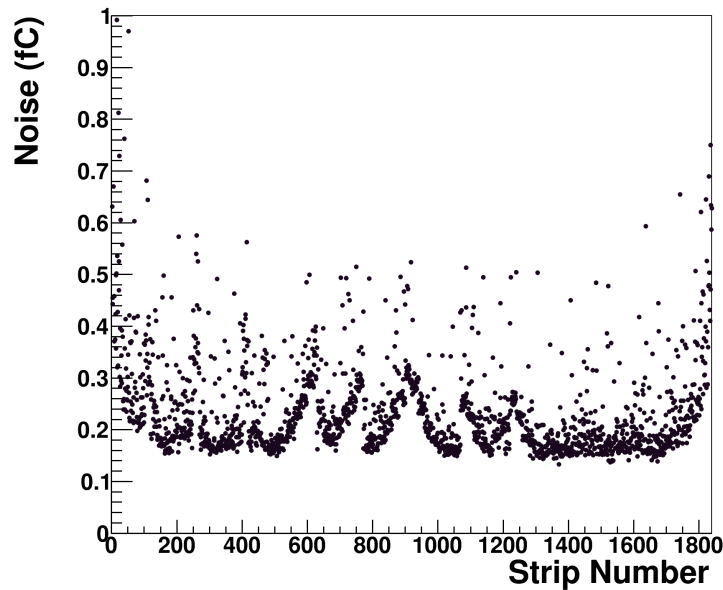
Measurements performed during the test beam campaign in March 2020 include the dampened LVDS amplitudes. In addition, during the March 2020 test beam campaign, all sensors have been glued into the frame, finishing the Lycoris module assembly. The noise distribution for S47 during the March test beam campaign depicted in Figure 10.32 has a similar location for the main peak. However, more channels located in the tail of the distribution. Looking at the noise mapped to the strip number (see Figure 10.33) shows that, while the central peak distribution for the right half is lowered, it is still present and of similar size to the peak for the other side. This is true for all Lycoris modules tested and indicates that the LVDS lines were not responsible for the noise. Furthermore, all channels show a more erratic behavior compared to the July 2019 data. In addition, the edges of the Lycoris



**Figure 10.31** – Noise values of channels mapped to KPiX channels recorded during the July 2019 Test beam campaign in Area T24/1.



**Figure 10.32** – Distribution of 1840 noise values for the strips of sensor S47 recorded during the March 2020 Test beam campaign in Area T24/1. The value of noise for each strip is given by  $\sigma = MAD \cdot 1.4826$  of the true charge distribution.

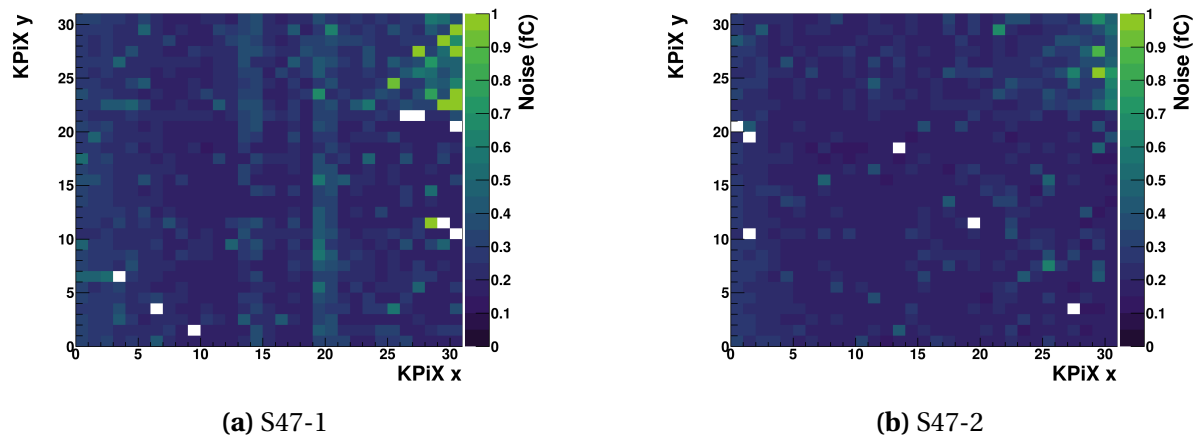


**Figure 10.33** – Noise mapped to the sensor strip numbers for S47 recorded during the March 2020 Test beam campaign in Area T24

module show increased noise that was not present beforehand. The noise mapped to the KPiX are depicted in Figure 10.37b and Figure 10.37a. The effect of increased noise in the edge of the Lycoris modules could be a result of newly made coupling between the floating cassette and the Lycoris modules as the edge with increased noise is where the Lycoris modules are screwed into the cassette. However the edge channels are also located furthest from the power pads meaning it cannot be ruled out that this is an effect of the distance to the power connection similar with the *stale data* issue encountered in section 10.2 though this does not explain why it was not present until the sensors were glued into the frame. Investigation into whether a grounding of the cassette could help remedy this increase in noise were planned but could not be completed for this thesis.

Lastly, measurements performed during the August 2020 test beam campaign show significantly improved noise performance as is shown in Figure 10.35 to Figure 10.37. Especially the noise spikes that were present in the March 2020 test beam campaign run Figure 10.33 are significantly suppressed in the August 2020 test beam campaign as shown in Figure 10.36. No changes were performed to the system except:

- The KPiX opening window was adjusted to start at 4000 BCC and end at 8191 BCC as opposed to the typical start at 1000 BCC and end at 4000 BCC which is explored further in Section 10.4.1.1.



**Figure 10.34** – Noise mapped to KPiX channels recorded during the March 2020 Test beam campaign in Area T24.

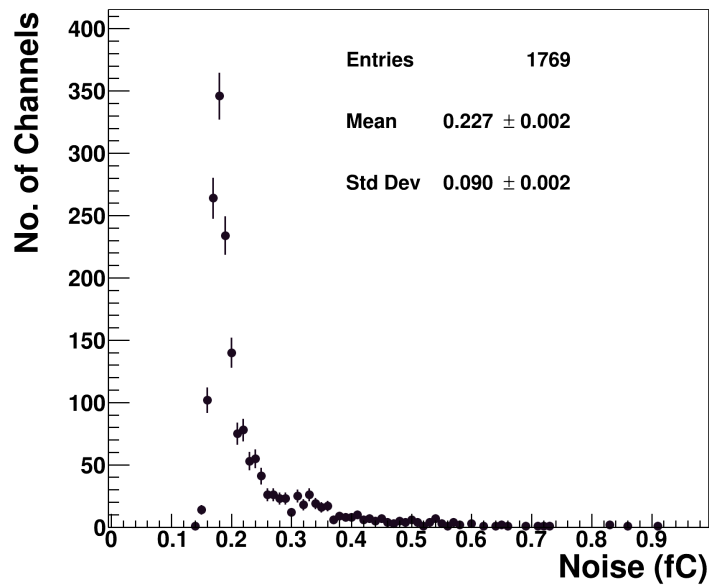
- The Chiller used for the AZALEA water cooling was moved further away from the system and connected into a separate power plug as other groups have reported noise being coupled into their system via this connection [106].

While the time window affects to overall noise within the system, it does not impact specific channels more than others (see Section 10.4.1.1).

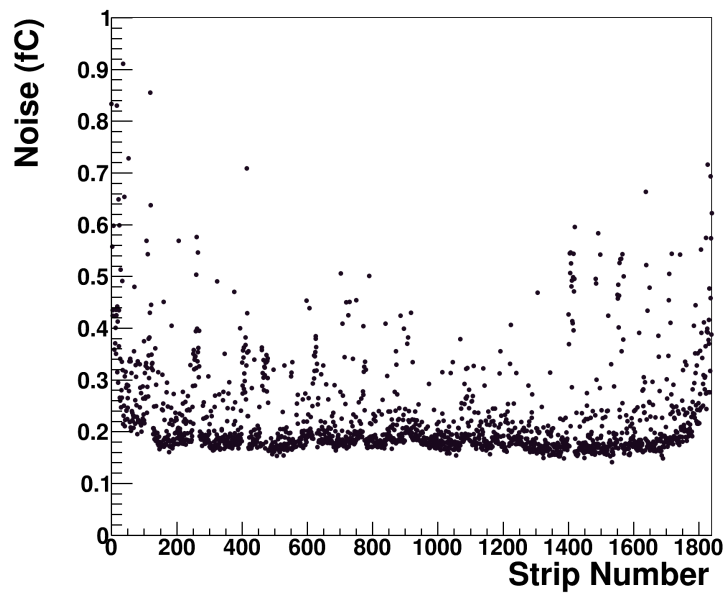
The most likely candidate for the noise is insufficient filtering of noise on the power lines resulting in noise injection that was reduced by removing the chiller from the same power lines. As the selection of clusters is done at a threshold of four times the noise value this results in an effective hit threshold of about 0.8 fC for most channels which is far below the MPV for charge deposition of 3 fC.

#### 10.4.1.1 Noise time structure

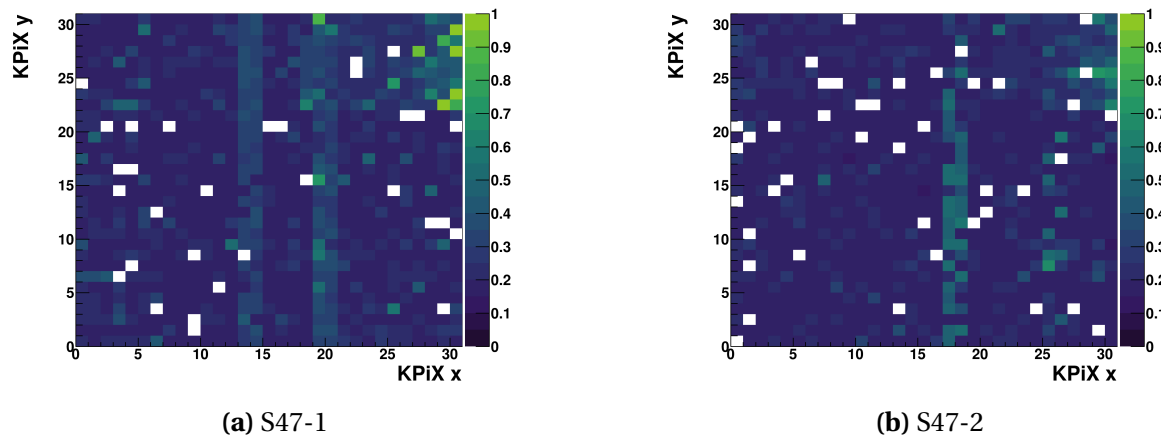
As mentioned in Section 8.3, standard KPiX operation is chosen to run from 1000 BCC to 4000 BCC. The reason for this choice lies within the noise performance of the ASIC at different timing windows. The effect of different time windows was tested in the laboratory using the same Lycoris modules as used during the March 2020 test beam campaign. The measurements were performed using internal trigger inhibitions within KPiX while using an external *auto trigger* with a 48 Hz trigger frequency generated by the AIDA TLU. This ensures that for the longest time window of 0 to 8191 BCC the system is guaranteed to have a trigger in each acquisition. The KPiX and the trigger are not synchronized to one another. This means, that the trigger will shift relative to the KPiX acquisition for each new acquisi-



**Figure 10.35** – Distribution of 1840 noise values for the strips of sensor S47 recorded during the August 2020 Test beam campaign in Area T24/1. The value of noise for each strip is given by  $\sigma = MAD \cdot 1.4826$  of the true charge distribution.



**Figure 10.36** – Noise mapped to the sensor strip numbers for S47 recorded during the August 2020 Test beam campaign in Area T24

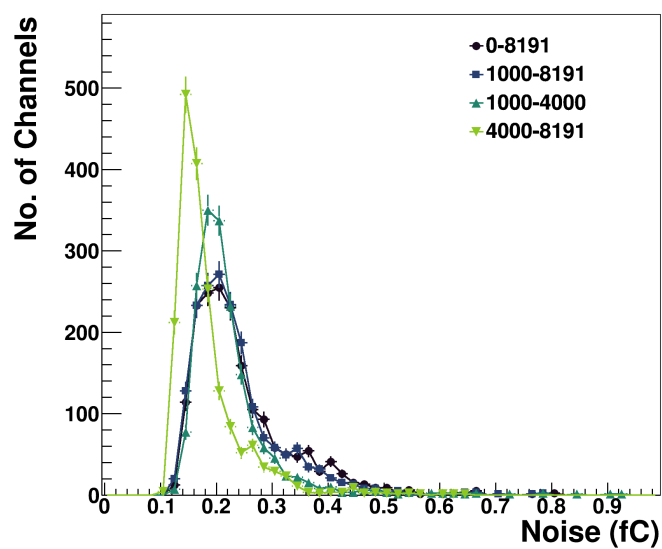


**Figure 10.37** – Noise mapped to KPIX channels recorded during the August 2020 Test beam campaign in Area T24.

tion, ensuring that the triggers can happen in the entire opening window. In addition, even when two triggers are close together within the KPIX cycle, the system was powered down in between the two measurements due to power pulsing which should decouple the results from one another.

The effect of the different opening windows on the noise is exemplified in Figure 10.38 which shows the noise distribution for all 1840 connected strips S47 using different time windows. The largest window ranging from 0 to 8191 BCC shows the overall highest amount of noise where the peak is located at higher noise values, is wider and possesses a longer tail to large values which is similar to results of the window from 1000 to 8191 BCC though the mean noise is slightly lower. When limiting the end point of the measurement to 4000 BCC, more channels are located in the peak as opposed to the tail of the distribution. Finally, when limiting the window to a late opening from 4000 to 8191 BCC the largest effect is seen, in that not only do more channels move from the tail to the peak, the entire peak gets shifted downwards to lower values. The mean noise of the four opening windows can be found in Table 10.3 and based on the improved mean noise performance the window of 4000 BCC to 8191 BCC is used to determine the Lycoris module performance.

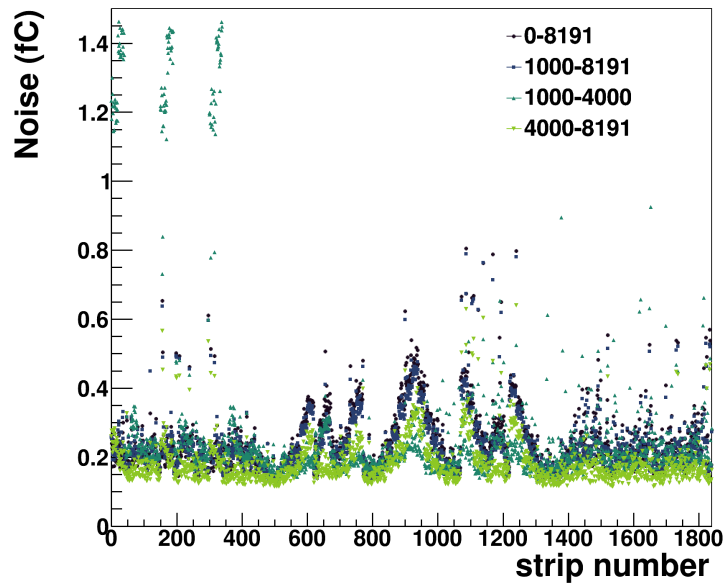
All channels show a similar reduction in noise when adjusting the time windows to later within the KPIX acquisition cycle (see Figure 10.39). Comparing two data sets with the same 1000 to 4000 BCC opening window which were taken a few days apart to one another (see Figure 10.40) shows that the noise spikes in the center are not dependent on the time opening window. It seems most likely that while the systems noise performance differs between the different opening windows, the appearance of the noise spikes is related to noise in-



**Figure 10.38** – Noise distribution of S47 for different time opening windows.

Opening Window	Mean Noise
0 – 8191 BCC	0.24 fC
1000 – 8191 BCC	0.23 fC
1000 – 4000 BCC	0.22 fC
4000 – 8191 BCC	0.18 fC

**Table 10.3** – Mean noise for different opening windows for S47



**Figure 10.39** – Noise plotted against the time at which the trigger was registered within the KPiX acquisition phase of S47 for different time opening windows.

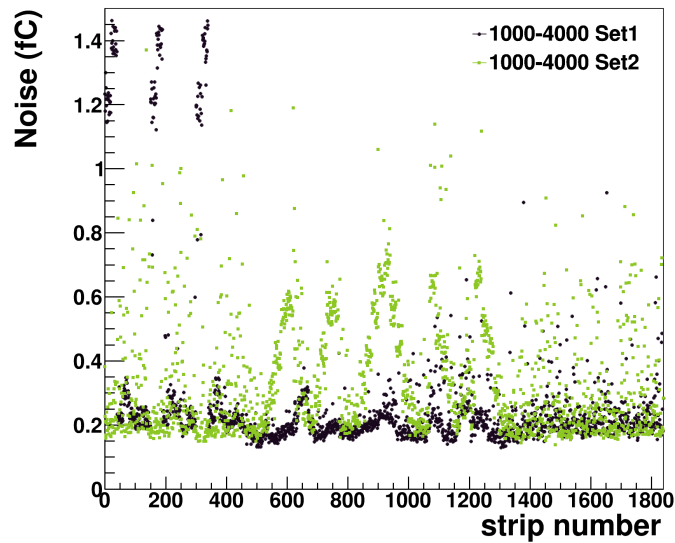
duced into the system from the outside.

Several aspects of the noise performance for different time windows are not fully understood. Analyzing the noise versus the KPiX time, the time at which the KPiX system received its trigger within the acquisition cycle many different pictures open up which rarely look the same between different data sets. The noise plotted against the time within the KPiX *acquisition cycle* is depicted in Figure 10.41. The time window from 4000 to 8191 shows a fairly calm behavior with a parabolic noise development. The noise starts at a value of 0.2fC which gradually reduces to 0.14fC at 6000BCC after which it again rises to 0.2fC at 8191BCC. The other three time windows appear to show two different effects that are superimposed upon one another.

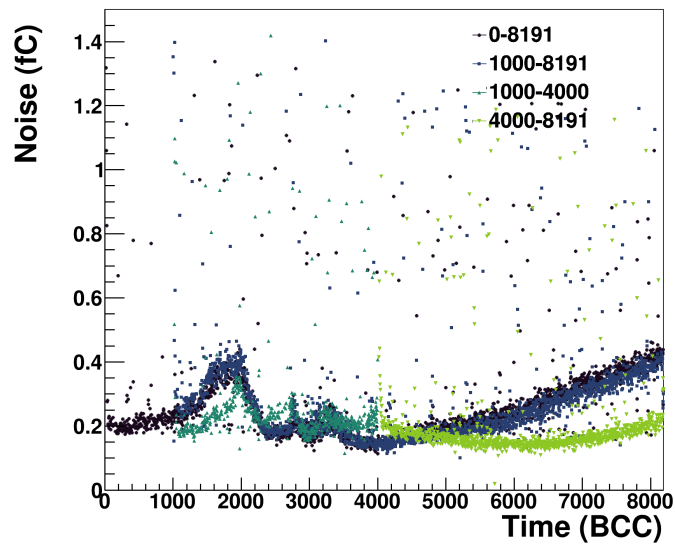
The 1000 to 8191BCC set as well as the 0 to 8191BCC set both have a minimum at around 4000BCC which rises afterwards. Before 4000BCC the distributions show a more erratic behavior with irregular noise spikes. Each point represents its own *acquisition cycle* meaning that whatever is responsible for the noise generates it synchronous to the KPiX over a duration of several milliseconds in between which the KPiX is powered down.

Further investigation has shown, that a possible candidate for the noise lies within the digital back-end of the system. The time of the trigger is recorded via a gray coded (see Table 5) 13 bit counter. It has been found that the noise in the system shows a correlation to

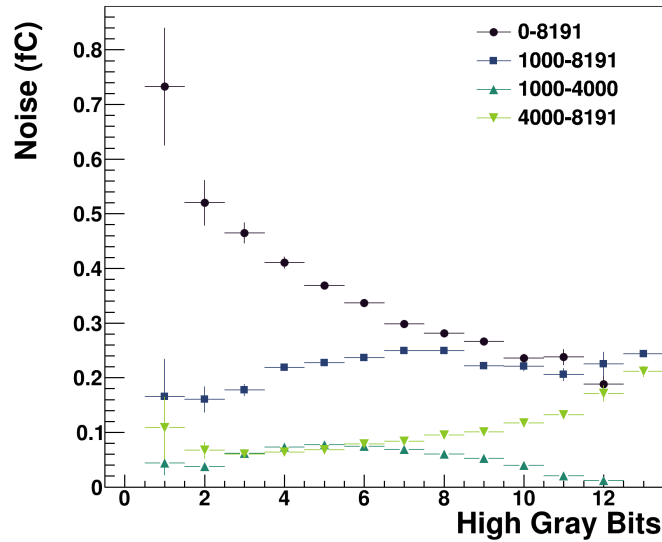




**Figure 10.40** – Noise plotted against the Strip number of S47 for two different data sets of the 1000 to 4000 BCC opening window in the same laboratory configuration.



**Figure 10.41** – Noise plotted against the Strip number of S47 for different time opening windows.

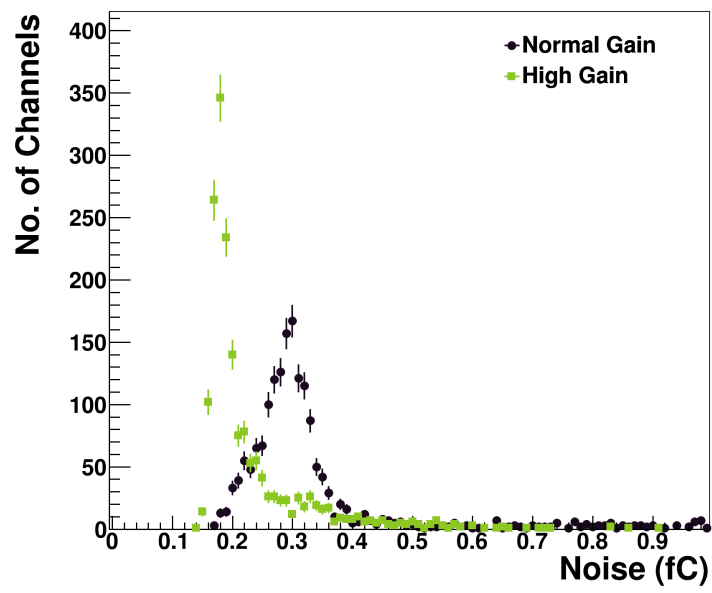


**Figure 10.42** – Noise plotted against the the gray coded bits. An entry is filled into the corresponding bin if the bit is set to high at the point of measurement.

how many gray coded bits are set to high (see Figure 10.42). Therefore it cannot be ruled out that an issue with the digital back-end is responsible for the time correlated noise between different *acquisition cycle* as in external triggering operation 1024 bits have to be written into the register which could result in fluctuations on the power line and consequently noise injection into the system. Conclusive evidence would have to be gathered from a simulation of the digital back-end which was not within the time frame of this thesis.

### High Gain versus Normal Gain

External triggering measurements were performed in both normal gain and high gain operation in order to investigate potential performance differences between the two. Figure 10.43 depicts the noise distribution of S47 recorded during the August 2020 test beam campaign, once operated in normal gain and once in high gain. In high gain operation the mean noise in the system KPiX is slightly lower at  $N_{\text{high}} = 0.2 \text{ fC}$  compared to  $N_{\text{normal}} = 0.3 \text{ fC}$  during normal gain operation. This behavior is common among all Lycoris modules operated at the DESY II Test Beam Facility. The most likely explanation is that noise is introduced downstream of the front-end. This height of this noise component is independent of the gain operation and is therefore lower relative to the signal in high gain than in normal gain. As a result, all measurements concerning the Lycoris module performance focus on data taken in high gain operation for its improved noise performance relative to the normal



**Figure 10.43** – Noise distribution of S47 for different gain settings.

gain operation.

## 10.5 Tracking results

Tracking results are all results gathered from tracks generated by the AZALEA system. The Lycoris system was considered a DUT to gain more detailed insight into the sensor sub structure. For this search, clusters on the Lycoris modules within a distance of  $y_{\text{assign}} = 250 \mu\text{m}$  to the projected track position before any GBL track corrections are accepted and in the case of multiple clusters within the window the closest cluster is taken. All clusters hereafter are only those that are assigned to an AZALEA and are referred to as *tagged hits*.

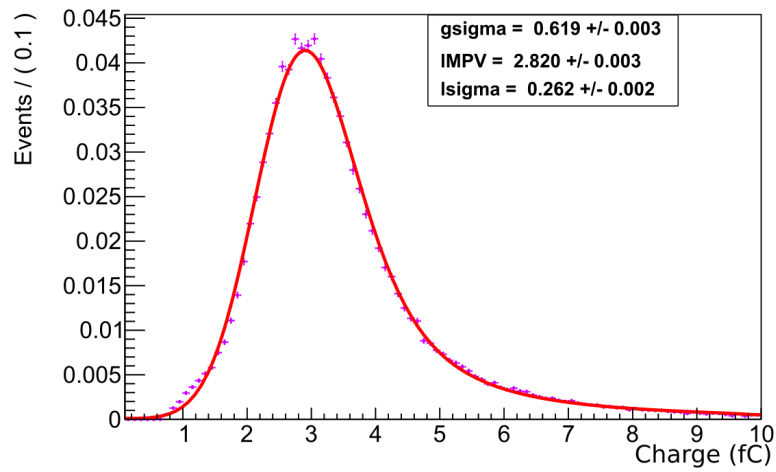
### 10.5.1 Charge of *Tagged Hits*

As mentioned in Section 6.2.1, the sensor has a thickness of  $320 \mu\text{m}$  which, based upon what was mentioned in Section 2.1, results in an expected MPV of  $3.6 \text{fC}$  (see section 2.1.3). This expectation is compared with the charge of *tagged hits* as the assignment to the track should filter out a significant amount of noise based clusters. The charge distribution of all *tagged hits* is shown in Figure 10.44 with a Landau-Gauss convolution fitted to the distribution using ROOFIT. The MPV of the Landau fit results in a value of  $MPV_{\text{Landau}} = 2.82 \text{fC}$  and a mean value of  $\text{Mean} = 3.52 \text{fC}$  which is below the expected value for the MPV of  $3.6 \text{fC}$ . The reason for this is in parts due to the readout structure of the Lycoris module. Half of the strips are floating and are read out via the capacitively coupled readout strips. Based on section 3.1.5, less charge is expected on floating strips as a result of charge loss via coupling to the back-plane. It was also found, that the AIDA TLU possesses a minimum internal trigger delay of about  $140 \text{ns}$  [47]. This, in combination with cable delays, could result in the charge collection of the system being started too late resulting in not all charge being integrated. Unfortunately it was not possible to perform further tests to investigate this cause further within the scope of this thesis. The slight bump of entries at low charge values visible in the plot is a result of incorrectly reconstructed clusters and is addressed below.

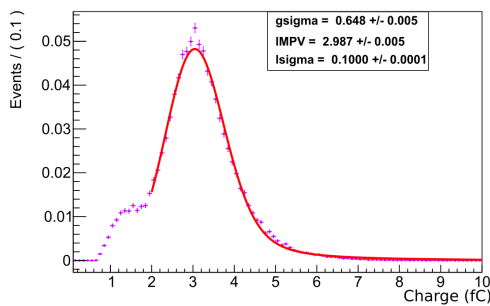
#### Charge for Different Cluster Sizes

The determination of whether a cluster is based on a floating strip hit or a readout strip hit can be done via correlation of the cluster size. For a floating strip the charge is shared between the two adjacent strips meaning most two strip clusters are the result of a floating strip clusters, while most one strip clusters are the result of a readout strip clusters.

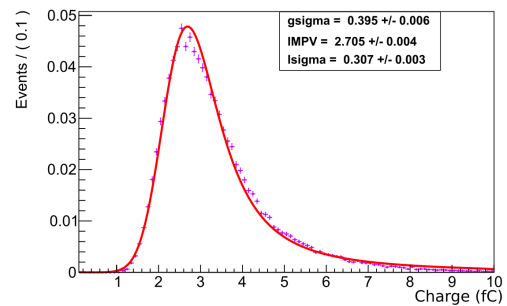
Figure 10.45 shows the charge of all *tagged hits* split into the different cluster sizes. The most apparent effect of splitting the charge into the different cluster sizes is seen for the



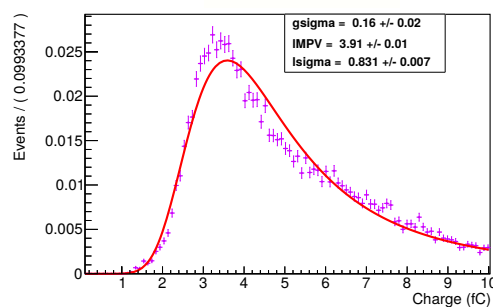
**Figure 10.44** – Charge of *tagged hits* generated by the AZALEA system with a Landau-Gauss convolution fit.



(a) Cluster size one



(b) Cluster size two



(c) Cluster size three and above

**Figure 10.45** – Charge of *tagged hits* with Landau-Gauss convolution fits, split into different cluster sizes.



**Figure 10.46** – Sketch showing the sub cell of the SiD sensor.

charge of all size one clusters. There are two separate rise points in the distribution with the first rise in entries starting at around 0.7fC which flattens out at 1.5fC before rising once more. The reason for the early rise lies in floating strip hits splitting the charge into the adjacent strips of which one drops below the  $S/N_{\text{strip}} \geq 2$  cut as a result of the significant variance in the noise of different strips. This indicates a high pollution of size one clusters with floating strip hits.

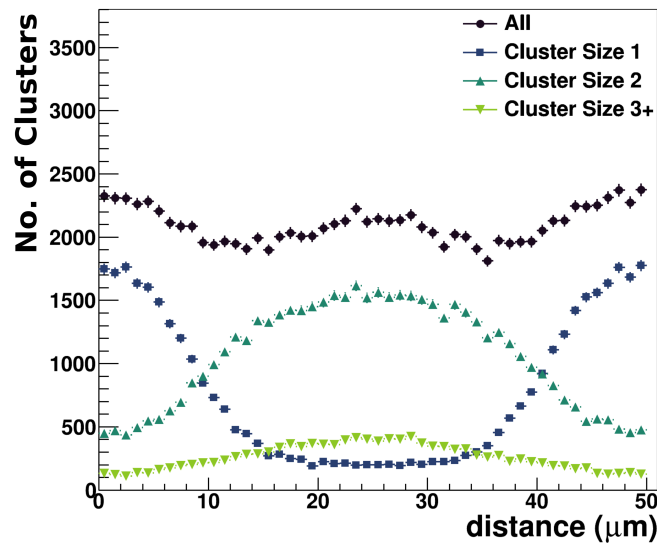
The size two cluster distribution does not have any striking features in the distribution. Comparing the MPV of the Landau distribution between the size one and size two clusters one can see that the MPV of the Landau distribution is lower for size two clusters ( $MPV_{\text{size2}} = 2.7\text{fC}$ ) compared to size one clusters ( $MPV_{\text{size1}} = 2.99\text{fC}$ ). All clusters of size three and more show a heavily skewed distribution to high charge values. The reason is that many of these clusters are a result of large angle scattering and  $\delta$  electrons, both of which deposit higher charge within the sensor over a larger area.

### Charge based on Track Hit Position

A more reliable method of determining whether a *tagged hit* is a readout strip hit or a floating strip hit can be performed using the information gained by the AZALEA telescope. Instead of relying on the position of the cluster or its size, the local hit position  $y_{\text{loc}}$  is determined via the projected track position using the GBL track projection.

The sensor is a regular repeating structure of floating and readout strips and can be folded back on a two readout strip section to increase statistics. A sketch of such a section is depicted in Figure 10.46. Using this, a better understanding of the relation between the cluster size and the hit position is achieved.

Figure 10.47 is a 1D histogram for all *tagged hits* that were assigned to an AZALEA gen-



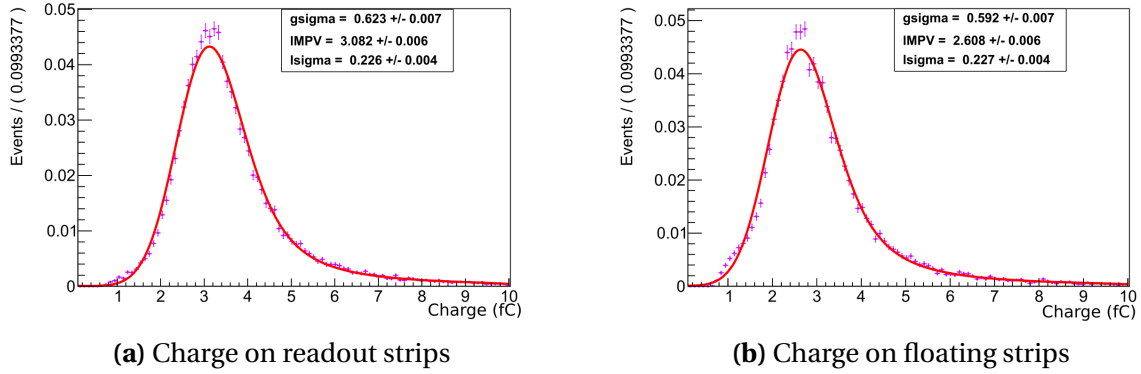
**Figure 10.47** – Number of clusters on the sensor sub-cell split into different cluster sizes.

erated track split into different cluster sizes. The x axis of the histogram shows the local track hit position as determined by the AZALEA telescope projected to the sub cell shown in Figure 10.46. Half of the readout strips are located at  $0 \mu\text{m}$  and  $50 \mu\text{m}$  with the floating strips at located at  $25 \mu\text{m}$ . The histogram shows the expected connection between the hit position and the cluster size though it also shows that while there is a correlation, a significant portion of size one clusters are located near a floating strip and vice versa. For clusters with three or more strips the distribution is slightly favored towards to center as a result of two hit floating clusters being assigned as three hit by adding a noise strip to the cluster though with a fairly flat distribution as the occurrence of delta electrons is independent of the position hit.

Using the cell sub-structure the readout and floating strip hit are defined based on the hit location of the track within the sub cell  $y_{\text{sub-cell}}$ .

- **Readout hit:** If the projected hit location within the sub cell is located at:  
 $y_{\text{sub-cell}} < 12.5 \mu\text{m}$  or  $y_{\text{sub-cell}} > 37.5 \mu\text{m}$ .
- **Floating hit:** If the projected hit location within the sub cell is located at:  
 $37.5 \mu\text{m} \geq y_{\text{sub-cell}} \geq 12.5 \mu\text{m}$ .

The results of this split are shown in Figure 10.48. Figure 10.48a shows the charge on all readout strip hits and Figure 10.48b shows the charge on floating strip hits. Both distributions show a robust Landau-Gauss convolution with a  $MPV_{\text{floating}} = 2.61 \text{ fC}$  and  $MPV_{\text{readout}} =$



**Figure 10.48** – Charge of *tagged hits* after splitting hits into readout strip hits and floating strip hits.

3.08 fC, with similar Landau and Gaussian sigmas and with a similar amount of entries for the floating hits and readout hits.

From the ratio of the two most probable values the amount of charge lost due to coupling to the back-plane evaluates to:

$$Q_{\text{total}} = Q_{\text{readout}} = Q_{\text{floating}} + Q_{\text{backplane}} \Rightarrow \frac{Q_{\text{backplane}}}{Q_{\text{readout}}} = 1 - \frac{Q_{\text{floating}}}{Q_{\text{readout}}} \Rightarrow \frac{Q_{\text{backplane}}}{Q_{\text{readout}}} = 1 - 0.85 = 0.15. \quad (10.2)$$

Using the 15% loss, the ratio between the inter-strip capacitance and the capacitance to the back-plane evaluates to (3.9):

$$C_b / C_{\text{ss}} = 0.088. \quad (10.3)$$

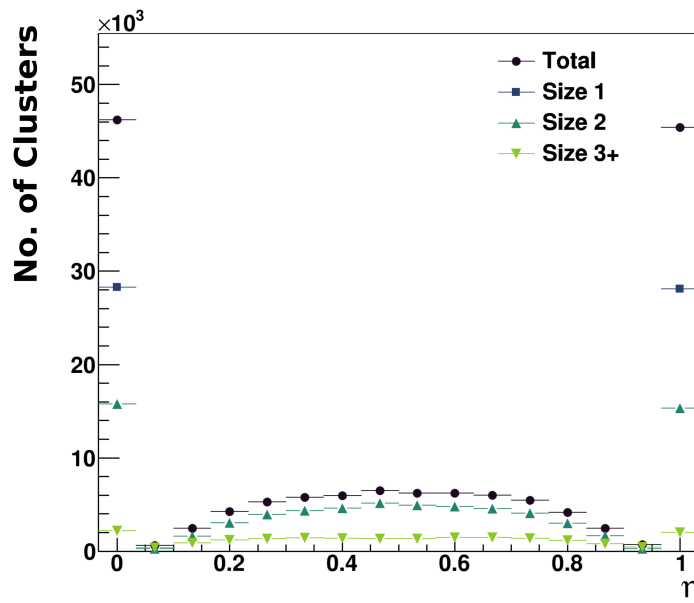
This is significantly larger than the value obtained via the inter-strip capacitance measurement presented in section 7.2.3. As is pointed out there, the results from the direct measurement are not without question and should be repeated with the changes to the measurement setup that are mentioned there.

### Eta Distribution of Tagged Hits

Using the hit position information of the AZALEA telescope allows the calculation of the eta distribution of all clusters which is defined as [3]:

$$\eta = \frac{Q_{\text{left}}}{Q_{\text{left}} + Q_{\text{right}}}.$$





**Figure 10.49** –  $\eta$  distribution of all *tagged hits*.

$Q_{\text{left}}$  is the charge of all strips for which the strip position is lower than the projected track hit position  $y_{\text{strip}} < y_{\text{track-hit}}$ .  $Q_{\text{right}}$  is the charge of all strips for which the strip position is higher than the projected track hit position  $y_{\text{strip}} > y_{\text{track-hit}}$ . The distribution depicted in Figure 10.49 shows the  $\eta$  distribution for different cluster sizes. Single strip cluster can only be located to either side of the projected hit position and as such  $\eta = 1$  or  $\eta = 0$  are the only possibilities. For two strip clusters in most cases the projected hit location is located between the two strips that make the cluster with a peak in the center that reduces the closer the distribution goes to either  $\eta = 0$  or  $\eta = 1$ . This stems from the fact that most two strip clusters are produced via the charge sharing resulting from hitting a floating strip which spreads the charge equally to its adjacent strips.

## 10.5.2 Bias Voltage Impact on Lycoris Module Performance

As mentioned in section 3.1.4, the gathered charge, as well as the cluster size and collection speed depend on the bias voltage applied to the sensor. By varying the bias voltage of the Lycoris module between 0V (underdepleted) and 150V (overdepleted) the relation is investigated further.

### Cluster Charge versus Bias Voltage

Performing measurements with an under-depleted Lycoris module should result in a lowered charge yield as a result of the reduced size of the depletion zone. This allows for an independent verification of the results gathered from the CV measurements (see section 7.2.2) through which the sensors depletion voltage is derived. Figure 10.50 depicts the registered charge on readout strip clusters for different bias voltage levels. A few key aspects of the plot are clearly visible.

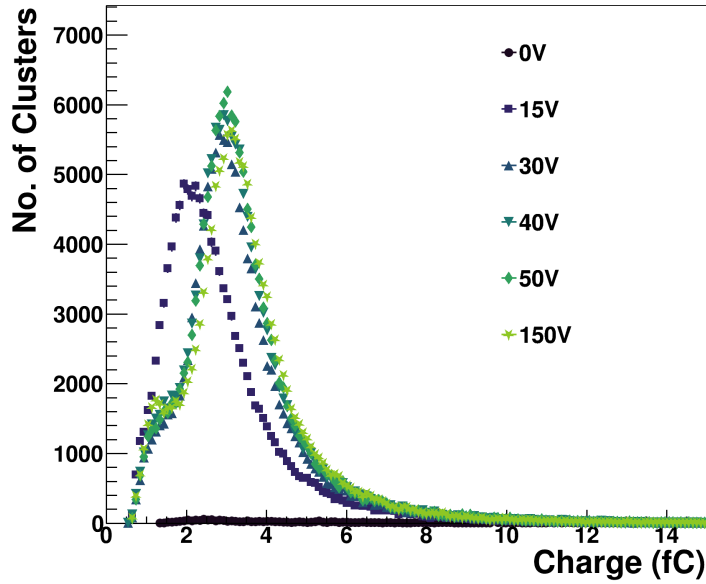
The amount of *tagged hits* when the Lycoris module is operated without any bias is extremely low. This is as expected as not only is the charge yield extremely low because of the small depletion zone resulting in only few clusters with charge above the threshold, because of the low depletion channels are connected as they are not sufficiently isolated.

Of greater interest are the charge distributions at voltage levels which are below the previously calculated depletion voltage. The dark blue squares show the distribution at a bias voltage 15V showing that the overall amount of clusters reduced. In addition, the peak of the distribution is shifted to lowered values. The same is true to a lesser extent for the distribution at a bias voltage of 30V which is depicted in the dark blue upwards triangles. The fall off after the peak is happening at lower charge values compared to higher bias voltages. The distributions show only minor differences for higher bias voltages. This confirms the previously found results that the depletion voltage of the Lycoris module is at  $\approx 40\text{V}$  (see section 7.2.2).

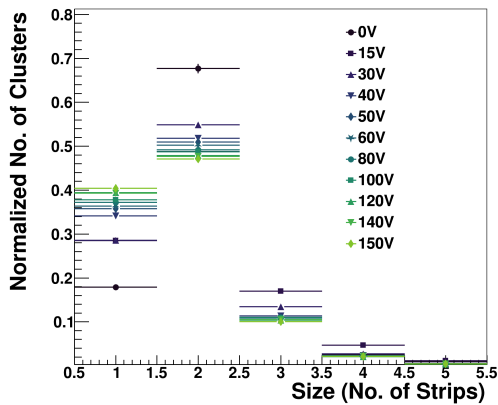
### Cluster Size as a Function of Bias Voltage

Investigation of the Lycoris module performance were performed by looking at the cluster size distribution of *tagged hits* for different bias voltage levels. This is done in order to verify the relation between the charge spread through diffusion and the bias voltage. Both a distribution and a mean cluster size value, normalized to the amount of entries, are depicted in Figure 10.51. Figure 10.51a shows the expected behavior that with increasing bias voltage, due to reduced diffusion within the sensor, more clusters consisting of single strip entries are reconstructed.

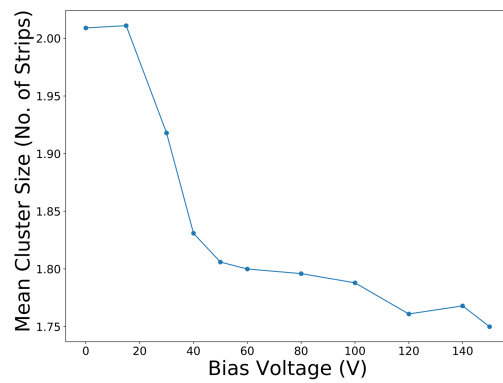
Figure 10.51b shows the mean cluster size versus the bias voltage in which one can see that the cluster size undergoes a large change once the depletion voltage of the Lycoris module is reached as the entire volume is depleted and all charge is collected via drift. Afterwards the size is only reduced slightly as a further increase of the bias voltage only increases the drift field within the Lycoris module resulting in a quicker charge collection



**Figure 10.50** – Charge distribution of all readout strip clusters on AZALEA track for different bias voltages.

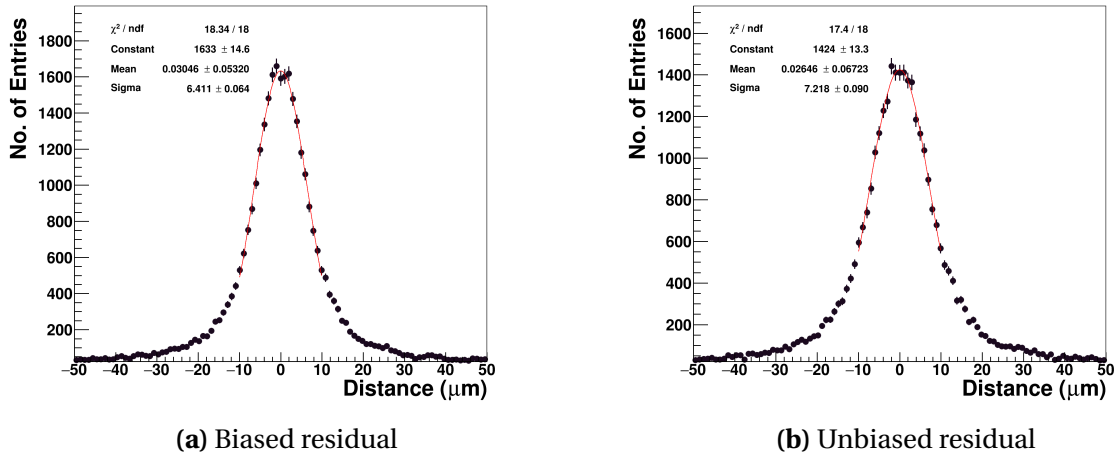


**(a)** Entries vs cluster size



**(b)** Mean cluster size vs bias voltage

**Figure 10.51** – Relation of the cluster size for all tagged clusters at different bias voltages.



**Figure 10.52** – Residuals of the projected track hit to the cluster position for S47.

at the electrodes reducing the time the charge can spread via diffusion.

### 10.5.3 Single Point Resolution

The AZALEA telescope can be used to determine the single point resolution of the Lycoris modules. The residual between the projected track position at the location of the Lycoris module and the Lycoris hit location is compared. The DUT hit can be included to the fit for what is referred to as a biased residual or excluded for an unbiased residual (see Section 4.2.4).

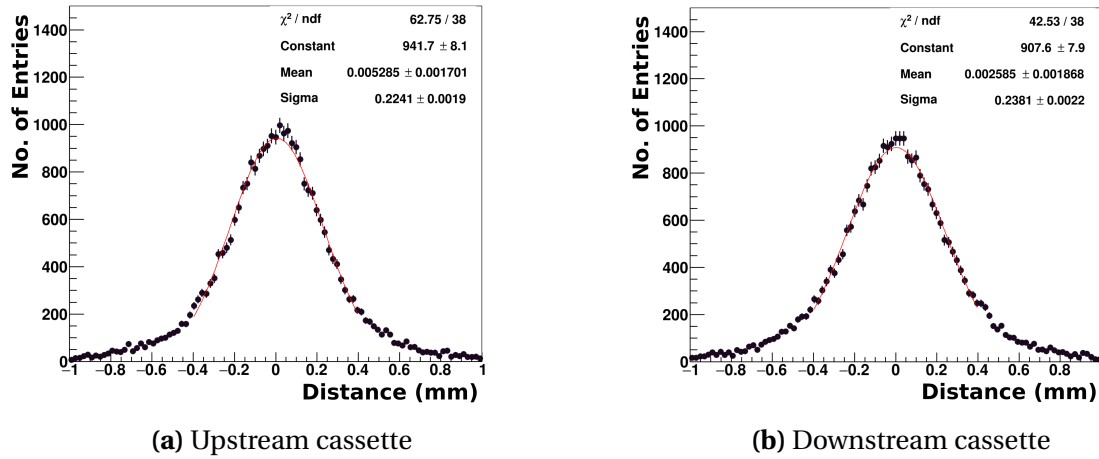
Figure 10.52b shows the unbiased residual distribution between the projected track hit generated by the AZALEA telescope and the cluster position on the Lycoris module. The resolution is determined by performing a fit to the Gaussian core of the distribution. The fit has a width of  $\sigma_{\text{unbiased}} = (7.45 \pm 0.07) \mu\text{m}$ . Similarly, Figure 10.52a shows the biased residual distribution with a Gaussian fit of width  $\sigma_{\text{biased}} = (6.69 \pm 0.05) \mu\text{m}$ . As the unbiased result includes also the fit errors in its results, the true resolution of the system is determined by calculation of the geometric mean of the biased and unbiased fit widths [39]:

$$\sigma_{\text{SinglePoint}} = \sqrt{\sigma_{\text{unbiased}} \cdot \sigma_{\text{biased}}} = (6.80 \pm 0.07) \mu\text{m}. \quad (10.4)$$

The results for the six Lycoris modules used during the March 2020 and August 2020 beam campaigns are listed in Table 10.4. The resolution of all six Lycoris modules is below the necessary single point resolution of  $\sigma_{\text{req-y}} = 10 \mu\text{m}$  the system was required to have in order to determine the momentum resolution with a high enough resolution to be usable to verify

Lycoris module	$\sigma_{\text{biased}} (\mu\text{m})$	$\sigma_{\text{unbiased}} (\mu\text{m})$	Single point resolution ( $\mu\text{m}$ )
S59	$6.64 \pm 0.07$	$7.55 \pm 0.11$	$7.08 \pm 0.09$
S40	$6.30 \pm 0.06$	$7.05 \pm 0.09$	$6.66 \pm 0.08$
S43	$6.64 \pm 0.07$	$7.45 \pm 0.10$	$7.03 \pm 0.09$
S48	$6.38 \pm 0.06$	$7.08 \pm 0.09$	$6.72 \pm 0.08$
S47	$6.41 \pm 0.06$	$7.22 \pm 0.09$	$6.80 \pm 0.07$
S46	$6.55 \pm 0.07$	$7.24 \pm 0.09$	$6.89 \pm 0.08$

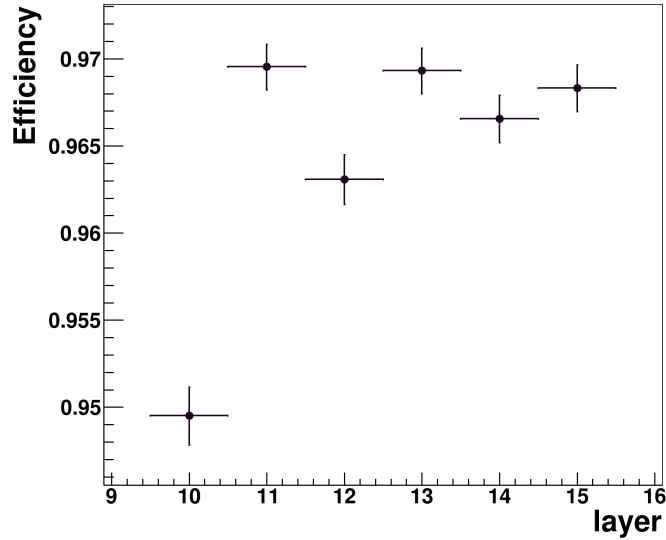
**Table 10.4** – Fit results of the Gaussian fit to the biased and unbiased residuals of Lycoris modules



**Figure 10.53** – S-triplet residual in x to the projected track hit.

the LPTPC results.

As a result of the cassette configuration, a single Lycoris module is incapable of determining the x position as a result of the insufficient stereo angle. In order to determine the x position, a minimum of two layers are required. The resolution of the system in x is determined via the residual of the AZALEA track  $x_{\text{track}}$  to the x position at the *S-triplet* (see section 4.2.3)  $x_{\text{trip}}$  that is calculated separately for each cassette. As the cassette triplet is generated independent from the AZALEA track finding, the distribution is always unbiased and as such a upper limit to the achievable resolution. Figure 10.53 shows the residuals for both cassettes independently with a Gaussian fit to the peak of the distribution shows a resolution of  $\sigma_{x\text{-down}} = (224 \pm 2) \mu\text{m}$  and  $\sigma_{x\text{-up}} = (238 \pm 2) \mu\text{m}$  which for both was below the necessary resolution in x of  $\sigma_{\text{req-x}} = 1 \text{ mm}$ .



**Figure 10.54** – Efficiency for all six Lycoris layers for all AZALEA tracks that are matched in time.

#### 10.5.4 Single Plane Efficiency

Using the AZALEA telescope, an independent determination of the efficiency of the Lycoris modules is possible. This is done by searching for *tagged hits*. The total number of *tagged hits* on each plane is divided by the total number of AZALEA tracks as each track is supposed to be visible in each Lycoris module. Many tracks in the AZALEA system can be found which, as a result of the differing frame readout time, are not necessarily present within the Lycoris system, resulting in a seemingly lowered efficiency. For this measurement, the Timepix3 layer is used to determine the timestamp of tracks within the AZALEA system (see section 8.3.2) in order to reevaluate which tracks can be found by the Lycoris modules. Using only tracks which have an assigned Timepix3 hit and using the time of the Timepix3 hit to correlate with the time of the Lycoris hits results in the histogram shown in Figure 10.54 for the single plane efficiencies of all tracks which are guaranteed to be present within the Lycoris system. The resulting efficiency for the different planes is shown in Table 10.5. An average single plane efficiency of  $\rho_{\text{single}} = (96.3 \pm 0.1)\%$  and a resulting track efficiency of  $\rho_{\text{track}} = 82.8\%$  for tracks with a minimum of five hits is achieved.

This is below values for other sensors such as the sensor used in final detectors such as the CMS [107] or ATLAS [61] experiment but still sufficient for operation at the test beam as it simply requires a slight increase in running time to gather the necessary statistics. The reason as to why the Lycoris modules do not reach a higher efficiency lies in the large

Lycoris module	Efficiency
S59	$(95.0 \pm 0.2) \%$
S40	$(97.0 \pm 0.1) \%$
S43	$(96.2 \pm 0.1) \%$
S48	$(96.7 \pm 0.1) \%$
S47	$(96.6 \pm 0.1) \%$
S46	$(96.7 \pm 0.1) \%$

**Table 10.5** – Single plane efficiency for the six Lycoris modules in the test beam.

noise irregularities present in certain strips (see section 10.4.1) and if they can be eliminated should result in a large increase in the overall efficiency of the Lycoris modules.

## 10.6 Summary

Lycoris module tests were performed including tests of the three main operating modes. It was found that for many of the Lycoris modules an asynchronous data transfer is seen which was the result of slight delays in the end of the digitization phase between different KPiX ASIC that resulted in some KPiX not being operable together. The problem was resolved via slight adjustments to the software induced delay between the end of the acquisition phase and the start of the pre-charge phase. In addition, the DAQ was adjusted to allow running even if the data is sent out asynchronous. These events are flagged for debugging and are not used for any analysis.

The calibration performance of many different Lycoris modules were investigated in which it was found that all higher *buckets*, the analog storage containers within the KPiX, are unusable at standard operating values due to *stale data* which is more likely to appear the larger the distance between the channel and the KPiX power pads. This problem points towards an issue within the KPiX where a latch is not cleared resulting in the same data being read out over and over. While a permanent fix of the problem would require a new ASIC, a recent firmware change that allows the increase of the pre-charge clock period beyond the current limits has shown to be a possible solution for this problem. It was also found that the time allocated for the start-up phase of the KPiX acquisition cycle impacts the amount channels with a good digital response in which some KPiX perform better with a slightly increased start-up phase. Further increases however were found to negatively impact all KPiX tested. Finally, it was found that the overall digital response of the channels strongly depends on the ambient humidity. Measurements with both a climate chamber

and a drying oven have shown that increasing levels of humidity negatively impacts the digital response of the channel during calibration. As the impact lasts beyond direct exposure but could be resolved via baking of the sensors at 60°C the conclusion is that this is most likely due to leakage of the injection capacitor through the input line as a result of reduced sheet resistance due to accumulation of water on the module surface which required all further sensor test to be performed in a dry environment.

The internal triggering operation of the system was tested at the test beam, first by performing the monster suppression in order to operate the system at higher trigger thresholds and finally determining the response of the system to the beam. In this operation it was found that there exists unwanted cross talk between the two KPiX ASIC on the tracker sensor as the overall noise is reduced when only one of the two KPiX are operated. It was found that even with a gradual disabling of channels it is not possible with the current iteration of the KPiX ASIC achieve a sufficiently low threshold while ensuring that most channels on the ASIC are not disabled. The system was put into the beam at a higher threshold in which the general feasibility of the internal triggering operation was verified. The system shows a clear difference in the system response with beam hitting the sensor compared to without. Nonetheless, the overall single plane efficiency of the system in internal triggering was determined to be about  $\approx 1\%$  proving that the system is not usable as a telescope in internal triggering operation.

The Lycoris modules were tested in external triggering operation in which it was found that the sensors have strong correlation between the channel location and the noise performance of the channels. Many noise sources could be eliminated with modifications to the electronics and operating parameters. Some noise source persist and it is difficult to determine the sources of this noise as they are correlated to structures in both KPiX and sensor space making either of them a candidate for their existence. It was found, that the opening window during which the KPiX is capable of recording data has a large impact on the overall noise performance. Due to the structure that stays consistent over large time frames of multiple milli seconds, the noise source has to be synchronous to the operation of the KPiX and can potentially be an issue of the digital back-end inducing time correlated noise into the system. This might be a result from the upscaling from 64 to 1024 channels between KPiX generations during which no changes to the digital back-end were conducted. A mean noise value of 0.18fC was achieved for the Lycoris modules and these settings are used for all test beam measurements investigating the systems performance as a DUT within the AZALEA telescope.

Using Lycoris as a DUT, it was found that while the overall distribution fits extremely



well to the expectations shown in section 2.1.3, the modules have a slightly lowered amount of registered charge which is due to both the floating strips and some difficulties in which the minimum delay stemming from the AIDA TLU [47] results in a possibly non optimized charge collection. The response was investigated further for the different cluster sizes and local hit locations in which it was shown that floating strip clusters, that were determined using the local track projection, record on average 15% less charge which is lost to the back-plane. Both the single point resolution and single plane efficiency of the Lycoris modules were determined using the tracks generated by the AZALEA telescope. Using both biased and unbiased fits it was shown that all Lycoris modules tested in the August 2020 test beam campaign achieve a single point resolution between  $\sigma_y = 6.66 \mu\text{m}$  and  $\sigma_y = 7.08 \mu\text{m}$  in y direction as well as a triplet resolution along x of  $\sigma_x = 224 \mu\text{m}$  to  $\sigma_x = 238 \mu\text{m}$ . This means that the modules easily achieve the minimum resolutions set in section 6.1 of resolutions better than  $\sigma_{\text{req-y}} = 10 \mu\text{m}$  and  $\sigma_{\text{req-x}} = 1 \text{mm}$ .

The modules tested have all achieved efficiencies between  $\rho_{\text{single}} = 95.0\%$  and  $\rho_{\text{single}} = 97.0\%$  resulting in a combined track efficiency of  $\rho_{\text{track}} = 82.8\%$ . This is in parts due to noise irregularities still present within the sensor. While the Lycoris modules are not yet at a level which is expected for operation in a final detector [107][61], their performance is sufficient for operation as a telescope as it simply means a slight increase in running time to gather the necessary statistics.



# Chapter 11

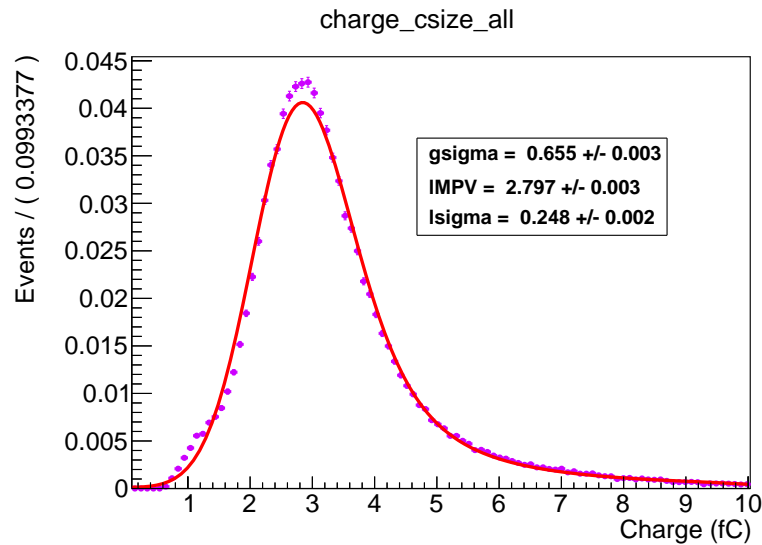
## Lycoris Telescope Performance

After verifying the performance of the Lycoris modules, the full system performance is tested to conclude the thesis. This is key, as the project is supposed to develop a reference system to be used to investigate other DUTs. The systems performance as a telescope is a combination of the previously determined Lycoris module performance and the performance of the track finding and fitting algorithm which was tailor made for this system. The algorithm tackles the issues of operating a six layer strip telescope with one-dimensional resolution on each plane, as traditional algorithms for pixel telescopes do not work. The algorithm used is based on *EUTelpy* [35] and is described in section 4.2.3. A description of the mathematical calculations are found in section J. All cluster cuts used for the standalone track finding and fitting are the same as in the azalea based track finding described in section 9.2.2.2. The chapter starts by comparing key module performance values that were determined using the AZALEA based track finding and fitting with the results gathered by the tailor made standalone track finding and fitting. For the standalone algorithm to be valid it needs to provide similar results to the AZALEA track finding and fitting algorithm.

### 11.1 Lycoris Track Finding and Fitting

#### 11.1.1 Charge on Tagged Hits

The physical charge deposited within the Lycoris module is independent of the method of track finding and fitting and only depends on the physical sensor and ASIC parameters. As such, for the standalone algorithm to be correct, the resulting charge distribution should be similar to the one that was determined independently by the AZALEA based



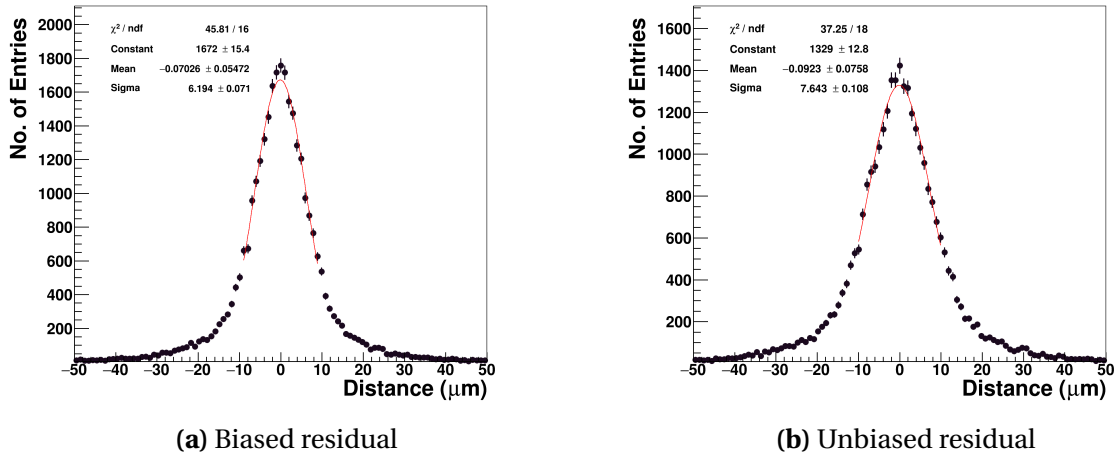
**Figure 11.1** – Charge distribution of all clusters on the standalone track generated by the Lycoris telescope.

tracks shown in section 10.5.1.

Figure 11.1 shows the charge distribution of clusters used to generate a track using the Lycoris standalone track finding and fitting. A Landau-Gauss convolution is fitted to the distribution. 2.80 fC for the most probable value and 0.25 fC for the Landau width and 0.66 fC for the Gaussian width of the distribution are extracted. The charge for clusters on tracks generated by the AZALEA telescope which is shown in Figure 10.44 have a MPV of 2.82 fC and a width of 0.26 fC for the Landau and 0.62 fC for the Gaussian. This shows that both algorithms select similar hits to one another and that there are no larger differences in the final selection of hits on track indicating that the algorithm itself performs a valid selection of tracks.

### 11.1.2 Hit Residuals

The single point resolution is heavily biased to the four stereo layers as the track is build using them (see section 4.2.3). Only the axial layers, which are used to filter out noise clusters, are unbiased from the track finding and can be used to determine the single point resolution. Figure 11.2a shows the residual for biased tracks and Figure 11.2b shows the residual for unbiased tracks (see section 4.2.4), both for layer 13 with a Gaussian fit limited to the gaussian core of the center to determine the single point resolution. The resolution of the system is calculated using the geometric mean of the biased and unbiased resolution



**Figure 11.2** – Biased and unbiased residual of the projected track hit to the cluster position for S43.

Lycoris module	$\sigma_{\text{biased}}$ ( $\mu\text{m}$ )	$\sigma_{\text{unbiased}}$ ( $\mu\text{m}$ )	Single point resolution ( $\mu\text{m}$ )
S43	$6.19 \pm 0.07$	$7.64 \pm 0.11$	$6.88 \pm 0.09$
S48	$6.06 \pm 0.07$	$7.52 \pm 0.10$	$6.75 \pm 0.08$

**Table 11.1** – Fit results of the Gaussian fit to the biased and unbiased residuals of the two axial test beam sensors.

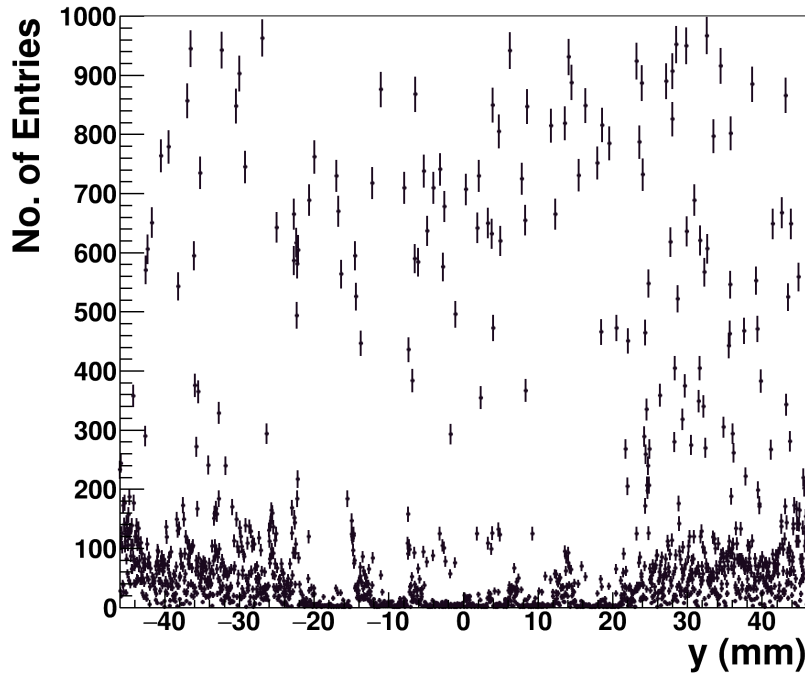
to be [35]:

$$\sigma_{\text{SinglePoint}} = \sqrt{\sigma_{\text{unbiased}} \cdot \sigma_{\text{biased}}} = (6.88 \pm 0.09) \mu\text{m}. \quad (11.1)$$

which is similar to the resolution determined by the AZALEA system in section 10.5.3.

## 11.2 Lycoris Telescope Tracking Efficiency

Determining the standalone track finding efficiency is not possible for the single layers with the current version of the track finding and fitting algorithm. The system uses only six strip layers with dedicated roles for the different layers in that the four stereo layers are used to determine the track parameters and the two axial layers are used to filter out noise combinations. Tracks are currently heavily biased in that tracks can only be found if they have a hit on each of the stereo layers and at least one axial layer. As such a determination of the efficiency of every single layer similar to the method used with the AZALEA system is currently not possible. Instead, the average efficiency of the system is determined. The number of tracks found is compared to the total number of events. 25000 triggers are



**Figure 11.3** – Local *cluster* positions on S47 for a run without beam

recorded in the data sample. Assuming that each trigger is equivalent to a particle passing through the Lycoris module that means for a fully efficient system a minimum of one track per event is expected. By limiting ourselves to six hit tracks a total of 19595 events with at least one track is found from which the track efficiency is calculated to:

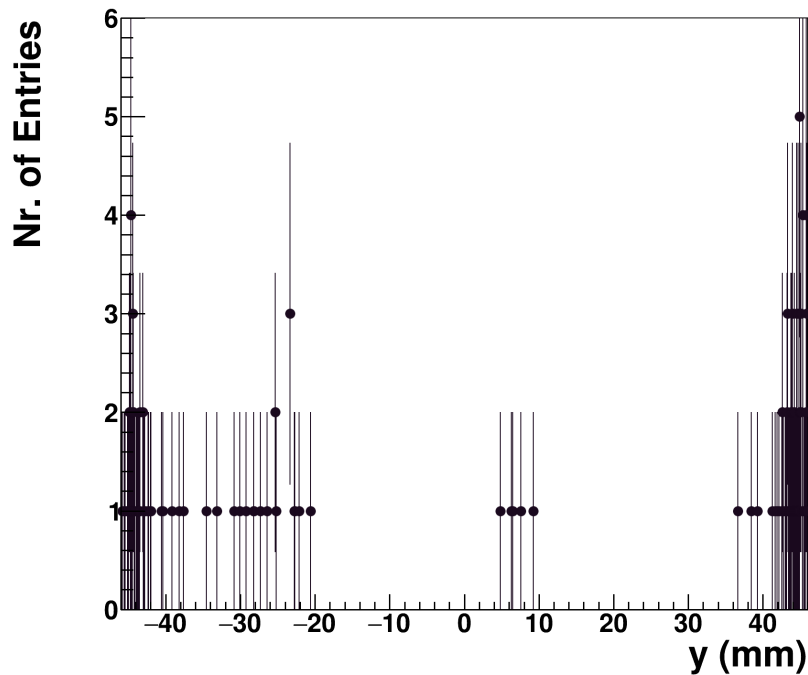
$$\eta_{\text{track}} = \frac{N_{\text{found}}}{N_{\text{total}}} = \frac{19595}{25000} = 0.784. \quad (11.2)$$

The average single plane efficiency of the sensors is calculated to be:

$$\eta_{\text{plane}} = \sqrt[6]{\eta_{\text{track}}} = \sqrt[6]{0.784} = 0.96. \quad (11.3)$$

This agrees well with the average efficiency determined for the single layers determined by the AZALEA system calculated in section 10.5.4. As both efficiencies are similar to each other, the algorithm itself has close to 100% efficiency.

In addition, the fake track rate of the system is determined using the reconstructed tracks of a data run without any beam. All steps are the same as for data with beam and only noise *clusters* above our *S/N* threshold are taken into account for track finding and fitting. A distribution of these *clusters* is depicted in Figure 11.3 for S47. Most of the noise



**Figure 11.4** – Local positions of all *clusters* on reconstructed tracks from a run without beam

clusters are located at the edge which is a result of the increased noise that was described in section 10.4.1 and that is present in all of the Lycoris modules. Performing the same method of track finding and fitting as before results in two tracks consisting of six clusters and 29 tracks consisting of five clusters in a sample of 25000 events. A detailed look at these tracks reveals that not only do many of the tracks reconstructed this way have a very poor  $\chi^2$  value, almost all tracks reconstructed like this are located at the edges of the Lycoris module where most of the noise clusters are located.

The width of these noise regions is on the order of a few millimeters at both edges. This means, that within the test beam setup where all sensors are aligned relative to one another all six layers have high noise regions that overlap with one another which results in the reconstruction of noise tracks.

Until the noise at the edges of the Lycoris module is understood and removed it makes sense to limit the track finding and fitting outside of the edges of the Lycoris module in order to increase the purity of the system.

### 11.3 Momentum Resolution of the Lycoris Telescope

In order to determine the momentum resolution of the system, an independent measurement of the curvature is required. Without a reference the achievable resolution is limited to the spread of the momentum of particles after interaction from the PCMAG wall which was described in section 6.1. While measurements were performed with a magnetic field in the August 2019 campaign, the measurements performed in area T24/1 were heavily influenced by the, at that time, poor performance of the Lycoris sensors used at the test beam. The noise performance as well as the calibration performance, in combination with the requirement of six clusters, do not allow for qualitative studies within the PCMAG.

The momentum resolution of the system is instead determined using the setup in area T24. For this, a GBL refit is performed for which the refit is allowed to adjust the curvature of the fit even though no magnetic field and therefore no curvature is present in the data. This is done by telling GBL of the presence of a non zero magnetic field, this makes GBL try to fit a curvature to the measurement points resulting in the determination of five measurement parameters instead of four [37]. The expected curvature is zero, meaning that every value that differs from this result reflects the curvature resolution of the system. The curvature within GBL is expressed as  $q/P$  and the magnetic field strength is set to  $B = 1\text{ T}$  to reflect the PCMAG strength and to receive values in  $1\text{ (GeV/c)}^{-1}$ .

The residual of  $q/P$  is depicted in Figure 11.5. The plot is centered around zero with the variation of the  $q/P$  parameter being the resolution of the system which, by performing a gaussian fit, is found to be around  $\sigma_{(q/P)} = (6.82 \pm 0.06) \times 10^{-2}\text{ GeV}^{-1}$ . The relation between  $q/P$  and the curvature  $\kappa$  are given by (4.12):

$$\kappa = (q/P) \cdot B \cdot c, \quad (11.4)$$

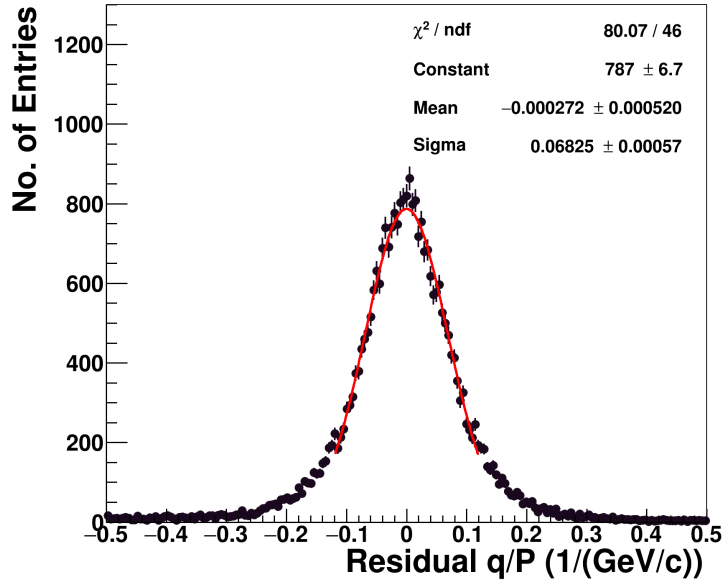
from which we calculate the resolution of the curvature as:

$$\sigma_{\kappa\text{-T24}}^{meas} = \sigma_{(q/P)} \cdot B \cdot c = (2.05 \pm 0.02) \times 10^{-5}\text{ mm}^{-1}. \quad (11.5)$$

$B = 1\text{ T}$  is the aforementioned magnetic field strength and  $c$  is the speed of light which is only present as to cancel with the  $1/c$  within the chosen units. Changing the magnetic field to  $0.5\text{ T}$  results in a change for the received value in  $\sigma_{(q/P)}$  from GBL but results in the same value for the curvature resolution  $\sigma_{\kappa}$ .

To estimate the achievable resolution with the PCMAG configuration, the results gathered here are compared with a simulation of the T24 setup, similar to the one performed in





**Figure 11.5** – Residual of  $q/P$  after GBL refit with a curvature that can be adjusted by the refit in order to improve upon the fit result even when no curvature is physically possible.

section 6.3. The result for this setup is:

$$\sigma_{\kappa-T24}^{sim} = 2.18 \times 10^{-5} \text{ mm}^{-1}, \quad (11.6)$$

which shows that both the simulation and the measurement result in a similar curvature resolution with the measured resolution being slightly better than the simulated resolution.

The difference between the T24 and the T24/1 configuration of the Lycoris telescope is only the significantly reduced lever arm in Area T24 of 4.52 cm compared to the 80.9 cm long lever arm in area T24/1. Hence, in order to determine the achievable resolution a simulation can be performed for the configuration in T24/1 similar to the one above for T24. As the direct measurement within area T24 is shown to be slightly better than the simulated result the simulated result is taken as an upper limit to the achievable momentum resolution in area T24/1.

Using the increased lever arm, the simulated curvature resolution for the setup in T24/1 is:

$$\sigma_{\kappa-T24/1}^{sim} = 1.08 \times 10^{-6} \text{ mm}^{-1}, \quad (11.7)$$

which results in an inverse momentum resolution of:

$$\sigma_{(q/P)-T24/1}^{sim} = 3.6 \times 10^{-3} \text{ GeV}^{-1} = 3.6 \times 10^{-6} \text{ MeV}^{-1}. \quad (11.8)$$

This is below the momentum resolution of  $\sigma_{\text{req-q/P}} = 4.584 \times 10^{-6} \text{ MeV}^{-1}$  (see section 6.1) that the LCTPC prototype is expected to achieve. Therefore, the Lycoris telescope should be capable of fulfilling its primary purpose of this configuration as a reference in order to determine the momentum resolution of the LCTPC prototype.

## 11.4 Summary

This chapter focuses on some of the standalone results gathered from the Lycoris telescope system. The system is shown to be capable of performing the necessary measurements as a standalone device using the tailor made standalone track finding and fitting algorithm. The system performance is similar to the results gathered from the AZALEA telescope in terms of charge deposition, resolution and track efficiency which are all shown to be sufficient for use as a reference telescope.

However, the structured noise that was mentioned in section 9.2.2.2 poses a problem in the standalone track reconstruction. It is possible to reconstruct fake tracks from hose hits, as the noise is spatially correlated along all sensors. At the time of writing, the outer edges of the sensors should not be considered in the analysis as almost all fake tracks that were found are located at the edges near the correlated noise spikes. Further studies should be conducted on where this noise comes from and how to eliminate it.

While no results in T24/1 could be gathered in which the performance of the installed Lycoris modules was sufficient for track finding and fitting, the curvature resolution of the system could be determined within the T24 configuration from the August 2020 test beam campaign by allowing GBL to use the curvature as a free fitting parameter. The measured results compare favorably with simulation showing a slightly better with a curvature resolution of  $\sigma_{\kappa-T24}^{meas} = (2.05 \pm 0.02) \times 10^{-5} \text{ mm}^{-1}$  compared to the simulated resolution of  $\sigma_{\kappa-T24}^{sim} = 2.18 \times 10^{-5} \text{ mm}^{-1}$ . Using the simulated result as an upper limit of the achievable momentum resolution, a simulation with the increased lever arm of the T24/1 configuration was performed from which the achievable momentum resolution of the Lycoris telescope within the T24/1 PCMAG solenoid was determined to be better than  $\sigma_{(q/P)-T24/1}^{sim} = 3.6 \times 10^{-6} \text{ MeV}^{-1}$  which is sufficient for the main purpose as a reference to the LCTPC prototype that is projected to achieve a resolution of  $\sigma_{\text{req-P}} = 4.584 \times 10^{-6} \text{ MeV}^{-1}$ .

# Conclusion and Outlook

Results gathered from current particle physics experiments push the necessity for future experiments into the foreground in the search for physics beyond the SM. Silicon telescope systems used at test beam facilities are both a tool which provides insight into detector components and an opportunity for development of novel sensor systems. This thesis encompasses the full life cycle of a particle physics detector.

The Lycoris telescope was designed and built based on a novel design of a large  $92 \times 92 \text{ mm}^2$  active area  $320 \mu\text{m}$  thick silicon strip sensor intended to be used as the SiD outer tracking layer. The sensor uses extra metal layers to route signal to the KPiX ASIC that is bump-bonded on top of the sensor. This results in a  $25 \mu\text{m}$  pitch between strips of which every second is kept floating to improve the resolution without increasing the number of readout channels. This thesis presents the first time in which a sensor of this type was successfully assembled. The sensor is proven to work within the system specifications both in terms of its electrical- as well as its tracking performance. 22 sensors have been successfully assembled in this thesis about ten of which have been studied during test beam campaigns at the DESY II Test Beam Facility. Studies of the sensors include:

- measurements of the sensor depletion and inter-strip capacitance,
- investigation into its calibration performance,
- studies of both the internal and external triggering modes,
- verified the operation within a magnetic field,
- detailed investigations into the system as a DUT using a reference telescope,
- verified the systems functionality as a standalone tracking sensor.

The large parameter space of options and extensive information provided by the system allowed and required an extensive analysis of the data which was adapted to handle the different types of information gathered by the system only some of which is presented in this thesis.

Parameter	Requirement	Achieved
Area A	$\approx 10 \times 10 \text{ cm}^2$	$9.2 \times 9.2 \text{ cm}^2$
Thickness d	$\leq 37 \text{ mm}$	33 mm
Length L	$\leq 1300 \text{ mm}$	321 mm
$\sigma_y$	$\leq 10 \mu\text{m}$	$\approx 7 \mu\text{m}$
$\sigma_x$	$\leq 1 \text{ mm}$	$\approx 230 \mu\text{m}$
Nr. of layers	$\geq 3/5$ (Pixels/Strips)	6 Strips
Total radiation length per arm $X/X_0$	$\leq 2.1 \%$	0.4 %
Inv. momentum resolution $\sigma_{(q/P)}$	$\leq 4.584 \times 10^{-6} \text{ MeV}^{-1}$	$\leq 3.6 \times 10^{-6} \text{ MeV}^{-1}$
Single plane efficiency $\eta_{\text{plane}}$	$\approx 100 \%$	96 %

**Table 11.2** – Required and achieved parameters for the Lycoris telescope.

In multiple test beam campaigns the single plane efficiency of the sensor was found to be at around 96% with an average  $S/N = 15$  and an achievable spatial resolution of about  $7 \mu\text{m}$  far below many of the currently used silicon strip sensors as for example at the LHC. The novel design meant that on average the only material within the path of the beam is limited to the  $320 \mu\text{m}$  thick sensor resulting in an average material budget of about 0.4%. A new six layer strip telescope was designed and commissioned in this thesis using the sensor. Data gathered by the telescope was used to develop a new track finding and fitting that is shown to provide excellent track finding and fitting efficiency based on the sensor performance gathered by the reference telescope chapter 11. Based on results of the Lycoris telescope performance, an upper limit of the achievable momentum resolution within a 1 T magnetic field was performed which was found to be at about  $3.6 \times 10^{-6} \text{ MeV}^{-1}$ . This is below the requirements set forth by the LCTPC prototype of  $\sigma_{\text{req-P}} = 4.584 \times 10^{-6} \text{ MeV}^{-1}$  meaning that the system configuration investigated in this thesis should fulfill its main purpose as a reference detector for the LCTPC.

The Lycoris telescope performance is shown to be sufficient for use as a reference telescope at the DESY II Test Beam Facility (see chapter 6, section 10.6 and section 11.4) and surpasses all requirements, except for the efficiency which, while slightly below the requirement, is sufficient for operation at the test beam as it simply requires a slight increase in the measurement statistics taken. The requirements and results are tabled in Table 11.2.

Nonetheless, many results gathered in this thesis show possible improvements to the system for its use both as a telescope and a potential use in a later detector such as the SiD at the ILC of which a few are shortly mentioned here. Some of the improvements to the system are the decoupling of power lines on the *Kapton Flex Cable* (see section 10.3) or the addition

---

of a fourth layer to improve track finding (see section 4.2.3). Based on results gathered in this thesis a new iteration of the KPiX ASIC would improve many different aspects of the system such as its noise performance (see section 10.4.1), the higher *bucket* performance (see section 10.2) and the internal trigger performance (see section 10.3).



# Acknowledgments

I would like to thank Dr. Ties Behnke for providing me the unique opportunity to work on a project which encompasses all steps necessary in building a particle detector and for his support in the project and my time as a PhD student.

I also express my thanks to Prof. Dr Erika Garutti who agreed to be one of my PhD supervisors and her support in different steps of the project.

Dr. Marcel Stanitzki has my utmost gratitude for his incredible support in all aspects of this thesis, be it hardware, software or physics. He is a fundamental pillar of this work without whom this would not have been possible.

I would like to express special thanks to all collaboration members at SLAC without whom this project would not exist. I would like to thank three members in particular: Prof. Dr. Martin Breidenbach who, as the KPiX mastermind, provided invaluable insight and stimulating discussion during our weekly collaboration meetings and I thank him for being my host during my stay at SLAC.

Dr. Dietrich R. Freytag whose insight into the KPiX ASIC and whose standalone analysis of data I collected has allowed a quick identification of issues and who was always willing to discuss ideas for the project.

Benjamin A. Reese who designed the new Software and Firmware for the project and provided crucial support for it. His participation in the first test beam campaign with the full telescope system at DESY was invaluable.

Dr. Mengqing Wu has my sincere gratitude as someone who accompanied this project as a post doc since the first year of my PhD. Her work on the project and support of myself have proven to be crucial for its success.

Special thanks go out to Dr. Lennart Huth who, in the one and a half years I got to know him, has become an irreplaceable asset to my work. His willingness to criticize and correct my work as a PhD Student and to discuss some of the finer points of detector development and analysis have proven to be invaluable for this work.

I wish to thank Ralf Diener who has been a great support for my work as a PhD student who was always willing to hear about issues and help resolve them. His company made many days of the work more pleasant and he has provided me with great support at the DESY II Test Beam Facility.

I also would like to express my gratitude to Dr. Dimitra Tsionou whose preparatory work of the project allowed a smooth take over of the project and who has given me a lot of support in the year I got to know her.

I thank Dr. Claus Kleinwort for his continued guidance of my venture into the field of particle tracking and his immeasurable contributions to the analysis necessary to achieve these results. His support of the project and willingness to discuss problems and misunderstandings of mine have allowed me to get greater insight into particle tracking.

I would like to express special thanks to all members of the FLC TRCK sub-group. I thank my fellow PhD students, Ulrich Einhaus, Oleksiy Fedorchuk and Paul Malek for the great workplace atmosphere and the fun time I had during my PhD work discussing our different projects during meetings and breaks.

My gratitude also goes out to the technical staff including Volker Prah, Oliver Schäfer, Berndt Beyer, Torsten Külper and Ole Arndt Bach. Many fruitful discussions into the world of electronics and mechanics arose from my interactions with them and their help has proven to be irreplaceable for completing the hardware aspects of this thesis.

I express my gratitude to all members of the FLC group. You have provided help and company in these years providing me with greater insight into the field of particle physics and detectors. I thank all of you for being great colleagues with whom I could discuss many aspects of physics.

I express my gratitude to Prof. Dr. Jim Brau from the University of Oregon for the insightful



discussions of the results of this project during our weekly collaboration meeting.

I wish to thank Dr. Sergio Diez Cornell for help with different electronic equipment, advice on gluing and for giving me the opportunity to perform measurements at the DAF.

I would also like to express my gratitude to Simon Spannagel for his help with Corryvreckan.

I would also like to express my thanks to Dr. Jan Dreyling Eschweiler, Olin Pinto, Paul Malek, Ulrich Einhaus, Dr. Felix Sefkow, Dr. Katja Krüger, Daniel Heuchel, Dr. Mengqing Wu, Dr. Lennart Huth, Ralf Diener, Dr. Eldwan Brianne, Valdimir Bocharnikov, Dr. Dimitra TSIONOU and Amanda Steinhebel for taking part in test beam shifts during some of the many different test beam campaigns that were conducted in this Thesis.

Last but certainly not least, I dedicate this thesis to my family, especially my father, my mother and my brother, who have supported my endeavor to pursue the field of physics since my school years and who have granted me all the support I could ever ask for and more.



# **Appendices**



## A MIP stopping power

Particle	Energy at MIP	MIP mass stopping power
Electron	$3.3 \cdot m_e$	$1.5 \text{ MeVcm}^2/\text{g}$
Positron	$3.7 \cdot m_e$	$1.46 \text{ MeVcm}^2/\text{g}$
Muon	$3.58 \cdot m_e$	$1.66 \text{ MeVcm}^2/\text{g}$

**Table 3** – Minimal Ionizing Particle loss for different particle types[3].

## B Silicon Properties

Property		Value
Atomic Number	$Z$	14
Mass	$A$	28.09U
Density	$\rho$	2.3 g/cm <sup>3</sup>
Electron mobility	$\mu_e$	1450 cm <sup>2</sup> V/s
Hole mobility	$\mu_h$	500 cm <sup>2</sup> V/s
Electron lifetime	$\tau_e$	> 100 $\mu$ s
Hole lifetime	$\tau_h$	> 100 $\mu$ s
Crystal structure		Diamond
Band gap	indirect	1.2 eV
	direct	3.4 eV
e-h pair creation energy		3.65 eV
Dielectric constant	$\epsilon$	11.9
Intrinsic charge density		$1.01 \times 10^{10}$ cm <sup>-3</sup>
Specific resistivity		$2.3 \times 10^5$ $\Omega$ cm
Radiation length	$X_0$	9.36 cm
Number of valence electrons		4

**Table 4** – The properties of silicon relevant for tracking detectors [23].

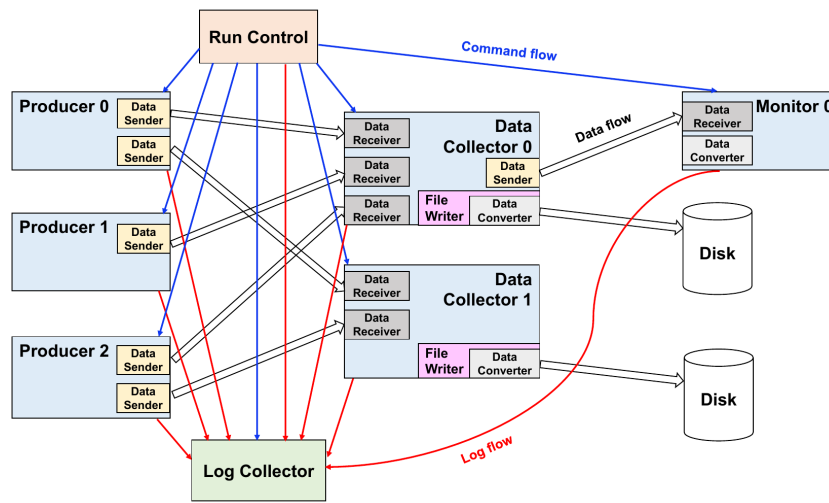
## C EUDAQ2

The original version of EUDAQ [108] was designed to be used as the Data Acquisition (DAQ) for the EUDET-type telescopes which were introduced in Section 5.3 as part of the EUDET project [44]. EUDAQ2 is an updated version of EUDAQ, which is more flexible and allows for an easy way to implement the combined data taking of different hardware participants [81]. The core design idea of EUDAQ2 is that the setup can be split into different run-time instances with different roles.

The roles are:

- The *Producers* represent the individual hardware components and are used to control the different hardware devices, be it TLU, detectors, stages and others. Two different methods for the implementation of *Producers* exist. In the "internal" loop the producer manages all START and STOP commands as well as the all error handling. In the "external" loop EUDAQ2 collects the data made available by the producer without managing the readout.
- *DataCollectors* which collect the data from detectors, and either send it to the online Monitoring or convert the data and write it to disk.
- The *Monitor* can receive data from *DataCollectors* it uses to perform online monitoring of data quality.
- The *LogCollector* gathers all logging data from the *Producers* and the *Monitor* providing a central instance to collect all logging information.
- The *RunControl* acts as the central hub for all aforementioned components. It is responsible for starting and stopping a data taking run. It is also responsible for the initialization and configuration of the different *Producers*. The *RunControl* is connected to each producer via TCP/IP using a custom protocol.
- The *OfflineTools* offer among other functionality the possibility to read, merge and split EUDAQ2 data.

A schematic overview of the relation between the different run-time instances described above is shown in Figure 6. The blue arrows show the command flow from the *RunControl* to the *Producers*, *DataCollectors* and the *Monitor*. The large white arrows show the data flow from the *Producers* to the *DataCollectors* with the subsequent flow to the *Monitor* or the storage disk. As shown, each *Producer* can send data to multiple *DataCollectors* and each *DataCollector* is capable of receiving data from multiple *Producers*. Data can be con-



**Figure 6** – Schematic overview of the relation between the different EUDAQ2 components.[81]

verted and written to disk while also being shown simultaneously via the *Monitor* which performs its own Data conversion for monitoring of the data.

The red arrows show the flow of logging data from every single run-time instance to the *LogCollector*. The *RunControl* first sends out an initialization command based on an init-file to all connected Devices which is used for verifying functional communication via a handshake and to perform one time initialization which need not be repeated such as programming the clock chip on the AIDA TLU.

After initialization, the system can be configured. This is used to change settings in the device such as the position of a stage or the trigger settings within the AIDA TLU. The settings are performed via a config-file and a new configuration of the system can be performed without the need of a new initialization by manually updating the configuration file and sending it to the devices anew.

The system sends out a combined start signal in order to ensure that devices run in sync which is required for a later combination of the data streams. The running status can be stopped prematurely before any criteria in the config-file are fulfilled and the entire system can be reset to revert back to a state before initialization which is required when the system moves into the error state, after one of the participants has reported an error.

Data stored on disk is automatically provided with an event type, a run number and an event number by EUDAQ while allowing the assignment of more optional tags such as a time stamp, a trigger number and more. The separation of hardware components from the



---

*RunControl* via *Producers* and *DataCollectors* allows to implement new hardware devices without interference with the core of EUDAQ2.

## D Grey Code

Decimal	Binary	Gray
0	000	000
1	001	001
2	010	011
3	011	010
4	100	110
5	101	111
6	110	101
7	111	100

**Table 5** – Gray code example

## E Pin mapping

HDMI PIN	TLU Signal	HDMI PIN	TLU Signal
1	CLK <sub>p</sub>	11	GND
2	GND	12	SPARE <sub>n</sub>
3	CLK <sub>n</sub>	13	n.c.
4	CONTROL <sub>p</sub>	14	+3.3V power
5	GND	15	TRIGGER <sub>p</sub>
6	CONTROL <sub>n</sub>	16	TRIGGER <sub>n</sub>
7	BUSY <sub>p</sub>	17	GND
8	GND	18	n.c.
9	BUSY <sub>n</sub>	19	n.c.
10	SPARE <sub>p</sub>		

**Table 6** – HDMI pin mapping of the AIDA TLU [47]

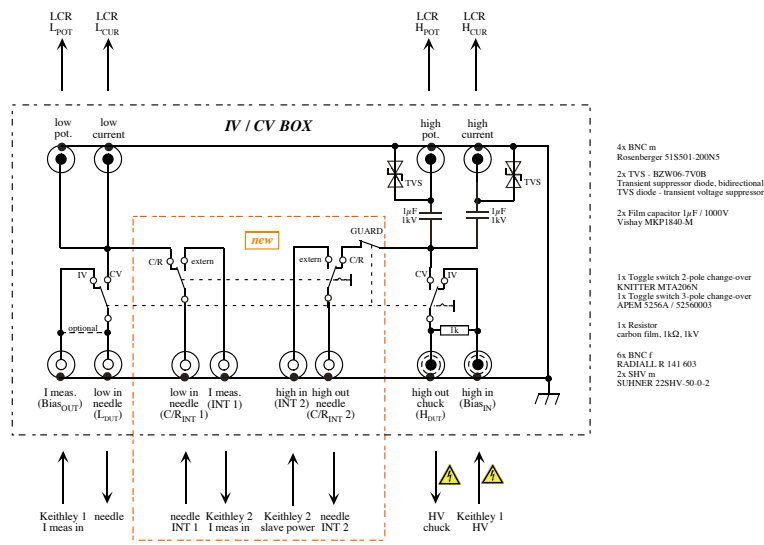
Pin	Signal	Pin	Signal	Pin	Signal	Pin	Signal
1	TRIG <sub>p</sub>	11	DATA <sub>2</sub>	21	CMD <sub>1</sub>	31	CAS SDA
2	TRIG <sub>n</sub>	12	GND <sub>cas</sub>	22	GND <sub>cas</sub>	32	GND <sub>cas</sub>
3	CLK <sub>p</sub>	13	DATA <sub>3</sub>	23	CMD <sub>2</sub>	33	CAS SCL
4	CLK <sub>n</sub>	14	GND <sub>cas</sub>	24	GND <sub>cas</sub>	34	GND <sub>cas</sub>
5	RESET	15	DATA <sub>4</sub>	25	CMD <sub>3</sub>	35	CAS 2.5V
6	GND <sub>cas</sub>	16	GND <sub>cas</sub>	26	GND <sub>cas</sub>	36	CAS 2.0V
7	DATA <sub>0</sub>	17	DATA <sub>5</sub>	27	CMD <sub>4</sub>	37	CAS 2.5V
8	GND <sub>cas</sub>	18	GND <sub>cas</sub>	28	GND <sub>cas</sub>	38	CAS 2.0V
9	DATA <sub>1</sub>	19	CMD <sub>0</sub>	29	CMD <sub>5</sub>	39	CAS 2.5V
10	GND <sub>cas</sub>	20	GND <sub>cas</sub>	30	GND <sub>cas</sub>	40	CAS 2.0V

**Table 7** – Signal cable pin mapping

Pinnumber	Description	Pinnumber	Description		
1	Bias <sub>p</sub>	11		21	AGND <sub>2</sub> 31
2	Bias <sub>n</sub>	12	CLK <sub>n2</sub>	22	AVDD <sub>2</sub> 32 CLK <sub>n1</sub>
3		13		23	AGND <sub>1</sub> 33
4	DVDD <sub>2</sub>	14	TRIG <sub>p2</sub>	24	DVDD <sub>1</sub> 34 TRIG <sub>p1</sub>
5		15		25	AGND <sub>1</sub> 35
6	CMD <sub>2</sub>	16	TRIG <sub>n2</sub>	26	CMD <sub>1</sub> 36 TRIG <sub>n1</sub>
7	DGND <sub>2</sub>	17		27	DGND <sub>1</sub> 37
8	RST <sub>2</sub>	18	DOUT <sub>2</sub>	28	RST <sub>1</sub> 38 DOUT <sub>1</sub>
9	DGND <sub>2</sub>	19	AGND <sub>2</sub>	29	DGND <sub>1</sub> 39 AVDD <sub>1</sub>
10	CLK <sub>p2</sub>	20	VREF <sub>2</sub>	30	CLK <sub>p1</sub> 40 VREF <sub>1</sub>

**Table 8** – *Kapton Flex Cable* pin mapping

## F IV/CV switchbox



- 4x BNC m
- Rosenberger 51SS01-200NS
- 2x TVS: BZM06-7V0B
- Transient suppressor diode, bidirectional
- TVS diode - transient voltage suppressor
- 2x Film capacitor 1µF / 1000V
- Vishay MKP1840-M
- 1x Toggle switch 2 pole change-over
- KNITZER MTA200N
- 1x Toggle switch 3 pole change-over
- APEM 5256A / 52560003
- 1x Resistor
- carbon film, 1kΩ, 1kV
- 6x BNC f
- RADWELL R 141 603
- 2x SHV m
- SEHNER 22SHV-50-0-2


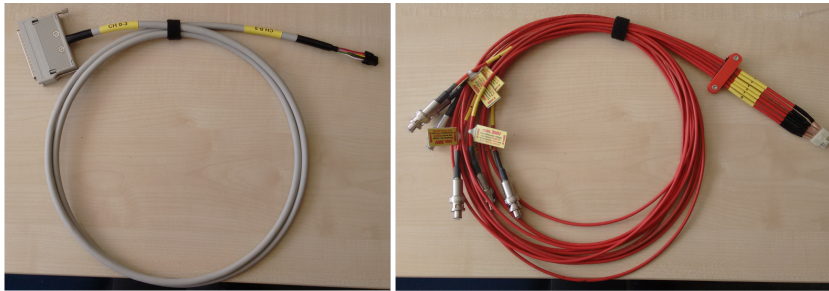
Drawn	Name	Date	Scale	Replacement for:	 HELMHOLTZ GEMEINSCHAFT	Curr. no.:
Mod	F. Kilgus	02.08.15	1:1	<b>Probe Station                      IV/CV box for LCR meter                      circuit diagram</b>		Page 1 of 1
Mod	F. Kilgus	09.08.15				
Mod	F. Kilgus	27.08.15				
Mod						

Figure 7 – (Top) Picture of the CV/IV switch box used to internally reconnect the probes to the correct devices. (Bottom) Technical drawing of the CV/IV switch box.

## G Custom cabling

The HV module is connected to the master cassette board via a custom adapter cable translating from the SHV connector used on the Wiener PS to an Amphenol Minitek 12 pin 2 mm pitch connector [109] (see Figure 8 right) . This limits the safe voltage that can be supplied to the cassette to 300V, which is the limitation of the connector. One of the LV modules connects to the master cassette board, which is also done via a custom made cable that connects to the 37 pin Sub-D connector on the Wiener PS and has on the other side an Amphenol Minitek 8 pin 2 mm pitch connector [109] (see Figure 8 left). A separate LV module output is connected to the KPiX DAQ board via a custom made cable splitting the 37 pin Sub-D output connector to banana connectors which are then used to connect to the four pin ATX Molex connector on the DAQ board [77]. The pin mapping of the custom



**Figure 8** – Picture of the custom made LV cable (left) and HV cable (right) used to connect the power supply with the cassette board

LV and HV cables are given in table 9 and table 10.

SHV number	Amphenol Pin	Connection
1	1	Bias <sub>0</sub>
1	2	Bias <sub>1</sub>
2	3	Bias <sub>2</sub>
2	4	Bias <sub>3</sub>
3	5	Bias <sub>4</sub>
3	6	Bias <sub>5</sub>
4	7	Bias <sub>0</sub> <sup>return</sup>
4	8	Bias <sub>1</sub> <sup>return</sup>
5	9	Bias <sub>2</sub> <sup>return</sup>
5	10	Bias <sub>3</sub> <sup>return</sup>
6	11	Bias <sub>4</sub> <sup>return</sup>
6	12	Bias <sub>5</sub> <sup>return</sup>

**Table 9** – Custom HV cable pin mapping. Bias<sub>0</sub> to Bias<sub>2</sub> are the bias for the first stack of sensors and Bias<sub>3</sub> to Bias<sub>5</sub> are forwarded to the slave cassette board.

Sub-D pin	Amphenol Pin	Connection
20	1	A <sub>Master</sub>
24	2	D <sub>Master</sub>
28	3	A <sub>Slave</sub>
32	4	D <sub>Slave</sub>
1	5	A <sub>Master</sub> <sup>GND</sup>
5	6	D <sub>Master</sub> <sup>GND</sup>
9	7	A <sub>Slave</sub> <sup>GND</sup>
13	8	D <sub>Slave</sub> <sup>GND</sup>
19	-	Chassis GND

**Table 10** – Custom LV cable pin mapping. A/D<sub>Master</sub> are analog and digital voltages to the master board and A/D<sub>Slave</sub> are the analog and digital voltages forwarded to the slave cassette board. the same applies for the GND connections.

## H The KPiX YAML file

The settings for the FPGA and the KPiX readout chip are given by a YAML file. The options are given in the table below

Option	Description	Value range
CalMeanCount	Number of baseline values to be taken during Calibration	No Limit
CalDacMax	Sets upper DAC limit of calibration point for charge injection	0-255
CalDacMin	Sets lower DAC limit of calibration point for charge injection	0-255
CalDacStep	Describes the step size of the DAC value injection (1 = Every DAC value)	1-255
CalDacCount	Number of repeat injections for each DAC value	No Limit
CalChanMax	Sets end channel to be calibrated	0-1023
CalChanMin	Sets start channel to be calibrated	0-1023
runRate	Sets the acquisition frequency. Can be set to "auto" to have maximum rate	1-30Hz/auto
	Below are internal software variables holding current state. Not actual variable for changing in yml	
CalState	Variable holding status of calibration (such as injection)	
CalChannel	Variable holding current calibration channel value	
CalDac	Variable holding current calibration DAC injection value	

**Table 11** – DesyTrackerRunControl



Option	Description	Value range
DesyTracker enable	Whether the entire block is enabled or not	True/False
AxiVersion enable	Whether the entire block is enabled or not	True/False
ScratchPad	32-bit test register in FPGA firmware so that software to verify it can talk to FPGA	0x000000
TluMonitor enable	Whether the entire block is enabled or not	True/False
ClkSel	Which clock should be used to generate the 200MHz baseline	EthClk/TluClk
KPiXDaqCore enable	Whether the entire block is enabled or not	True/False
SysConfig enable	Whether the entire block is enabled or not	True/False
RawDataMode	Debug mode that makes the firmware produce output data even if a channel/bucket has no hits	True/False
AutoReadDisable	Can be set to True in order to force the sending of a command to KPiX before it begins the readout	True/False
KPiXClockGen enable	Whether the entire block is enabled or not	True/False
ClkSelReadout	Sets the readout clock period in units of $10\text{ ns} \cdot ([value] + 1)$	4-255
ClkSelDigitize	Sets the digitize clock period in units of $10\text{ ns} \cdot ([value] + 1)$	4-255
ClkSelAcquire	Sets the acquisition clock period in units of $10\text{ ns} \cdot ([value] + 1)$	4-255
ClkSelIdle	Sets the acquisition clock period in units of $10\text{ ns} \cdot ([value] + 1)$	4-255
ClkSelPrecharge	Sets the acquisition clock period in units of $10\text{ ns} \cdot ([value] + 1)$	4-4095
SampleDelay	Controls the sample point by adding a delay in number of clock cycles before DATA line is sampled. E.g. 3 means data line will be sampled $(3 + 1) \cdot 5\text{ ns}$ (200 MHz clock) cycles after each rising edge of the KPiX clock	0-255
SampleEdge	Sets whether to sample on rising or falling Edge	Rise/Fall
AcquisitionControl enable	Whether the entire block is enabled or not	True/False
ExtTrigSrc	Source for the external trigger Signal	Disabled/BncTrig/Lemo0/Lemo1/TluSpill/TluStart/TluTrigger/EthAcq/EthStart
ExtTimestampSrc	Source for the external timestamp Signal	Same as above
ExtAcquisitionSrc	Source for the external signal to start Acquisition	Same as above
ExtStartSrc	Source for an external run start signal	Same as above
Calibrate	Whether it is a Calibration run or not	True/False
KpixAsicArray enable	Whether the entire block is enabled or not	True/False
KpixAsic[*] enable	Whether a specific Kpix block is enabled	True/False
CfgAutoReadDisable	When set to true KPiX only begins Data readout when a command is sent to it.	True/False

Table 12 – DesyTracker

Option	Description	Value range
CfgForceTemp	Force whether Kpix temperature data should be read out	True/False
CfgDisableTemp	Disable Kpix temperature module	True/False
CfgAutoStatusReadEn		True/False
TimeResetOn	Set the number of cycles from the start of an acquisition cycle to wait before asserting reset.	0-[TimeBunchClkDelay(TBCD)]
TimeResetOff	Set the number of cycles from the start of an acquisition cycle to wait before setting reset back to zero	[TimeResetOn]-[TBCD]
TimeOffsetNullOff	Offsets of the system are sampled by switching all discriminators into a follower mode and impressing the levels into capacitors at the inverting inputs of the discriminators. This is a kind of double correlated sampling applied to the full acquisition cycle. At OffsetNullOff the follower mode is terminated.	0-[TBCD]
TimeLeakageNullOff	Leakage compensation for DC coupled sensor	0-[TBCD]
TimeDeselDelay	Time at which the desel_all_cells signal is asserted to the analog side of KPiX	0-[TBCD]
TimeBunchClkDelay	Sets the duration of the start up phase in units of MCC (acq.clock periods)	0-Uint16
TimeDigitizeDelay	How many clock cycles to wait between acquisition and digitization. (Affects synchronization for unknown reasons)	0-
TimePowerUpOn	Set on which MCC analog power net currents are raised to operative levels	0-[TBCD]
TimePowerUpDig	Set on which MCC digital power net currents are raised to operative levels	0-[TBCD]
TimeThreshOff	At this time a threshold is applied to the bottom terminal of the capacitor holding the offset level. In the current version of KPiX some buffers get very slow due to power drops on busses and the transition from follower to discriminator takes time.	0-[TBCD]
TrigInhibitOff	How many BunchClockCounts (BCC) of the acquisition a trigger should be suppressed	0-8191
BunchClockCount	How many BCC the acquisition phase should last for	0-8191
Cal0Delay	Delay in BCC on when first calibration DAC injection happens	0-8191
Cal1Delay	Delay in BCC on when second calibration DAC injection happens relative to the first	0-8191
Cal2Delay	Delay in BCC on when third calibration DAC injection happens relative to the second	0-8191
Cal3Delay	Delay in BCC on when fourth calibration DAC injection happens relative to the third	0-8191
CalCount	How many buckets should be Calibrated	1-4

Table 13 – DesyTracker

Option	Description	Value range
DacRampThresh	Wilkinson converter threshold. Can be raised to generate a offset for conversion result	0-255
DacRangeThreshold	Signal amplitude at which the dynamic switch to enables the 10pF capacitor	0-255
DacCalibration	Sets the calibration amplitude but is overwritten in calibration to run through prescribed cycle	0-255
DacEventThreshold	Internal bias level, not to be changed	-
DacShaperBias	Bias level of the shaper, not to be changed	-
DacDefaultAnalog	A bias level impressed on the analog bus before connection to the analog storage capacitor	
DacThresholdA	Setting the DAC threshold level for threshold A which is used in self triggering	0-255
DacThresholdB	Setting the DAC threshold level for threshold B which is used in self triggering	0-255
CntrlDisPerReset	Option for a periodic reset in synchronism with the ILC bunch structure is disabled	True/False
CntrlEnDcReset	Enables DC reset used for all non-synchronous data	True/False
CntrlHighGain	Set whether the system should operate in high gain	True/False
CntrlNearNeighbor	Option to trigger a neighboring pixel even if it is below threshold. Only partially matched layout of tracker and requires changes.	True/False
CntrlCalSource	Set which calibration level should be used (external not in use)	Disable/ Internal/ External
CntrlForceTrigSource	Force trigger to be of a certain type	Disable/ Internal/ External
CntrlHoldTime	Sets how long the signal should be sampled in units of BCC (8x = 1 BCC, 40 = 2 BCC etc.)	Increasing order (8x, 40x, 24x, 56x, 16x, 48x, 32x, 64x)
CntrlCalibHigh	Whether to enable the the parallel 5pF capacitor in the calibration injection for bucket 0	True/False
CntrlShortIntEn	Option to reduce integration time for data in the storage capacitors from 0.5 to 0.2 $\mu$ s	
CntrlForceLowGain	Set whether the system should operate in low gain	True/False
	Setting both CntrlForceLowGain and CntrlHighGain to False operates the system in normal gain	
CntrlLeakNullDisable	Disabled leakage null compensation entirely	True/False
CntrlPolarity	Set polarity of input signals	Positive/Negative (normally set to Positive)
CntrlTrigDisable	Disable self triggering of KPiX	True/False
CntrlDisPwrCycle	Disable power cycling of the champ (no shut off phase)	True/False
CntrlFeCurr	Sets the current in the frontEnd	0-uA (unit is important)

Table 14 – DesyTracker

Option	Description	Value range
CntrlDiffTime	Sets the differentiation time to the shaper	Normal/Half/ Third/Quarter
CntrlMonSource	Option to bring out two analog signals from channel 8. Will be removed with next submission	None/Amp/Shaper
Chan_0_31	Used to manually disable channels (D) or set them to Thresholds (A/B) or to Calibrate (C), 32 channels per row, example: AAADAAAA ... means channel 3 is disabled	A/B/C/D
KpixAsic[X] enable	Sets whether the system should expect a KPIX in slot X	X=0-24 (but 24 always needs to be True for the virtual KPIX on the FPGA board) True/False
KpixDataRxArray enable	Whether the entire block is enabled or not	True/False
KpixDataRx[*] enable	Whether data should be sent out by the KPIX in all slots (wildcard)	True/False (should always be True)

**Table 15** – DesyTracker

## I *Kapton Flex Cable* gluing step by step

1. Placing the rubber stamp upside down into the Kapton flex holder plate and the SiD sensor into the sensor holder plate and attaching both to the vacuum after aligning them
2. Kapton flex holder plate is placed beneath the custom pickup tool onto the aluminum plate and vacuum is turned on after aligning the holder plate using the fine thread screws
3. Pickup tool is moved down and vacuum of the holder plate is turned of while the vacuum of the pickup tool is turned on which grabs the stamp
4. The Kapton flex is placed into the now empty Kapton flex holder plate which is attached to vacuum after aligning the cable within the holder plate.
5. Araldite2011 glue is mixed 1:1 by volume using the mixing cannulas and is poured into the Teflon glue bath.
6. The bath is placed onto the aluminum platform beneath the stamp which is lowered into it
7. After retracting the stamp from the bath, the bath is exchanged by the sensor holder plate with the sensor.

8. After aligning it the sensor holder plate is held in place by the vacuum and the stamp is lowered onto the sensor.
9. After retracting the stamp, the sensor holder plate is moved and the vacuum of the pickup tool is disabled in order to remove the stamp from the pickup tool.
10. The Kapton flex holder plate with the cable is placed, aligned and sucked onto the aluminum plate after which the vacuum pickup tool is lowered and the vacuum of the plate and the pickup tool are switched off/on to grab the Kapton flex.
11. The sensor holder plate holding the sensor with the glue applied to it is placed, aligned and sucked onto the aluminum plate after which the pickup tool is lowered to place the Kapton flex onto the sensor. The vacuum of the pickup tool is turned off and the system is kept in this state for a minimum of 10 hours.
12. After hardening of the glue, the large bias pad which is not glued to the top of the sensor is bent around the edge to the backside of the sensor after applying a small amount of silver epoxy 8331 using a metal spatula.
13. The pad is then pressed against the sensor backside using a small 20 g brass weight pressing onto the front side and kept in that position for 24 hours to allow the epoxy to harden.

## J Lycoris track finding

The parameters and coordinate systems used are the ones described in chapter 4.

### J.1 Strip road search

For the strip road search finder we start by separating the six *measurement layers* into the two axial and four stereo layers. Four of the six layers, typically the four stereo layers, are referred to as *seed layers* which are used to build track candidates as they build a pseudo pixelated layer as a result of their differing stereo angles. The two axial layers are used as *test layers* to check the validity of the track in order to remove invalid track combinations. A layer is only considered valid when its number of correlated hits is greater than zero but below eight in order to avoid noisy event layers blowing up the combinatorics. If such a busy event layer is found the event is considered too noisy and is subsequently dropped. Additionally, a track is constructed only when the number of hits on the track is  $N_{\text{hits}} > 4$ . In the case that two sensor layers have no valid hits, no tracks can be reconstructed for the event. In general, a position  $\begin{pmatrix} x & y \end{pmatrix}^T$  on a track can be written as

$$\begin{pmatrix} x \\ y \end{pmatrix} = \begin{pmatrix} x_0 + \frac{dx}{dz} \cdot z \\ y_0 + \frac{dy}{dz} \cdot z \end{pmatrix}$$

with the aforementioned (section 4.2.3) track parameters and the position  $z$  along the axis  $e_z$ . In order to account for the rotation around the  $e_z$  axis of the stereo layers mentioned in section 6.3 a projection of the track onto a *measurement layer* which consist of any Lycoris strip sensor layer needs to be performed such that the measured hit  $m$  is given by

$$m = \begin{pmatrix} x \\ y \end{pmatrix} \cdot \begin{pmatrix} p_{xi} \\ p_{yi} \end{pmatrix} = p_{xi} \cdot x_0 + p_{xi} \cdot z \cdot \frac{dx}{dz} + p_{yi} \cdot y_0 + p_{yi} \cdot z \cdot \frac{dy}{dz} = \begin{pmatrix} p_{xi} \\ p_{yi} \\ p_{xi} \cdot z \\ p_{yi} \cdot z \end{pmatrix} \cdot \begin{pmatrix} x_0 \\ y_0 \\ dx/dz \\ dy/dz \end{pmatrix},$$

with  $p_{xi}$  and  $p_{yi}$  being variables representing the value of the rotation of the measurement layer described in section 4.2.1 which corresponds to the strip measurement direction in

the global system. The vector

$$\left( p_{xi} \quad p_{yi} \quad p_{xi \cdot z} \quad p_{yi \cdot z} \right)^T$$

is the *derivative*  $\vec{d}$  which results from the projection of the four track parameters to a *measurement layer*. As we have four *measurement layers* through which the track is generated the formula can be expressed via matrix multiplication

$$\vec{m} = \begin{pmatrix} m_1 \\ m_2 \\ m_3 \\ m_4 \end{pmatrix} = \mathbf{D} \cdot \begin{pmatrix} x_0 \\ y_0 \\ dx/dz \\ dy/dz \end{pmatrix} = \begin{pmatrix} p_{x1} & p_{y1} & p_{x1 \cdot z_1} & p_{y1 \cdot z_1} \\ p_{x2} & p_{y2} & p_{x2 \cdot z_2} & p_{y2 \cdot z_2} \\ p_{x3} & p_{y3} & p_{x3 \cdot z_3} & p_{y3 \cdot z_3} \\ p_{x4} & p_{y4} & p_{x4 \cdot z_4} & p_{y4 \cdot z_4} \end{pmatrix} \cdot \begin{pmatrix} x_0 \\ y_0 \\ dx/dz \\ dy/dz \end{pmatrix}.$$

A unique solution exists for the track parameters if the matrix  $\mathbf{D}$  is invertible which we can calculate by multiplying the inverted matrix  $\mathbf{D}^{-1}$  from the left such that

$$\begin{pmatrix} x_0 \\ y_0 \\ dx/dz \\ dy/dz \end{pmatrix} = \mathbf{D}^{-1} \cdot \vec{m}.$$

This is performed for all possible combinations of hits in the four *seed layers* to find track candidates. We then project the track candidates to the location of the *test layers* and search for unique hits. Such a hit is considered valid if it is within a distance of  $d = r_{\text{projected}} - r_{\text{test}} < 200 \mu\text{m}$  to the projected hit position. Out of all valid tracks, only the best track is selected based on its maximum number of hits  $N_{\text{hits}}$  and  $\chi^2/ndf$ . All hits from the rest of the tracks are unassigned and the entire procedure is reiterated until there are no longer enough layers with hits left to generate tracks or no more tracks are found.

## J.2 Striplet finder

For the *S-triplet finder* we separate the layers based on which cassette they are located in. We start with an initial assumption of the angles of the beam track  $(dx/dz)_{\text{initial}}$  and  $(dy/dz)_{\text{initial}}$ . In most of our cases these initial angles are taken equal to zero with only a correction as a result of the curvature within a magnetic field. With this assumption we

can build a track using the two stereo layers within each cassette in order to build a *strip doublet* as now the position on a track is given by

$$\begin{pmatrix} x \\ y \end{pmatrix} = \begin{pmatrix} x_0 + \frac{dx}{dz}_{\text{initial}} z \\ y_0 + \frac{dy}{dz}_{\text{initial}} z \end{pmatrix} = \begin{pmatrix} x'_0 \\ y'_0 \end{pmatrix}.$$

Similar to the *strip road search* we need to project the track hit to the *measurement layer* which in the case of the stereo layers is angled to the beam in order to get the measurement hit  $m$ .

$$m_i = \begin{pmatrix} x \\ y \end{pmatrix} \cdot \begin{pmatrix} p_x \\ p_y \end{pmatrix} = \begin{pmatrix} x'_0 \\ y'_0 \end{pmatrix} \cdot \begin{pmatrix} p_x \\ p_y \end{pmatrix}$$

which, for two measurement  $m_1$  and  $m_2$  can be written via the multiplication of a 2x2 matrix to the track parameters.

$$\vec{m} = \begin{pmatrix} m_1 \\ m_2 \end{pmatrix} = \mathbf{D} \cdot \begin{pmatrix} x'_0 \\ y'_0 \end{pmatrix} = \begin{pmatrix} p_{x1} & p_{y1} \\ p_{x2} & p_{y2} \end{pmatrix} \cdot \begin{pmatrix} x'_0 \\ y'_0 \end{pmatrix}.$$

This equation possesses a unique solution for the track parameters in the case that  $\mathbf{D}$  is invertible. This solution can be calculated by multiplying the inverted matrix  $\mathbf{D}^{-1}$  from the left so that

$$\begin{pmatrix} x'_0 \\ y'_0 \end{pmatrix} = \mathbf{D}^{-1} \cdot \vec{m}.$$

We then apply a cut on the doublet track values such that a doublet is only valid if  $x'_0 < 50\text{mm}$  and  $y'_0 < 10\text{mm}$ . The  $z$  position of the doublet is defined as the center between  $z$  locations of the two stereo layers  $z_1$  and  $z_2$  such that  $z_{\text{dbl}} = \frac{z_1 + z_2}{2}$ . Using the initial value of the slope in  $x$  we perform a correction on the  $y$  value of the doublet such that

$$x_{\text{dbl}} = x'_0; \quad y_{\text{dbl}} = y'_0 - y_{\text{corr}}$$

with

$$y_{\text{corr}} = \frac{dy}{dz} \cdot dz = \frac{dx}{dy} \cdot \frac{dy}{dz} \cdot dz = \left( \frac{dx}{dz} \right)_{\text{initial}} \cdot \tan(\gamma) \cdot \frac{z_1 - z_2}{2}$$

with  $\gamma$  being the stereo angle mentioned in section 4.2.1 and  $\frac{z_1 - z_2}{2}$  being the distance along the  $z$  axis between the doublet and the stereo layer. The doublet track is then projected to the axial layer within the cassette where we check whether the distance between the



projected doublet hit and a hit in the axial layer  $d$  is below the cut value of  $d = r_{\text{projected}} - r_{\text{axial}} < 100 \mu\text{m}$ . If this is the case we use the axial layer to correct the slope of the *S-triplet* track in y

$$\left(\frac{dy}{dz}\right)_{\text{trp}} = \left(\frac{dy}{dz}\right)_{\text{initial}} + \left(\frac{dy}{dz}\right)_{\text{corr}}$$

with

$$\left(\frac{dy}{dz}\right)_{\text{corr}} = \frac{d}{z_{\text{axial}} - z_{\text{dbl}}}$$

where  $z_{\text{axial}}$  is the z position of the axial layer. We then use the slope in y to perform a correction on the x position of the triplet similar to the previous correction for y in the doublet using the slope in x so that

$$x_{\text{trp}} = x'_0 - x_{\text{corr}}; \quad y_{\text{trp}} = y_{\text{dbl}}$$

with

$$x_{\text{corr}} = \frac{dx}{dz} \cdot dz = \frac{dx}{dy} \cdot \frac{dy}{dz} \cdot dz = \frac{\left(\frac{dy}{dz}\right)_{\text{trp}}}{\tan(\gamma)} \cdot \frac{z_1 - z_2}{2}.$$

this is repeated for both cassettes until no more *S-triplets* can be found.

After finding all *S-triplets* we try to match *S-triplets* between the two cassettes. We start by matching the *S-triplet* slopes, ensuring that the difference between the curvature corrected slope difference in y is below the cut value of

$$\Delta \left(\frac{dy}{dz}\right)_{\text{corr}} = \left| \left(\frac{dy}{dz}\right)_{\text{corr1}} - \left(\frac{dy}{dz}\right)_{\text{corr2}} \right| < 0.01 \text{rad}.$$

Using the slopes in x and y we project the *S-triplet* position to the center between the two *S-triplets* so that

$$x_{\text{proj}}^i = x_{\text{trp}}^i + \left(\frac{dx}{dz}\right)^i \cdot \Delta z^i; \quad y_{\text{proj}}^i = y_{\text{trp}}^i + \left(\frac{dy}{dz}\right)_{\text{corr}}^i \cdot \Delta z^i$$

with  $\Delta z^i$  being the distance from the location of the triplet  $i$  to the center between the triplets. We then require that the difference between the projected hit locations lies below

$$\Delta x = \left| x_{\text{proj}}^1 - x_{\text{proj}}^2 \right| < 10 \text{mm}$$

and

$$\Delta y = \left| y_{\text{proj}}^1 - y_{\text{proj}}^2 \right| < 1 \text{mm}.$$

The two *S-triplets* are matched if they fulfill all three of these criteria. For two *S-triplets* to be combined into a *S-triplet track* we additionally require double uniqueness between *S-triplets*, meaning that we only combine two *S-triplets* into a *S-triplet track* in the case that both of the *S-triplets* have exactly one match, that is each other. All other *S-triplets* are dropped to ensure a high purity of the *S-triplet tracks*. Using the *S-triplet tracks* we perform a correction on the momentum of the particle using the slope of the *S-triplet track* which is used as input for the following track fitting.

## K Alignment

In order to reach the projected precision of a  $\leq 10 \mu\text{m}$  for the Lycoris telescope, precise knowledge of the sensor position in similar precision as the expected resolution is a must. Correlated geometry distortions / displacements of the sensors can introduce a bias on the track parameters without changing the mean  $\chi^2$ . During installation no external tools were available to determine the position and angles of the sensors to an accuracy higher than  $O(1) \text{ mm}$  and  $O(5)^\circ$  respectively. As such, the precise determination of the sensor positions/angles has to be done by aligning the sensors to tracks generated by the particle beam. Particle track based alignment is based on the reduction of the track fit  $\chi^2$  which can be described as the sum over the residual between the predicted particle hit position  $v_{ip}(\tau_j, \mathbf{p})$  and the measured particle hit position  $v_{im}$  divided by the measurement uncertainty  $\sigma_i$ .

$$\chi^2 = \sum_j \sum_i z_{ij}(\tau_j, \mathbf{p}) = \sum_j \sum_i \left( \frac{v_{im} - v_{ip}(\tau_j, \mathbf{p})}{\sigma_i} \right)^2 \quad (9)$$

$i, j$  are the indices for all hits and tracks respectively while  $\tau_j, \mathbf{p}$  are the track parameters and parameters based on which the hit prediction is performed. In order to perform track based alignment the track parameters need to be overconstrained to allow a variation of the positions and angles of singular planes in order to minimize this  $\chi^2$ . The method by which this  $\chi^2$  is minimized in this thesis is the MillepedeII algorithm [38] which performs a linearization of the  $\chi^2$  where linear equality constraints can be invoked via Lagrangian multipliers. This method has the advantage that it correctly estimates the errors and correlations of the fitted parameters. In effect the alignment parameters can be added to equation (4.13) by linear changes in the residuals based on the geometric correction parameters

$\delta p$  and the track correction parameters  $\delta\tau$  so that

$$\chi^2 = \sum_j \sum_i z_{ij}(\tau_j, \mathbf{p}) = \sum_j \sum_i \left( \frac{v_{im} - v_{ip}(\tau_{0j}, \mathbf{p}_0) + \frac{\partial v_{ip}}{\partial \mathbf{p}} \delta \mathbf{p} + \frac{\partial v_{ip}}{\partial \tau_j} \delta \tau_j}{\sigma_i} \right)^2 \quad (10)$$

Where  $\mathbf{p}_0$  are the initial geometric and  $\tau_0$  are the initial track parameters. The minimization of the  $\chi^2$  function can be written via a partitioned matrix as [110]

$$\begin{pmatrix} \Sigma C_j & \cdots & \mathbf{G}_j & \cdots \\ \vdots & \ddots & \mathbf{0} & \mathbf{0} \\ \mathbf{G}_j^T & \mathbf{0} & \Gamma_j & \mathbf{0} \\ \vdots & \mathbf{0} & \mathbf{0} & \ddots \end{pmatrix} \cdot \begin{pmatrix} \delta \mathbf{p} \\ \vdots \\ \delta \tau_j \\ \vdots \end{pmatrix} = - \begin{pmatrix} \Sigma b_j \\ \vdots \\ \beta_j \\ \vdots \end{pmatrix} \quad (11)$$

$C_j$  is a symmetric matrix of dimension equal to the number of global parameters  $n$  whose constituents are calculated from the global derivatives  $\frac{\partial v_{ip}}{\partial \mathbf{p}}$ .  $\Gamma_j$  is another symmetric matrix with dimension equal to the number of local parameters  $\nu$  which depends only on the  $j$ -th local measurement and the local derivatives  $\frac{\partial v_{ip}}{\partial \tau_j}$ .  $G_j$  is a matrix with  $n$  number of rows and  $\nu$  number of columns which provides the only relation between the global measurements and the local track parameters. In the alignment procedure only the global parameters are of interest which allows to ignore the corrections to the local track parameters and therefore reduce the matrix using

$$C' = \sum_i C_i - \sum_i G_i \Gamma_i^{-1} G_i^T \quad b' = \sum_i b_i - \sum_i G_i (\Gamma_i^{-1} \beta_i) \quad (12)$$

to a set of  $n$  normal equations in the form of

$$\begin{pmatrix} C' \end{pmatrix} = \begin{pmatrix} \mathbf{p} \end{pmatrix} = - \begin{pmatrix} \mathbf{b}' \end{pmatrix} \quad (13)$$

from which the correction vector to the global parameters  $p$  can be calculated by inversion of the matrix  $C'$ . While an exact result is received by this solution, multiple iterations have

	function ( $f(z)$ )	Influence( $z$ )
	$\chi^2 = \frac{z^2}{2}$	$z$
Huber	$\begin{cases} \frac{z^2}{2} & \text{if }  z  < C_H \\ C_H( z  - C_H/2) & \text{if }  z  > C_H \end{cases}$	$\begin{cases} z \\ C_H \end{cases}$
Cauchy	$\frac{C_C^2}{2} \ln \left( 1 + \left( \frac{z}{C_C} \right)^2 \right)$	$\frac{z}{1 + \left( \frac{z}{C_C} \right)^2}$

**Table 16** – Outlier weighting functions

to be performed in the cases that:

- the equation depends non-linearly on the global parameters which requires the linearization via Taylor expansion,
- the data contains outliers that have to either be removed with gradually tightening cuts or via down-weighting,
- the accuracy of the data is not know beforehand and has to be determined from the data requiring a rerun after a more accurate determination of the accuracy.

Outliers can appear for example in the cases that a hit is incorrectly assigned to a track. A cut on the track fit  $\chi^2$  is used to filter out wrongly reconstructed tracks. Because of the generally larger  $\chi^2$  before the first alignment iteration these cuts have to be tightened gradually with the number of alignment steps as the  $\chi^2$  decreases. The  $\chi^2$  of wrongly reconstructed tracks generally does not improve with the alignment gradually cutting them out further and further with each iteration. Furthermore, the impact of outliers on the minimization can be reduced by minimizing a function  $F$  of the normalized residuals instead of the  $\chi^2$  function with

$$F(\mathbf{p}, \tau_i) = \sum_j f(z_j(\tau_i, \mathbf{a})) \quad (14)$$

where  $f$  are the Cauchy or the Huber functions described in table 16. which for standard values of  $C_H = 1.345$  and  $C_C = 2.3849$  keeps the efficiency for Gaussian data without outliers at 95%. Even then certain degrees of freedom may be undefined and require the introduction of equality constraint equations such as *zero global displacement* or *zero rotation* for the whole setup. Such constraints are handled via Lagrange multipliers  $\lambda$  within the Millepede2 framework which are added per constraint to the function  $F(\mathbf{p})$ . More details to this can be found in [38] and [94] As a result of outliers the process is repeated iteratively until the corrections received from Millepede are of the same order as the errors of the measure-

ments the changes are no longer statistically significant. Additionally only triplet finder tracks are considered when using the alignment as before alignment high purity tracks are more important than a high efficiency finder like the *road search*

In section [4.2.1](#) it was mentioned that only small rotations around and translations along the z axis were considered based on installation specifications. These specifications are the starting parameters for the track based alignment used in order to reduce the number of iterative steps required to find a good alignment.



# List of Tables

5.1	Different secondary target materials and thickness for the three test beam lines [41] . . . . .	50
6.1	Design performance of the LCTPC prototype [56]. . . . .	62
6.2	GEANT4 momentum resolution in units of $1 \times 10^{-6} \text{ MeV}^{-1}$ for different configurations of the sensors spatial resolution and the distance between outermost layers within an arm based on a system with 4 layers [56]. . . . .	64
6.3	Final requirements to the telescope system [60]. . . . .	66
6.4	SiD layer thickness . . . . .	70
6.5	Probe pads of the SiD sensor . . . . .	73
6.6	Standard KPjX clock periods . . . . .	78
6.7	Sensor orientations as seen by beam particles . . . . .	83
8.1	Layer configuration with name of which sensors were used in the setup as well as their corresponding position along the z axis. . . . .	126
8.2	Layer configuration with name of which sensors were used in the setup as well as their corresponding position along the z axis. . . . .	128
8.3	Event synchronization between AZALEA and Lycoris via the TLU. . . . .	134
9.1	Mean and RMS of the beam and no beam runs of Figure 9.7 . . . . .	148
9.2	Statistics for the two different common modes based on the different triggering schemes shown in Figure 9.9. . . . .	150
9.3	Number of entries for different strip cuts for the two plots showing the normalized number of entries versus the size of the reconstructed cluster. Once for all reconstructed clusters and once only for clusters with $S/N_{\text{cluster}} \geq 4$ which is the final quality cut that was chosen. . . . .	156
10.1	Pearson correlation entries . . . . .	166

10.2	Timed internal trigger entries for the six different Lycoris modules. . . . .	188
10.3	Mean noise for different opening windows for S47 . . . . .	197
10.4	Fit results of the Gaussian fit to the biased and unbiased residuals of Lycoris modules . . . . .	211
10.5	Single plane efficiency for the six Lycoris modules in the test beam. . . . .	213
11.1	Fit results of the Gaussian fit to the biased and unbiased residuals of the two axial test beam sensors. . . . .	219
11.2	Required and achieved parameters for the Lycoris telescope. . . . .	226
3	Minimal Ionizing Particle loss for different particle types[3]. . . . .	235
4	The properties of silicon relevant for tracking detectors [23]. . . . .	236
5	Gray code example . . . . .	240
6	HDMI pin mapping of the AIDA TLU [47] . . . . .	241
7	Signal cable pin mapping . . . . .	241
8	<i>Kapton Flex Cable</i> pin mapping . . . . .	242
9	Custom HV cable pin mapping. Bias <sub>0</sub> to Bias <sub>2</sub> are the bias for the first stack of sensors and Bias <sub>3</sub> to Bias <sub>5</sub> are forwarded to the slave cassette board. . . . .	245
10	Custom LV cable pin mapping. A/D <sub>Master</sub> are analog and digital voltages to the master board and A/D <sub>Slave</sub> are the analog and digital voltages forwarded to the slave cassette board. the same applies for the GND connections. . . . .	245
11	DesyTrackerRunControl . . . . .	246
12	DesyTracker . . . . .	247
13	DesyTracker . . . . .	248
14	DesyTracker . . . . .	249
15	DesyTracker . . . . .	250
16	Outlier weighting functions . . . . .	258



# List of Figures

- 1.1 The Standard Model of particle physics. Adapted from [4] . . . . . 4
- 2.1 Stopping power for a muons and protons in copper as a function of the momentum [3]. . . . . 13
- 2.2 Mean energy loss of positrons and electrons in Lead [3]. . . . . 14
- 2.3 Energy loss of 500 MeV pions in silicon of different thickness[3]. . . . . 15
- 2.4 One dimensional sketch of multiple coulomb scattering of the particle in material [3]. . . . . 16
- 3.1 Slice of the different components of the CMS detector [22]. . . . . 20
- 3.2 Band gaps for the different types of solids.  $E_f$  is the fermi energy and  $E_g$  is the band gap energy between the valence and conduction band. . . . . 21
- 3.3 Charge drift in a reverse biased pn-junction generated by the energy loss of a traversing particle. . . . . 24
- 3.4 Silicon sensor with segmented readout electrodes in the form of high concentration  $p^+$ -doped acceptor implanted silicon within the n-doped bulk. When getting closer to the electrodes the field lines, depicted as the black arrows pointing down, stop being parallel and funnel the charge to the closest electrodes. . . . . 26
- 3.5 The floating strips are capacitively coupled to the adjacent readout strips as a result of their inter-strip capacitance as a result of their parallel path through the sensor. When signal is registered on the "floating" strip a signal is induced in the adjacent strips based on the ratio of the inter-strip capacitance  $C_{ss}$  to the strip-to-backplane capacitance  $C_b$ . Pictures adapted from [21] . . . . . 27
- 3.6 Example of a hybrid chip and sketch of the connection method. . . . . 29

3.7	Picture of the Mimosa26 pixel sensor on its carrier board as used at the DESY II Test Beam Facility [31]. . . . .	30
3.8	Structure of modern CMOS based MAPS [23]. . . . .	31
4.1	Local coordinate system for the sensor. Depending on angles to the beam the local coordinates can depend on all three global parameters. . . . .	36
4.2	Sketch explaining the <i>triplet finder</i> and <i>road search</i> track finding algorithms. The black vertical lines are the measurement layers. The solid lines are the starting layers from which the algorithm starts and the dashed lines are used for pickup of further hits. . . . .	39
4.3	Sketch explaining the effect of the GBL refit [38]. . . . .	41
4.4	Biased and unbiased residual of the projected track hit to the cluster position for S43. . . . .	42
5.1	Measurement of the particle intensity within DESY (grey histogram) and the corresponding particle energy (black line) throughout two DESY injection cycles. [41] . . . . .	48
5.2	Sketch showing the DESY II Test Beam Facility [41]. . . . .	49
5.3	Sketch of the relation between the <i>uptime</i> and the chosen energy for the sinusoidal DESY II energy cycle. . . . .	51
5.4	Time difference between the injection signal at 0 and the appearance of test beam particles in T24 over a whole injection cycle. [41] . . . . .	52
5.5	Beginning and end point for the test beam <i>uptime</i> for different energies measured via the T24 beam monitors. The grey area is the <i>uptime</i> . . . . .	53
5.6	Particle flux measured at the T24 beam monitors before the secondary collimator within the area. [41] . . . . .	53
5.7	Picture of the AIDA TLU rack unit. . . . .	54
5.8	AIDA Mode operation for the TLU with synchronization T0 and synchronization to the DESY II <i>uptime</i> via the $E_{\min}$ signal via the use of a shutter. [47] . . . . .	55
5.9	Picture of the EUDET Type telescope within testbeam area T24 [31]. . . . .	58

- 5.10 Sketch showing the workings of the EUDET telescope readout. The readout is split into frames each of which take  $115.2\ \mu\text{s}$  to readout. Two of them are combined into an event shown by the two colors. The diagonal line running through the frame signals the rolling shutter readout position with the time shown on x axis. A particle could be located in a row that has already been read out by the rolling shutter as such it is only read out once the rolling shutter once more reads out the row in question signified by the dotted line connecting the particle location to the diagonal line. The second event shows that nothing will be read out in the case that no trigger arrives with a particle. 59
- 5.11 Picture of the PCMAG superconducting solenoid located in Area T24/1 without the four additional rails used for the Lycoris telescope. . . . . 60
- 6.1 Particle momentum distribution after interaction with magnet wall through Data in black and simulation in green [57]. . . . . 63
- 6.2 Sketch showing the functionality of an external reference within the PCMAG to determine correct momentum resolution and the used coordinate system. 63
- 6.3 *GEANT4* simulation result for the particle hit location at the entry and exit of the PCMAG [56]. . . . . 66
- 6.4 Sketch showing relation between sensor height  $y$  and available space  $a$ . . . . 67
- 6.5 Picture of an SiD strip sensor with flip chip bonded ASICs- The three squares are regions of the sensor shown in microscopic pictures in Figure 6.8a (azure), Figure 6.8b (black) and Figure 6.10 (blue). . . . . 68
- 6.6 Sketch of the readout layers of the SiD sensor . . . . . 69
- 6.7 Microscope picture of the cross section of a SiD sensor. . . . . 70
- 6.8 Microscope pictures of the SiD sensor routing layers. . . . . 71
- 6.9 Microscope picture showing the via connection from the *coupling layer* to the *routing layer* which transfers signal to the ASIC. . . . . 71
- 6.10 Sketch of the locations of the different connections of the bump-bond pads to the wire-bond pads and *coupling layer*. The names C0 to C1024 is based on the name of the corresponding KPiX channel which is connected to this bump-bond pad. . . . . 72
- 6.11 Plot showing the relation between the pad number on the x axis and the corresponding strip number on the y axis for the two sensor halves. . . . . 73
- 6.12 Microscopic picture of the bottom side of a bare KPiX ASIC which in the picture is flipped over and connected to via wirebonds. . . . . 74

6.13	Simplified block diagram for the analog core of a single KPiX readout channel [70]. . . . .	75
6.14	Sketch of the KPiX power pulsing acquisition cycle. . . . .	77
6.15	Helix track parameter resolutions dependent on the size of the stereo angles in relation to the previously mentioned PCMAG coordinate system. . . . .	82
6.16	Correlations from the GBL simulation between the different parameters. . .	83
6.17	Helix track parameter resolution dependency on the stereo angle. . . . .	84
6.18	Expected parameter resolution for a helical fit within PCMAG using Lycoris sensors in a 0, -2, +2, +2, -2, 0 degree orientation. . . . .	85
6.19	CAD drawing of a Lycoris cassette which are used to house the sensors for telescope operations[71]. . . . .	86
6.20	CAD drawing of the Lycoris cassette that is used to house the sensors of the telescope [71]. . . . .	87
6.21	Sketch of the installation of sensors within the Cassette. . . . .	88
6.22	Picture of an SiD sensor installed in the Torlon frame. . . . .	89
6.23	CAD drawing of the rail system that holds the two cassettes within the PCMAG[71]. The aluminum cart is depicted in light blue and the cassette is depicted in orange. The red arrow depicts the electron path. . . . .	89
6.24	Block diagram showing the electronic connections between the different devices required for the Lycoris telescope. . . . .	90
6.25	Picture of the KPiX DAQ Board. . . . .	92
6.26	Picture of front (top) and back (bottom) of the KPiX Cassette Master Board. .	93
6.27	Picture of a <i>Kapton Flex Cable</i> . . . . .	94
6.28	Picture of oxidized <i>Kapton Flex Cable</i> pads. . . . .	95
6.29	Control and data flow to and from the different DAQ system objects. The dashed lines are optional as the system can be operated in a mode without them. In the case that a dashed line becomes a solid line, like with the clock lines, it means that the DAQ in-between decides whether to use the optional input or not, based on the configuration that was sent. . . . .	97
6.30	Example of clear text meta data from a calibration run. . . . .	98
7.1	Microscope picture of the cross section of a Lycoris module at the bump bond.	101
7.2	Picture of the gluing tool used for the gluing of the <i>Kapton Flex Cable</i> onto the SiD tracker sensors. Based on the tool used by the University of Hamburg CMS pixel group for the assembly of their modules [84]. . . . .	102

7.3	Custom made vacuum pick-up tool and rubber stamp. . . . .	103
7.4	Microscope picture of the wire-bonds connecting the <i>Kapton Flex Cable</i> to the KPiX chip via the sensor <i>routing layer</i> . . . . .	104
7.5	Picture of the opened probe station dark box. . . . .	105
7.6	Picture of a test structure pad after destructive discharge. . . . .	108
7.7	(Top) Picture of an SiD test structure on the DAF probe station for inter-strip measurements. (Bottom) Microscopic view of the same test structure with the needle placement. . . . .	109
7.8	Current measurements of the SiD sensor for different bias voltages before and after major steps. The different stages are highlighted in the legend. . . .	110
7.9	Capacitance measurements of the SiD sensor for different bias voltages before and after major steps. The different stages are highlighted in the legend.	111
7.10	Capacitance measurements of the SiD sensor for a 1 kHz and 10 kHz AC frequency. The measurement accurately reflects the effect of the increased frequency based on (7.2). . . . .	112
7.11	Inverse square capacitance value versus bias voltage for S41 with linear regressions to the flattened part and the early rise. . . . .	113
7.12	<i>IV</i> curves for all 29 <i>Bare</i> sensors. . . . .	114
7.13	$C^{-2}V$ curves for all 29 <i>Bare</i> sensors (top) and the corresponding distribution for their depletion voltages (bottom). . . . .	115
7.14	<i>IV</i> curves for some of the <i>WireBonded</i> SiD sensors. S41 and S43 are representative for all sensors which show no change in their behavior. S32 and S55 on the other hand show a very sudden large increase in the dark current which indicates a full breakdown which was not present for the <i>Bare</i> sensors.	116
7.15	Current measurements of the SiD sensor S55 for different bias voltages before and after major steps. The different stages are highlighted in the legend.	116
7.16	<i>IV</i> measurement for SiD test structure in a pristine condition and after glue was applied to the center of the structure as shown in the microscope picture.	118
7.17	<i>IV</i> measurement for SiD test structure in a pristine condition and after glue was applied to the ring surrounding the structure as shown in the microscope picture. . . . .	118
7.18	<i>IV</i> measurement for SiD test structure in a pristine condition and after glue was applied to over the Poly-SiR including the ring structure and pads as shown in the microscope picture. . . . .	119
7.19	Inter-strip and normal CV measurement of the SiD test structure 39. . . . .	120

7.20	Sketch of a three strip silicon sensor electronic circuit equivalence. . . . .	120
8.1	T24 setup during operation with three AZALEA layers in front and behind two Lycoris cassettes. The Timepix3 was located on the leftmost layer located after the last AZALEA layer. . . . .	124
8.2	Sketch showing the layer numbering between the different sensor layers in area T24. Lycoris layers are shown in green, AZALEA layers in black and the Timepix3 layer in azure. The beam direction is indicated by the orange arrow.	125
8.3	Sketch showing the angles and orientation of the Lycoris layers within their cassettes. . . . .	126
8.4	Sketch showing the layer numbering between the different sensor layers in area T24. Lycoris layers are shown in green, AZALEA layers in black. The beam direction is indicated by the orange arrow. . . . .	128
8.5	T24/1 setup during operation with six AZALEA layers located between two Lycoris cassettes. . . . .	129
8.6	Sketch of the data/signal flow between the different devices used at the test beam setups . . . . .	130
8.7	Sketch of the data synchronization between Lycoris and AZALEA . The TLU records the Trigger ID similar to the AZALEA system while also recording the timestamp of the trigger. The times of the TLU triggers can be compared with the list of trigger times received from Lycoris in order to perform an event by event matching. The Timepix3 operates via internal triggers at a much higher precision and is not limited by external shutters. . . . .	133
8.8	Minimum time difference between the TLU timestamp and the KPix timestamp after synchronization. . . . .	135
8.9	Sketch explaining the different number of recorded tracks within the AZALEA system compared to the Lycoris system. . . . .	135
8.10	Time difference between events recorded by the Timepix3 system relative to events recorded by the Lycoris system. . . . .	136
9.1	Flowchart showing a step by step of the analysis for the data sets gathered by the different detectors used during a test beam analysis. . . . .	140

- 9.2 Single channel charge calibration result in ADC vs DAC. The visible kink at 246 DAC is a result of an internal DAC to voltage conversion that transitions from one method to another. The linear regression does not take this into account and therefore results in a bad fit. It is used to more accurately show the difference between DAC value and fC value. . . . . 143
- 9.3 Single channel charge calibration result in ADC vs fC. . . . . 144
- 9.4 Slope distribution of *bucket* zero calibrations for all channels in a single KPiX 145
- 9.5 Distribution of the pearson correlation coefficient for all *bucket zero* calibration results of a single KPiX. . . . . 146
- 9.6 Raw baseline distribution for channel 290 of S47-2. The pedestal is asymmetric with a tail to lower ADC values which is due to leakage of capacitors resulting in a pedestal drift. . . . . 147
- 9.7 Pedestal comparison for S47-2 for four different runs, two with and two without any beam passing through the Lycoris module. Each entry represents one of the 1024 channels of the KPiX ASIC. . . . . 148
- 9.8 Distribution of all recorded charge after pedestal subtraction and calibration conversion for channel 290 of S47-2. . . . . 149
- 9.9 Common mode distribution of S47-2 once for beam triggered data with semi random time distribution and once for a forced trigger which results in each channel recording their baseline at the exact same time during the acquisition cycle. . . . . 151
- 9.10 Distribution of true charge  $Q^{\text{true}}$  after pedestal subtraction, calibration conversion and common mode subtraction for channel 290 of S47-2. The green curve shows a comparison to the distribution shown in Figure 9.8 before common mode subtraction and the statistics shown here are only for the new black curve with the old stats already shown in Figure 9.8. . . . . 152
- 9.11 2D histogram showing the true charge  $Q^{\text{true}}$  recorded versus the sensor strip number once for a run with beam and once for a run without beam. . . . . 152
- 9.12 Number of clusters versus the size of the reconstructed cluster, normalized to the total amount of reconstructed clusters, for different input  $(S/N)_{\text{strip}}$  cut values without any cut on the final reconstructed cluster significance. . . 155
- 9.13 Number of clusters versus the size of the reconstructed cluster, normalized to the total amount of reconstructed clusters, for different input  $S/N_{\text{strip}}$  cut values with a cut on the combined cluster Signal over Noise of  $S/N_{\text{cluster}} \geq 4$ . 155

- 9.14 Histogram showing the position distribution of all clusters with  $S/N_{\text{cluster}} \geq 4$  once for a run with beam and once for a run without beam. The single channels with large amounts of entries are noisy channels which are not masked here. . . . . 157
- 9.15 The time distribution of triggers in an acquisition in units of BCC without beam. A trigger inhibition was set to 1000 BCC resulting in no triggers being registered before that. The peak is a result of a large amount of triggers which only starts lowering because each channel reaches the maximum amount of triggers allowed. . . . . 158
- 9.16 The time distribution of triggers in an acquisition in units of BCC with beam and *monster event* suppression. A trigger inhibition was set to 1000 BCC resulting in no triggers being registered before that. . . . . 159
- 9.17 Minimal difference value between the internally record channel trigger time and the externally recorded scintillator trigger signal time in externally triggered beam operation. Except for single triggers, all triggers are located in the two main peaks. . . . . 161
- 10.1 Probe of the analog current (green) and the data readout lines of KPiX S59-1 (pink) and KPiX S59-2 (yellow) during an *acquisition cycle*. The small box on top of the picture reflects the full *acquisition cycle* with the azure box showing the zoomed area of the *acquisition cycle* that is shown in detail in the larger picture. . . . . 164
- 10.2 Probe of the analog current (green) and the data readout lines of KPiX S59-1 (pink) and KPiX S59-2 (yellow) during an *acquisition cycle*. The zoom is focused on the end of the digitization phase and the start of the readout phase of the *acquisition cycle*. . . . . 165
- 10.3 Digital response to injected charge during calibration. . . . . 167
- 10.4 Slope distributions for all 1024 channels of S59-1 for the four different *buckets*. 167
- 10.5 Slope distributions for all 1024 channels of S42-2 for the four different *buckets*. 168
- 10.6 Slope distributions mapped to the location of the channel on KPiX S59-1 for two different *buckets*. . . . . 169
- 10.7 Calibration slopes for S43-2 bucket 1 for different pre-charge clock values. . 170
- 10.8 Calibration slopes of S43-1 in high gain operation for different start-up phase durations. . . . . 170



- 
- 10.9 Calibration slopes of S40-1 in high gain operation for different start-up phase durations. . . . . 171
- 10.10 Calibration slopes of S53-1 in normal gain operation in the laboratory and area T24/1 at the DESY II Test Beam Facility . . . . . 172
- 10.11 Picture of the opened climate chamber with the styrofoam dark box which houses the Lycoris module during operation. . . . . 173
- 10.12 Picture of the inside of the styrofoam darkbox with a single Lycoris module and adapter board which replaces the cassette board in the system setup. . . 174
- 10.13 Relation between the set humidity of the climate chamber and the measured humidity of the external device. . . . . 175
- 10.14 Calibration slopes for S41-2 for different levels of relative humidity. . . . . 175
- 10.15 Calibration of S41-2 channel 557 for different levels of relative humidity. The dashed lines are the linear response fit from which the slope is extracted. . . . 176
- 10.16 Calibration of S41-2 channel 200 for different levels of relative humidity. The dashed lines are the linear response fit from which the slope is normally extracted. In this case they are simply there to guide the eye as to the overall development of the digital response for increased humidity . . . . . 177
- 10.17 Calibration of S41-2 channel 898 for different levels of relative humidity. The dashed lines are the linear response fit from which the slope is extracted. . . . 177
- 10.18 Calibration slopes mapped onto KPiX space. The white blocks fall outside the z-range and are located at or below zero. . . . . 178
- 10.19 Calibration slopes for S34 for different levels of relative humidity. The negative slopes are a result where the response to an early charge injection is as expected but at later injections the no response is seen resulting in a negative slope of the linear regression. . . . . 179
- 10.20 S41-2 calibration slope distribution at 25%RH, 95%RH and at 25%RH after exposure to the 95%RH environment. . . . . 180
- 10.21 Calibration slope distribution for all channels of the KPiX on S33 after different levels of baking. . . . . 181
- 10.22 Calibration slope for channel 557 of S33-2. . . . . 182

10.23	Number of triggers normalized to the number of acquisitions for S59 shown against the sensor strip number for a threshold of 200 DAC. The channels with spikes relative to the baseline are primary candidates for channels that cause <i>monster events</i> . Only one half of the sensor is activated in the green plot resulting in no triggers for the right half of the plot. The overall lowered amount of triggers even in the left half indicates unwanted cross talk between the two KPiX. . . . .	183
10.24	Number of triggers normalized to the number of acquisitions for S59-1 shown against the sensor strip number for a threshold of 230 DAC = 3.23 fC for three different channel disabling maps. . . . .	185
10.25	Number of noise triggers normalized to the number of acquisitions for S43-2 shown against the sensor strip number for a threshold of 230 DAC = 3.23 fC for three different channel disabling maps. . . . .	186
10.26	Number of triggers normalized to the number of acquisitions for two Lycoris modules shown against the local Lycoris module position for a threshold of 230 DAC = 3.23 fC with beam in black and without beam in green. . . . .	187
10.27	Number of triggers normalized to the number of acquisitions with the requirement that an external trigger was recorded two to three BCC after the internal trigger for Lycoris modules shown against the local Lycoris module coordinate for a threshold of 230 DAC = 3.23 fC. . . . .	188
10.28	Number of how often a certain amount of external triggers were recorded within a single acquisition cycle . . . . .	189
10.29	Distribution of 1840 noise values for the strips of sensor S47 recorded during the July 2019 Test beam campaign in Area T24/1. The value of noise for each strip is given by $\sigma = MAD \cdot 1.4826$ of the true charge distribution. . . . .	190
10.30	Noise values of channels mapped to the sensor strip numbers for S47 recorded during the July 2019 Test beam campaign in Area T24/1 . . . . .	191
10.31	Noise values of channels mapped to KPiX channels recorded during the July 2019 Test beam campaign in Area T24/1. . . . .	192
10.32	Distribution of 1840 noise values for the strips of sensor S47 recorded during the March 2020 Test beam campaign in Area T24/1. The value of noise for each strip is given by $\sigma = MAD \cdot 1.4826$ of the true charge distribution. . . . .	192
10.33	Noise mapped to the sensor strip numbers for S47 recorded during the March 2020 Test beam campaign in Area T24 . . . . .	193

10.34	Noise mapped to KPiX channels recorded during the March 2020 Test beam campaign in Area T24. . . . .	194
10.35	Distribution of 1840 noise values for the strips of sensor S47 recorded during the August 2020 Test beam campaign in Area T24/1. The value of noise for each strip is given by $\sigma = MAD \cdot 1.4826$ of the true charge distribution. . . . .	195
10.36	Noise mapped to the sensor strip numbers for S47 recorded during the August 2020 Test beam campaign in Area T24 . . . . .	195
10.37	Noise mapped to KPiX channels recorded during the August 2020 Test beam campaign in Area T24. . . . .	196
10.38	Noise distribution of S47 for different time opening windows. . . . .	197
10.39	Noise plotted against the time at which the trigger was registered within the KPiX acquisition phase of S47 for different time opening windows. . . . .	198
10.40	Noise plotted against the Strip number of S47 for two different data sets of the 1000 to 4000 BCC opening window in the same laboratory configuration. . . . .	199
10.41	Noise plotted against the Strip number of S47 for different time opening windows. . . . .	199
10.42	Noise plotted against the the gray coded bits. An entry is filled into the corresponding bin if the bit is set to high at the point of measurement. . . . .	200
10.43	Noise distribution of S47 for different gain settings. . . . .	201
10.44	Charge of <i>tagged hits</i> generated by the AZALEA system with a Landau-Gauss convolution fit. . . . .	203
10.45	Charge of <i>tagged hits</i> with Landau-Gauss convolution fits, split into different cluster sizes. . . . .	203
10.46	Sketch showing the sub cell of the SiD sensor. . . . .	204
10.47	Number of clusters on the sensor sub-cell split into different cluster sizes. . . . .	205
10.48	Charge of <i>tagged hits</i> after splitting hits into readout strip hits and floating strip hits. . . . .	206
10.49	$\eta$ distribution of all <i>tagged hits</i> . . . . .	207
10.50	Charge distribution of all readout strip clusters on AZALEA track for different bias voltages. . . . .	209
10.51	Relation of the cluster size for all tagged clusters at different bias voltages. . . . .	209
10.52	Residuals of the projected track hit to the cluster position for S47. . . . .	210
10.53	S-triplet residual in x to the projected track hit. . . . .	211
10.54	Efficiency for all six Lycoris layers for all AZALEA tracks that are matched in time. . . . .	212

---

11.1	Charge distribution of all clusters on the standalone track generated by the Lycoris telescope. . . . .	218
11.2	Biased and unbiased residual of the projected track hit to the cluster position for S43. . . . .	219
11.3	Local <i>cluster</i> positions on S47 for a run without beam . . . . .	220
11.4	Local positions of all <i>clusters</i> on reconstructed tracks from a run without beam	221
11.5	Residual of $q/P$ after GBL refit with a curvature that can be adjusted by the refit in order to improve upon the fit result even when no curvature is physically possible. . . . .	223
6	Schematic overview of the relation between the different EUDAQ2 components.	[81]238
7	(Top) Picture of the CV/IV switch box used to internally reconnect the probes to the correct devices. (Bottom) Technical drawing of the CV/IV switch box.	243
8	Picture of the custom made LV cable (left) and HV cable (right) used to connect the power supply with the cassette board . . . . .	244





# Bibliography

- [1] H. Abramowicz *et al.*, “The International Linear Collider Technical Design Report - Volume 4: Detectors,” 6 2013.
  
- [2] T. Behnke, J. E. Brau, B. Foster, J. Fuster, M. Harrison, J. M. Paterson, M. Peskin, M. Stanitzki, N. Walker, and H. Yamamoto, “The International Linear Collider Technical Design Report - Volume 1: Executive Summary,” 2013. See also <http://www.linearcollider.org/ILC/TDR> . The full list of contributing institutes is inside the Report.
  
- [3] P. D. Group, P. A. Zyla, R. M. Barnett, J. Beringer, O. Dahl, D. A. Dwyer, D. E. Groom, C. J. Lin, K. S. Lugovsky, E. Pianori, D. J. Robinson, C. G. Wohl, W. M. Yao, K. Agashe, G. Aielli, B. C. Allanach, C. AMSler, M. Antonelli, E. C. Aschenauer, D. M. Asner, H. Baer, S. Banerjee, L. Baudis, C. W. Bauer, J. J. Beatty, V. I. Belousov, S. Bethke, A. Bettini, O. Biebel, K. M. Black, E. Blucher, O. Buchmuller, V. Burkert, M. A. Bychkov, R. N. Cahn, M. Carena, A. Ceccucci, A. Cerri, D. Chakraborty, R. S. Chivukula, G. Cowan, G. D’Ambrosio, T. Damour, D. de Florian, A. de Gouvêa, T. DeGrand, P. de Jong, G. Dissertori, B. A. Dobrescu, M. D’Onofrio, M. Doser, M. Drees, H. K. Dreiner, P. Eerola, U. Egede, S. Eidelman, J. Ellis, J. Erler, V. V. Ezhela, W. Fetscher, B. D. Fields, B. Foster, A. Freitas, H. Gallagher, L. Garren, H. J. Gerber, G. Gerbier, T. Gershon, Y. Gershtein, T. Gherghetta, A. A. Godizov, M. C. Gonzalez-Garcia, M. Goodman, C. Grab, A. V. Gritsan, C. Grojean, M. Grünewald, A. Gurtu, T. Gutsche, H. E. Haber, C. Hanhart, S. Hashimoto, Y. Hayato, A. Hebecker, S. Heinemeyer, B. Heltsley, J. J. Hernández-Rey, K. Hikasa, J. Hisano, A. Höcker, J. Holder, A. Holtkamp, J. Huston, T. Hyodo, K. F. Johnson, M. Kado, M. Karliner, U. F. Katz, M. Kenzie, V. A. Khoze, S. R. Klein, E. Klempt, R. V. Kowalewski, F. Krauss, M. Kreps, B. Krusche, Y. Kwon, O. Lahav, J. Laiho, L. P. Lellouch, J. Lesgourgues, A. R. Liddle, Z. Ligeti, C. Lippmann, T. M. Liss, L. Littenberg, C. Lourenço, S. B. Lugovsky, A. Lusiani, Y. Makida, F. Maltoni, T. Mannel, A. V. Manohar, W. J. Marciano, A. Masoni, J. Matthews, U. G. Meißner, M. Mikhasenko,

- D. J. Miller, D. Milstead, R. E. Mitchell, K. Mönig, P. Molaro, F. Moortgat, M. Moskvic, K. Nakamura, M. Narain, P. Nason, S. Navas, M. Neubert, P. Nevski, Y. Nir, K. A. Olive, C. Patrignani, J. A. Peacock, S. T. Petcov, V. A. Petrov, A. Pich, A. Piepke, A. Pomarol, S. Profumo, A. Quadt, K. Rabbertz, J. Rademacker, G. Raffelt, H. Ramani, M. Ramsey-Musolf, B. N. Ratcliff, P. Richardson, A. Ringwald, S. Roesler, S. Rolli, A. Romaniouk, L. J. Rosenberg, J. L. Rosner, G. Rybka, M. Ryskin, R. A. Ryutin, Y. Sakai, G. P. Salam, S. Sarkar, F. Sauli, O. Schneider, K. Scholberg, A. J. Schwartz, J. Schwiening, D. Scott, V. Sharma, S. R. Sharpe, T. Shutt, M. Silari, T. Sjöstrand, P. Skands, T. Skwarnicki, G. F. Smoot, A. Soffer, M. S. Sozzi, S. Spanier, C. Spiering, A. Stahl, S. L. Stone, Y. Sumino, T. Sumiyoshi, M. J. Syphers, F. Takahashi, M. Tanabashi, J. Tanaka, M. Taševský, K. Terashi, J. Terning, U. Thoma, R. S. Thorne, L. Tiator, M. Titov, N. P. Tkachenko, D. R. Tovey, K. Trabelsi, P. Urquijo, G. Valencia, R. Van de Water, N. Varelas, G. Venanzoni, L. Verde, M. G. Vincter, P. Vogel, W. Vogelsang, A. Vogt, V. Vorobyev, S. P. Wakely, W. Walkowiak, C. W. Walter, D. Wands, M. O. Wascko, D. H. Weinberg, E. J. Weinberg, M. White, L. R. Wiencke, S. Willocq, C. L. Woody, R. L. Workman, M. Yokoyama, R. Yoshida, G. Zanderighi, G. P. Zeller, O. V. Zenin, R. Y. Zhu, S. L. Zhu, F. Zimmermann, J. Anderson, T. Basaglia, V. S. Lugovsky, P. Schaffner, and W. Zheng, “Review of Particle Physics,” *Progress of Theoretical and Experimental Physics*, vol. 2020, 08 2020. 083C01.
- [4] C. Burgard and D. Galbraith, “Standard model of particle physics cern webfest 2012..” <http://davidgalbraith.org/portfolio/ux-standard-model-of-the-standard-model/>.
- [5] D. Griffiths, *Introduction to Elementary Particles, 2nd, Revised Edition*. Wiley, ISBN: 978-3-527-40601-2, 2008.
- [6] D. H. Perkins, *Introduction to High Energy Physics*. Cambridge University Press, 4 ed., 2000.
- [7] S. Chatrchyan *et al.*, “Observation of a New Boson at a Mass of 125 GeV with the CMS Experiment at the LHC,” *Phys. Lett. B*, vol. 716, pp. 30–61, 2012.
- [8] G. Aad *et al.*, “Observation of a new particle in the search for the Standard Model Higgs boson with the ATLAS detector at the LHC,” *Phys. Lett. B*, vol. 716, pp. 1–29, 2012.
- [9] V. C. Rubin, J. Ford, W. K., and N. Thonnard, “Rotational properties of 21 SC galaxies



- with a large range of luminosities and radii, from NGC 4605 ( $R=4\text{kpc}$ ) to UGC 2885 ( $R=122\text{kpc}$ ),” *Astrophysical Journal*, vol. 238, pp. 471–487, 1980.
- [10] P. Peebles and B. Ratra, “The Cosmological Constant and Dark Energy,” *Rev. Mod. Phys.*, vol. 75, pp. 559–606, 2003.
- [11] M. Gonzalez-Garcia and M. Maltoni, “Phenomenology with Massive Neutrinos,” *Phys. Rept.*, vol. 460, pp. 1–129, 2008.
- [12] L. Canetti, M. Drewes, and M. Shaposhnikov, “Matter and Antimatter in the Universe,” *New J. Phys.*, vol. 14, p. 095012, 2012.
- [13] K. Arndt *et al.*, “Technical design of the phase I Mu3e experiment,” 9 2020.
- [14] E. A. Uehling, “Penetration of heavy charged particles in matter,” *Ann. Rev. Nucl. Part. Sci.*, vol. 4, pp. 315–350, 1954.
- [15] S. M. Seltzer and M. J. Berger, “Improved procedure for calculating the collision stopping power of elements and compounds for electrons and positrons,” *The International Journal of Applied Radiation and Isotopes*, vol. 35, no. 7, pp. 665 – 676, 1984.
- [16] “56 - on the energy loss of fast particles by ionisation,” in *Collected Papers of L.D. Landau* (D. TER HAAR, ed.), pp. 417–424, Pergamon, 1965.
- [17] Y.-S. Tsai, “Pair Production and Bremsstrahlung of Charged Leptons,” *Rev. Mod. Phys.*, vol. 46, p. 815, 1974. [Erratum: *Rev. Mod. Phys.* 49, 421–423 (1977)].
- [18] V. L. Highland, “Some practical remarks on multiple scattering,” *Nuclear Instruments and Methods*, vol. 129, no. 2, pp. 497 – 499, 1975.
- [19] M. Jonker, J. Panman, F. Udo, J. Allaby, U. Amaldi, G. Barbiellini, W. Flegel, W. Koza-necki, K. Mess, M. Metcalf, J. Meyer, P. Monacelli, R. Orr, A. Wetherell, K. Winter, V. Blobel, F. Büsser, P. Gall, H. Grote, B. Kröger, E. Metz, F. Niebergall, K. Ranitzsch, P. Stähelin, P. Gorbunov, E. Grigoriev, V. Kaftanov, V. Khovansky, A. Rosanov, A. Baroncelli, R. Biancastelli, B. Borgia, C. Bosio, A. Capone, F. Ferroni, E. Longo, F. de Notaristefani, P. Pistilli, C. Santoni, and V. Valente, “Measurement of the cross section of antineutrino scattering on electrons,” *Physics Letters B*, vol. 105, no. 2, pp. 242–248, 1981.
- [20] J. N. Marx and D. R. Nygren, “The Time Projection Chamber,” *Phys. Today*, vol. 31N10, pp. 46–53, 1978.

- [21] *Semiconductor Detector Systems*. Oxford University Press, 2005.
- [22] J. Williams, “Cms particle detection summary..” <https://twiki.cern.ch/twiki/bin/view/CMSPublic/W> accessed 28th of September 2020.
- [23] H. Kolanoski and N. Wermes, *Teilchendetektoren - Grundlagen und Anwendungen*. Springer, ISBN : 978-3-662-45349-0, 2016.
- [24] E. Belau, R. Klanner, G. Lutz, E. Neugebauer, H. Seebrunner, A. Wylie, T. Böhringer, L. Hubbeling, P. Weilhammer, J. Kemmer, U. Kötz, and M. Riebesell, “Charge collection in silicon strip detectors,” *Nuclear Instruments and Methods in Physics Research*, vol. 214, no. 2, pp. 253–260, 1983.
- [25] A. Velyka and H. Jansen, “Development and simulations of Enhanced Lateral Drift Sensors,” *JINST*, vol. 14, no. 05, p. C05005, 2019.
- [26] U. Husemann, “A new pixel detector for the cms experiment.” [http://www-ekp.physik.uni-karlsruhe.de/husemann/talks/husemann\\_cms\\_pixel\\_heidelberg\\_20120508.pdf](http://www-ekp.physik.uni-karlsruhe.de/husemann/talks/husemann_cms_pixel_heidelberg_20120508.pdf), 2012. accessed 12th of October 2020.
- [27] “Cern knowledge transfer timepix3 web page.” <https://kt.cern/technologies/timepix3>.
- [28] M. Lupberger, “The Pixel-TPC: first results from an 8-InGrid module,” *JINST*, vol. 9, no. 01, p. C01033, 2014.
- [29] J. Brau, M. Breidenbach, A. Dragone, G. Fields, R. Frey, D. Freytag, M. Freytag, C. Gallagher, G. Haller, R. Herbst, B. Holbrook, R. Lander, A. Moskaleva, C. Neher, T. Nelson, S. Schier, B. Schumm, D. Strom, M. Tripathi, and M. Woods, “Kpix - a 1,024 channel readout asic for the ilc,” in *2012 IEEE Nuclear Science Symposium and Medical Imaging Conference Record (NSS/MIC)*, pp. 1857–1860, 2012.
- [30] R. Bailey *et al.*, “Measurement of the lifetime of charged and neutral D mesons with high resolution silicon strip detectors,” *Z. Phys. C*, vol. 28, pp. 357–363, 1985.
- [31] “Beam telescopes at desy web page..” <https://telescopes.desy.de/>. accessed 24th of October 2020.
- [32] I. Perić, P. Fischer, C. Kreidl, H. Hanh Nguyen, H. Augustin, N. Berger, M. Kiehn, A.-K. Perrevoort, A. Schöning, D. Wiedner, S. Feigl, T. Heim, L. Meng, D. Münstermann,

- M. Benoit, D. Dannheim, F. Bompard, P. Breugnon, J.-C. Clemens, D. Fougeron, J. Liu, P. Pangaud, A. Rozanov, M. Barbero, M. Backhaus, F. Hügging, H. Krüger, F. Lütticke, C. Mariñas, T. Obermann, M. Garcia-Sciveres, B. Schwenker, A. Dierlamm, A. La Rosa, and A. Miucci, “High-voltage pixel detectors in commercial cmos technologies for atlas, clic and mu3e experiments,” *Nuclear Instruments and Methods in Physics Research Section A: Accelerators, Spectrometers, Detectors and Associated Equipment*, vol. 731, pp. 131 – 136, 2013. PIXEL 2012.
- [33] P. V. Hough, “Method and means for recognizing complex patterns,” 12 1962. DOE Patent.
- [34] T. Basar, *A New Approach to Linear Filtering and Prediction Problems*, pp. 167–179. 2001.
- [35] “Private communication with claus kleinwort from desy.”
- [36] C. Kleinwort, “General Broken Lines as advanced track fitting method,” *Nucl. Instrum. Meth.*, vol. A673, pp. 107–110, 2012.
- [37] C. Kleinwort, “General broken lines web page..” <https://www.desy.de/kleinwrt/GBL/doc/cpp/html/index.html>. accessed 26th of October 2020.
- [38] V. Blobel, C. Kleinwort, and F. Meier, “Fast alignment of a complex tracking detector using advanced track models,” *Computer Physics Communications*, vol. 182, no. 9, pp. 1760 – 1763, 2011. Computer Physics Communications Special Edition for Conference on Computational Physics Trondheim, Norway, June 23-26, 2010.
- [39] R. Carnegie, M. Dixit, J. Dubeau, D. Karlen, J.-P. Martin, H. Mes, and K. Sachs, “Resolution studies of cosmic-ray tracks in a tpc with gem readout,” *Nuclear Instruments and Methods in Physics Research Section A: Accelerators, Spectrometers, Detectors and Associated Equipment*, vol. 538, no. 1, pp. 372–383, 2005.
- [40] C. Kleinwort, “Millepede-ii web page..” <https://www.desy.de/kleinwrt/MP2/doc/html/>. accessed 26th of October 2020.
- [41] R. Diener *et al.*, “The DESY II Test Beam Facility,” *Nucl. Instrum. Meth.*, vol. A922, pp. 265–286, 2019.
- [42] G. Hemmie, “Desy ii, a new injector for the desy storage rings petra and doris ii,” *IEEE Transactions on Nuclear Science*, vol. 30, no. 4, pp. 2028–2030, 1983.

- [43] G. Hemmie, U. Berghaus, H. Bottcher, E. Dabkowski, H. R. Heller, G. Meyer, G. Nawrath, F. Schwickert, K. Sinram, G. Wobke, and H. Wumpelmann, "Design, construction and performance of the desy ii magnets," *IEEE Transactions on Nuclear Science*, vol. 32, no. 5, pp. 3625–3627, 1985.
- [44] "Eudet project web page." <https://www.eudet.org/>.
- [45] "Aida project web page." <http://aida-old.web.cern.ch/aida-old/index.html>.
- [46] "Aida2020 project web page." <http://aida2020.web.cern.ch/>.
- [47] P. Baesso, D. Cussans, and J. Goldstein, "The AIDA-2020 TLU: a flexible trigger logic unit for test beam facilities," *Journal of Instrumentation*, vol. 14, pp. P09019–P09019, sep 2019.
- [48] H. Jansen *et al.*, "Performance of the EUDET-type beam telescopes," *EPJ Tech. Instrum.*, vol. 3, no. 1, p. 7, 2016.
- [49] "Homepage of the eudet-type beam telescopes." <https://telescopes.desy.de/>.
- [50] J. Baudot, G. Bertolone, A. Brogna, G. Claus, C. Colledani, Y. Degerli, R. De Masi, A. Dorokhov, G. Dozière, W. Dulinski, M. Gelin, M. Goffe, A. Himmi, F. Guilloux, C. Hu-Guo, K. Jaaskelainen, M. Koziel, F. Morel, F. Orsini, M. Specht, I. Valin, G. Voutsinas, and M. Winter, "First test results of mimosa-26, a fast cmos sensor with integrated zero suppression and digitized output," in *2009 IEEE Nuclear Science Symposium Conference Record (NSS/MIC)*, pp. 1169–1173, 2009.
- [51] A. Himmi, A. Doziere, O. Torheim, C. Hu-Guo, and A. Winter, "A Zero Suppression Micro-Circuit for Binary Readout CMOS Monolithic Sensors," 2009.
- [52] A. Yamamoto *et al.*, "Balloon borne experiment with a superconducting solenoidal magnet spectrometer," 1 1993.
- [53] A. Yamamoto, T. Mito, T. Haruyama, Y. Makida, H. Inoue, N. Kimura, H. Yamaoka, Y. Doi, K. Nakamura, and J. Nishimura, "CONCEPTUAL DESIGN OF A THIN SUPERCONDUCTING SOLENOID FOR PARTICLE ASTROPHYSICS," *IEEE Trans. Magnetics*, vol. 24, no. 2, p. 11508, 1988.
- [54] C. Grefe, "Magnetic Field Map for a Large TPC Prototype," dipl., Universität Hamburg, Hamburg, 2008. Universität Hamburg, Diplomarbeit, 2008.

- [55] T. Behnke, K. Dehmelt, R. Diener, L. Steder, T. Matsuda, V. Prahl, and P. Schade, “A lightweight field cage for a large TPC prototype for the ILC,” *Journal of Instrumentation*, vol. 5, pp. P10011–P10011, oct 2010.
- [56] D. Tsionou, “WP15: Upgrade of test beam infrastructure Task 15.3 Improvements of the DESY test beam infrastructure,” 1st AIDA-2020 Annual Meeting, Hamburg (Germany), 13 Jun 2016 - 14 Jun 2016, Jun 2016.
- [57] F. J. Mueller, *Development of a Triple GEM Readout Module for a Time Projection Chamber & Measurement Accuracies of Hadronic Higgs Branching Fractions in  $vvH$  at a 350 GeV ILC*. Dr., Universitat Hamburg, Hamburg, 2016. Universität Hamburg, Diss., 2016.
- [58] R. Gluckstern, “Uncertainties in track momentum and direction, due to multiple scattering and measurement errors,” *Nuclear Instruments and Methods*, vol. 24, pp. 381–389, 1963.
- [59] S. Agostinelli, J. Allison, K. Amako, J. Apostolakis, H. Araujo, P. Arce, M. Asai, D. Axen, S. Banerjee, G. Barrand, F. Behner, L. Bellagamba, J. Boudreau, L. Broglia, A. Brunengo, H. Burkhardt, S. Chauvie, J. Chuma, R. Chytracsek, G. Cooperman, G. Cosmo, P. Degtyarenko, A. Dell’Acqua, G. Depaola, D. Dietrich, R. Enami, A. Feliciello, C. Ferguson, H. Fesefeldt, G. Folger, F. Foppiano, A. Forti, S. Garelli, S. Giani, R. Giannitrapani, D. Gibin, J. Gómez Cadenas, I. González, G. Gracia Abril, G. Greeniaus, W. Greiner, V. Grichine, A. Grossheim, S. Guatelli, P. Gumplinger, R. Hamatsu, K. Hashimoto, H. Hasui, A. Heikkinen, A. Howard, V. Ivanchenko, A. Johnson, F. Jones, J. Kallenbach, N. Kanaya, M. Kawabata, Y. Kawabata, M. Kawaguti, S. Kelner, P. Kent, A. Kimura, T. Kodama, R. Kokoulin, M. Kossov, H. Kurashige, E. Lamanna, T. Lampén, V. Lara, V. Lefebure, F. Lei, M. Liendl, W. Lockman, F. Longo, S. Magni, M. Maire, E. Medernach, K. Minamimoto, P. Mora de Freitas, Y. Morita, K. Murakami, M. Nagamatu, R. Nartallo, P. Nieminen, T. Nishimura, K. Ohtsubo, M. Okamura, S. O’Neale, Y. Oohata, K. Paech, J. Perl, A. Pfeiffer, M. Pia, F. Ranjard, A. Rybin, S. Sadilov, E. Di Salvo, G. Santin, T. Sasaki, N. Savvas, Y. Sawada, S. Scherer, S. Sei, V. Sirotenko, D. Smith, N. Starkov, H. Stoecker, J. Sulikimo, M. Takahata, S. Tanaka, E. Tcherniaev, E. Safai Tehrani, M. Tropeano, P. Truscott, H. Uno, L. Urban, P. Urban, M. Verderi, A. Walkden, W. Wander, H. Weber, J. Wellisch, T. Wenaus, D. Williams, D. Wright, T. Yamada, H. Yoshida, and D. Zschesche, “Geant4—a simulation toolkit,” *Nuclear*

*Instruments and Methods in Physics Research Section A: Accelerators, Spectrometers, Detectors and Associated Equipment*, vol. 506, no. 3, pp. 250 – 303, 2003.

- [60] “Private communication with dimitra tsionou from desy.”
- [61] T. A. collaboration, “Operation and performance of the ATLAS semiconductor tracker,” *Journal of Instrumentation*, vol. 9, pp. P08009–P08009, aug 2014.
- [62] V. Veszpremi, “Operation and performance of the CMS tracker,” *Journal of Instrumentation*, vol. 9, pp. C03005–C03005, mar 2014.
- [63] V. Chiochia, “The zeus micro-vertex detector,” *Nuclear Instruments and Methods in Physics Research Section A: Accelerators, Spectrometers, Detectors and Associated Equipment*, vol. 501, p. 60–64, Mar 2003.
- [64] A. Savoy-Navarro, “Overview of the SiLC R and D Activities,” in *International Linear Collider Workshop (LCWS08 and ILC08)*, 3 2009.
- [65] D. Freytag, R. Herbst, J. Brau, M. Breidenbach, R. Frey, G. Haller, B. Holbrook, R. Lander, T. Nelson, V. Radeka, D. Strom, and M. Tripathi, “Kpix, an array of self triggered charge sensitive cells generating digital time and amplitude information.,” in *2008 IEEE Nuclear Science Symposium Conference Record*, pp. 3447–3450, 2008.
- [66] J. Brau *et al.*, “A silicon-tungsten electromagnetic calorimeter with integrated electronics for the International Linear Collider,” *J. Phys. Conf. Ser.*, vol. 404, p. 012067, 2012.
- [67] “Hamamatsu photonics homepage..” <https://www.hamamatsu.com>.
- [68] “Tsmc homepage..” <https://www.tsmc.com>.
- [69] “The International Linear Collider Technical Design Report - Volume 3.II: Accelerator Baseline Design,” 2013.
- [70] J. Brau *et al.*, “Lycoris- a large-area, high resolution beam telescope,” *Prepared for JINST currently a placeholder*, 2020.
- [71] “Private communication with volker prahl from desy.”
- [72] “Festo homepage..” <https://www.festo.com/us/en/>.
- [73] “Rogue daq web page.” <https://slaclab.github.io/rogue/>.

- [74] “Wiener power electronics hv/lv module web page.” <http://www.wiener-d.com/sc/power-supplies/mpod-lvhv/>.
- [75] “Samtec ehf connector web page.” <https://www.samtec.com/products/ehf>.
- [76] “Molex power connectors home page.” [https://www.molex.com/molex/products/group/power\\_con](https://www.molex.com/molex/products/group/power_con)
- [77] “Molex connector data sheet.” [https://www.molex.com/webdocs/datasheets/pdf/en-us/0039012040\\_CRIMP\\_HOUSINGS.pdf](https://www.molex.com/webdocs/datasheets/pdf/en-us/0039012040_CRIMP_HOUSINGS.pdf).
- [78] “Samtec erf5 connector web page.” <https://www.samtec.com/products/erf5>.
- [79] “Samtec erm5 connector web page.” <https://www.samtec.com/products/erm5>.
- [80] “Private communication with benjamin a. reese from slac.”
- [81] Y. Liu *et al.*, “EUDAQ2—A flexible data acquisition software framework for common test beams,” *JINST*, vol. 14, no. 10, p. P10033, 2019.
- [82] “Araldite2011 technical data sheet.” <https://www.intertronics.co.uk/wp-content/uploads/2015/12/ara2011.pdf>.
- [83] “8331 silver conductive epoxy data sheet.” <https://www.mgchemicals.com/downloads/tds/tds-8331-2parts.pdf>.
- [84] “Private communication with prof. dr. erika garutti from university hamburg,” 2018.
- [85] “Heraeus wire bond data sheet.” [https://www.heraeus.com/media/media/het/doc\\_het/products\\_and\\_solutions\\_het\\_documents/bonding\\_wires\\_documents/Brochure\\_Bonding\\_Wire.pdf](https://www.heraeus.com/media/media/het/doc_het/products_and_solutions_het_documents/bonding_wires_documents/Brochure_Bonding_Wire.pdf).
- [86] “Keithley 6517b data sheet.” <https://www.tek.com/datasheet/high-resistance-low-current-electrometers-series-6500-6430/model-6517b-electrometer-high-r>.
- [87] “Agilent e4980 precision lcr meter.” <https://www.keysight.com/en/pd-715495-pn-E4980A/precision-lcr-meter-20-hz-to-2-mhz>.
- [88] “Keithley 6485 data sheet.” <https://www.tek.com/datasheet/series-6400-picoammeters/model-6485-picoammeter>.
- [89] “Private communication with timothy knight nelson from slac.”

- [90] T. Poikela, J. Plosila, T. Westerlund, M. Campbell, M. D. Gaspari, X. Llopart, V. Gromov, R. Kluit, M. van Beuzekom, F. Zappone, V. Zivkovic, C. Brezina, K. Desch, Y. Fu, and A. Kruth, “Timepix3: a 65k channel hybrid pixel readout chip with simultaneous ToA/ToT and sparse readout,” *Journal of Instrumentation*, vol. 9, pp. C05013–C05013, may 2014.
- [91] D. Dannheim *et al.*, “Corryvreckan: A Modular 4D Track Reconstruction and Analysis Software for Test Beam Data,” 11 2020.
- [92] T. Bisanz, H. Jansen, J.-H. Arling, A. Bulgheroni, J. Dreyling-Eschweiler, T. Eichhorn, I. Gregor, P. Hamnett, C. Kleinwort, A. Morton, H. Perrey, M. Queitsch-Maitland, E. Rossi, and S. Spannagel, “EU Telescope: A modular reconstruction framework for beam telescope data,” *Journal of Instrumentation*, vol. 15, pp. P09020–P09020, sep 2020.
- [93] R. Brun and F. Rademakers, “Root — an object oriented data analysis framework,” *Nuclear Instruments and Methods in Physics Research Section A: Accelerators, Spectrometers, Detectors and Associated Equipment*, vol. 389, no. 1, pp. 81 – 86, 1997. *New Computing Techniques in Physics Research V*.
- [94] V. Blobel, “Software alignment for tracking detectors,” *Nucl. Instrum. Meth.*, vol. A566, pp. 5–13, 2006.
- [95] “Private communication with dietrich r. freytag from slac,” 2020.
- [96] “Especc sh-242 benchtop climate chamber.” [https://espec.com/na/products/model/sh\\_242](https://espec.com/na/products/model/sh_242).
- [97] “Tti cpx400dp dc power supply.” <https://www.aimtti.com/product-category/dc-power-supplies/aim-cpxseries>.
- [98] “Tektronix series 2400 sourcemeter.” <https://www.tek.com/datasheet/series-2400-sourcemeter-instruments>.
- [99] “Fluke 975 airmeter.” <https://www.fluke.com/en-us/product/building-infrastructure/indoor-air-quality-testing/fluke-975>.
- [100] T. Poehlsen, E. Fretwurst, R. Klanner, S. Schuwalow, J. Schwandt, and J. Zhang, “Charge losses in segmented silicon sensors at the Si-SiO<sub>2</sub> interface,” *Nucl. Instrum. Meth. A*, vol. 700, pp. 22–39, 2013.



- [101] T. Poehlsen, E. Fretwurst, R. Klanner, J. Schwandt, and J. Zhang, “Time dependence of charge losses at the  $Si-SiO_2$  interface in  $p^+n$ -silicon strip sensors,” *Nucl. Instrum. Meth. A*, vol. 731, pp. 172–176, 2013.
- [102] T. Poehlsen, J. Becker, E. Fretwurst, R. Klanner, J. Schwandt, and J. Zhang, “Study of the accumulation layer and charge losses at the Si-SiO<sub>2</sub> interface in p+n-silicon strip sensors,” *Nucl. Instrum. Meth. A*, vol. 721, pp. 26–34, 2013.
- [103] H. W. Kraner, Z. Li, and E. Fretwurst, “The Use of the signal current pulse shape to study the internal electric field profile and trapping effects in neutron damaged silicon detectors,” *Nucl. Instrum. Meth. A*, vol. 326, pp. 350–356, 1993.
- [104] J. Becker, E. Fretwurst, and R. Klanner, “Measurements of charge carrier mobilities and drift velocity saturation in bulk silicon of  $\langle 111 \rangle$  and  $\langle 100 \rangle$  crystal orientation at high electric fields,” *Solid State Electron.*, vol. 56, p. 104, 2011.
- [105] J. Fernández-Tejero, P. Allport, O. Aviñó, K. Dette, V. Fadeyev, C. Fleta, D. Gillberg, L. Gonella, K. Hara, C. Helling, B. Hommels, J. Keller, C. Klein, T. Koffas, V. Latonova, M. Mikestikova, R. Orr, S. Pyatt, C. Scharf, U. Soldevila, E. Staats, J. Thomas, M. Ullán, Y. Unno, M. Vellvehí, and S. Wada, “Humidity sensitivity of large area silicon sensors: Study and implications,” *Nuclear Instruments and Methods in Physics Research Section A: Accelerators, Spectrometers, Detectors and Associated Equipment*, vol. 978, p. 164406, 2020.
- [106] “Private communication with lennart huth from desy.”
- [107] S. Chatrchyan *et al.*, “The CMS Experiment at the CERN LHC,” *JINST*, vol. 3, p. S08004, 2008.
- [108] P. Ahlburg *et al.*, “EUDAQ-a data acquisition software framework for common beam telescopes,” *JINST*, vol. 15, no. 01, p. P01038, 2020.
- [109] “Amphenol minitek connector web page.” <https://www.amphenol-icc.com/product-series/minitek-200mm-wtb.html>.
- [110] V. Blobel and E. Lohrmann, *Statistische und Numerische Methoden der Datenanalyse*. Teubner, ISBN 978-3-935702-66-9 (e-Buch), 2012.



## **Eidesstattliche Versicherung**

Hiermit versichere ich an Eides statt, die vorliegende Dissertationsschrift selbst verfasst und keine anderen als die angegebenen Hilfsmittel und Quellen benutzt zu haben.

Die eingereichte schriftliche Fassung entspricht der auf dem elektronischen Speichermedium.

Die Dissertation wurde in der vorgelegten oder einer ähnlichen Form nicht schon einmal in einem früheren Promotionsverfahren angenommen oder als ungenügend beurteilt.

## **Declaration on Oath**

I hereby declare, on oath, that I have written the present dissertation by my own and have not used other than the acknowledged resources and aids.

Hamburg, den 24/02/2021

Uwe Krämer